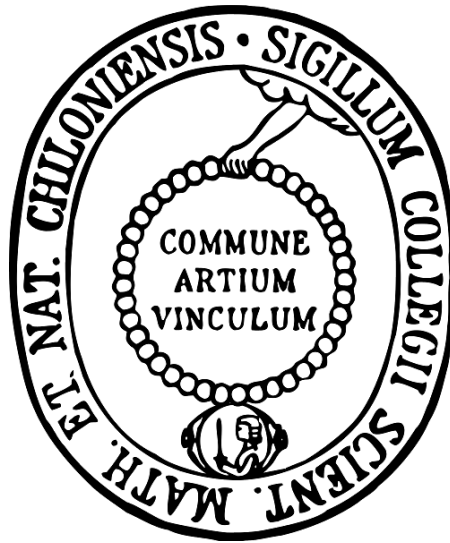


Photoactivatable Kinase Inhibitors



Dissertation

zur Erlangung des Doktorgrades

der Mathematisch-Naturwissenschaftlichen Fakultät

der Christian-Albrechts-Universität zu Kiel

vorgelegt von

Rebecca Horbert

Kiel 2015

Erster Gutachter:	Prof. Dr. Christian Peifer
Zweiter Gutachter:	Prof. Dr. Thomas Kunze
Tag der mündlichen Prüfung:	17.11.2015
Zum Druck genehmigt:	17.11.2015
	Prof. Dr. Wolfgang J. Duschl (Dekan)

*We are each gifted in a unique and important way.
It is our privilege and our adventure to discover
our own special light.*

Evelyn Mary Dunbar

ABSTRACT

Photochemistry and kinase inhibitor research have both independently been of major scientific interest in the last decades. The objective of this study was therefore to combine both research fields by the development of photoactivatable kinase inhibitors. Herein, the fascinating possibilities of photochemistry were applied on a unique group of pharmacological agents.

This study reports on photoactivatable prodrugs of VEGFR inhibitors and the approved BRAF inhibitor vemurafenib. The latter shows impressive outcomes in the personalized treatment of malignant melanoma, but side effects and drug resistance limit therapeutic results. In order to conquer these limitations and to create powerful biological tools for kinase and cancer research, so-called caged prodrugs were developed. Photoremovable protecting groups (PPGs) were thus implemented at crucial pharmacophoric functionalities of the inhibitors in order to diminish their biological effects. This approach provides control over the activation of molecules triggered by ultraviolet light. First, the hinge binder moiety of vemurafenib, a 7-azaindole, was investigated concerning its properties as a leaving group in the photolysis reaction. Several PPGs were then examined with regard to chemical accessibility and release characteristics. Next, photoactivatable prodrugs of vemurafenib and VEGFR inhibitors, a diarylmalimide and a carbazole, were designed and synthesized. Their photochemical features were subsequently investigated. *In vitro* evaluation proved the loss-of-function of the prodrugs and the light-dependent recovery of efficacy in kinase and cellular assays.

The approved VEGFR inhibitor axitinib was furthermore investigated as a photoswitchable kinase inhibitor. Based on molecular modeling, the (*Z*)-isomer should be significantly less active toward the targets of (*E*)-axitinib. It was therefore explored if the inhibitory effect of axitinib could be turned on and off triggered by irradiation. The switching properties of the photoinduced *E-Z* isomerization were thus examined. Interestingly, the formation of a (*Z*)-axitinib tautomer was observed. *In vitro* analyses demonstrated the decreased efficacy of the (*Z*)-isomer at an enzymatic level. These results, however, did not translate into cell proliferation assays leaving the paradoxically more active (*Z*)-isomer for future investigation.

In conclusion, the first photoactivatable vemurafenib and VEGFR inhibitor prodrugs have been synthesized and characterized in the course of this study. A decreased potency of the (*Z*)-stereoisomer of axitinib has been demonstrated in enzymatic assays. The applicability of axitinib as a photoswitch remains to be confirmed in further biological assays.

KURZZUSAMMENFASSUNG

Photochemie und die Entwicklung von Kinaseinhibitoren stehen seit Jahrzehnten unabhängig voneinander im Fokus der Wissenschaft. Das Ziel dieser Arbeit war daher, beide Forschungsgebiete durch die Entwicklung photoaktivierbarer Kinaseinhibitoren miteinander zu verknüpfen. Die faszinierenden Möglichkeiten der Photochemie wurden dabei auf eine einzigartige Gruppe pharmakologischer Substanzen angewendet.

Diese Arbeit berichtet über photoaktivierbare Prodrugs von VEGFR-Inhibitoren sowie des zugelassenen BRAF-Inhibitors Vemurafenib. Dieser zeigt beeindruckende Erfolge in der personalisierten Behandlung des malignen Melanoms, jedoch limitiert durch Nebenwirkungen und Resistenzen. Um diesen Limitierungen zu begegnen und um leistungsfähige Werkzeuge für die Kinase- und Krebsforschung bereitzustellen, wurden sogenannte *caged prodrugs* entwickelt. Dazu wurden photoabspaltbare Schutzgruppen (PPGs) an zentralen pharmakophoren Gruppen der Inhibitoren angebracht, um diese biologisch zu inaktivieren. Dies erlaubt die Kontrolle über die Aktivierung von Molekülen durch ultraviolettes Licht. Zunächst wurde der *hinge-binder* des Vemurafenibs, das 7-Azaindol, hinsichtlich seiner Eigenschaft als Abgangsgruppe in der Photolyse-Reaktion näher untersucht. Verschiedene PPGs wurden bezüglich chemischer Zugänglichkeit und Freisetzung gegenübergestellt. Anschließend wurden *caged prodrugs* des Vemurafenibs sowie Inhibitoren aus der Klasse der Diarylmaleimide bzw. Carbazole designt und synthetisiert. Ihre photochemischen Eigenschaften wurden untersucht. *In vitro*-Experimente bestätigten den Wirkungsverlust der Prodrugs sowie die lichtabhängige Wiederherstellung der Wirkung in Kinase- und Zellassays.

Ferner wurde der zugelassene VEGFR-Inhibitor Axitinib als photoschaltbarer Kinaseinhibitor untersucht. *Molecular modeling* legte nahe, dass das (*Z*)-Stereoisomer schwächer wirksam sei als das (*E*)-Isomer. Daher wurde untersucht, ob die Wirkung von Axitinib durch Bestrahlung reversibel geschaltet werden kann. Interessanterweise konnte dabei die Bildung eines Tautomers des (*Z*)-Isomers beobachtet werden. *In vitro*-Studien zeigten eine Verringerung des hemmenden Effekts des (*Z*)-Isomers auf enzymatischer Ebene. Diese Ergebnisse übertrugen sich allerdings nicht auf Zell-Proliferations-Assays. Die hierin paradoxerweise gesteigerte Wirkung des (*Z*)-Isomers sollte daher noch eingehender untersucht werden.

Im Rahmen dieser Arbeit wurden die ersten photoaktivierbaren Vemurafenib- und VEGFR-Inhibitor-Prodrugs synthetisiert und charakterisiert. Die verringerte Wirkung des Axitinib- (*Z*)-Stereoisomers wurde in enzymatischen Assays nachgewiesen. Die Anwendbarkeit als Photoschalter muss jedoch noch in weiteren biologischen Testsystemen bestätigt werden.

TABLE OF CONTENTS

1. Introduction	1
1.1 Activation by Light.....	2
1.1.1 Caging Concept	3
1.1.2 Photoswitches	6
1.1.3 Ultraviolet Light	8
1.2 Kinase Inhibitors	10
1.2.1 Protein Kinases	15
1.2.2 BRAF ^{V600E} Inhibitor Vemurafenib	22
1.2.3 VEGFR Inhibitors Diarylmaleimide and Carbazole.....	25
1.2.4 VEGFR Inhibitor Axitinib.....	28
2. Aims and Objectives.....	30
2.1 Caged Vemurafenib.....	30
2.2 Caged Diarylmaleimides and Carbazole	33
2.3 Photoswitchable Axitinib	34
3. Results and Discussion	35
3.1 Caged Vemurafenib.....	35
3.1.1 Molecular Modeling	35
3.1.2 UV Stability.....	38
3.1.3 Synthesis	39
3.1.4 Photochemical Characterization	48
3.1.5 Biological Evaluation	58
3.2 Caged Diarylmaleimides and Carbazole	64
3.2.1 Molecular Modeling	64
3.2.2 Synthesis.....	67
3.2.3 Photochemical Characterization	70
3.2.4 Biological Evaluation	73
3.3 Photoswitchable Axitinib	78
3.3.1 Molecular Modeling	78
3.3.2 Synthesis and Tautomerism.....	80
3.3.3 Photochemical Characterization	83
3.3.4 Biological Evaluation	85
4. Conclusion.....	91
4.1 Caged Vemurafenib.....	91
4.2 Caged Diarylmaleimides and Carbazole	94
4.3 Photoswitchable Axitinib	95

5. Experimental	96
5.1 Molecular Modeling	96
5.2 Photoexperiments	97
5.2.1 UV/vis Absorption Spectra.....	97
5.2.2 UV Stability.....	97
5.2.3 Photoactivation	98
5.2.4 Photoswitching Experiments	98
5.3 Chemical Synthesis and Characterization	99
5.3.1 Reagents and Solvents	99
5.3.2 Flash Chromatography.....	99
5.3.3 TLC.....	99
5.3.4 HPLC	99
5.3.5 Melting Point	100
5.3.6 NMR	100
5.3.7 LC-MS	100
5.3.8 HRMS	101
5.3.9 X-ray Crystallography	101
5.3.10 Chemical Synthesis.....	102
5.4 Biological Evaluation	140
5.4.1 Kinase Assays (K _d values)	140
5.4.2 Kinase Assays (IC ₅₀ values)	140
5.4.3 Kinase Profiling	141
5.4.4 Cell Culture.....	142
5.4.5 Proliferative Assays	143
5.4.6 Stability in Cellular Medium	143
5.4.7 Western Blot Analyses	144
6. References	146
7. Appendix	159
Table of Abbreviations	170
Table of Compounds	173
Lebenslauf	178
Erklärung	179
Danksagung	181

1. INTRODUCTION

Photochemistry and the development of kinase inhibitors are both disciplines that have independently received much attention by the research community over the last decades. It is therefore rather surprising that the combination of both fields has been neglected so far.

Activation by light provides precise spatial and temporal control of biological processes.¹⁻⁵ This offers unparalleled opportunities to understand and influence complex biochemical mechanisms, even in living cells.² The introduction of kinase inhibitors was a milestone in modern drug discovery and revolutionized targeted cancer therapy.^{6,7} However, lack of efficacy, limited selectivity, the occurrence of therapy-limiting side effects, and the emergence of tumor resistances illustrate the urgent need for novel drug candidates as well as innovative therapeutic approaches.^{6,8} New concepts that are able to reduce adverse events and overcome tumor resistance would be of significant benefit.^{6,8}

The objective of this study, therefore, was to combine both research fields by the development of photoactivatable kinase inhibitors. The fascinating possibilities of photochemistry were herein applied on a unique group of pharmacological substances.

1.1 ACTIVATION BY LIGHT

Spatial and temporal control of biological processes is a fascinating challenge.⁵ Light seems to be an ideal trigger for an external control of biochemical mechanisms due to its high spatiotemporal resolution as well as non-invasive and orthogonal character.⁵ Furthermore, it does not cause contamination of the sample; wavelength and intensity can be regulated with high precision, *e.g.* with lasers or microscopes.⁵ Rapid concentration jumps of the active form of a light-responsive molecule can be achieved providing precise control of area, time, and dosage.²

The photocontrol of biologically active compounds offers outstanding experimental possibilities.⁹ Photoactivatable ligands have become important tools in drug discovery and drug development.⁹ They are used for a wide range of applications including target identification, determination of ligand affinity resp. selectivity, and detection of binding sites.⁹ The selectivity of drugs can furthermore be increased by controlling their activity with light.⁵ This might be beneficial with regard to the occurrence of side effects or the emergence of resistances.⁵ Not only small molecules have nowadays undergone this strategy, but also nucleic acids, peptides, and even large proteins.⁴

In general, there are different strategies to control the activity of molecules by irradiation. They can either be irreversibly activated by light (so-called *caged compounds*) or reversibly switched between an active and an inactive form (*photoswitches*).^{3,4,10}

1.1.1 Caging Concept

Caged compounds can be activated by irradiation with light.^{10,11} The implementation of photoremovable protection groups (PPGs) provides control over the release of bioactive molecules triggered by ultraviolet (UV) light (Figure 1).^{1,2} Higher drug concentrations can therefore be reached in the area of interest, sparing other compartments.² The photo prodrug concept is essentially based on the blockade of a pharmacophoric group. The PPG is thus attached to the drug molecule by a covalent bond.² This bond has then to be cleaved by radiant energy, releasing the parent bioactive compound.²

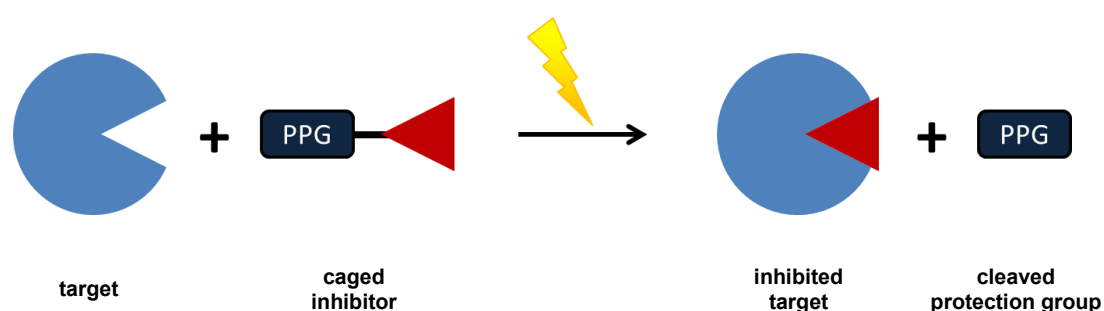


Figure 1. Schematic representation of the caging principle. An inhibitor is covalently linked to a PPG and thus biologically inactive (“caged”). Irradiation with UV light cleaves this bond and the bioactive compound is released.

The first and most prominent example is certainly the photorelease of caged adenosine triphosphate (ATP) by Kaplan and co-workers in 1978.¹² Intensive research has since then been carried out in the field of photochemistry concerning various classes of protecting groups and evaluation of their photocharacteristics.^{4,9–11,13–15} Klán *et al.*¹⁰ defined six main categories of PPGs with more than twenty subcategories (Figure 2). Hundreds of derivatives have been specified within these classes, attachable to a variety of leaving groups and offering a wide range of absorption maxima and release characteristics.

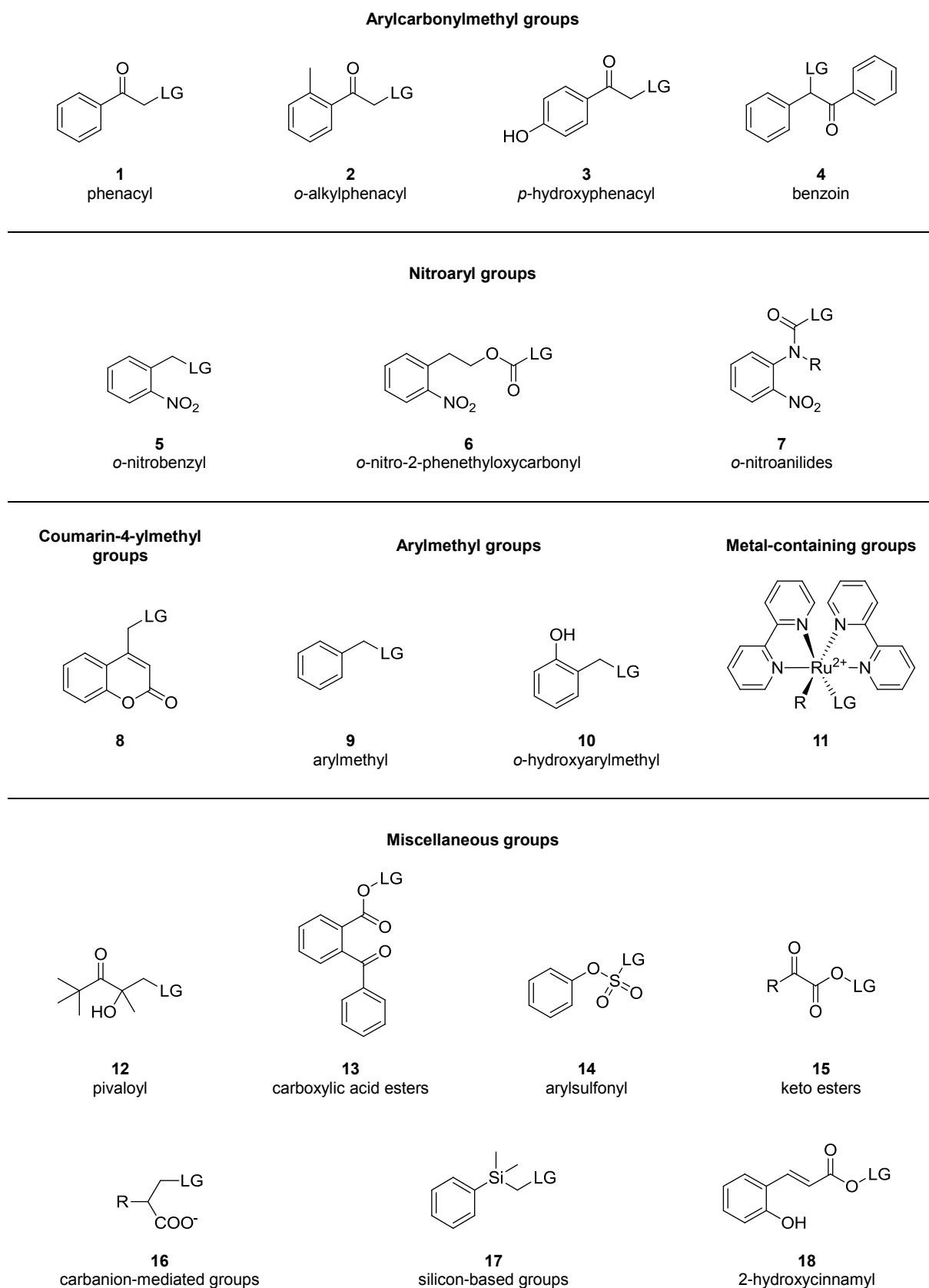


Figure 2. Chemical structures of diverse PPGs classes.¹⁰ LG = leaving group.

Nevertheless, none of these PPGs can be considered to provide perfect characteristics in all criteria.^{10,13} An individual selection has therefore to be made depending on the intended application. This choice is based on the following parameters and requirements:

- low intrinsic activity of the caged compound and good stability under assay conditions prior to photolysis; good solubility and permeability;
- high absorption coefficients at a nonhazardous wavelength > 300 nm, high quantum yield (efficiency for release), clean and quantitative photoreaction;
- biocompatible photochemical by-products with low absorption at the irradiation wavelength; and
- for time-resolved work, the release rate of the bioagent must exceed that of the response investigated.^{10,13}

o-Nitrobenzyl derivatives have by far been the most commonly used PPGs.¹ A broad spectrum of derivatives has been established with different absorption wavelengths and the ability to be attached to a variety of leaving groups.^{10,16–19} Photolysis of these prodrugs forms potentially toxic by-products, though, containing a reactive nitroso function (*e.g.* *o*-nitrosobenzaldehyde) with strong innate absorption.¹ To conquer these disadvantages a high number of alternative PPGs has been developed.

While the caging concept has been successfully applied on various bioagents, there are only a few reports on photoactivatable kinase inhibitors. Morckel *et al.* for instance created a photoactivatable small-molecule Rho kinase inhibitor.²⁰ This tool compound was used to uncover molecular mechanisms of embryonic development in *Xenopus laevis* by targeting specific regions of the living embryo.²⁰ In addition, small molecular equivalents of Src kinase have been caged²¹ as well as peptidic PKA inhibitors²². Light-regulated protein kinase C peptide-based sensors²³ and tyrosine kinase reporters²⁴ have furthermore been described. In our group, Zindler *et al.* recently reported about the design, synthesis, and characterization of a photoactivatable caged prodrug of imatinib.²⁵

Activation of caged compounds remains irreversible though. But for many pharmacological applications a reversible activation and deactivation of kinase inhibitors would be of high value for an improved control over the effects of active molecules.

1.1.2 Photoswitches

Important biological processes are regulated by light in a reversible manner *e.g.* vision²⁶ and photosynthesis^{3,27}. Photons are absorbed by a chromophore leading to a conformational transformation. The term *photoswitch* is therefore used for molecules which switch reversibly between two or more isomeric forms induced by light.³

A broad range of synthetic photoswitches has been designed.³ These molecular switches undergo conformational changes in their structure depending on the wavelength of the irradiated light.³ They can be characterized by the absorption maxima of their isoforms and by their photostationary state (PPS). This term is defined as a steady state reached by a reacting chemical system when light has been absorbed.²⁸ Szymański *et al.*³ list six categories of molecular photoswitches (Table 1). They differentiate between chromophores that switch between *E* and *Z* configuration (azobenzenes, stilbenes, and hemithioindigos) and chromophores that interconvert between closed and open forms (spiropyrans, diarylethenes, and fulgides). The change in the three-dimensional (3D) geometry then modifies the biological effect. The most studied synthetic photoswitches are azobenzenes.²⁹ A photoswitchable RET kinase inhibitor bearing an azobenzene group has recently been described.³⁰

The approved kinase inhibitors axitinib (**19**) and sunitinib (**20**) exhibit photosensitivity.^{31,32} Both inhibitors are diarylethenes (Figure 3), but do not convert to a closed form upon irradiation. Instead an *E-Z* isomerization can be observed. They might, therefore, also be described as stilbene-like.

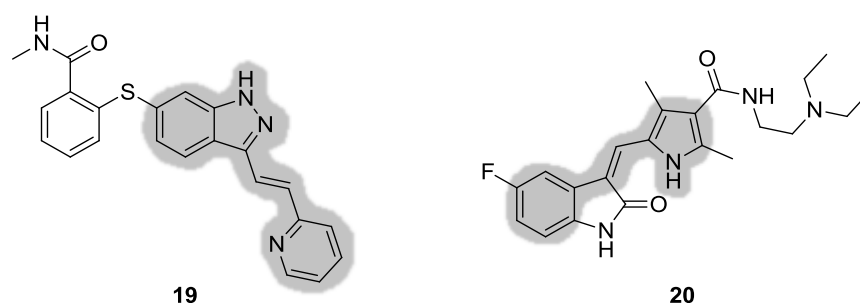
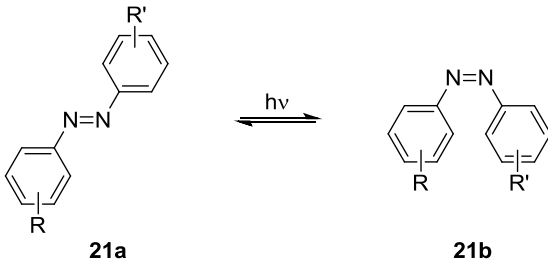
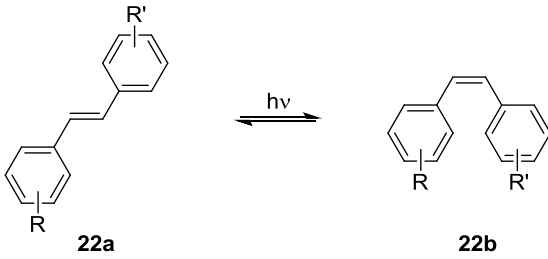
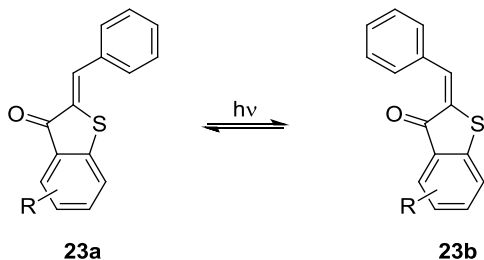
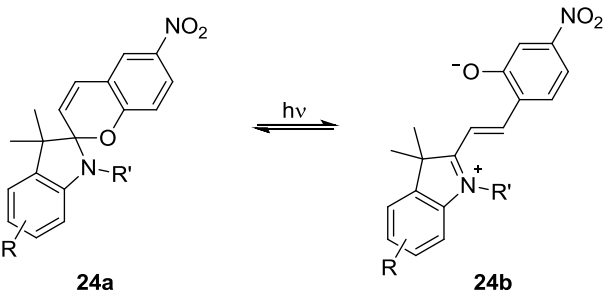
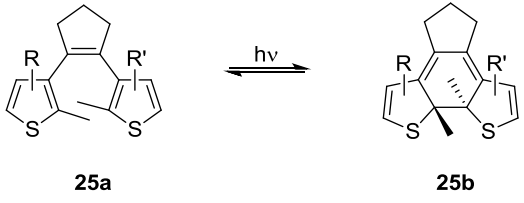
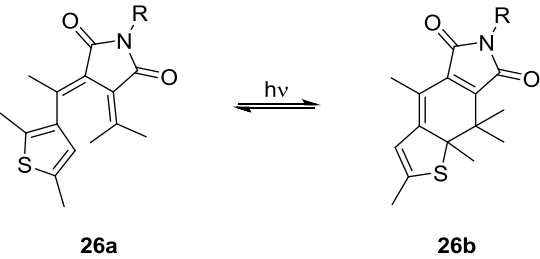


Figure 3. Chemical structures of the light-sensitive approved kinase inhibitors axitinib (**19**) and sunitinib (**20**). The diarylethene structural element is highlighted in grey.

This light-dependent isomerization offers an interesting starting point for the development of innovative photoswitchable kinase inhibitors.

Table 1. Groups of molecular photoswitches.³

Photoswitches	Light-induced Isomerization
Azobenzenes	 <p style="text-align: center;"> $\text{21a} \xrightleftharpoons{h\nu} \text{21b}$ </p>
Stilbenes	 <p style="text-align: center;"> $\text{22a} \xrightleftharpoons{h\nu} \text{22b}$ </p>
Hemithioindigos	 <p style="text-align: center;"> $\text{23a} \xrightleftharpoons{h\nu} \text{23b}$ </p>
Spiropyrans	 <p style="text-align: center;"> $\text{24a} \xrightleftharpoons{h\nu} \text{24b}$ </p>
Diarylethenes	 <p style="text-align: center;"> $\text{25a} \xrightleftharpoons{h\nu} \text{25b}$ </p>
Thiophenefulgides	 <p style="text-align: center;"> $\text{26a} \xrightleftharpoons{h\nu} \text{26b}$ </p>

1.1.3 Ultraviolet Light

Sunlight is composed of a continuous spectrum of electromagnetic radiation and can be divided into three sections:

- ultraviolet (UV, wavelength range 100-400 nm)
- visible (vis, 400-750 nm), and
- infrared (IR, 750 nm-500 μ m) light.^{33,34}

UV radiation can further be subdivided into UVA, UVB, and UVC (Table 2).³⁴ It interacts with chemical molecules, particularly organic compounds, and thus causes *e.g.* fluorescence excitation or initiates chemical reactions. UV light shows distinct biological effects and has been used for many scientific applications, for instance in the field of photochemistry.^{14,33}

Table 2. Classification of UV light wavelength ranges and corresponding biological effects.^{33,34}

Name	Abbreviation	Wavelength	Biological Effects
Ultraviolet A (near UV)	UVA	315-400 nm	Skin tanning Photoaging Carcinogenic effects
Ultraviolet B	UVB	280-315 nm	Photosynthesis of vitamin D Erythema Carcinogenic effects DNA damage Photokeratitis
Ultraviolet C	UVC	100-280 nm	Photokeratitis Microbiocidal effects

UV light sources

The spectrum of the sunlight contains only a small amount of UV radiation.³⁵ Artificial light sources like mercury or xenon arcs, often in combination with optical filters, are mostly used in photochemistry.^{2,35} Lasers emit precisely focused monochromatic light with high power and have been used for multiple applications.^{2,35}

In this work, light-emitting diodes (LEDs) have been used which have undergone a rapid development in the past years. They are semiconductors and emit light over a narrow wavelength range (± 10 nm).³⁵ A large type variety with emission between the near UV and the IR light range are commercially available.¹ The development of models with an emission below 365 nm, however, is in early stages and intensities are still very low.³⁵ LEDs are small devices with high intensity, do not need a warm-up period and can be flexibly assembled. They are therefore convenient for chemical and biochemical applications.

Medicinal applications

Besides the various damaging effects of UV irradiation on biological systems, it has also been utilized as a therapeutic agent for various dermatological diseases.³³ Plant extracts that contain the natural photosensitizer psoralen (**27**, Figure 4), a coumarin derivative, have been topically applied followed by sunlight exposure in Egypt thousands of years ago.³³ This remedy was used as a treatment for vitiligo (leucoderma), a chronic skin disease which is characterized by the loss of pigmentation.^{33,34} The first modern clinical studies with topical and oral psoralens were reported in 1948.^{36,37} Orally administration of 8-methoxypsoralen (8-MOP, **28**, Figure 4) and subsequent irradiation with UVA light proved to be effective against psoriasis, mycosis, vitiligo, and atopic dermatitis.³⁸ This type of photochemotherapy is also called PUVA (psoralen plus UVA) therapy.³³ Psoralens herein act as DNA intercalators and form, upon UVA irradiation, monoadducts as well as covalent interstrand cross-links with thymine residues which induces apoptosis.³⁹ UVB radiation has also been successfully applied for clearing psoriasis.⁴⁰ However, these phototherapies are associated with acute and chronic side effects of UV light on human skin.^{33,41}

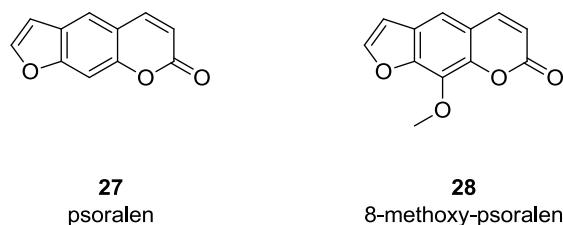


Figure 4. Chemical structures of the furocoumarins psoralen (**27**) and 8-methoxy-psoralen (8-MOP, **28**).

1.2 KINASE INHIBITORS

Protein kinases have become one of the most pursued targets in pharmacological research in the last decades.⁴² Due to their key role in cellular signaling, the misregulation of kinase activity is the cause for many diseases. Besides various forms of cancer, their regulation is *e.g.* critical for the development of inflammatory diseases, Alzheimer's, and Parkinson's disease.^{43–45}

Kinase inhibitors have been successfully established over the past 15 years, especially in cancer treatment. To date, there are 28 FDA (Food and Drug Administration) approved small-molecule kinase inhibitors (smKI); half of which have been approved in the past three years.^{42,46} For an overview of these drugs, their targets, and indications as well as dates of approval, see Table 3. The corresponding chemical structures are shown in Figures 5, 6, and 7.

The approval of imatinib (**31**, Figure 5) in 2001 was a milestone in modern drug discovery and revolutionized targeted cancer therapy.⁴⁷ An unparalleled development of innovative drugs was set in motion. Further eight protein kinase inhibitors were introduced into therapy until 2009. Meanwhile, the knowledge about kinase signaling networks and associated pathology steadily grew.⁴² Since 2011 a tremendous number of 19 new inhibitors has been approved and numerous candidates are currently in the pipeline.⁴²

Even though these molecules are structurally very homogeneous and many chemical features have been *recycled* for the development of the successors, innovations are yet achieved. New targets have been addressed; accomplishments with regard to potency and selectivity have been made.⁴² The first lipid kinase inhibitor, namely idelalisib^{48,49} (**51**, Figure 7), was approved in 2014; all other compounds represent protein kinase inhibitors. With respect to afatinib⁵⁰ and ibrutinib⁵¹ (**52** and **53**, Figure 7), the first two covalent binding, thus irreversible inhibitors were introduced in 2013.⁵² The first allosteric inhibitor, trametinib (**54**, Figure 7), was also launched in 2013.⁵³

However, despite the progress already being made in the field of kinase inhibitor research, the current treatments concentrate on a very limited number of target proteins. In addition, severe side effects and rapidly emerging resistances often limit the therapeutic prospects. But more than one million publications on kinases in the past years, over 5000 crystal structures, and current achievements in the development of kinase assays allow looking into the future optimistically.⁴²

Table 3. Currently FDA approved small-molecule kinase inhibitors.^{42,45,46,54-56} INN, international nonproprietary name; ALL, acute lymphoblastic leukemia; CLL, chronic lymphocytic leukemia; CML, chronic myeloid leukemia; CRC, colorectal cancer; FL, follicular lymphoma; GIST, gastrointestinal stromal tumor; HCC, hepatocellular cancer; MCL, mantle cell lymphoma; NSCLC, non-small cell lung cancer; RCC, renal cell carcinoma; SLL, small lymphocytic leukemia.

INN	Trade Name	Binding Mode, Type	Main Target(s)	Indication(s)	First FDA Approval
Afatinib	Gilotrif	I, covalent	EGFR, HER2/4	NSCLC	2013
Axitinib	Inlyta	I	VEGFR, PDGFR, cKIT	RCC	2012
Bosutinib	Bosulif	I	ABL, SRC	CML	2012
Cabozantinib	Cometriq	II	VEGFR, PDGFR, KIT, MET	thyroid cancer	2012
Ceritinib	Zykadia	I	ALK, IGF-1R, InsR, ROS1	NSCLC	2014
Crizotinib	Xalcori/Xalkori	I	ALK, MET	NSCLC	2011
Dabrafenib	Tafinlar	I	BRAF	melanoma	2013
Dasatinib	Sprycel	I	ABL, PDGFR, KIT, SRC	CML, ALL	2006
Erlotinib	Tarceva	I	EGFR	NSCLC, pancreatic cancer	2004
Gefitinib	Iressa	I	EGFR	NSCLC	2003
Ibrutinib	Imbruvica	I, covalent	BTK	MCL, CLL	2013
Idelalisib	Zydelig	I	PI3K	CLL, FL, SLL	2014
Imatinib	Gleevec/Glivec	II	ABL, PDGFR, KIT	CML, GIST	2001
Lapatinib	Tykerb/Tyverb	I ⁵⁶ , II ⁵⁷	HER2, EGFR	breast cancer	2007
Lenvatinib	Lenvima	I ⁵⁵ , II ⁴²	VEGFR, FGFR, PDGFR, KIT	thyroid cancer	2015
Nilotinib	Tasigna	II	ABL, PDGFR, KIT	CML	2007
Nintedanib	Ofev	II	FGFR, PDGFR, VEGFR	idiopathic pulmonary fibrosis	2014
Palbociclib	Ibrance	I	CDK4/6	breast cancer	2015
Pazopanib	Votrient	I ⁵⁶ , II ⁴²	VEGFR, PDGFR, KIT	RCC	2009
Ponatinib	Iclusig	II	ABL, VEGFR, PDGFR, FGFR	CML, ALL	2012
Regorafenib	Stivarga	II	VEGFR, ABL, BRAF, KIT, PDGFR	CRC, GIST	2012
Ruxolitinib	Jakafi/Jakavi	I	JAK	myelofibrosis	2011
Sorafenib	Nexavar	II	VEGFR, PDGFR, KIT, BRAF	RCC, HCC, thyroid cancer	2005
Sunitinib	Sutent	I	VEGFR, KIT, PDGFR, FLT3	RCC, GIST	2006
Tofacitinib	Xeljanz	I	JAK	rheumatoid arthritis	2012
Trametinib	Mekinist	III	MEK	melanoma	2013
Vandetanib	Caprelsa	I	EGFR, VEGFR, RET, FGFR	thyroid cancer	2011
Vemurafenib	Zelboraf	I	BRAF	melanoma	2011

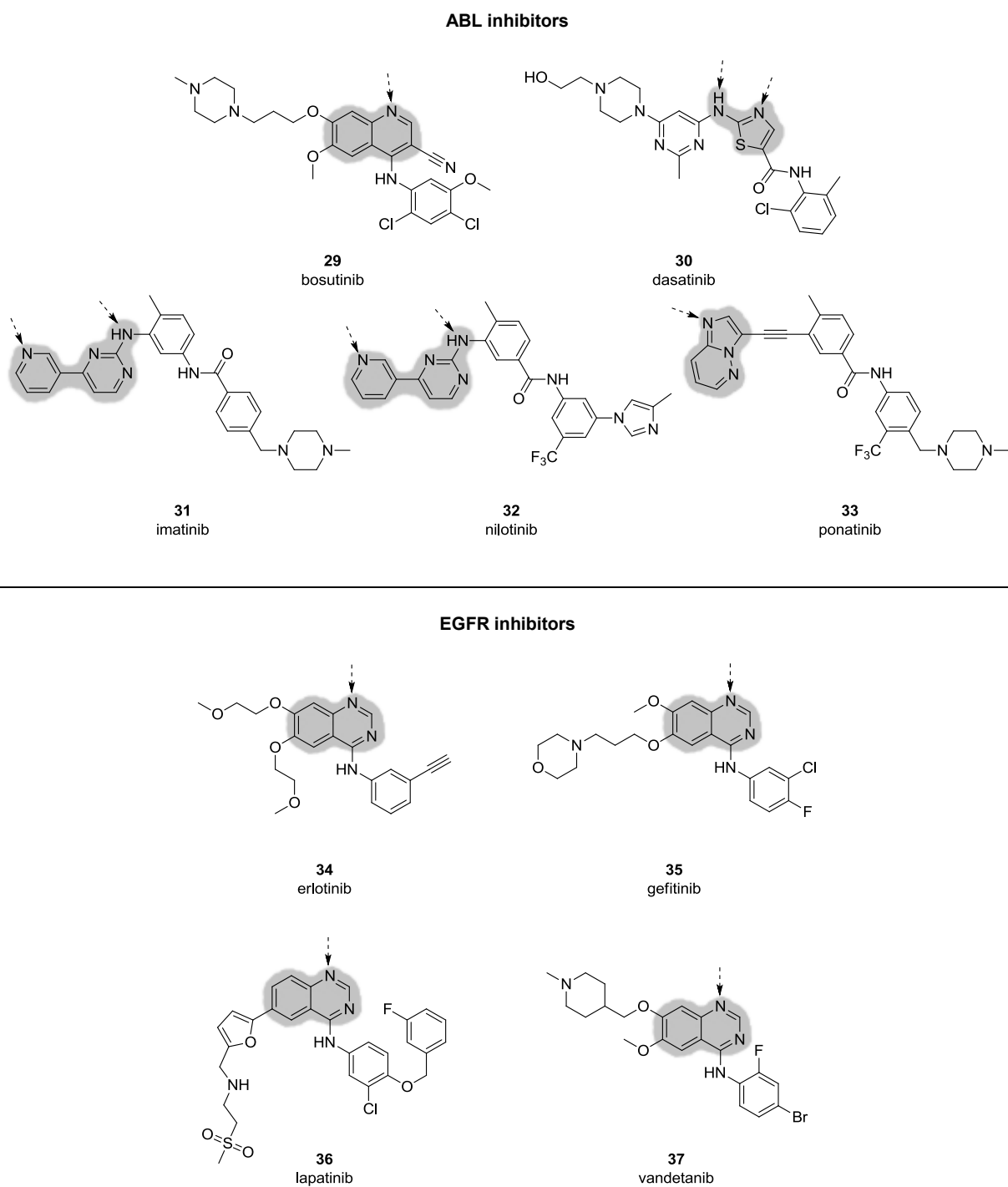


Figure 5. Chemical structures of FDA approved small molecule ABL and EGFR inhibitors.⁴² Structural elements that bind in the adenine pocket are highlighted in grey. Dashed arrows indicate hydrogen bonds toward the backbone of the hinge region.

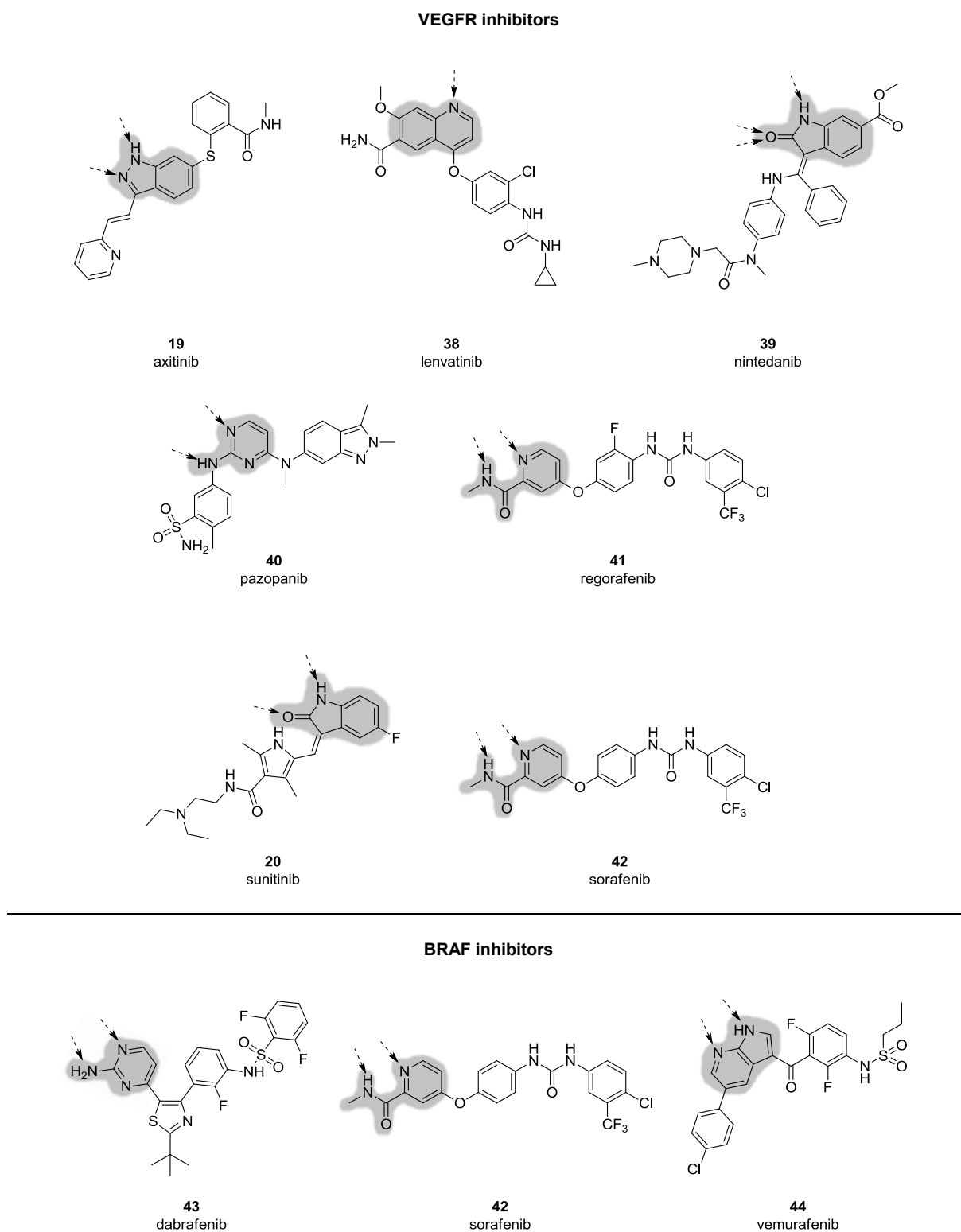


Figure 6. Chemical structures of FDA approved small molecule VEGFR and BRAF inhibitors.⁴² Structural elements that bind in the adenine pocket are highlighted in grey. Dashed arrows indicate hydrogen bonds toward the backbone of the hinge region.

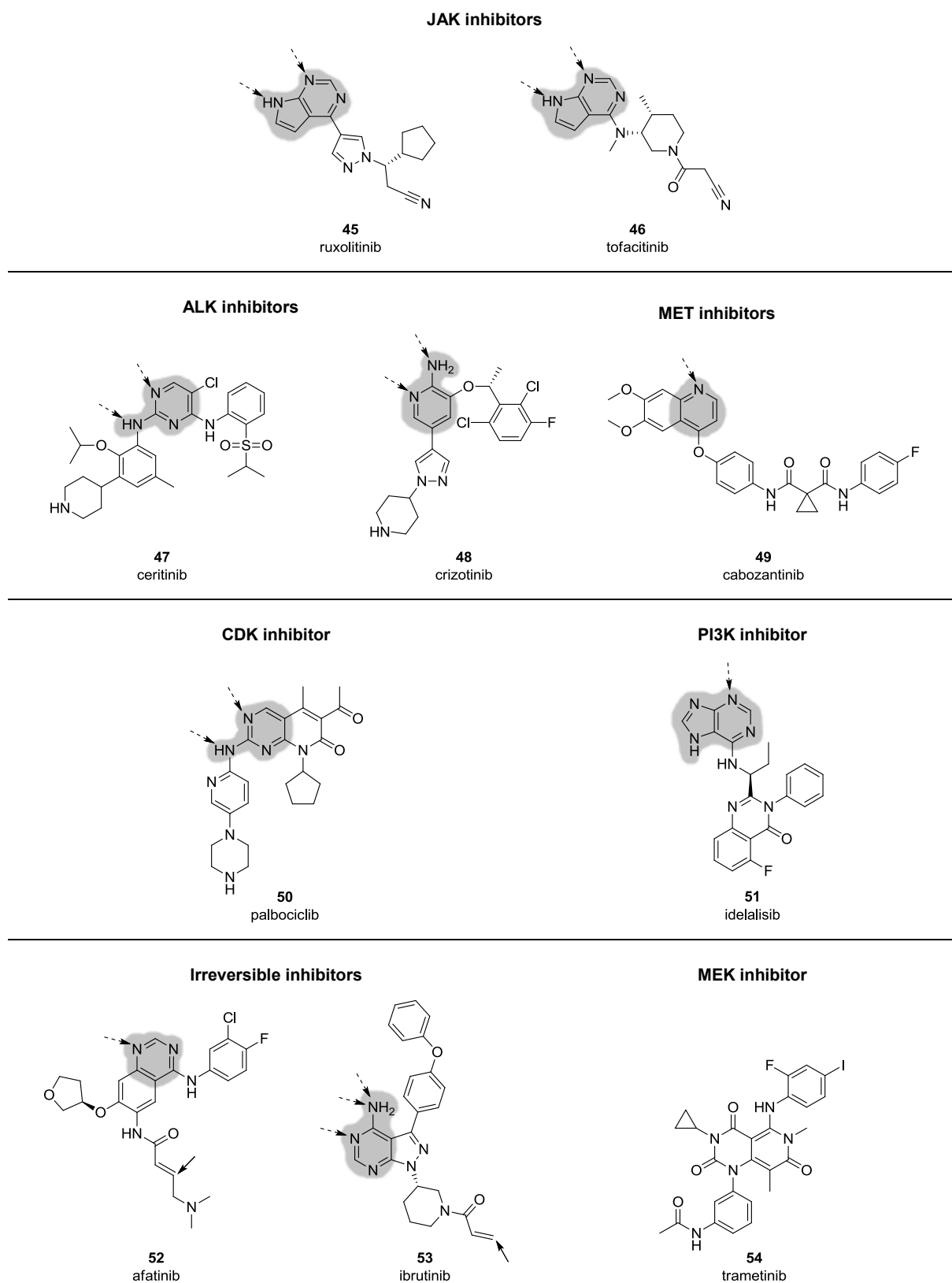


Figure 7. Chemical structures of further FDA approved small-molecule kinase inhibitors.⁴² Structural elements that bind in the adenine pocket are highlighted in grey. Dashed arrows indicate hydrogen bonds toward the backbone of the hinge region. Solid arrows show where reactive nucleophilic cysteine residues of the target protein attack Michael acceptor groups of the two irreversible inhibitors.

1.2.1 Protein Kinases

Function and signal transduction

Protein kinases are phosphotransferases; in other words, enzymes that catalyze the transfer of the γ -phosphate group of ATP onto a substrate.⁵⁸ Signal proteins are thus phosphorylated at the hydroxyl group of specific amino acid residues, in the majority of cases serine/threonine or tyrosine residues.⁵⁸ Signal transduction cascades are mediated in this way regulating many cellular activities including proliferation, survival, apoptosis, metabolism, transcription, and differentiation.⁵⁹ Because of their versatile role in cellular processes, misregulation of kinases like overexpression or hyperactivity due to mutations is the cause for many diseases. Kinases have therefore become important targets in drug discovery.^{7,60}

Kinase structure

Although human kinases are quite diverse in their primary amino acid sequences, their 3D structures show a high degree of similarity.⁴² The structure of the kinase domain is highly conserved since most of them use ATP as a common cofactor.⁶¹ As Figure 8 illustrates, protein kinases consist of an N-terminal lobe (N-lobe) which is linked *via* a so-called *hinge region* to a C-terminal lobe (C-lobe).⁷ The otherwise β -sheet dominated N-lobe also contains an α C-helix whose conformation plays a key role in the regulation of the kinase function. The C-lobe, on the other hand, contains mostly α -helices.⁷ The ATP binding pocket is located in the cleft between both lobes, where the backbone of the hinge region is addressed by the adenosine moiety of ATP by two hydrogen bonds.⁷ Most kinase inhibitors bind in the adenine pocket of the active site and also form hydrogen bonds toward the hinge-region (Figures 5, 6, and 7).^{7,45}

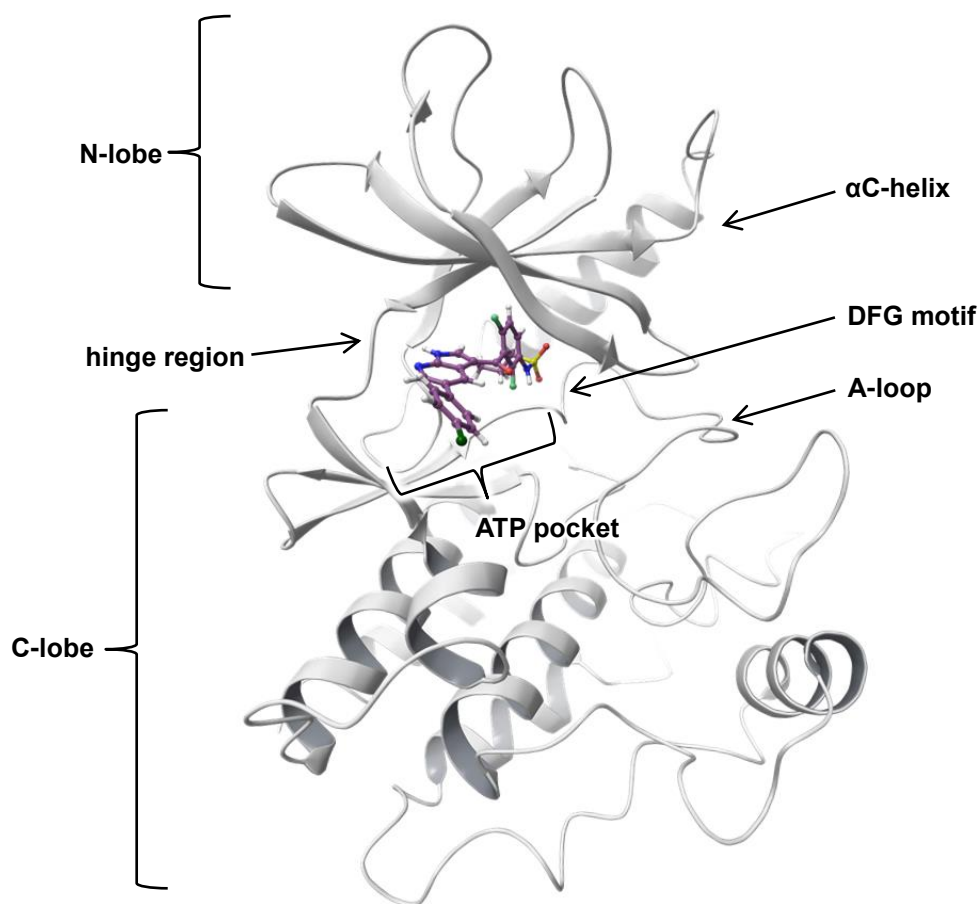


Figure 8. General structure of protein kinases.⁷ The structure of kinases is exemplified on the serine/threonine protein kinase BRAF^{V600E} (pdb 3OG7⁶²). The hinge region connects the N-terminal and the C-terminal lobe. The cofactor ATP and most kinase inhibitors bind in the cleft between both lobes, the ATP binding pocket, interacting with the hinge region. In this example, the A-loop is in the active conformation and the ATP pocket is occupied by vemurafenib (44, Figure 6).

The access to the active site is controlled by a flexible activation loop (A-loop), which starts with the conserved amino acid sequence Asp-Phe-Gly (DFG motif).⁴² The aspartate residue of this motif further complexes a magnesium ion (Mg^{2+}) which is crucial for the phosphate transfer from ATP to the substrate.⁵⁸ The A-loop contains several activation sites itself whose phosphorylation induces conformational changes regulating the activity of the kinase.⁶³ In the inactive conformation, the A-loop blocks the active site (DFG_{out} conformation) and prevents ATP from binding.⁸ Upon phosphorylation of the A-loop, the DFG motif flaps deeper into the binding pocket (DFG_{in} conformation) permitting ATP access to its binding pocket.^{42,45}

According to the pharmacophore model of Traxler and Furet⁶⁴, the ATP binding site itself consists of the highly conserved adenine-binding region, ribose pocket (sugar pocket), and phosphate-binding region (Figure 9).⁶¹ Adjacent to these, a hydrophobic pocket (hydrophobic pocket I, HP I), an allosteric hydrophobic back pocket (deep pocket) and a surface-exposed hydrophobic region (HP II) are located.^{45,61} The latter three are non-conserved pockets because they are not occupied by ATP. Addressing these regions therefore allows the design of selective ATP competitive kinase inhibitors (Figures 10 and 11).^{45,60,61} The access to the HP I is partially hindered by the *gatekeeper*, an amino acid residue that varies between individual kinases.⁶⁵ Gatekeeper mutations are often the cause of acquired kinase inhibitor resistances.⁶⁶

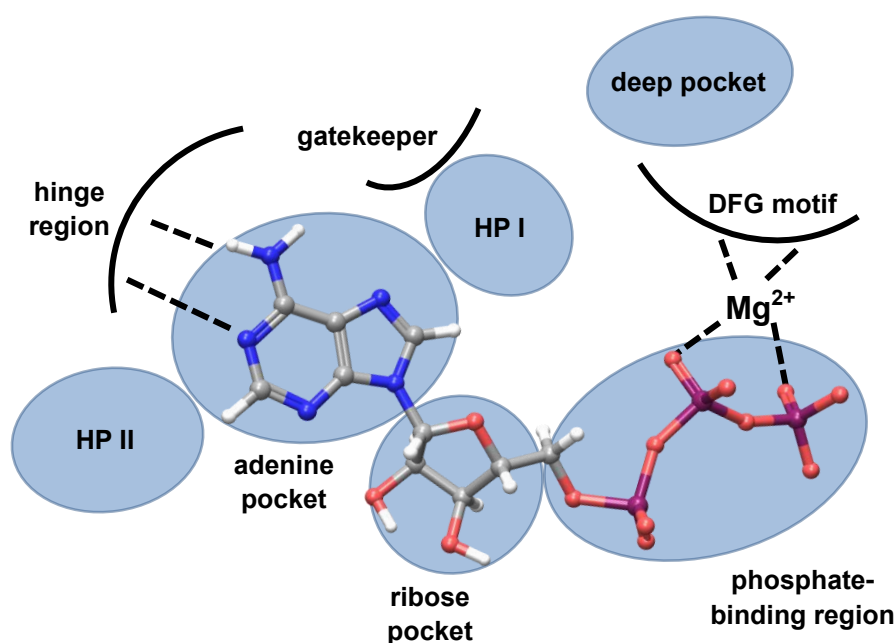


Figure 9. Model of the ATP binding pocket.^{45,58,61,64} Interactions of ATP with important structural elements and pharmacophore regions are shown.

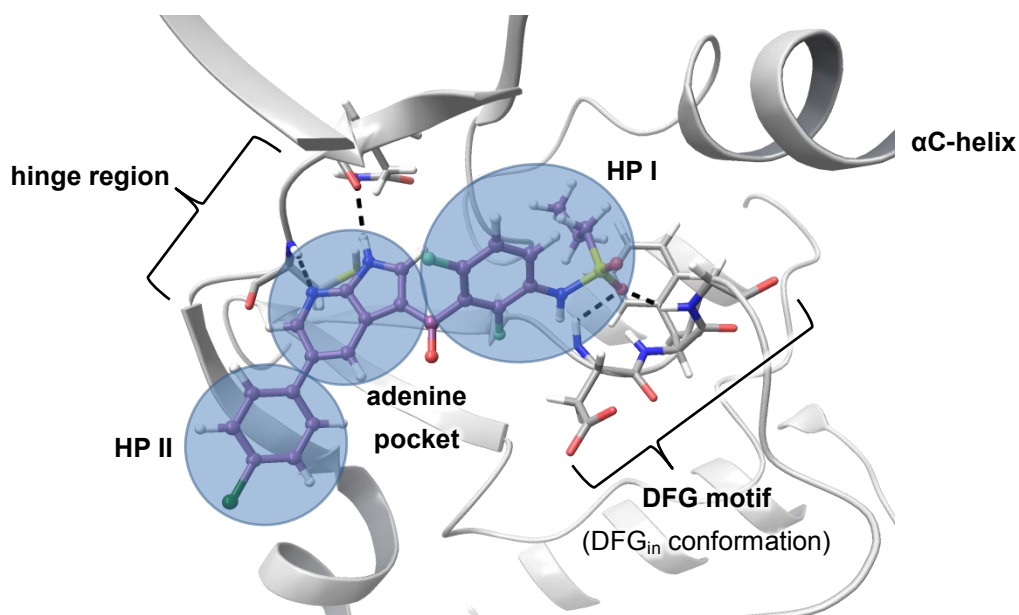


Figure 10. Pharmacophore model of a type I inhibitor in the ATP binding site (DFG_{in} conformation).^{45,64} Addressed binding pockets of a type I inhibitor are exemplified on vemurafenib (**44**, Figure 6) interacting with the ATP pocket of BRAF^{V600E} (pdb 3OG7⁶²) in the active conformation. The entrance to the deep pocket is blocked by the phenylalanine residue of the DFG motif.

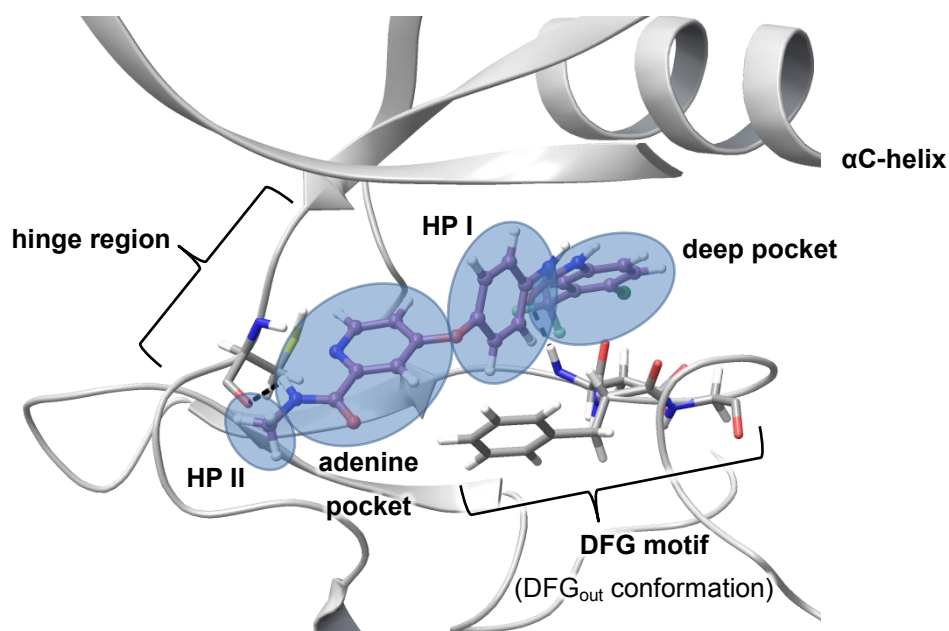


Figure 11. Pharmacophore model of a type II inhibitor in the ATP binding site (DFG_{out} conformation).^{45,64} Addressed binding pockets of a type II inhibitor are exemplified on sorafenib (**42**, Figure 6) interacting with the ATP pocket of VEGFR2 (pdb 4ASD⁶⁷) in the inactive conformation. The phenylalanine residue of the DFG motif is flapped toward the ATP binding site so that the entrance to the deep pocket is unblocked and can thus be addressed by the inhibitor.

Binding modes of kinase inhibitors

Kinase inhibitors can be categorized by binding modes (Table 4).^{7,8,42,45,56} Most compounds represent reversible inhibitors binding into the ATP site. Four types can be differentiated with regard to the addressed binding pockets and the adopted kinase conformation upon binding.

Type I inhibitors bind to the active form of the kinase (DFG_{in} inhibitors).⁴⁵ The access to the deep pocket is thus blocked by the DFG motif.⁸ Hydrogen bonds are formed by heterocycles of the inhibitor toward the backbone of the protein's hinge region.^{45,56} Addressing the neighboring hydrophobic pockets can improve selectivity, since the ATP pocket itself is highly conserved throughout all kinase families.⁸

Type II inhibitors, on the other hand, bind to and thus stabilize the enzymatically inactive kinase configuration (DFG_{out} inhibitors).⁸ The DFG motif is herein flapped outward from the ATP binding site permitting access to the deep pocket.⁴² The A-loop adopts the inactive conformation blocking the access of ATP to the adenine pocket.⁸ Besides the hinge region, the allosteric back pocket is addressed by type II inhibitors which are therefore also called *deep pocket binders*.⁶⁸ This approach offers better chances for selectivity since this region is less conserved.⁸ Slow on/off binding kinetics and stabilization of the inactive kinase state explain why relatively weak type II inhibitors can show very potent cellular efficacy.⁶⁹

Type III inhibitors exclusively bind in allosteric regions *adjacent* to the active site without making any contact with the ATP pocket itself.⁴² In the type IV binding mode an allosteric site *remote* from the ATP pocket is addressed.⁴² In both cases, the DFG_{out} conformation is stabilized hindering ATP to access to the active site and thus inhibiting the enzyme's function.⁸

Irreversible kinase inhibitors covalently bind to a reactive nucleophilic residue of the protein.⁴² The two approved representatives, afatinib and ibrutinib (**52** resp. **53**, Figure 7), bear a Michael acceptor functionality which is attacked by a nucleophilic cysteine residue proximal to the ATP binding site.⁴² Both drugs are initial type I binders before becoming actually covalently bound, but irreversible inhibitors of the other types are likewise feasible. The covalent approach aims to increase specificity and potency, although toxicity concerns have been raised.^{42,52}

Table 4. Binding mode classification of kinase inhibitors.^{7,42,45,56} Small-molecule kinase inhibitors can be divided into reversible and irreversible inhibitors. Types I to IV additionally differentiate regarding the addressed binding pockets of the target protein and the stabilized kinase conformation.

Type	Binding Kinetics	Addressed Pockets	Kinase Conformation	Examples
I	ATP competitive, reversible (fast)	adenine pocket, HP I / HP II	active (DFG _{in})	gefitinib
I (covalent)	initially ATP competitive, irreversible	adenine pocket, HP I / HP II	active (DFG _{in})	afatinib, ibrutinib
II	ATP competitive with allosteric component, reversible (slow)	adenine pocket, deep pocket, HP I / HP II	inactive (DFG _{out})	imatinib, sorafenib
III (allosteric)	non-ATP competitive, reversible	deep pocket, HP I / HP II	inactive (DFG _{out})	trametinib
IV (allosteric)	non-ATP competitive, reversible	allosteric pocket (remote from ATP pocket, e.g. substrate binding domain ⁷⁰)	inactive (DFG _{out})	only experimental compounds (e.g. GNF-2) ⁵⁶

Alternative and revised classifications have further been suggested. Irreversible inhibitors, for instance, have also been declared as the fifth class of inhibitors.⁷⁰ Some inhibitors, e.g. dasatinib (**30**, Figure 5), have been observed to bind to conformations that are intermediate between DFG_{in} and DFG_{out}.⁵⁶ A hybrid binding mode (classified by type I^{I/II} or type V) with mixed characteristics of types I and II has therefore been discussed.^{56,58}

McTigue *et al.* have intensively studied the binding modes of VEGFR inhibitors.⁶⁷ They argued that declared type I inhibitors like axitinib and sunitinib (**19** resp. **20**, Figure 6) bind to the DFG_{out} conformation without interaction with the deep pocket and categorize them as a new type IV. The difference to type II inhibitors like sorafenib (**42**, Figure 6) lies, according to them, in the conformation of the juxtamembrane domain.⁶⁷ New pharmacophore models have been designed based on these results.⁷¹

According to Okamoto *et al.* sunitinib as a type I inhibitor shows fast binding kinetics and binds to the DFG_{in} conformation, whereas sorafenib as a type II inhibitor shows slow binding kinetics and binds to DFG_{out}.⁵⁵ They demonstrated that lenvatinib (**38**, Figure 6) exhibits a prolonged residence time; it binds to the DFG_{in} conformation but additionally addresses the neighboring allosteric pocket. They therefore suggest calling these types of inhibitors type V.

Bivalent kinase inhibitors have additionally been reported and classified as type V inhibitors.⁷² They consist of an ATP competitive small molecule that is linked to a peptide ligand. The latter binds to a signaling interaction site of the targeted kinase in order to improve selectivity and potency.⁷³

Another model by Kornev *et al.* uses a nonlinear motif, the so-called regulatory or hydrophobic spine, for the explanation of the active and inactive conformation.⁷⁴ According to the model, a spine comprised of four hydrophobic residues is dynamically formed upon activation. Inhibitors can bind in the ATP pocket depending on the conformation of this spine and can thus be classified.

The traditional classification system cannot express all the subtleties and nuances of kinase inhibitor binding modes. The active and inactive conformation of the DFG motif are only two extremes between various possible kinase configurations due to the flexibility of the protein chain. New types of kinase inhibitors with novel binding modes are furthermore emerging. Zhao *et al.* therefore stated that classification should be made according to how inhibitors affect kinetic parameters of the kinase and whether they display competitive, non-competitive or mixed inhibition profiles.⁵⁶ But they also discussed the practical difficulties of this approach: this kind of enzymological data is rarely available for new kinase inhibitors; and the intracellular state of a kinase can hardly be reproduced in a test system due to complex post-translational and regulatory interactions in the cell. Crystallographic structures therefore provide an invaluable guide at the molecular level for medicinal chemists.⁵⁶

1.2.2 BRAF^{V600E} Inhibitor Vemurafenib

The RAS/RAF/MEK/ERK signal transduction cascade is an essential signaling network that governs proliferation, differentiation and cell survival (Figure 12).⁷⁵ Cellular responses to growth signals are mediated by this mitogen-activated protein kinase (MAPK) pathway, which is frequently deregulated in cancer.⁷⁶ The three isoforms ARAF, BRAF and CRAF are cytoplasmic serine/threonine kinases that are regulated by binding RAS.⁷⁶ Mutations in the BRAF gene occur in more than half of malignant melanomas and in a variety of other cancers.⁶² Whereat, a single substitution of glutamic acid for valine at position 600 (V600E, previously misnamed 599⁷⁷) is accounting for the majority of cases.⁶² BRAF^{V600E} thus becomes constitutively activated independent from RAS regulation.⁷⁸ When the oncogenic potential of the BRAF gene was recognized, multiple drug discovery approaches were launched.^{75,79}

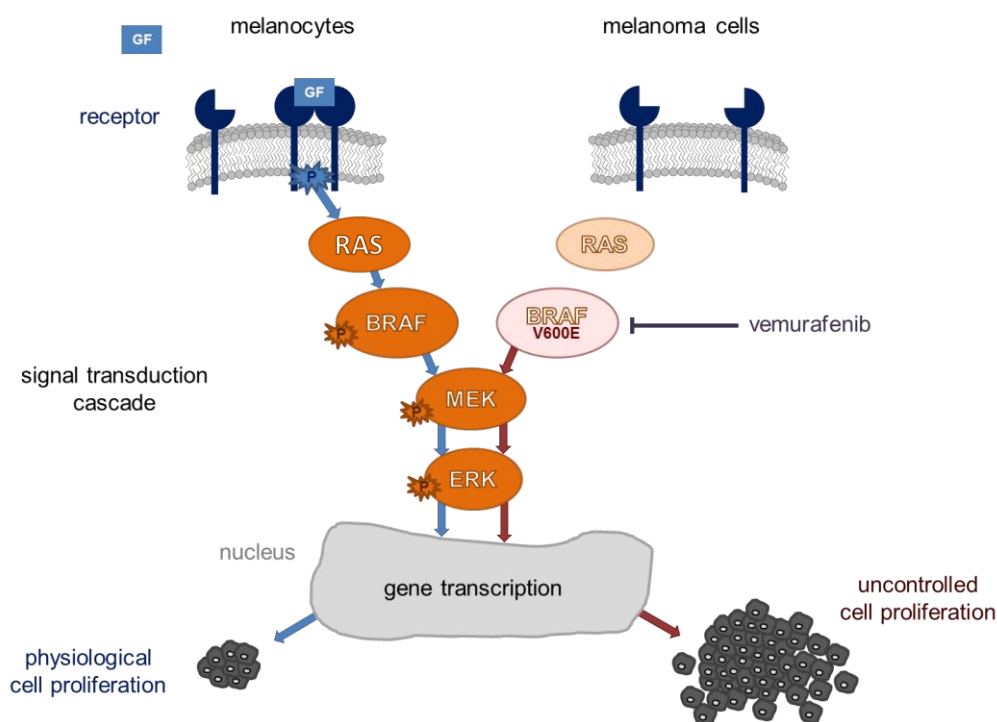


Figure 12. RAS/RAF/MEK/ERK signal transduction cascade.⁸⁰ On the left, the physiological pathway in melanocytes after binding of a growth factor (GF) is illustrated. The cascade leads to subsequent phosphorylation of RAS, BRAF, MEK, and ERK and therefore to a signal enhancement. Gene transcription is hence regulated resulting in physiological cell proliferation and cell survival. In certain melanoma cancer cells, as shown on the right, a gain-of-function mutation of BRAF leads to an up-regulation of this pathway and consequently to an uncontrolled cell proliferation.

Sorafenib (**42**, Figure 6) was initially developed as an anti-melanoma agent targeting RAF, but failed in clinical studies due to inefficacy.⁷⁸ However, further investigations revealed its anti-angiogenic effects by multi-target inhibition including VEGFR and PDGFR.⁷⁸ Sorafenib has thus been used since 2005 as an orphan drug (Nexavar, Bayer) for the treatment of renal cell and hepatocellular carcinoma.^{81–83}

A structure-guided approach subsequently led to the development of vemurafenib (**44**, Figure 6) with improved BRAF selectivity and efficacy.^{62,78} Vemurafenib was the first approved drug for the personalized treatment of BRAF-mutant cancer.^{62,78} The kinase inhibitor was discovered in 2005 and further developed under the research code PLX4032 by Plexxikon and Roche.^{62,78} It received approval under the trade name Zelboraf for the treatment of metastatic melanoma with BRAF^{V600} mutation in the United States and Europe in 2011 and 2012, respectively.^{62,78}

The introduction of vemurafenib into melanoma therapy showed impressive results. Remarkable response rates of 81% (phase I clinical trial⁸⁰) resp. over 50% (phase II and III clinical trials^{84,85}) were reached. The advantage over the comparative treatment with dacarbazine, an alkylating agent, was so evident that the FDA recommended a revision of the analysis plan so that patients in the control arm were permitted to receive vemurafenib as well.⁷⁸ But despite outstanding tumor regressions and distinctive improvements in survival, vemurafenib cannot cure metastatic melanoma. Moreover, a massive dosage of 960 mg twice daily is required for an optimal therapeutic effect.⁷⁸ An unacceptable toxicity was already documented at 1,120 mg twice a day.⁸⁶ This leads to a high incidence of severe adverse events such as arthralgia (joint pain), skin rash, and the development of squamous cell carcinoma in 26% of patients.⁸⁴ Most patients furthermore suffer from lethal relapse due to drug-resistance after only a few months of therapy. Investigations on mechanisms revealed that drug resistance is selected by continuous vemurafenib administration.⁸⁷ It could be demonstrated that resistant melanomas become drug dependent for their continued proliferation.⁸⁷ A discontinuous dosing strategy was therefore suggested.⁸⁷

In May resp. August 2013 dabrafenib (**43**, Figure 6), another mutant BRAF selective anti-melanoma agent, was approved by the FDA and the European Medicine Agency (EMA).⁴² Several other small molecules targeting BRAF are currently evaluated in clinical trials.⁸⁸

In order to reduce side effects and delay the formation of resistances, a light-mediated spatial and temporal control of BRAF inhibitors would be of great benefit. The development of photo prodrugs by introduction of PPGs might create novel therapeutic options and could enhance basic research by innovative tool compounds. Caged vemurafenib prodrugs are one of the main topics in this work. Von Drathen focused in his bachelor thesis on approaches for photoactivatable dabrafenib prodrugs.⁸⁹

1.2.3 VEGFR Inhibitors Diarylmaleimide and Carbazole

The vascular endothelial growth factor (VEGF) is an important mitogen in the physiological regulation of angiogenesis.^{90,91} Formation and growth of new blood vessels is a key process during embryogenesis and skeletal growth.⁹² In adult individuals, however, angiogenesis activities are rare with the exception of reproductive functions and wound healing.⁹³ Pathophysiological angiogenesis is beyond that associated with tumor growth and intraocular neovascular diseases.⁹¹ The first anti-angiogenetic drug was bevacizumab (trade name Avastin), a humanized anti-VEGF monoclonal antibody for cancer therapy.⁹⁴

There are five different VEGF ligands which represent homodimeric glycoproteins.⁹⁵ These growth factors bind to three receptor tyrosine kinase (RTK) isoforms, namely VEGFR1, VEGFR2, and VEGFR3.⁹⁵ The related receptors consist of seven extracellular immunoglobulin-like domains, a single transmembrane region, and an intracellular split tyrosine-kinase domain.⁹¹ VEGFR1 is responsible for hematopoietic cell development, VEGFR2 is critical for vascular endothelial function, and VEGFR3 regulates lymphatic endothelial cell function.⁹⁵ VEGF-A (also VEGF) is the most important stimulus for most physiological and pathological angiogenetic effects mediated by VEGFR2.⁹⁵ These effects on endothelial cells include proliferation, migration, survival, and permeability.⁹⁵

Upon binding of a growth factor two receptor proteins dimerize.⁹⁶ This induces autophosphorylation of the intracellular kinase domains triggering diverse signal transduction cascades.⁹⁷ Important signaling pathways and their respective cellular responses are shown in Figure 13.

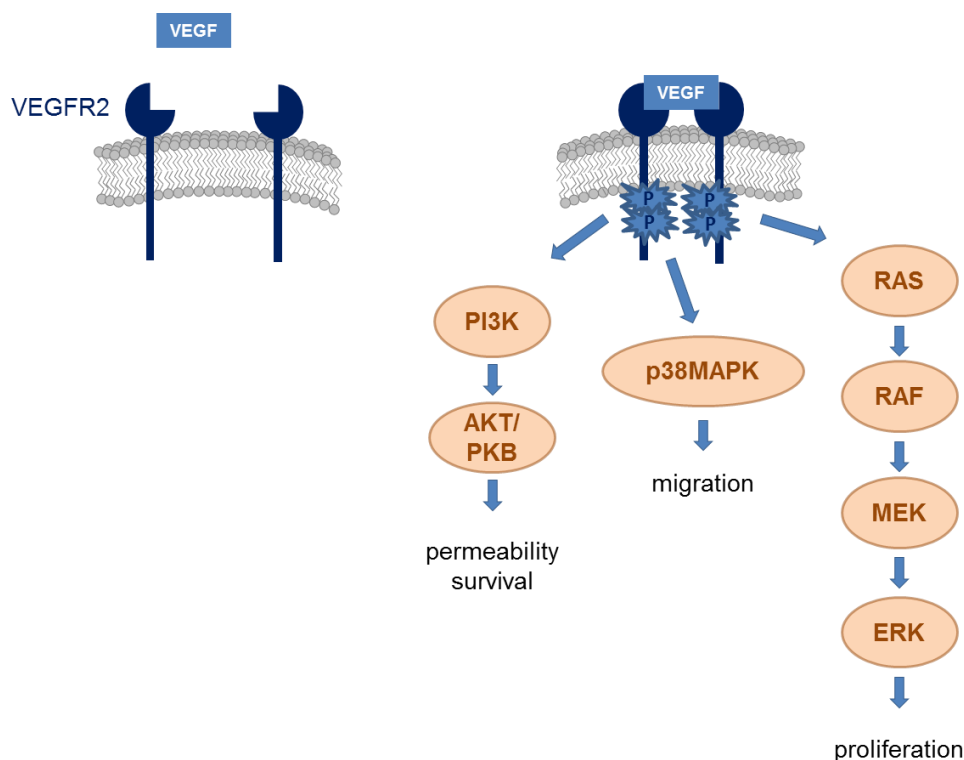


Figure 13. VEGF and VEGFR2 mediated signal transduction cascades.⁹⁷ The growth factor VEGF binds to the extracellular domain of the receptor tyrosine kinase VEGFR2. This is followed by the dimerization of two receptor monomers and autophosphorylation of the intracellular domains. This leads to the activation of a cascade of downstream protein pathways and to the indicated biological effects. Only crucial proteins of each pathway are shown.

Besides therapeutic antibodies, small molecule tyrosine kinase inhibitors (TKIs) targeting VEGFR have been developed.⁶⁷ Seven small molecule VEGFR inhibitors have been approved until today (Table 3).⁴² One of them, axitinib, is discussed in more detail in the next chapter. These agents are usually not highly specific for VEGFR and thus also hit other related tyrosine kinases *e.g.* platelet-derived growth factor receptor (PDGFR).⁹⁷ A high number of further VEGFR inhibitors are currently in the clinical development or have been developed as experimental substances.⁸⁸ Peifer *et al.* reported in 2006 about a novel class of potent VEGFR inhibitors, namely 3,4-diarylmaleimides, as anti-angiogenesis agents.^{98,99} Within this series compound **55** (Figure 14) showed the highest potency with a VEGFR2 IC₅₀ of 2.5 nM.⁹⁹

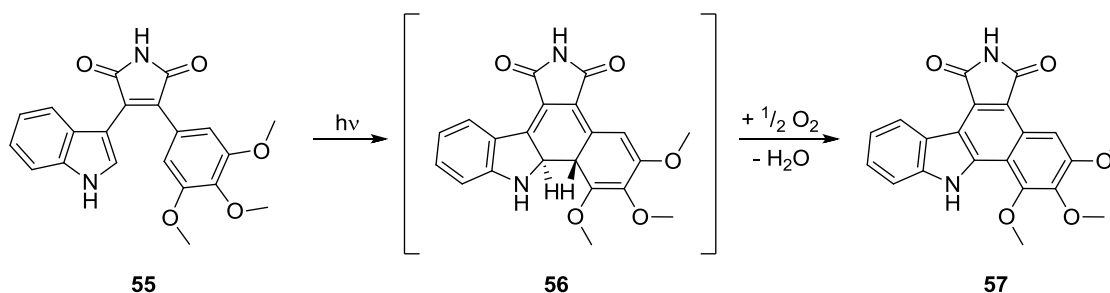


Figure 14. Light-induced 1,6- π -electrocyclization of diarylmaleimide **55** and subsequent oxidation of the intermediate **56** to the carbazole **57**.⁹⁸

Diarylmaleimide **55** seemed to be particularly interesting with regard to the photo project. Not only the high *in vivo* efficacy but also its light sensitivity made this compound an interesting candidate for a photoactivatable kinase inhibitor. Figure 14 shows that a cyclization reaction is taking place upon light exposure.⁹⁸ A non-planar intermediate (**56**) is formed at first which could not be isolated.⁹⁸ The latter is then oxidized to a planar carbazole structure in the next step. The carbazole represents a potent VEGFR inhibitor as well.⁹⁹ It furthermore shows strong fluorescence which additionally seemed to be advantageous for microscopic investigations regarding *e.g.* its distribution in cellular compartments.

1.2.4 VEGFR Inhibitor Axitinib

Targeted therapeutics addressing the VEGFR have revolutionized the treatment of metastatic renal cell carcinoma (RCC).¹⁰⁰ 90% of RCC patients show a mutation in the Von Hippel-Lindau (VHL) gene with an overproduction of the angiogenic factor VEGF.⁶⁷ The inhibition of VEGFR thus suppresses angiogenesis, cellular adhesion, and migration.⁶⁷

Since the introduction of the multi-kinase inhibitor sorafenib in 2005, the disease management of RCC has evolved rapidly.¹⁰¹ Second-generation VEGFR inhibitors such as axitinib (Inlyta, Pfizer) offer optimized potency and selectivity.¹⁰¹ Axitinib (**19**, Figure 6) is an indazole-derived, small molecule tyrosine kinase inhibitor.⁹² It has been approved for the therapy of advanced RCC in 2012.¹⁰¹ Its antiangiogenic effect is based on the inhibition of VEGFR1-3 at nanomolar concentrations.¹⁰¹ Other targets of axitinib are the highly related receptor tyrosine kinases PDGFR and cKIT.¹⁰¹ Their inhibition is, however, about eight-times weaker compared to VEGFR.¹⁰¹

Beyond the indication for kidney cancer, angiogenesis plays an important role in the genesis of many tumors. An expansion of the indication is therefore conceivable and several clinical trials are currently performed *e.g.* for the treatment of melanoma, hepatic, or prostate cancer.⁸⁸ Furthermore, axitinib was recently discovered to effectively inhibit a mutant of BCR-ABL1 that is often responsible for acquired drug resistance in the therapy of chronic myeloid leukemia (CML) with kinase inhibitors.¹⁰² In addition to its decisive role in cancer therapy, axitinib has been used in numerous *in vitro* and *in vivo* experiments.^{67,103,104}

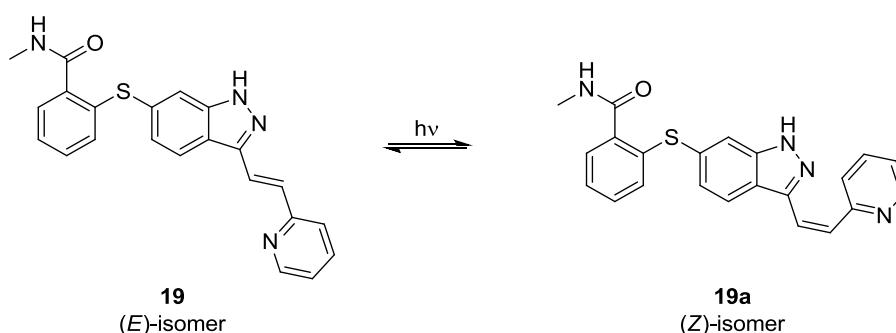


Figure 15. Light-induced *E-Z* isomerization of axitinib.

The structure of axitinib offers an interesting *E-Z* photoswitching option based on the diarylethene resp. stilbene-like moiety (Figure 15).³ It was hypothesized that the stereoisomers would thus exhibit different biological activities. The possibility to control the efficacy of axitinib by switching it on and off through irradiation would be of great benefit in various experimental settings.

2. AIMS AND OBJECTIVES

2.1 CAGED VEMURAFENIB

The goal of this project was the development of novel photoactivatable prodrugs of vemurafenib. The occurrence of therapy-limiting side effects as well as only temporarily efficacy illustrates the urgent need for new therapeutic approaches with kinase inhibitors.^{84–86} The caging approach might enable higher drug concentrations specifically generated by irradiation in cancer-afflicted tissues, resulting in a faster, more efficient regression with fewer side effects.^{4,10,14,30} Beyond novel therapeutic applications, these photo prodrugs could serve as experimental tools *e.g.* for kinetic or mechanistic studies.¹⁰⁵

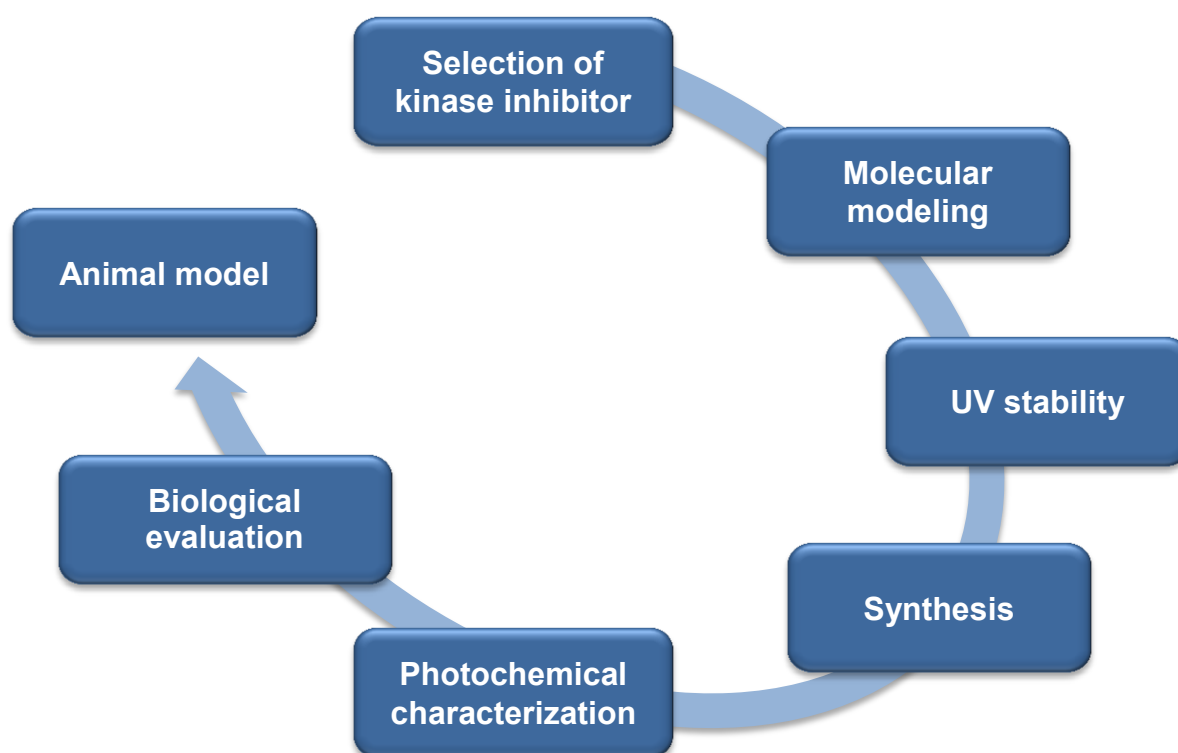


Figure 16. Workflow of the caged vemurafenib project. The presented strategy involves (1) selection of an appropriate candidate for the caging concept, (2) determination of suitable pharmacophore moieties, (3) demonstration of adequate UV stability of the active inhibitor, (4) synthesis of caged photo prodrugs, (5) photochemical characterization and photoactivation, and (6) *in vitro* evaluation of photoactivation. The long-term objective is (7) the proof of concept in animal studies.

The objective of this study was the design, synthesis, and biological evaluation of photoactivatable prodrugs of vemurafenib following the workflow illustrated in Figure 16. First, molecular modeling was to reveal promising pharmacophoric groups to be protected by PPGs (chapter 3.1.1). Afterwards an adequate UV stability at 365 nm of vemurafenib was to be verified in order to ensure that it is not degraded upon irradiation (chapter 3.1.2).

Diverse classes of PPGs were to be assessed regarding their chemical accessibility (chapter 3.1.3) and their photochemical characteristics (chapter 3.1.4), respectively. For the PPG assessment, a dummy compound was to be used in order to simplify the reactions conditions. The hinge binder scaffold of vemurafenib (**44**, Figure 17), represented by a 7-azaindole, was thus to be investigated concerning its intended role as a leaving group in a photoreaction.

Despite the enormous amount of data about PPGs, information on the photoprotection of *N*-heterocycles is rarely available.^{18–20} This is presumably due to the fact that nitrogen compounds represent poor leaving groups in the photolysis reaction.^{10,19} Type I and II kinase inhibitors typically address the hinge region by nitrogen functions (Figures 5, 6, and 7).⁷ This interaction is essential for the binding mode and its blockade is therefore especially interesting regarding the caging concept.

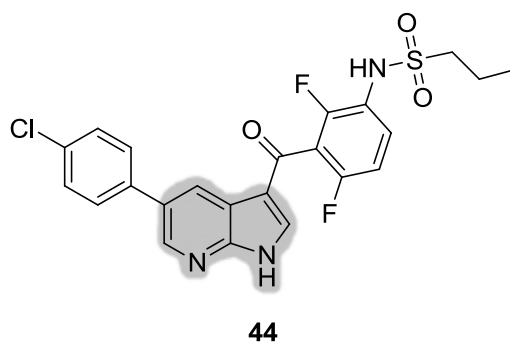


Figure 17. Chemical structure of vemurafenib (**44**). The hinge binder (7-azaindole) is highlighted in grey.

The question was if 7-azaindole could be released by the PPG at sufficient reaction rates or if further substituents would be necessary to stabilize transition states of the complex photolysis reaction (chapter 3.1.4). The objective was therefore to find the minimal structural requirement for the photoreaction. This identified fragment was consequently to be used as a dummy compound. Representatives from the following PPG classes were to be linked to this structure in order to compare their photochemical characteristics: *o*-nitrobenzyl, phenacyl, desyl, and coumarin moieties (Figure 18).

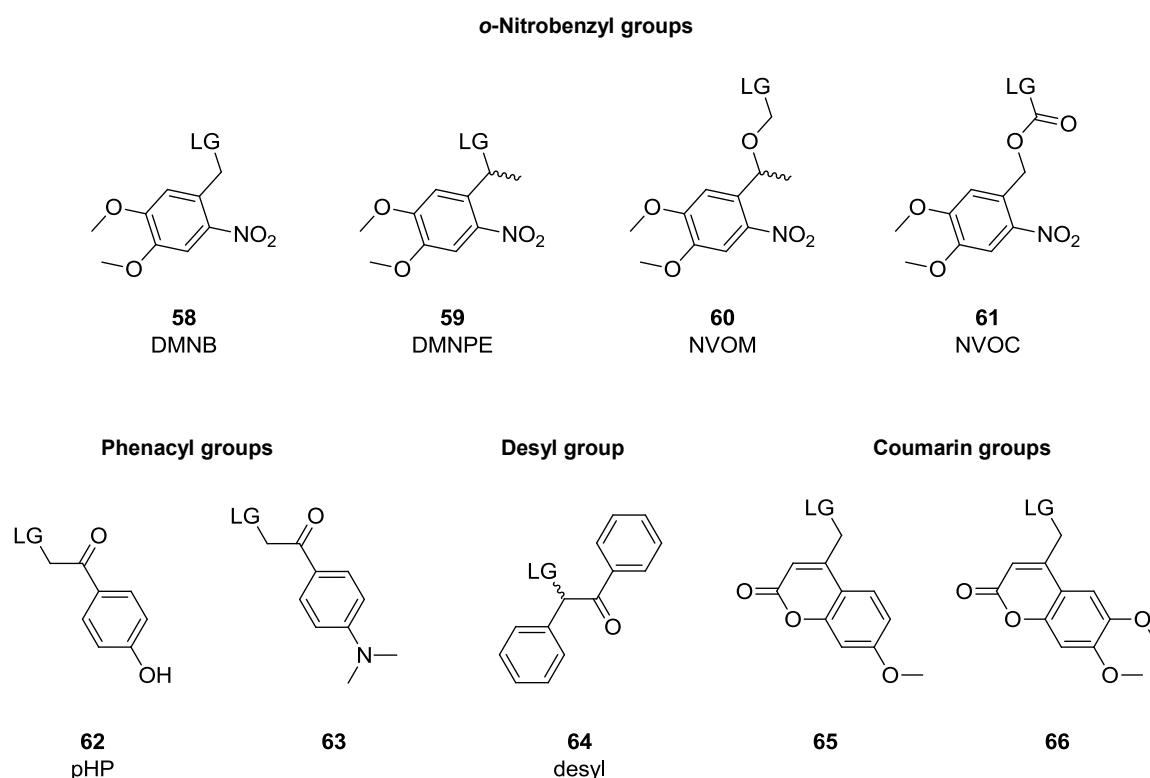


Figure 18. Selection of PPGs to be assessed in the vemurafenib project. LG = leaving group.

Based on these findings, PPGs with optimized photolysis characteristics were to be selected for the synthesis of vemurafenib prodrugs (chapter 3.1.3). These were next to be photochemically characterized (chapter 3.1.4). This included assignment of an optimal wavelength for deprotection and investigation of photoinduced release of vemurafenib. Determination of BRAF^{V600E} K_d values and a broad kinase selectivity profile for these compounds had subsequently to be performed to prove the intended loss-of-function by photoprotection. Finally, recovery of vemurafenib's efficacy by UV irradiation had to be demonstrated in enzymatic resp. cellular assays and the biological impact of the released protecting group biologically evaluated (chapter 3.1.5).

2.2 CAGED DIARYLMALEIMIDES AND CARBAZOLE

Besides the approved kinase inhibitor vemurafenib, the caging project included two experimental compounds: the diarylmaleimide **55** and the carbazole **57**.⁹⁸ An interesting aspect about these compounds is the light-induced conversion from the diarylmaleimide to the planar carbazole (Figure 14).⁹⁸ Both compounds represent potent VEGFR inhibitors. By this reaction, a 1,6- π -electrocyclization with subsequent oxidation, the non-planar intermediate **56** is formed.⁹⁸ This intermediate cannot be isolated. An *in situ* formation of **56** was therefore to be examined in photochemical and biological assays.

Additionally, both inhibitors were selected to be caged according to the strategy presented in chapter 2.1 (Figure 16). The objective of this approach was to develop photoactivatable VEGFR inhibitors as powerful pharmacological tools. Further focus was set on the exploration of another *N*-heterocycle, namely the maleimide moiety, as a leaving group for photolysis reactions.

The set-up of this project included the following steps:

- (1) determination of a suitable pharmacophore moiety by molecular modeling (chapter 3.2.1),
- (2) investigation of UV stability and light-induced conversion from **55** to **57** (chapter 3.2.3),
- (3) synthesis of caged photo prodrugs (chapter 3.2.2),
- (4) their photochemical characterization (chapter 3.2.3),
- (5) *in vitro* evaluation of the *in situ* formed **56**, and
- (6) *in vitro* evaluation of the photoactivated caged prodrugs (chapter 3.2.4).

2.3 PHOTOSWITCHABLE AXITINIB

The goal of this project was to investigate if axitinib can be used as a photoswitchable kinase inhibitor. The approved VEGFR inhibitor has shown excellent therapeutic results and has been used in a variety of biochemical assays.¹⁰¹ Based on the light-induced *E-Z* isomerization (Figure 15), the stilbene-like structure of axitinib offers an interesting photoswitching option which had not been reported in the academic field so far. As a photoswitch the biological effects of axitinib could be precisely turned on and off with high spatial and temporal control. This would offer opportunities both from a therapeutic point but also in basic kinase research.

The strategy involved the following steps:

- (1) molecular modeling and docking studies in order to predict the binding affinity of both stereoisomers **19** and **19a** (chapter 3.3.1),
- (2) isolation of axitinib's (*Z*)-stereoisomer (**19a**) (chapter 3.3.2),
- (3) photochemical characterization of the (*E*)- and the (*Z*)-stereoisomer (chapter 3.3.3),
- (4) exploration of the photoinduced *E-Z* isomerization depending on the irradiated wavelength (chapter 3.3.3), and
- (5) biological evaluation comparing the inhibitory efficiency of both stereoisomers, including enzymatic and cellular *in vitro* assays (chapter 3.3.4).

3. RESULTS AND DISCUSSION

3.1 CAGED VEMURAFENIB

3.1.1 Molecular Modeling

The ligand-protein interactions of vemurafenib (**44**, Figure 6) in the ATP pocket of BRAF^{V600E} (pdb 3OG7⁶²) were examined by molecular modeling (chapter 5.1). In order to design effectless vemurafenib prodrugs, it was necessary to define key pharmacophoric moieties of this kinase inhibitor to be subsequently blocked by PPGs.

In Figure 20 (A) and (B) the binding mode of vemurafenib in the ATP pocket of BRAF^{V600E} is shown (pdb 3OG7).⁶² Figure 19 shows the corresponding two-dimensional (2D) ligand-interaction diagram for clarity. The type I inhibitor vemurafenib is addressing two key H-bonds by its 7-azaindole moiety toward the hinge region.⁷ The sulfonamide NH residue of vemurafenib furthermore interacts with backbone amides of the DFG motif. Both the 7-azaindole and sulfonamide were hence considered to be suitable pharmacophoric moieties for photoprotection.

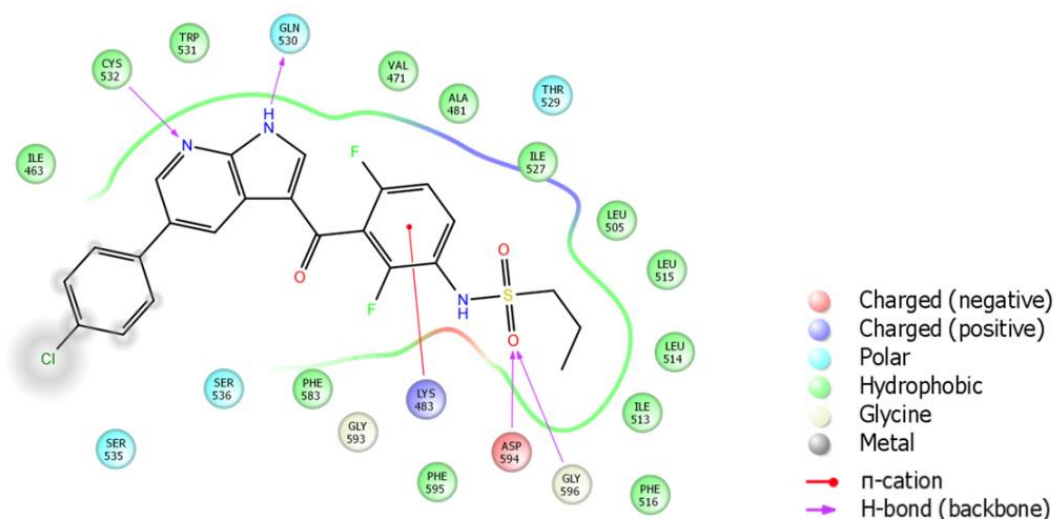


Figure 19. 2D ligand-interaction diagram of vemurafenib in BRAF^{V600E} (pdb 3OG7⁶²). H-bond interactions of the ligand toward the protein backbone are shown.

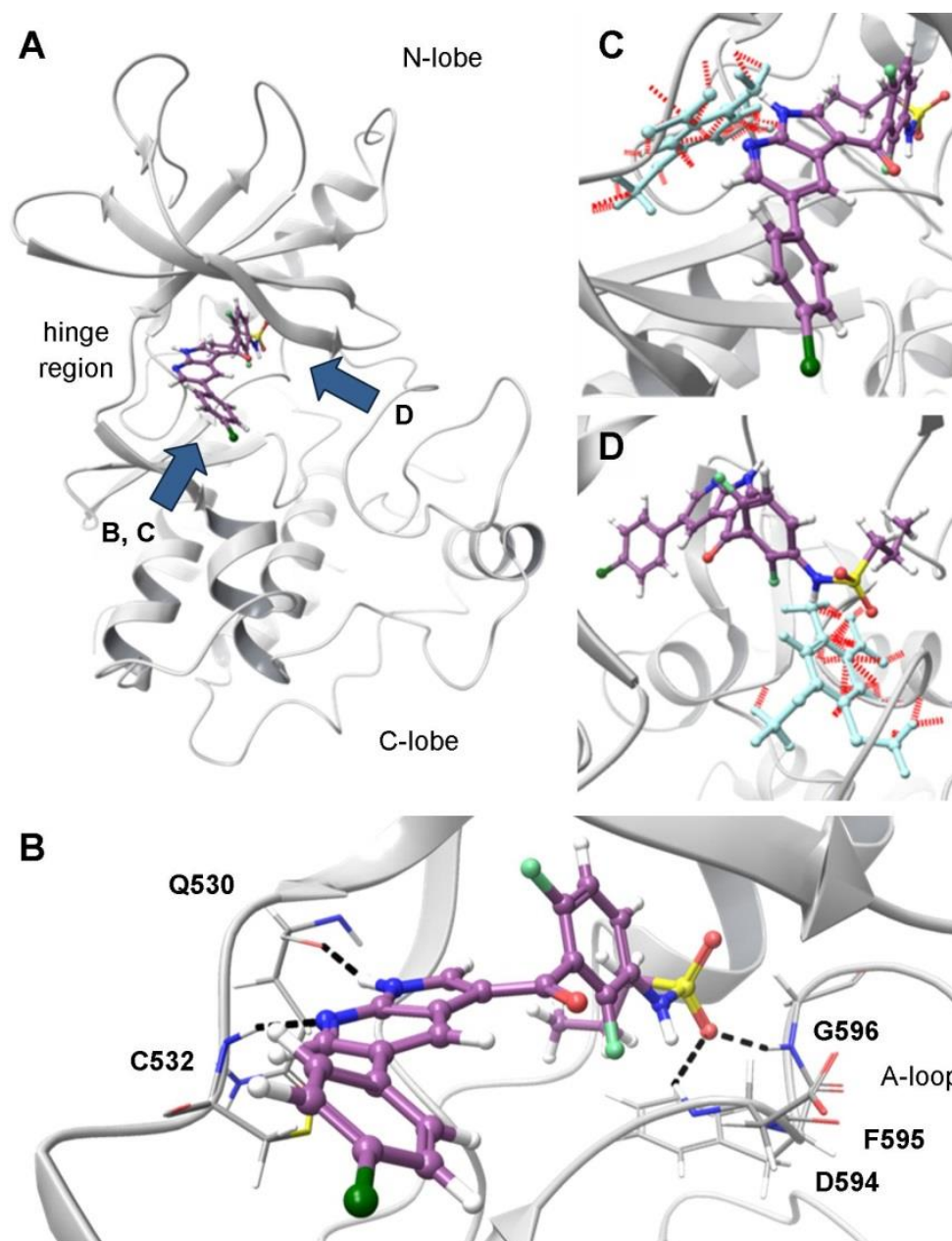


Figure 20. X-ray defined binding mode of vemurafenib in the ATP pocket of BRAF^{V600E} (pdb 3OG7⁶²) and determination of photoprotection sites. Arrows indicate the perspective of the enlarged views in (B), (C), and (D). Hydrogen bonds between the ligand and the protein backbone are indicated by black dotted lines. Red dashed lines represent steric clashes between the PPG and the target protein.

In line with this notion, superposition of modeled photoprotected vemurafenib derivatives **58** and **60** (Figure 21) in the active site of BRAF^{V600E} resulted in significant sterical clashes (Figure 20 (C) and (D)), indicating nonplausible binding modes. It was however assumed that blocking the azaindole NH moiety of vemurafenib's hinge binder would be more promising to demolish any affinity of the photoprotected prodrugs to other kinases since all type I and II inhibitors use this interaction.¹⁰⁶ On the other hand, prodrugs with a PPG attached to the sulfonamide residue might still show some affinity to kinases featuring a larger or more flexible binding pocket in this peripheral area.^{6,107}

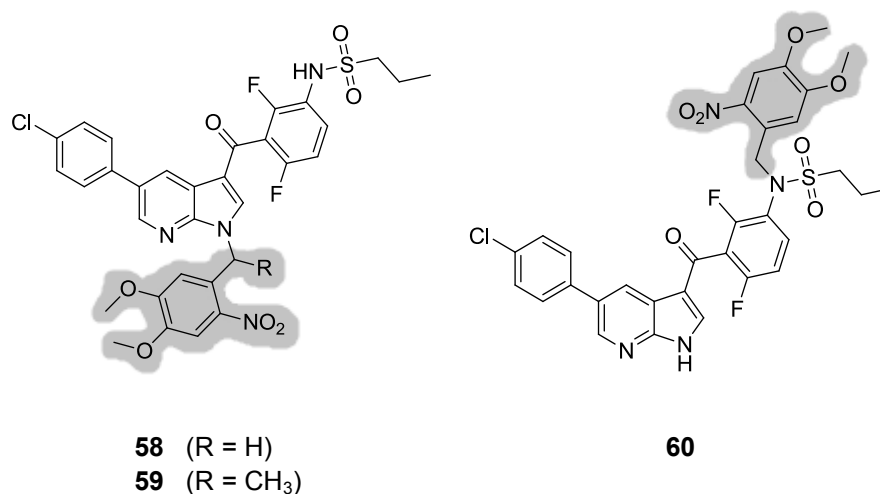


Figure 21. Chemical structures of caged vemurafenib prodrugs. The PPGs are highlighted in grey.

Motivated by the modeling data, both NH photoprotected vemurafenib analogs were synthesized as described in chapter 3.1.3. This allowed a comparison of their anticipated *in vitro* non-efficacy against the target enzyme BRAF^{V600E} and within a broad kinase panel to assess their specificity.

3.1.2 UV Stability

Reactivation of photoprotected prodrugs requires the parent compound's stability at the used wavelength of irradiated light. The drug molecule would otherwise be degraded immediately after its release or even before the covalent bond to the PPG is cleaved. The UV stability of vemurafenib was hence examined at 365 nm (chapter 5.2.2). As shown in chapter 3.1.4, this wavelength is suitable for the cleavage of the introduced PPGs. 10 mM (DMSO) and 0.01 mM (PBS buffer containing 10% DMSO) solutions of vemurafenib were irradiated for 20 min. HPLC analysis was used for content determination (chapter 5.3.4). Under these conditions, vemurafenib showed good stability over a period of 20 min (Figure 22).

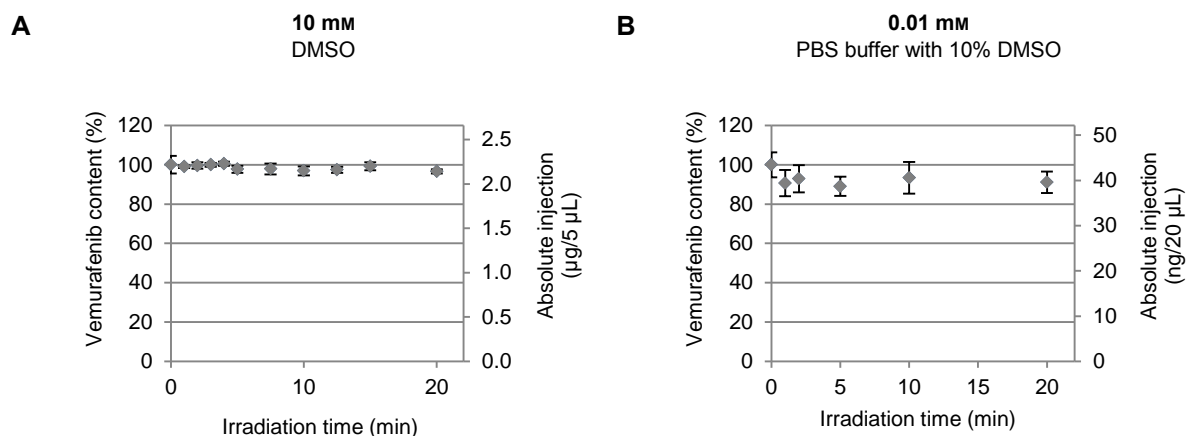


Figure 22. UV stability of vemurafenib. Stability of compound solutions in DMSO (A) resp. PBS buffer with 10% DMSO (B) against irradiation at 365 nm (LED source, 5.4 W) analyzed by HPLC.

3.1.3 Synthesis

DMNB protected azaindole derivatives

The hinge binder scaffold of vemurafenib was investigated in more detail to identify the essential core structure required for the PPG photoreaction. Since nitrogen compounds and particularly *N*-heterocycles represent poor leaving groups in photocleavage reactions, it was assumed that stabilization of transition states of the photolysis reaction would be critical. The deprotection mechanism is shown for *o*-nitrobenzyl caged compounds in Figure 23. Mesomeric and inductive effects by substituents of the leaving group play a key role for its release.¹⁹ Starting with 7-azaindole as a dummy compound, this moiety was expanded based on the structure of vemurafenib. An acetyl and a benzoyl substituent were further introduced as described below. Three caged azaindole analogs were thus synthesized (chapter 5.3.10) and their photochemical characteristics subsequently analyzed (chapter 3.1.4).

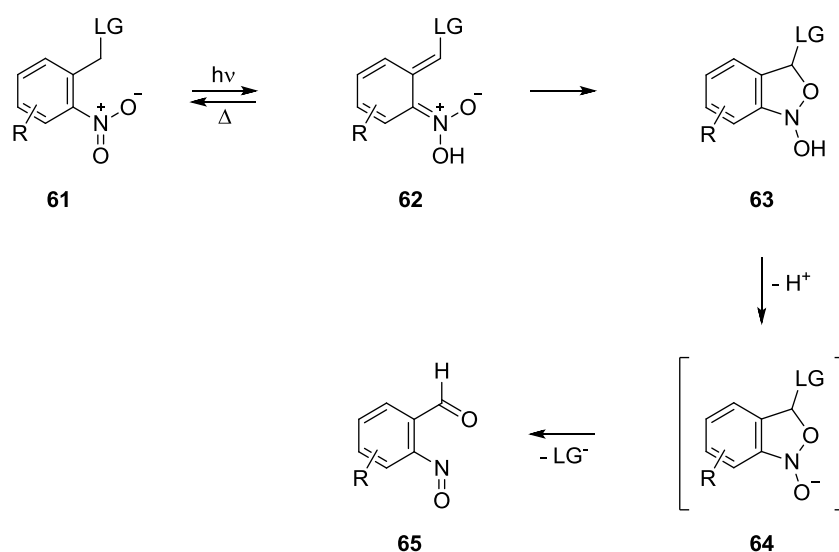


Figure 23. Release mechanism of *o*-nitrobenzyl caged compounds.^{19,108} A photoinduced H-atom transfer leads to the formation of a primary *aci*-nitro intermediate (**62**). The latter is consecutively cyclized to give a benzisoxazolol (**63**). After deprotonation, the leaving group is irreversibly cleaved and an *o*-nitrosobenzaldehyde (**65**) is formed. LG = leaving group.

7-Azaindole (**66**) and 3-acetyl-7-azaindole were commercially available. 3-benzoyl-7-azaindole (**67**) was prepared by a Friedel-Crafts acylation according to Zhang *et al.* (Figure 24, chapter 5.3.10)¹⁰⁹. The 7-azaindole was thus benzylated in 3-position using aluminium chloride as a Lewis acid catalyst.

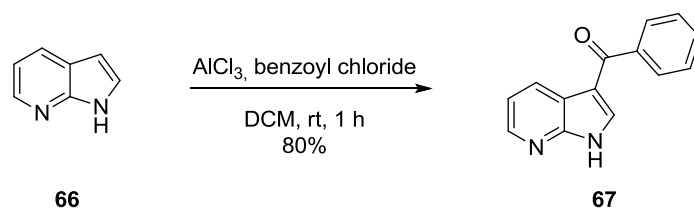


Figure 24. Preparation of 3-benzoyl-7-azaindole (67).

These three azaindoles were subsequently caged with the 4,5-dimethoxy-2-nitrobenzyl (DMNB) group¹¹⁰ as illustrated in Figure 25. This straightforward synthesis proceeds by a base catalyzed substitution reaction ($S_N1/2$). After deprotonation, the nitrogen anion acts as a nucleophile replacing the halogen atom in 4,5-dimethoxy-2-nitrobenzyl bromide (DMNB-Br).

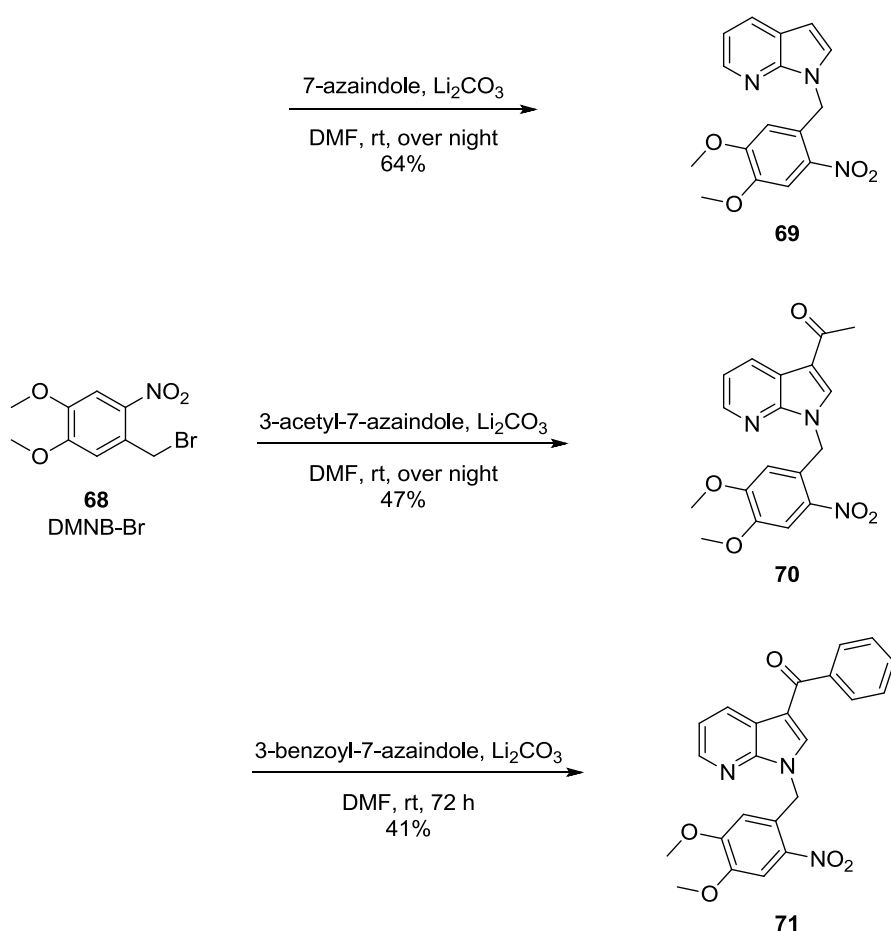


Figure 25. Synthesis of photoprotected azaindole derivatives 69, 70, and 71.

The three caged azaindole derivatives **69**, **70**, and **71** were then analyzed regarding their photocleavage characteristics; results and discussion are presented in chapter 3.1.4. 3-Benzoyl-7-azaindole (**67**) was thus identified to be crucial for photocleavage of the protection group. It was consequently utilized as a dummy compound for the comparison of different classes of PPGs in terms of chemical accessibility and uncaging characteristics.

Introduction of diverse PPG classes

A broad range of PPGs with different characteristics regarding *e.g.* attachable leaving groups, absorption maxima, release rates, and photochemical by-products are available. The designated dummy compound, 3-benzoyl-7-azaindole, was to be linked to a variety of PPGs in order to make a selection for caging of the kinase inhibitors.

First, three variations of the *o*-nitrobenzyl PPGs were to be introduced. The 1-(4,5-dimethoxy-2-nitrophenyl)ethyl (DMNPE) group bears a methyl function at the benzylic position in comparison to the DMNB group. In consequence of this, a less toxic ketone is released instead of a nitrosoaldehyde (Figure 23) which was interesting for the biological evaluation. The 6-nitroveratryloxymethyl (NVOM) and 6-nitroveratryloxycarbonyl (NVOC) group promised faster release rates due to the hemiaminal ether resp. carbamate structure in the caged nitrogen compounds.

The first two mentioned PPGs were prepared and linked to the dummy compound according to Figure 26 (chapter 5.3.10). Both synthetic strategies started with the nitration of 1-(3,4-dimethoxyphenyl)ethanone (**72**).¹¹¹ The obtained 1-(4,5-dimethoxy-2-nitrophenyl)-ethanone (**73**) was subsequently reduced to the corresponding alcohol **74** by reaction with sodium borohydride.¹¹²

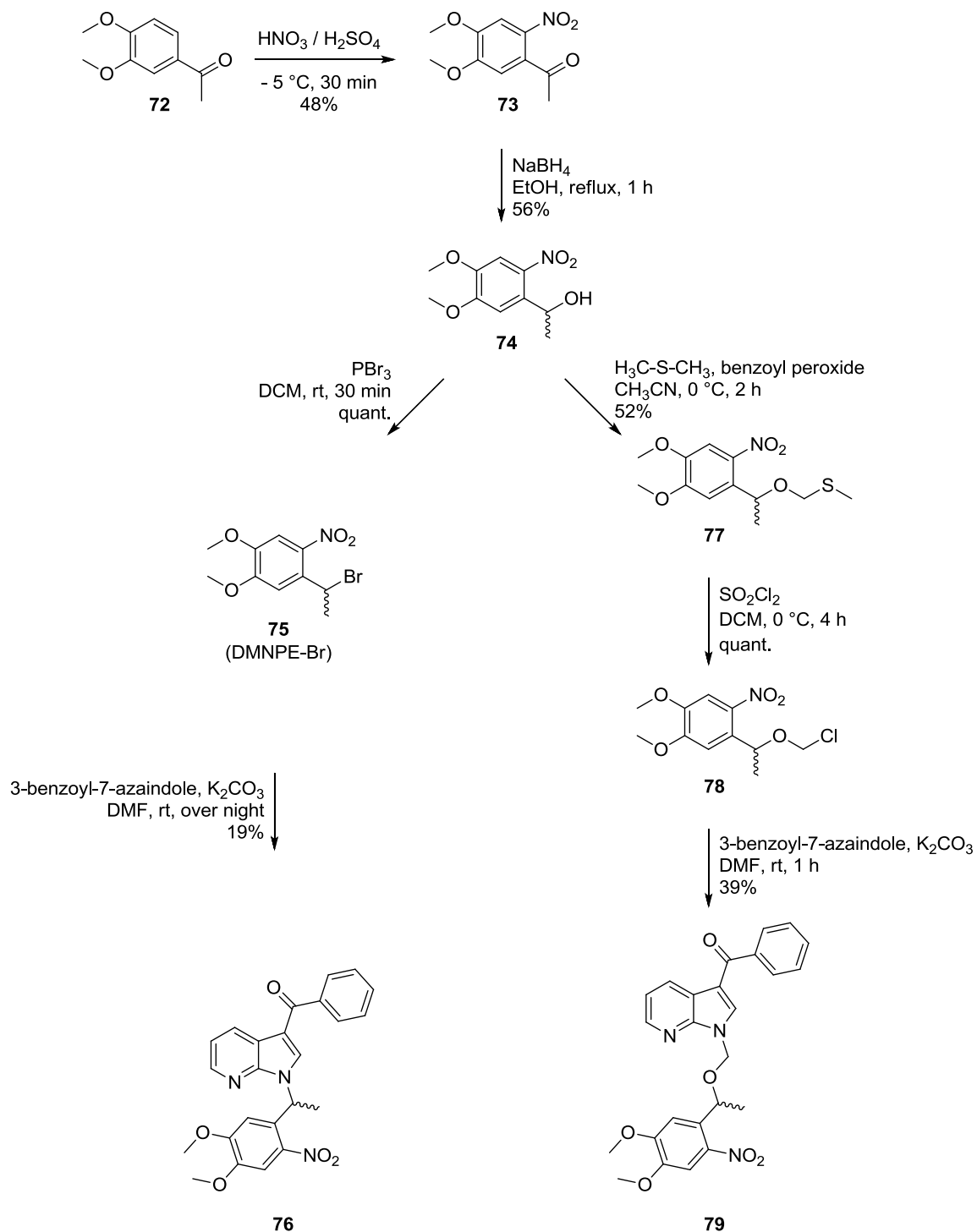


Figure 26. Protection of 3-benzoyl-7-azaindole (67) with *o*-nitrobenzyl derivatives affording caged prodrugs 76 and 79.

For the introduction of the DMNPE group into the 3-benzoyl-7-azaindole molecule, the hydroxyl moiety had first to be substituted by a bromine atom serving as an improved leaving group in compound **75**. This synthesis was performed by addition of phosphorus tribromide.¹¹³ Caging of the azaindole derivative was again a base catalyzed S_N reaction yielding the DMNPE caged **76**.¹¹⁰

For the preparation of the NVOM group, 1-(4,5-dimethoxy-2-nitrophenyl)ethanol (**74**) was treated with dimethyl sulfide and benzoyl peroxide as a radical initiator yielding **77**. To replace the methyl sulfide moiety by a chloride atom, sulfuryl chloride was used to produce **78**.¹⁸ Caging of 3-benzoyl-7-azaindole was once more achieved by a nucleophilic substitution to obtain NVOM caged **79**.¹¹⁰

Caging of 3-benzoyl-7-azaindole with the NVOC group was not successful (Figure 27). Apparently, DMNB caged **71** was formed after decarboxylation of 6-nitroveratryloxycarbonyl chloride (NVOC-Cl). Variation of the base (K₂CO₃), temperature (0 °C) and reaction under CO₂ atmosphere did not succeed either. The reagent might therefore be too instable due to ambient light exposure and a dark laboratory might be required.

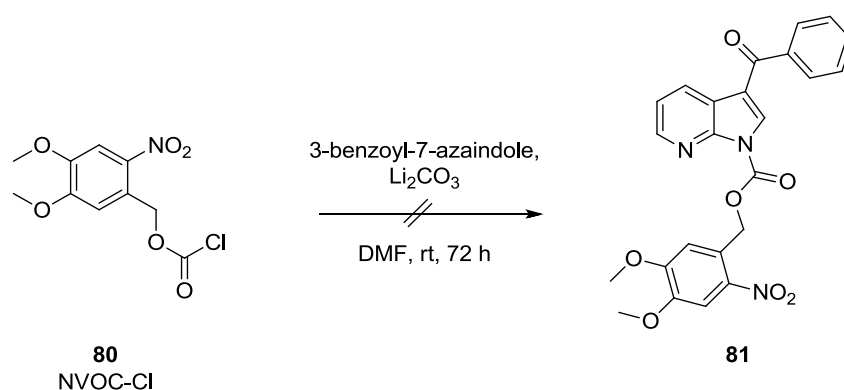


Figure 27. Failed protection of 3-benzoyl-7-azaindole (67) with NVOC-Cl.

In Figure 28 several one-step caging reactions are shown (chapter 5.3.10). *Via* the established route¹¹⁰ following PPGs were linked to 3-benzoyl-7-azaindole: 4-hydroxy-phenacyl (pHP, **82**), 4-(dimethylamino)phenacyl (**83**), 4-methyl-7-methoxycoumarin (**84**), 4-methyl-6,7-dimethoxycoumarin (**85**), and desyl (1,2-diphenylethanone, **86**).

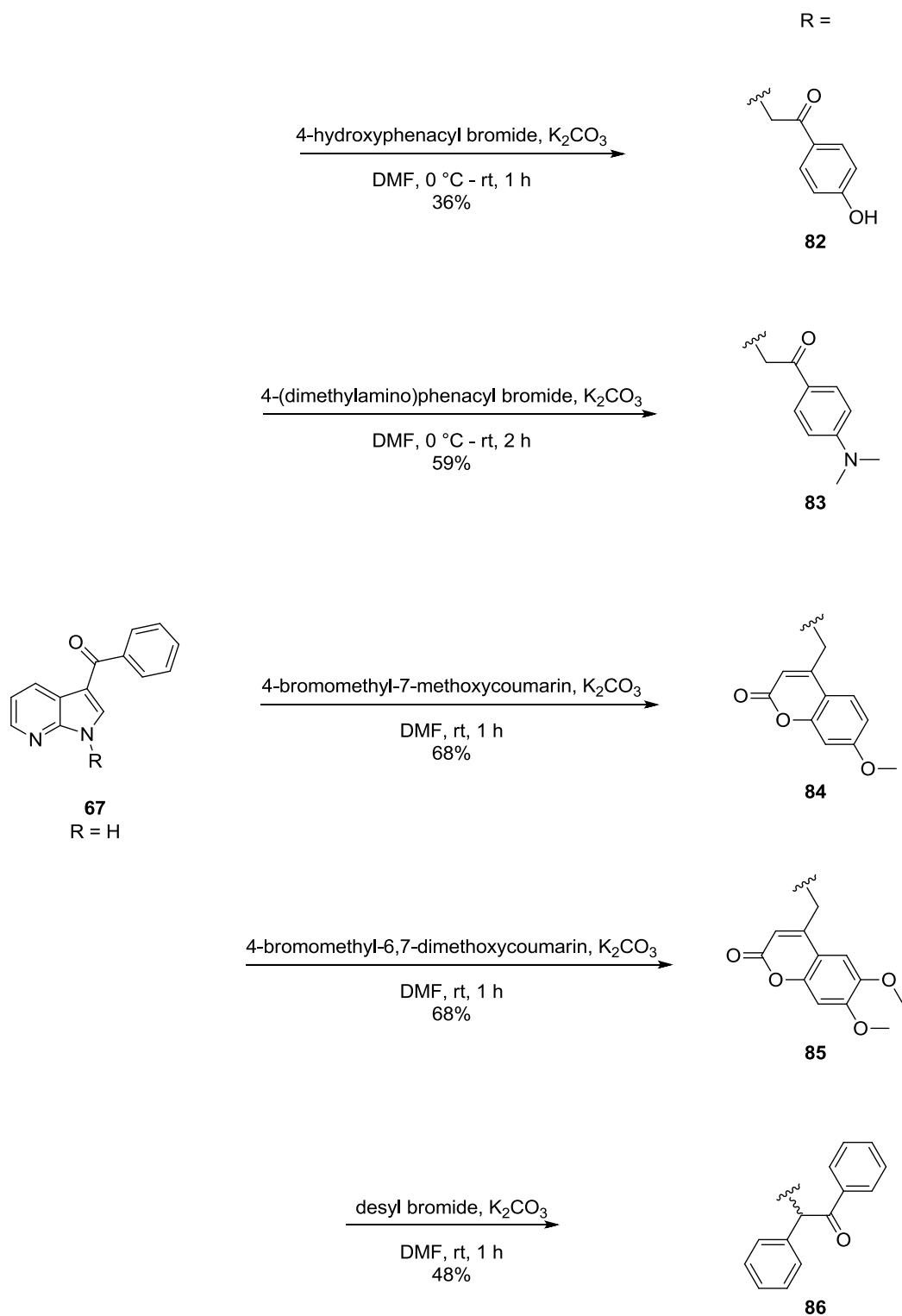


Figure 28. Protection of 3-benzoyl-7-azaindole (67) with diverse PPGs.

Vemurafenib prodrugs

Investigation of the binding mode revealed that both NH moieties within the vemurafenib structure should be appropriate for the caging concept (chapter 3.1.1). The azaindole and the sulfonamide function were therefore protected by PPGs as described in the following. This allowed a comparison of both protection sites regarding the kinetics of the photolysis reaction (chapter 3.1.4) and the influence on the biological activity (chapter 3.1.5).

Two *o*-nitrobenzylic PPGs were selected to be introduced into the vemurafenib molecule, namely the DMNB and the DMNPE moiety. Both PPGs had proven to be chemical accessible (see above) and to show fast and clean photolysis reactions when attached to 3-benzoyl-7-azaindole (chapter 3.1.4). The DMNB group produces a nitrosobenzaldehyde as a photo leaving group which is reported to be more toxic than the ketone formed by the DMNPE group.¹⁰ The biological effects of the released PPGs were thus to be investigated (chapter 3.1.5).

The use of DMNB-Br afforded the caged prodrugs **57**, **59**, and **87** (Figure 29). These compounds could be isolated by flash chromatography and were fully characterized. A comparable reaction was performed using DMNPE-Br (Figure 30). It is noteworthy that in this reaction, due to sterical hindrance at the sulfonamide, only the azaindole DMNPE protected derivative **59** was obtained and fully characterized. By-products were formed to small quantities and could not be isolated. LC-MS analysis indicated that the sulfonamide and the doubly protected derivatives **88** and **89** were formed analogously to the reaction above. In preliminary NMR analysis two sets of signals were identifiable for compound **88** which presumably belong to conformers as discussed in Figure 31. In case of the DMNPE doubly protected derivative **89**, a diastereomer pair (**89a/b**) was presumably formed due to the presence of two chiral centers. This hypothesis was supported by preliminary NMR studies and different chromatographical behavior of the compounds (Figure 32).

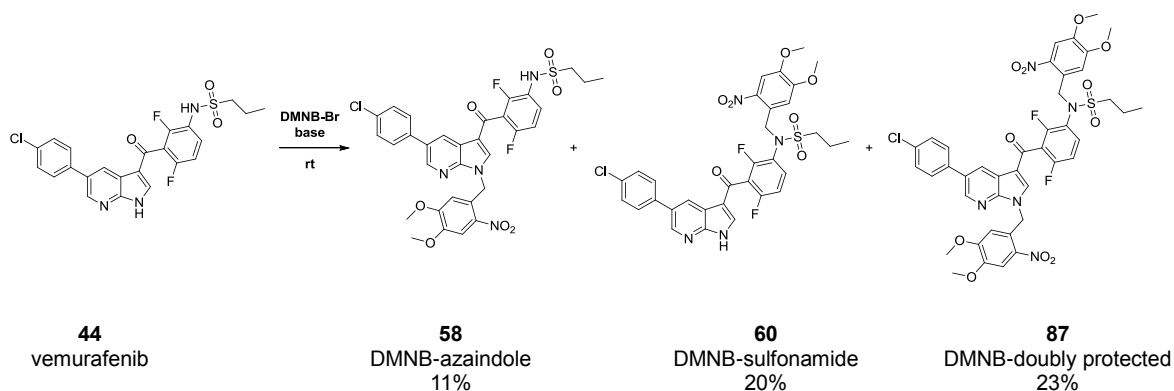


Figure 29. Synthesis of DMNB caged vemurafenib prodrugs **58** and **60**. The doubly protected **87** was formed as a by-product.

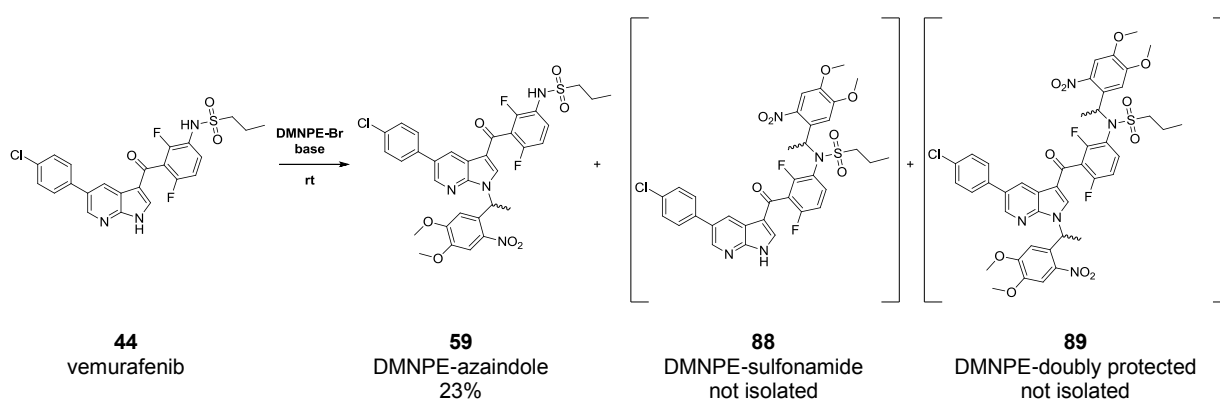


Figure 30. Synthesis of DMNPE caged vemurafenib prodrug **59**. According to preliminary NMR and LC-MS studies the sulfonamide protected **88** and the doubly protected **89** were formed as by-products in small quantities but could not be isolated.

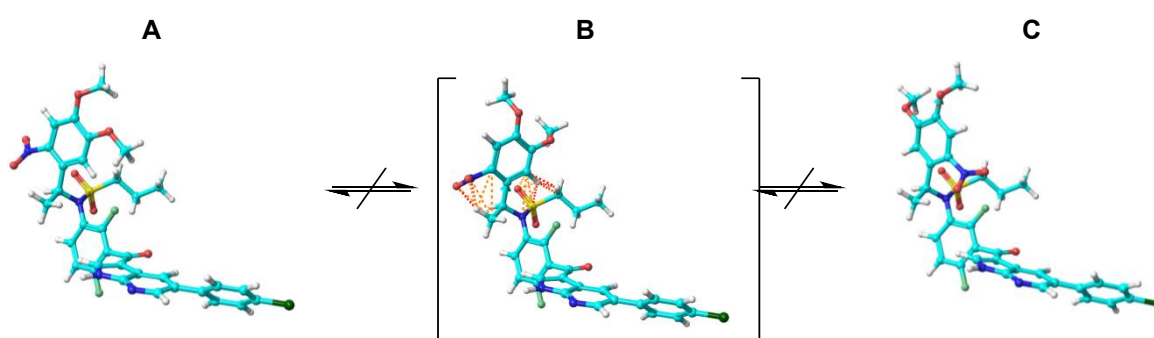


Figure 31. Modeled structures of proposed conformers of sulfonamide DMNPE protected vemurafenib (**88**). Due to sterical hindrance, DMNPE protection of vemurafenib's sulfonamide supposedly resulted in the formation of two conformers with separate NMR signal sets, shown in (A) and (C). Sterical clashes in the theoretical transition structure were calculated (B), which would hinder the rotation of the aromatic ring of the PPG.

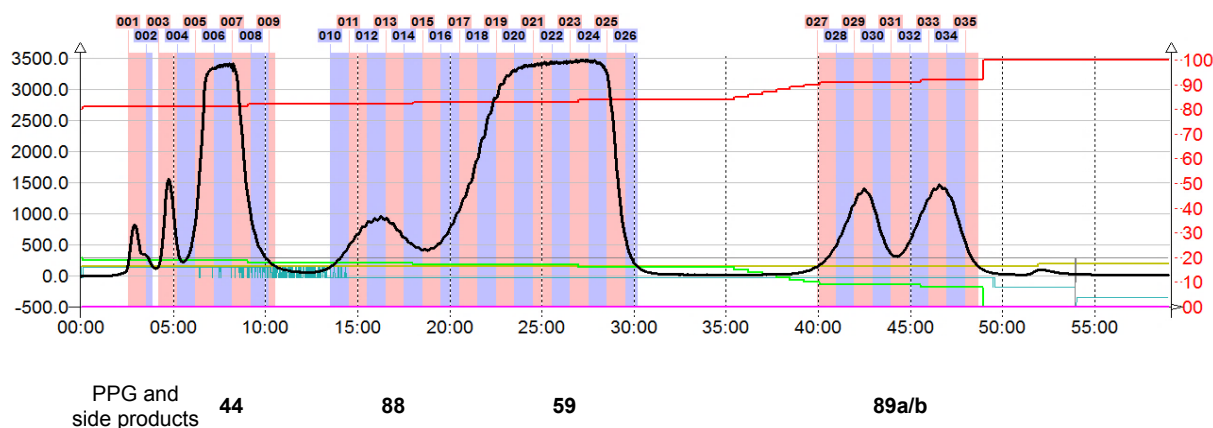


Figure 32. Chromatographic separation of DMNPE protected vemurafenib derivatives. In the S_N reaction of vemurafenib with DMNPE bromide a complex product mixture was formed. This figure shows the chromatographic separation of these products on a C18 reversed phase column. Non-reacted starting material can be assigned in the chromatogram. The DMNPE azaindole prodrug **59** was formed as the main product. Small quantities of the sulfonamide protected **88** and the doubly protected **89** were formed. The double peak (same m/z ratio) and preliminary NMR studies suggest that the latter represents a diastereomer pair (**89a/b**).

The azaindole and the sulfonamide DMNB photoprotected prodrugs **58** and **60** enabled a comparison between these two protection sites concerning their photorelease characteristics and their biological activities, respectively. Through irradiation, the DMNB group produces a nitrosobenzaldehyde, whereas a less toxic ketone is released by the DMNPE moiety.¹⁰ Compounds **58** and **59** hence allowed a comparison of these two PPGs regarding photokinetics and toxicity in cellular assays.

3.1.4 Photochemical Characterization

DMNB protected azaindole derivatives

In the first step, UV/vis absorption spectra of the caged compounds **69**, **70**, and **71** as well as their corresponding unprotected azaindole analogs were recorded to reveal an optimal wavelength for deprotection (chapter 5.2.1). Figure 33 demonstrates that there were only marginal differences between the spectra recorded in DMSO compared to those measured in an aqueous solvent. In all cases the unprotected azaindole derivatives did not absorb light with a wavelength above 350 nm; whereas the caged compounds showed an absorption peak between 350 and 360 nm. LEDs with emission wavelength of 365 nm were thus chosen for our irradiation experiments because of their high intensity and easy handling.

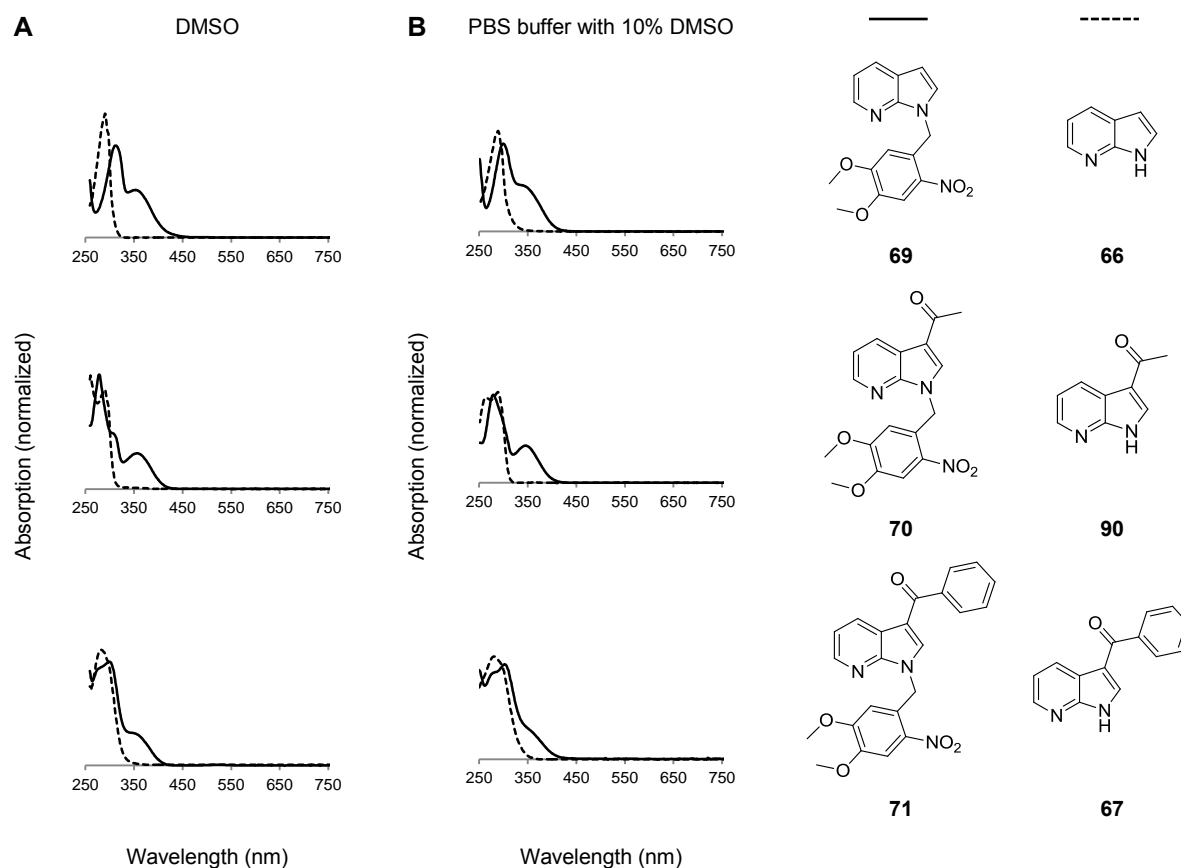


Figure 33. UV/vis absorption spectra of azaindole derivatives. UV/vis absorption spectra of photoprotected azaindole derivatives (solid lines) in comparison to their corresponding unprotected analogs (dashed lines) in (A) DMSO resp. (B) PBS buffer with 10% DMSO are shown.

Next, photocleavage upon UV irradiation of the caged azaindole derivatives **69**, **70**, and **71** was examined (chapter 5.2.3). The prodrugs were therefore dissolved in DMSO (1 mM) resp. buffer solution (0.01 mM) and irradiated by LEDs (365 nm, 5.4 W) for up to ten minutes. The ratio between caged and uncaged probe was analyzed time dependently by HPLC illustrated as peak area in % (Figure 34, chapter 5.3.4). Besides retention time, LC-MS analysis of the DMSO probes was used for proof of identity (chapter 5.3.7).

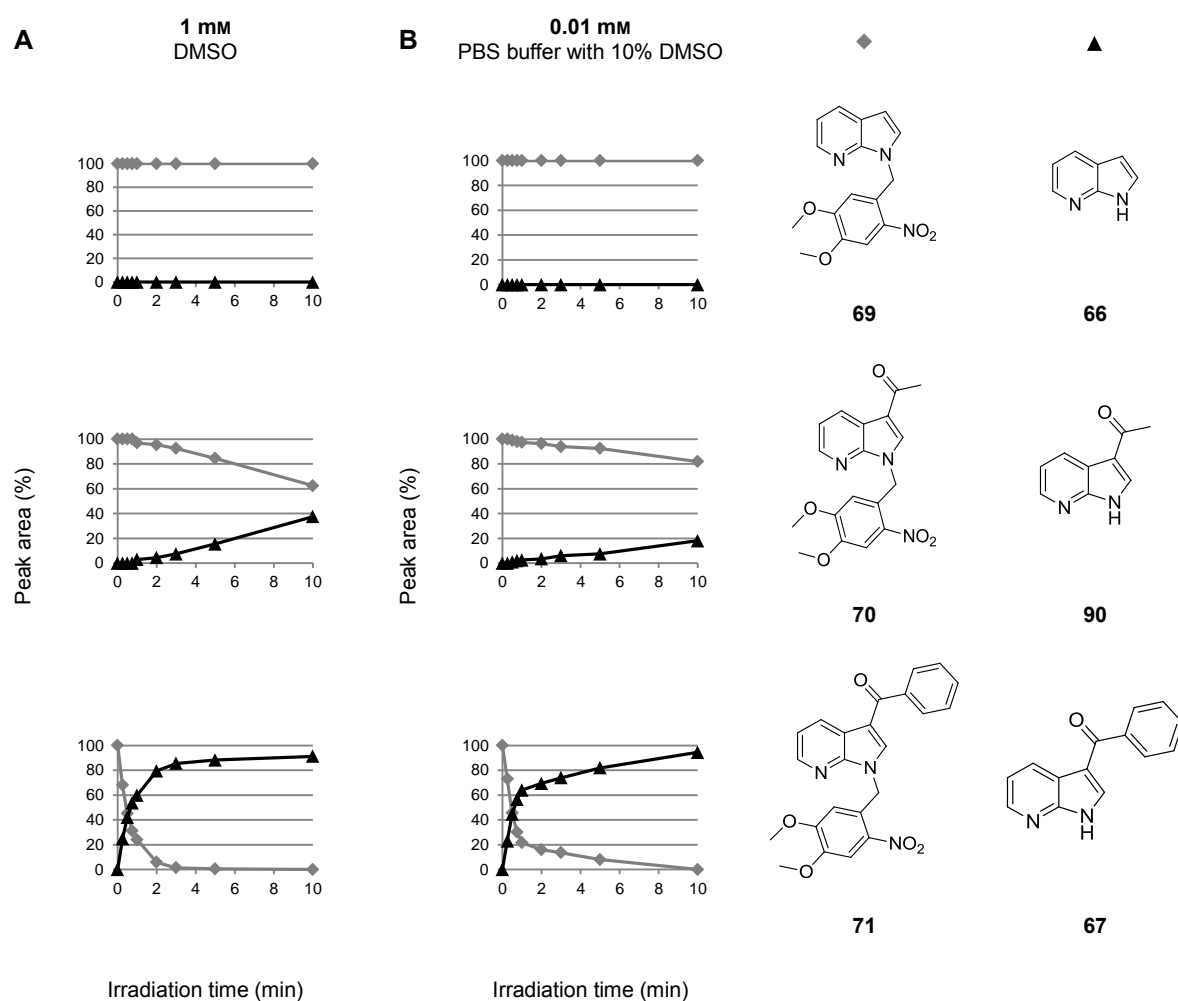


Figure 34. Photoactivation of the DMNB protected azaindole derivatives 69, 70, and 71. (A) 1 mM (DMSO) resp. (B) 0.01 mM (PBS buffer with 10% DMSO) compound solutions were irradiated at 365 nm (5.4 W) for up to 10 min and analyzed time dependently by HPLC and LC-MS. The amount of caged probe (diamonds) is plotted against the released azaindole analog (triangles).

Caged 7-azaindole **69** was perfectly stable against UV irradiation under these conditions and did not show any conversion. Apparently, the transition states of the release mechanism shown in chapter 3.1.3 (Figure 23) could not be stabilized by this leaving group. Photoprotected 3-acetyl-7-azaindole **70** could be uncaged but at a very slow reaction rate. However, the 3-benzoyl-7-azaindole prodrug **71** showed good photorelease characteristics. Concentration and solvent did not have a significant impact on the uncaging process.

The 3-benzoyl-7-azaindole motif can therefore be considered to be the essential vemurafenib fragment for a suitable photorelease of the *N*-heterocycle. The transition states of the photolysis reaction seem to be stabilized by an extended mesomeric system. Further investigations *e.g.* molecular calculations of binding energies have to clarify the details of the mechanisms of these findings.

Comparison of diverse PPG classes

Since 3-benzoyl-7-azaindole (**67**) was easily cleaved from the DMNB protection group, it had proven to be applicable as an *N*-heterocycle photo leaving group. **67** was therefore used as a dummy compound for further photoexperiments to compare different PPGs. Diverse representatives were thus synthetically linked to this molecule as described in chapter 3.1.3. In this section, Figure 35 gives a compact overview over the photocharacteristics of these diversely caged 3-benzoyl-7-azaindole prodrugs (chapters 5.2.1 and 5.2.3).

As expected, DMNPE protected **76** and NVOM caged **79** (both belonging to the *o*-nitrobenzyl PPG family) also showed a peak absorbance around 360 nm. Their photorelease upon irradiation at 365 nm was in fact very similar to that of DMNB protected **71**. The introduction of a methyl group resp. an ether bridge, thus, did not result in an accelerated reaction rate which is in contrast to the results reported in the literature¹⁰. The cleaved protection group of these two compounds however contains a ketone function instead of an aldehyde, which might be less toxic in biological experiments.¹⁰ Hence, they are potentially interesting for the photoprotection of *N*-heterocycles and for the following caging projects. As seen before for the DMNB derivatives, concentration and solvent did not have a significant impact on the uncaging process.

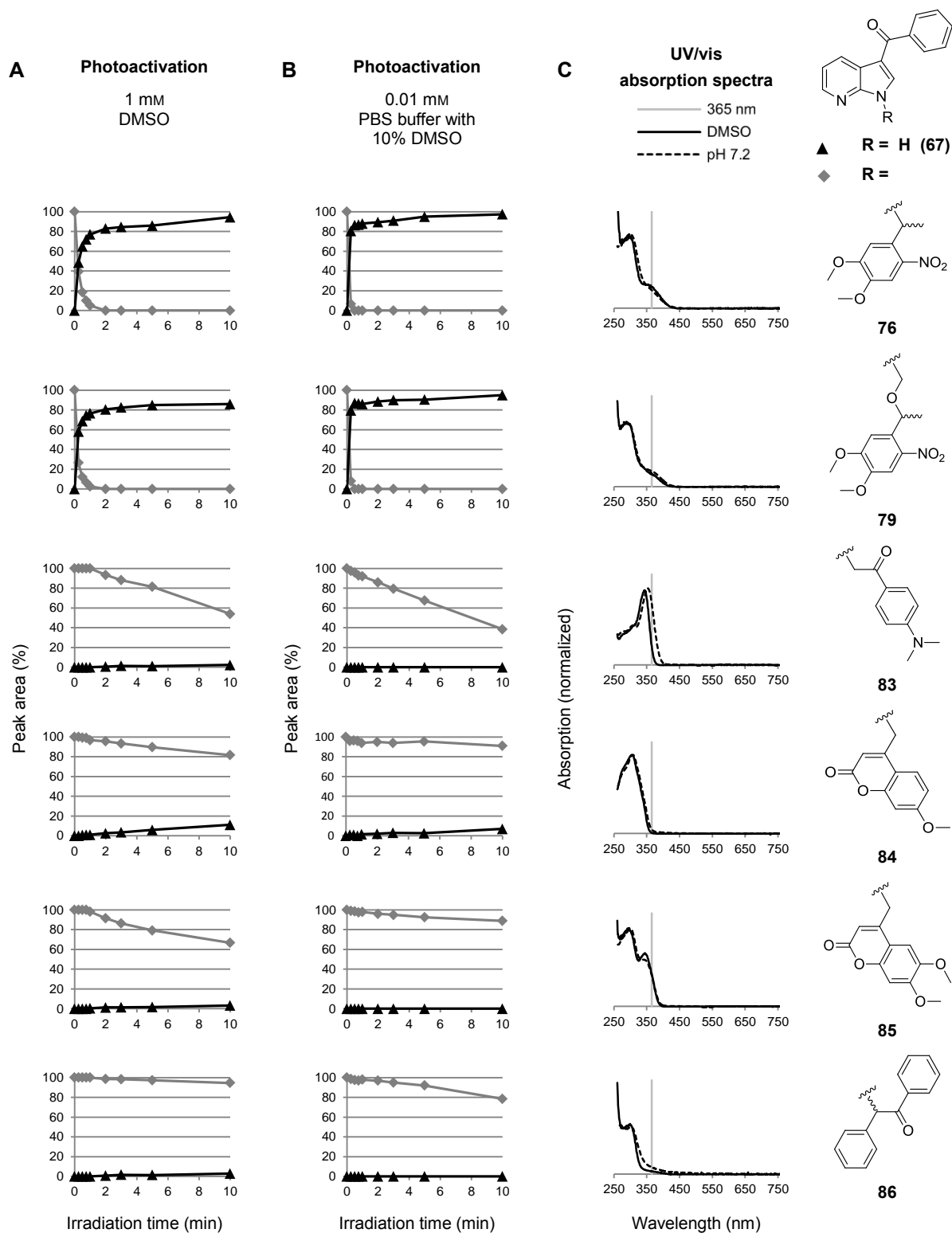


Figure 35. Photoactivation and UV/vis absorption spectra of differently caged 3-benzoyl-7-azaindole derivatives. (A) 1 mM (DMSO) resp. (B) 0.01 mM (PBS buffer with 10% DMSO) compound solutions were irradiated at 365 nm (5.4 W) for 10 min and analyzed time dependently by HPLC and LC-MS. The amount of caged probe (diamonds) is plotted against the released 3-benzoyl-7-azaindole (67, triangles). (C) UV/vis absorption spectra in DMSO resp. PBS buffer with 10% DMSO at pH 7.2.

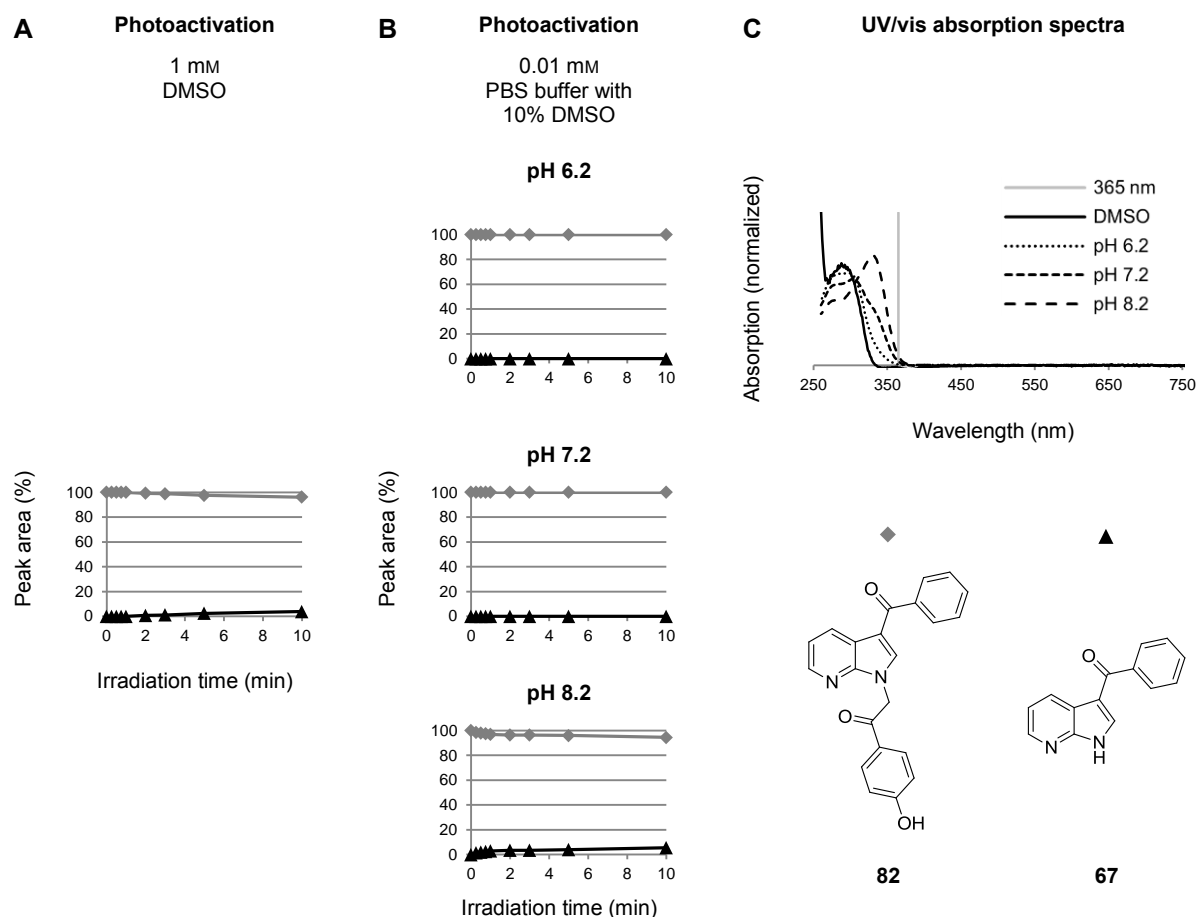


Figure 36. pH-Dependent photoactivation and UV/vis absorption spectra of 4-hydroxy-phenacyl (pHP) caged 3-benzoyl-7-azaindole (82**).** (A) 1 mM (DMSO) resp. (B) 0.01 mM (PBS buffer with 10% DMSO, pH 6.2, 7.2, and 8.2) compound solutions were irradiated at 365 nm (5.4 W) for 10 min and analyzed time dependently by HPLC and LC-MS. The amount of caged probe (diamonds) is plotted against the released 3-benzoyl-7-azaindole (**67**, triangles). (C) UV/vis absorption spectra in DMSO resp. PBS buffer with 10% DMSO at pH 6.2, 7.2, and 8.2.

The photocharacteristics of 4-hydroxy-phenacyl (pHP) caged **82** are presented separately in Figure 36. In DMSO **82** did not show absorption at 365 nm. It is therefore not surprising that only a small percentage of the prodrug was deprotected after ten minute irradiation. Notably, in an aqueous solvent the spectra showed a distinct pH dependency due to deprotonation of the acidic phenol group. The increase of the pH value (6.2, 7.2, and 8.2) caused a bathochromic shift leading to an ascending absorption at 365 nm. Nevertheless, this did not have an influence on the insufficient deprotection reaction. Lower wavelengths might improve the photolysis reaction but should be avoided for the irradiation of biological probes.

The related 4-(dimethylamino)phenacyl caged **83** showed an adequate absorption value at 365 nm in DMSO and even higher, pH-independent (in the range between pH 6.2 and 8.2) values in an aqueous solvent (Figure 35). Irradiation of **83** at 365 nm however led to rapid unspecific degradation (products not characterized). Only traces of deprotected 3-benzoyl-7-azaindole could be detected. This PPG was thus considered to be unsuitable for the purpose of *N*-heterocycle photoprotection.

4-Methyl-7-methoxycoumarin caged **84** did not absorb light at a wavelength of 365 nm. More than 10% 3-benzoyl-7-azaindole could surprisingly be released after ten minutes of irradiation. This slow conversion is not convenient for biological applications though. The absorption band of another coumarin derivative, the 4-methyl-6,7-dimethoxycoumarin caged **85**, was shifted bathochromically. Irradiation however led to unspecific degradation (products not characterized) and only traces of 3-benzoyl-7-azaindole (**67**) were cleaved after ten minutes time.

The last investigated PPG was the desyl group. Both in DMSO and in buffer solution, caged compound **86** showed little absorption. After ten minutes only small quantities of 3-benzoyl-7-azaindole (**67**) were released by irradiation which was not sufficient enough for the caging project.

In conclusion, suitable PPGs for the dummy compound, 3-benzoyl-azaindole (**67**), could be defined by the presented systematic approach. The *o*-nitrobenzyl groups DMNB, DMNPE, and NVOM revealed clean photocleavage with comparable, rapid reaction rates. All other investigated PPGs did not provide satisfactory results. DMNB and DMNPE were thus selected as PPGs for the vemurafenib project in order to compare the impact of the different cleaved protection groups (aldehyde *vs.* ketone) in biological assays.

Vemurafenib prodrugs

For the prodrug concept, it is essential that the parent compound is released rapidly and quantitatively upon irradiation. UV/vis absorption spectra were recorded in order to find the optimal irradiation wavelength for deprotection of the vemurafenib prodrugs (Figure 37, chapter 5.2.1). Shortwave UV irradiation underneath 300 nm (UVB and UVC) might damage tissues or proteins because of their high energy. Vemurafenib itself furthermore showed absorption up to 350 nm. Irradiation with light below that wavelength might hence lead to instability of the parent compound. The prodrugs showed an additional absorption peak around 365 nm due to the introduced PPG. LEDs are advantageously available for this wavelength, show a high intensity and were therefore chosen for the photochemical and subsequent biological evaluation.

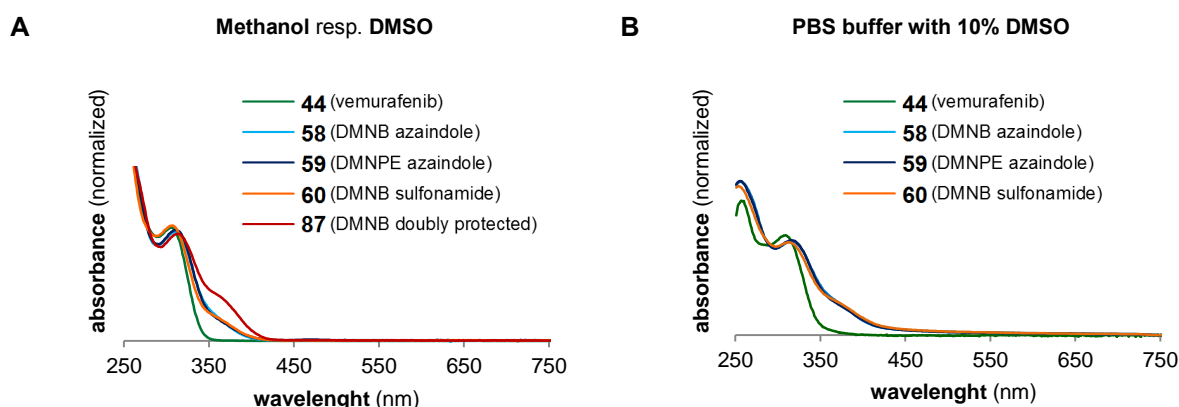


Figure 37. UV/vis absorption spectra of vemurafenib prodrugs in MeOH/DMSO (A) resp. PBS buffer with 10% DMSO (B).

In the following step, photorelease kinetics of the different vemurafenib prodrugs were studied (chapter 5.2.3). An LED reactor with an emission at 365 nm (5.4 W) was utilized to irradiate 1 mM (DMSO) and 0.01 mM (PBS buffer containing 10% DMSO) solutions of the compounds (Figure 38).

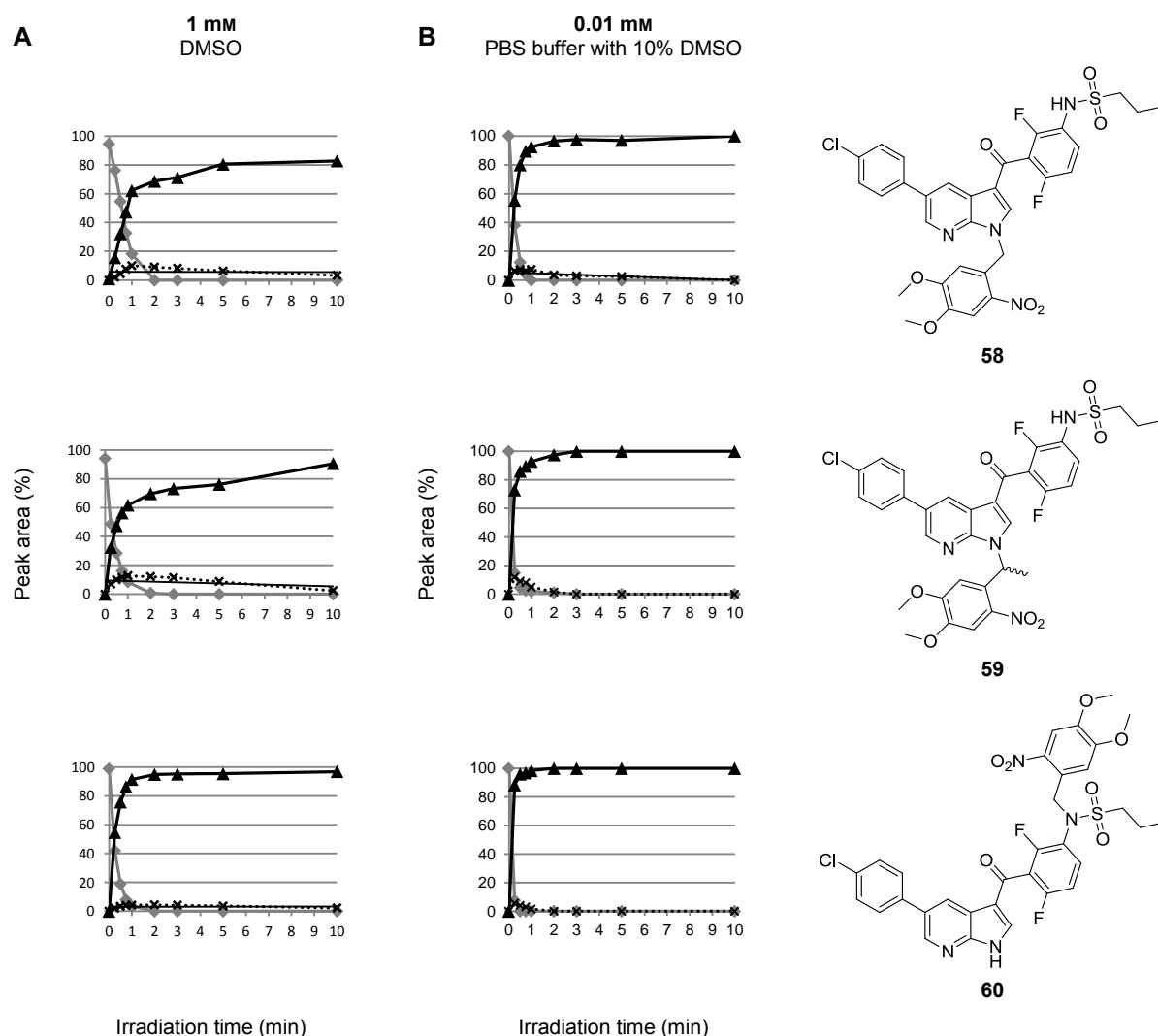


Figure 38. Photoactivation of the vemurafenib prodrugs **58**, **59**, and **60** in DMSO (A) resp. PBS buffer with 10% DMSO (B). The compound solutions were irradiated at 365 nm (5.4 W) for 10 min and analyzed by HPLC and LC-MS. The amount of caged probe (diamonds) is plotted against released vemurafenib (triangles). The formation of a cyclic benzisoxazolidine intermediate was observed (crosses); for further details, see Figure 39.

Upon irradiation in aqueous media, the sulfonamide protected derivative **60** showed fastest cleavage of the PPG. After 30 s, more than 90% of vemurafenib was released. Azaindole protected **58** and **59** were comparable to each other in their photocharacteristics. More than 90% of vemurafenib was released within 1 min. Similar results were obtained in pure DMSO; however, the slightly slower reaction rate is presumably based on higher compound concentration in this setting. In the literature, DMNPE is reported to have a higher quantum yield compared to that of DMNB.¹⁰ The assumption that **59** would show faster releasing characteristics than **58** could not be confirmed in our study. According to LC-MS and NMR studies, the formation of a cyclic benzisoxazolidine intermediate (**93**) could be observed; for a detailed discussion, see Figure 39.

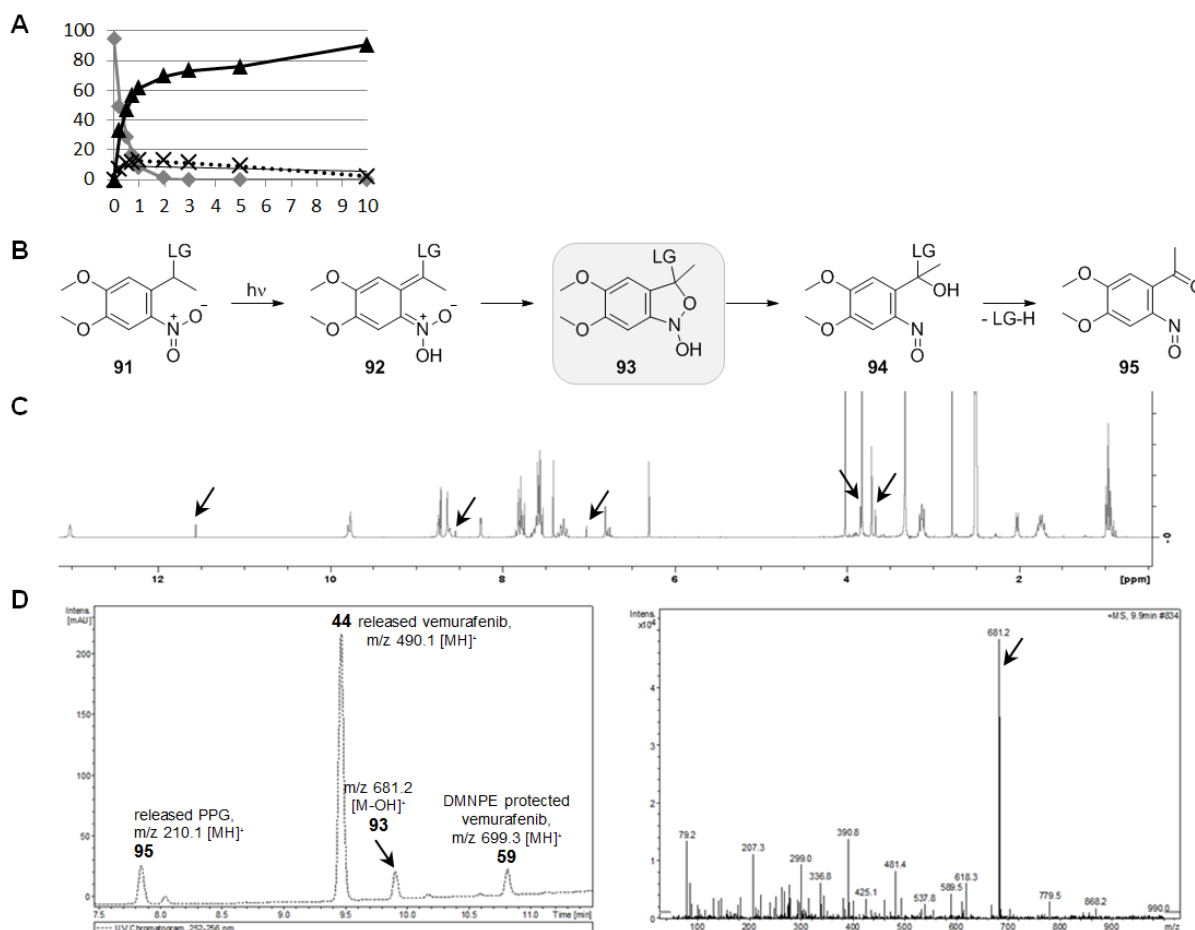


Figure 39. Photorelease of vemurafenib and cyclic benzisoxazolidine intermediate formation. (A) A 1 mM solution of compound **59** in DMSO was irradiated at 365 nm (5.4 W) for 10 min and analyzed by HPLC (chapter 5.2.3). The amount of caged probe (diamonds) and released vemurafenib (triangles) was analyzed time dependently. Additionally, the formation of an intermediate was observed (crosses). After 1 min its content reached up to 13% of the peak area as a maximum, before it was slowly degraded again. (B) The proposed cleavage mechanism of the DMNPE protecting group is presented.¹¹⁴ The cyclic benzisoxazolidine intermediate (**93**) was presumably detected by HPLC analysis of the irradiated solution (chapter 5.3.4). In the dark, the intermediate was stable in DMSO solution for several hours, which allowed further analysis. (C) In the mixed NMR spectrum of a 90 s irradiated probe the datasets of caged/uncaged vemurafenib and the cleaved PPG can be recognized (chapter 5.3.6). Besides, there are additional peaks (integral 0.1) that presumably belong to the intermediate (arrows). The sharp singlet of an exchangeable proton with a significant downfield shift of 11.6 ppm supposedly belongs to the N-OH group. (D, left) In the chromatogram of the LC-MS analysis the caged prodrug **59**, uncaged vemurafenib (**44**) and the cleaved PPG (**95**) can be identified (chapter 5.3.7). The intermediate shows a shorter retention time compared to **59** indicating a more polar molecule which supports the structure of **93**. (D, right) The MS spectrum revealed a signal of m/z 681 for the intermediate. A hydroxide ion is presumably eliminated by the cyclic benzisoxazolidine **93** during electrospray ionization. The ring opening of the benzisoxazolidine is furthermore reported to be the rate-determining step of this reaction, which would explain an accumulation of this intermediate.

In conclusion, both NH photoprotection sites proved to be suitable for rapid and quantitative photorelease of vemurafenib. The next question to be addressed was whether the protection of these moieties would actually diminish the effect on BRAF^{V600E} and also suppress the antiproliferative effect in cells.

3.1.5 Biological Evaluation

The major part of this chapter has been drafted by Boris Pinchuk in course of preparing the manuscript Horbert and Pinchuk *et al.*¹¹⁵. Minor modifications *e.g.* embedding of complementary data have been implemented in order to improve readability.

Kinase assays

Binding affinities of vemurafenib and caged compounds toward BRAF^{V600E} were determined (Table 5, chapter 5.4.1). In line with the modeling data, the caged compounds exhibited a lower binding affinity toward BRAF^{V600E} in comparison to that of vemurafenib.

Table 5. Kd values of vemurafenib (44) and the caged prodrugs 58, 59, and 60 toward BRAF^{V600E}.

Compound	44	58	59	60
Kd values	10 nM	440 nM	77 nM	79 nM

The lowest binding affinity was found for azaindole protected **58**. This is strong evidence that protection of the azaindole moiety forestalls the inhibitor-enzyme interaction. Surprisingly, **59** and **60** still show unexpected binding toward BRAF^{V600E} although their affinities are significantly less than that of vemurafenib (**44**). The determined affinities can be explained by minute quantities of unprotected active compound in the samples and/or instability of caged compounds resulting in the release of vemurafenib under the assay conditions. For investigations on the stability of the prodrugs in cellular growth medium (chapter 5.4.6), also see Figure 40.

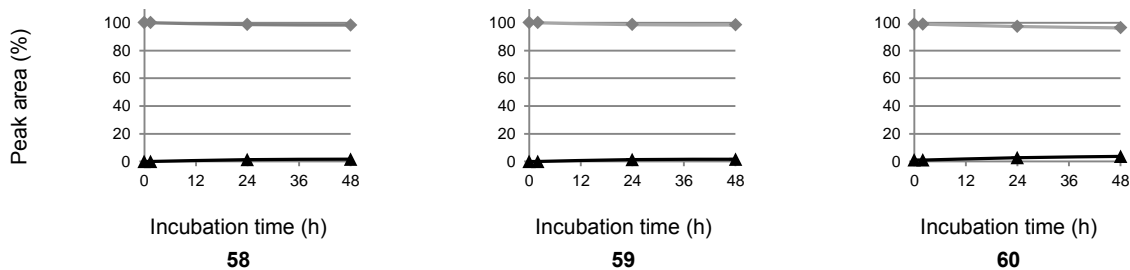


Figure 40. Stability of the vemurafenib prodrugs **58**, **59**, and **60** in cellular growth medium. 0.01 mM compound solutions (DMEM medium with 2 mM *L*-glutamine, 1 mM sodium pyruvate and 10% DMSO) were incubated in a 5% CO₂ humidified atmosphere at 37 °C for 48 h and analyzed by HPLC. The amount of caged probe (diamonds) is plotted against released vemurafenib (triangles). All three prodrugs showed a good stability under the described conditions.

A selectivity profile over 140 kinases for vemurafenib (**44**), **58**, and **60** at a concentration of 10 μM was subsequently performed (chapter 5.4.3). The results are presented as a heat map in Figure 41. Apparently, vemurafenib potently inhibited several other kinases besides BRAF^{V600E}. There are altogether 32 kinases whose activity was reduced to less than 30% under these test conditions. The most affected kinases were BRK, MAP4K5, and DDR2. This data indicates that vemurafenib is not highly selective at the tested concentration in biochemical assays. Sulfonamide caged compound **60** reduced the activity of 13 kinases to less than 30%. Its inhibitory potency against non-target kinases was diminished in comparison to that of vemurafenib. Some non-specific interactions were, however, still observable. Regarding this data, it can be assumed that protection of the sulfonamide residue prevents binding to BRAF^{V600E} but was still not sufficient enough to completely suppress inhibition of other kinases. In contrast, azaindole protected compound **58** inhibited only two kinases: MAP4K5 (7% residual activity) and RIPK2 (26% residual activity). These findings are in line with the initial assumption that blockade of the hinge binder, the azaindole moiety, would annihilate the affinity to kinases in general more effectively than the protection of the sulfonamide residue.



Figure 41. Kinase selectivity profiling of vemurafenib and caged prodrugs. The inhibitory effect of vemurafenib (**44**) and the caged derivatives **58** and **60**, respectively, was tested in a panel of 140 kinases. The residual activity of kinases was measured after incubation with 10 μM of each compound. The data is portrayed as a heat map of the mean activity of assay duplicates. The color code refers to the residual kinase activity ranging from red (low residual activity) to blue (high residual activity). Apparently, **58** inhibited significantly less kinases than vemurafenib and **60**. Details are shown in Supplementary Table 1 (Appendix).

Cellular assays

On the basis of the enzymatic data, it was supposed that the caged derivatives would show considerably less activity in cellular assays compared to that of vemurafenib. To prove this hypothesis, the anti-proliferative activity was investigated in cellular growth assays using the melanoma cell line SKMel13 which carries the BRAF^{V600E} mutation (chapters 5.4.4 and 5.4.5).¹¹⁶ Dose-response curves for the non-irradiated compounds were measured (Figure 42 (A)).

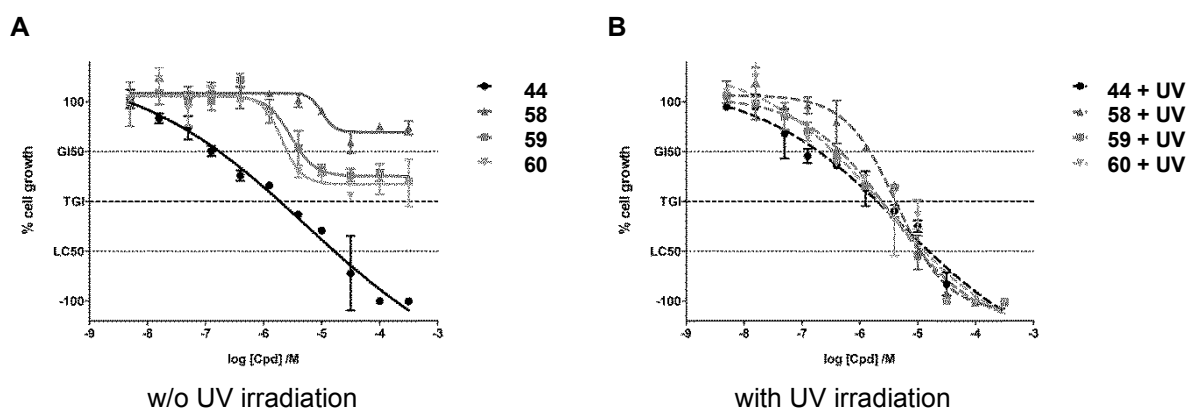


Figure 42. Activation of caged vemurafenib prodrugs in cell proliferation assays. The recovery of vemurafenib's efficacy by UV irradiation was demonstrated using SKMel13 cells. (A) Dose-response curves of vemurafenib (44) and the caged prodrugs 58, 59, and 60 were determined without UV irradiation. Cell growth was measured 48 h after incubation with the compounds. Vemurafenib clearly showed cytotoxic effects at concentrations above 1 μM . The caged derivatives did not exhibit cytotoxic activity: the TGI-mark was not reached even at high concentrations. (B) Cells were incubated for 1 h with the compounds and then irradiated at 365 nm (1.8 W) for 5 min. Cell growth was determined 48 h after incubation with the compounds. After irradiation the caged derivatives showed similar dose-response curves in comparison to active vemurafenib. GI₅₀ = 50% growth inhibition; TGI = total growth inhibition; LC₅₀ = 50% lethal concentration. (\pm SD, $n=4$)

Vemurafenib showed potent cytotoxic activity (GI₅₀ value 0.17 μM). This finding corresponds with previous studies that revealed a strong inhibition of V600E-positive melanoma cells by vemurafenib.^{117–119} In contrast, the caged compounds exhibited no cell toxicity toward the melanoma cells in the nanomolar range. Cytostatic effects occurred at considerably higher concentrations (GI₅₀ values: 4.3 μM for 59 and 2.6 μM for 60). Compound 58 did not show significant cell growth inhibition at all. The marginal cytostatic effects of the caged probes at higher concentrations could again be caused by minute impurities of unprotected vemurafenib or by off-target effects of the compounds.

It was next examined whether the inhibitory potency of the photoprotected compounds in cells could be restored upon UV irradiation. The cell growth assays described above were performed by irradiating the cells with UV light at 365 nm (1.8 W, 5 min) with and without compound incubation. The dose-response curves are presented in Figure 42 (B). In this assay, the UV irradiation at the applied dosage was well-tolerated by the cells. After UV irradiation, the prodrugs showed antiproliferative activity comparable to that of unprotected vemurafenib (GI_{50} values: 0.19 μM for vemurafenib, 1.5 μM for **58**, 0.46 μM for **59**, and 0.35 μM for **60**). The slightly reduced activity in comparison to that of vemurafenib might be explained by incomplete photorelease under the described conditions. Summarizing the results of the proliferative cell assays, it can be postulated that the irradiation of the caged compounds restores the potent activity of vemurafenib.

Having demonstrated the photoactivation of vemurafenib from its caged prodrugs, the effect of the cleaved PPG on cellular growth was investigated (chapters 5.4.4 and 5.4.5). The caged vemurafenib prodrugs were not suitable to answer this question because of the intrinsic toxicity of uncaged vemurafenib after irradiation. Two model compounds were therefore used (Figure 43): the presumably nontoxic *tert*-butyloxycarbonyl (BOC) protected *L*-alanine (**96**) and its DMNB photoprotected derivative (**97**).

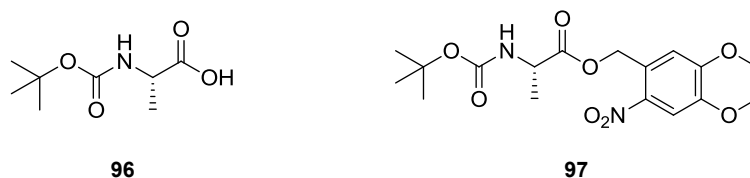


Figure 43. Chemical structures of BOC protected *L*-alanine (**96**) and its DMNB photoprotected derivative (**97**).

The effect of both compounds on the proliferation of SKMel13 cells was measured at first (Figure 44). Both protected amino acid derivatives did not show any antiproliferative effects even at high concentrations. The same experiment was repeated with UV irradiation (365 nm, 1.8 W). Irradiated **96** was still neither cytotoxic nor cytostatic. In contrast, **97** exhibited distinct antiproliferative activity after irradiation at concentrations above 10 μM (GI_{50} value 34.4 μM). It can therefore be assumed that the measured cell toxicity was caused by the cleaved DMNB. The toxic concentration (10 μM) however was approximately 100-fold higher than the efficacious concentration of the released vemurafenib (0.17 μM).

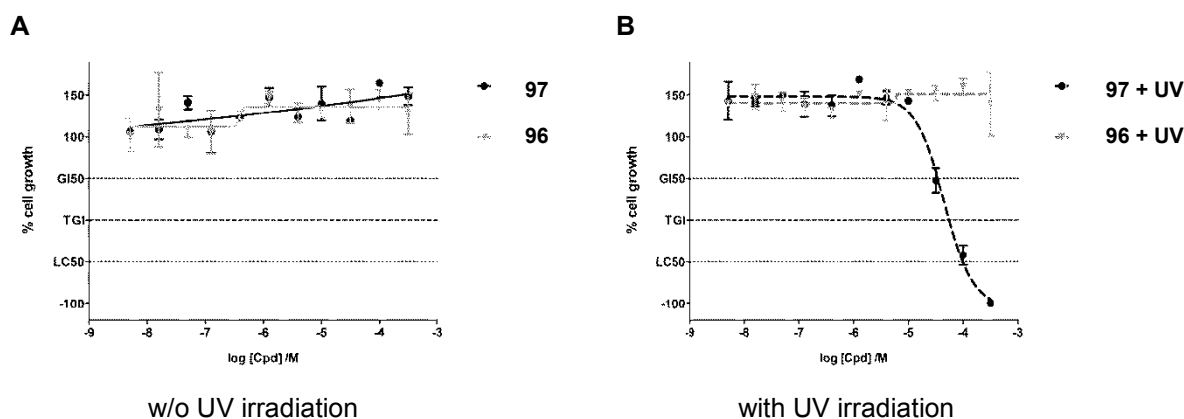


Figure 44. Effect of the photo released PPG on cell proliferation. (A) Dose-response curves of *L*-alanine derivative **96** and its photoprotected analog **97** in cell viability assays (SKMel13 cells) without UV irradiation. Cell growth was determined after 48 h incubation with compound solutions. Both compounds did not show anti-proliferative effects. (B) Dose-response curves of **96** and **97** in the same assay with UV irradiation. After 1 h incubation with compound solutions, cells were irradiated at 365 nm (1.8 W) for 5 min. Cell growth was again determined after 48 h. Herein, **97** showed anti-proliferative efficacy in concentrations above 10 μM providing evidence for the cytotoxicity of the cleaved PPG at higher concentrations. GI50 = 50% growth inhibition; TGI = total growth inhibition; LC50 = 50% lethal concentration. (\pm SD, $n=2$)

Western blots

In order to study the impact of vemurafenib and its caged derivatives on BRAF^{V600E} signaling, western blot analysis was performed on downstream Erk phosphorylation (Figure 45, chapter 5.4.7).

Erk phosphorylation in SKMel13 cells was investigated after incubation with compound solutions without irradiation. Total Erk was used as a loading control. As reported for a BRAF inhibitor, vemurafenib (**44**) displayed dose-dependent pErk inhibition at concentrations higher than 0.01 μM .^{62,117–119} The phosphorylation of Erk was completely blocked at concentrations above 0.1 μM . According to the biochemical data, the caged compounds **58** and **60** revealed significantly less inhibition of Erk phosphorylation. Even at a concentration of 10 μM , there were detectable signals of pErk.

Erk phosphorylation in cells was consecutively surveyed after incubation with compound solutions and subsequent UV irradiation. No alteration in pErk inhibition by vemurafenib (**44**) could be determined with or without irradiation. This demonstrates that the amount of phosphorylated Erk is not dependent on UV irradiation under the described conditions. After UV irradiation, **58** and **60** exhibited the same inhibitory potency on pErk as that of vemurafenib. A complete suppression of Erk phosphorylation was demonstrated for concentrations above 0.1 μM . Dose dependency correlated with that of vemurafenib. This indicates that the inhibitory efficacy of vemurafenib on BRAF^{V600E} signaling can be completely reactivated upon irradiation of the caged derivatives with UV light.

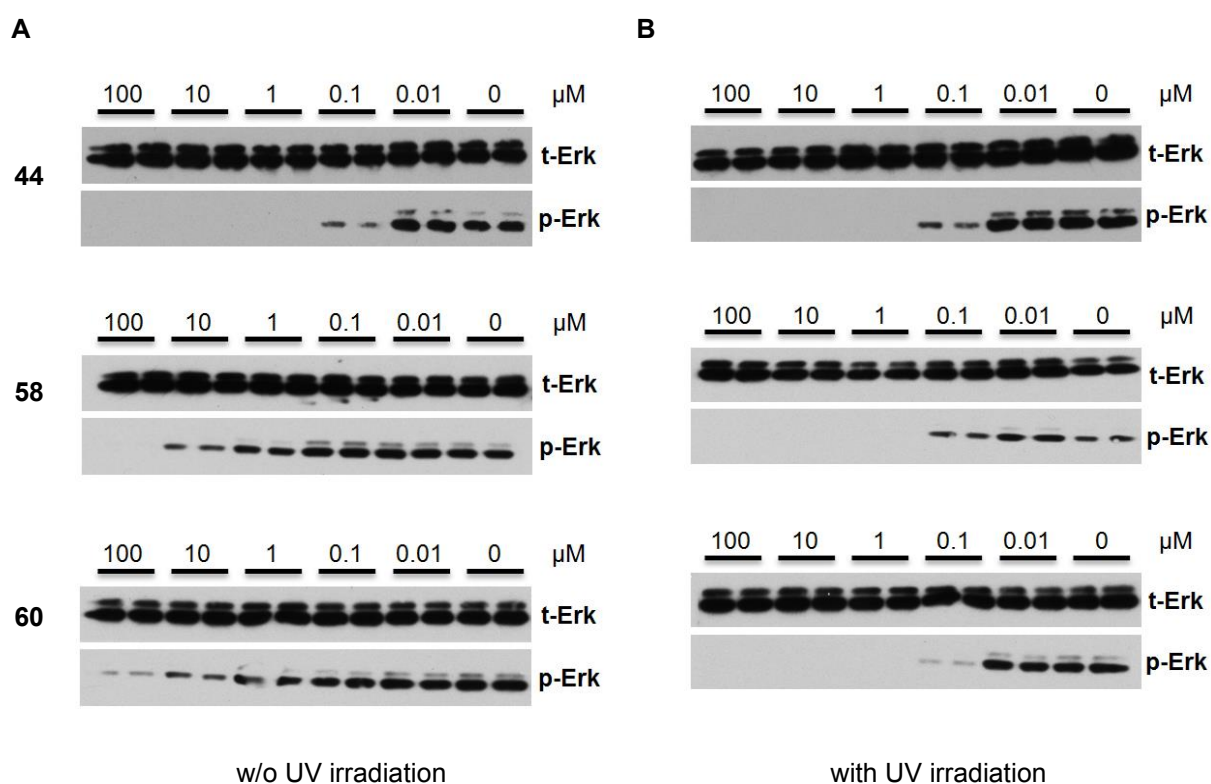


Figure 45. Activation of inhibitory effect of the caged prodrugs **58** and **60** on BRAF^{V600E} signaling *in vitro*. SKMel13 cells were treated for 1 h at 37 °C with solutions of vemurafenib (**44**) and caged prodrugs **58** resp. **60**. Subsequently, cells were lysed and immunoblotted. (A) Cells were not irradiated. (B) Cells were incubated for 1 h, irradiated at 365 nm (1.8 W) for 5 min and after further 1 h incubation lysed and immunoblotted. The experiments were carried out in duplicates. t-Erk = total Erk; p-Erk = phosphorylated Erk.

3.2 CAGED DIARYLMALEIMIDES AND CARBAZOLE

3.2.1 Molecular Modeling

The ligand-protein interactions of diarylmaleimide **55** and carbazole **57** in the ATP pocket of VEGFR2 were examined by molecular modeling (chapter 5.1). In order to design pharmacologically inactive photo prodrugs, key pharmacophoric moieties were defined within these kinase inhibitor structures to be subsequently blocked by PPGs.

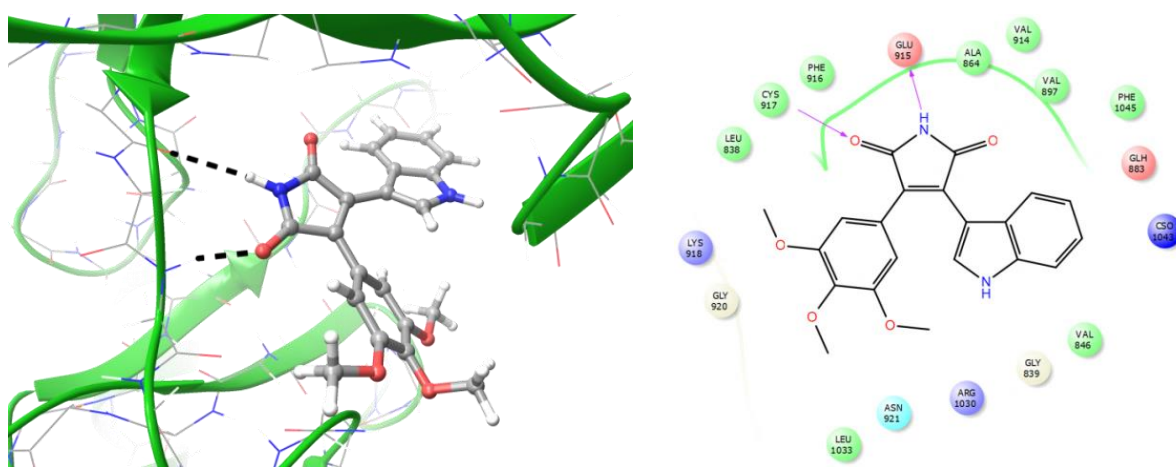


Figure 46. Binding mode of diarylmaleimide 55. Modeled 3D binding mode (left) and 2D ligand-interaction diagram (right) of **55** in the ATP pocket of VEGFR2 (pdb 3CJF¹²⁰). Black dotted lines resp. magenta arrows represent hydrogen bonds between the ligand and the backbone of the protein.

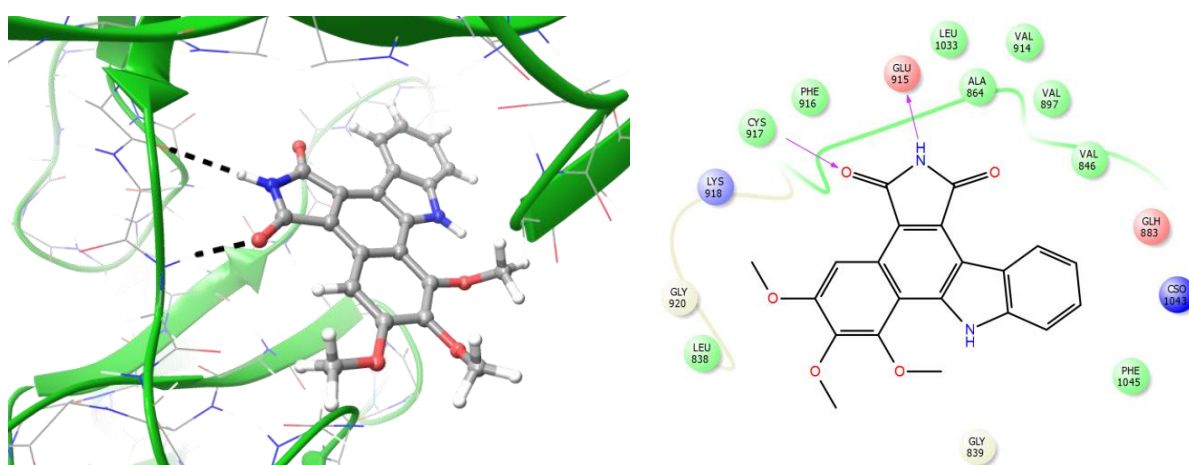


Figure 47. Binding mode of carbazole 57. Modeled 3D binding mode (left) and 2D ligand-interaction diagram (right) of **57** in the ATP pocket of VEGFR2 (pdb 3CJF¹²⁰). Black dotted lines resp. magenta arrows represent hydrogen bonds between the ligand and the backbone of the protein.

In Figure 46 the calculated 3D binding mode of **55** in the ATP pocket of VEGFR2 (pdb 3CJF¹²⁰) and the corresponding 2D ligand-interaction diagram are shown. Analogously, the calculated 3D binding mode and the corresponding 2D ligand-interaction diagram of **57**, docked in the same protein structure, are shown in Figure 47. The type I inhibitors form two key H-bonds with their imide moiety toward the hinge region. The indole NH moiety does not show a direct hydrogen bond toward the protein, but a water mediated interaction has been discussed by Peifer *et al.*⁹⁹

The imide function was however considered to be the most promising pharmacophoric moiety for photoprotection due to the central importance of the hinge region in the interaction with all type I and II inhibitors. In line with this notion, superposition of the modeled photoprotected derivatives **98**, **99**, and **100** (Figure 48) in the active site of VEGFR2 resulted in significant sterical clashes (exemplified with compound **100** in Figure 49). Likewise, docking of these caged compounds did not yield plausible binding modes (data not shown).

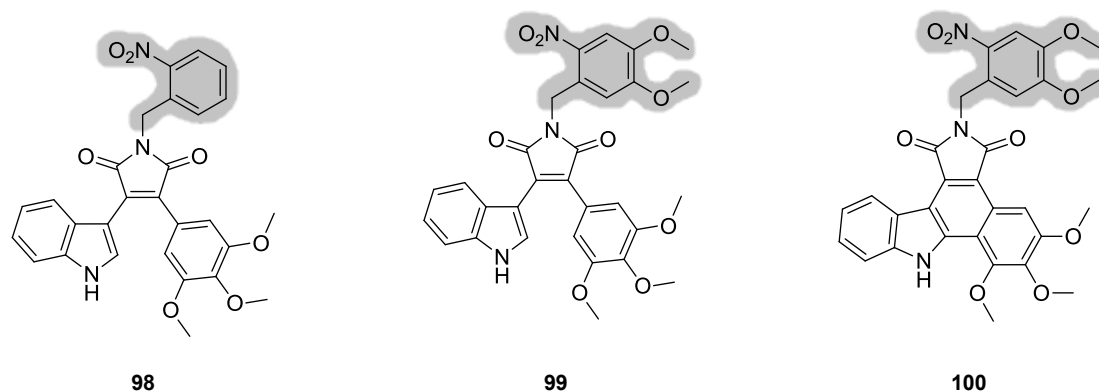


Figure 48. Chemical structures of NB/DMNB photoprotected diarylmaleimides **98** resp. **99** and photoprotected carbazole **100**. The PPGs are highlighted in grey.

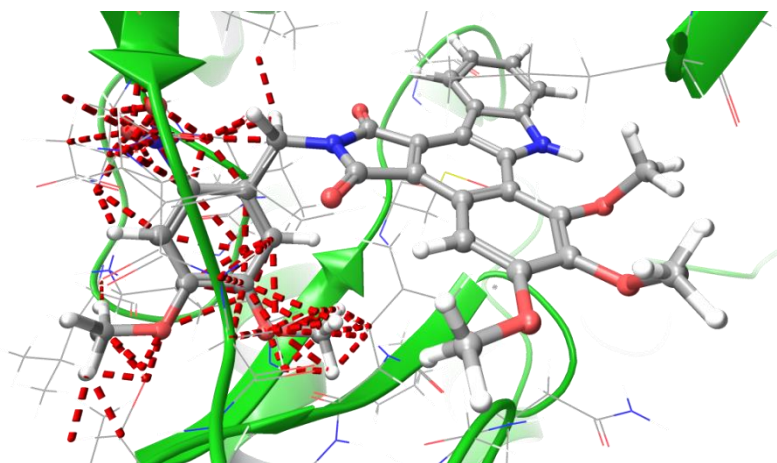


Figure 49. The DMNB caged carbazole 100 was positioned in the binding pocket of VEGFR2 (pdb 3CJF¹²⁰) imitating the core binding mode of its unprotected analog 57. Red dashed lines represent sterical clashes between the PPG and the hinge region of the protein.

3.2.2 Synthesis

The diarylmaleimide **55** was synthesized according to the procedure reported by Peifer *et al.*⁹⁸ (Figure 50, chapter 5.3.10). 3,4,5-Trimethoxyphenylacetamide (**102**) was synthesized by activation of the corresponding carboxylic acid (**101**) with thionyl chloride and subsequent treatment with aqueous ammonia solution. The indole-3-ethylglyoxylate (**104**) was subsequently obtained *via* Friedel-Crafts-type acylation of indole (**66**) with ethyl oxalyl chloride (**103**). A Knoevenagel condensation¹²¹ finally afforded the asymmetrically substituted 3,4-diarylmaleimide by ring closure.

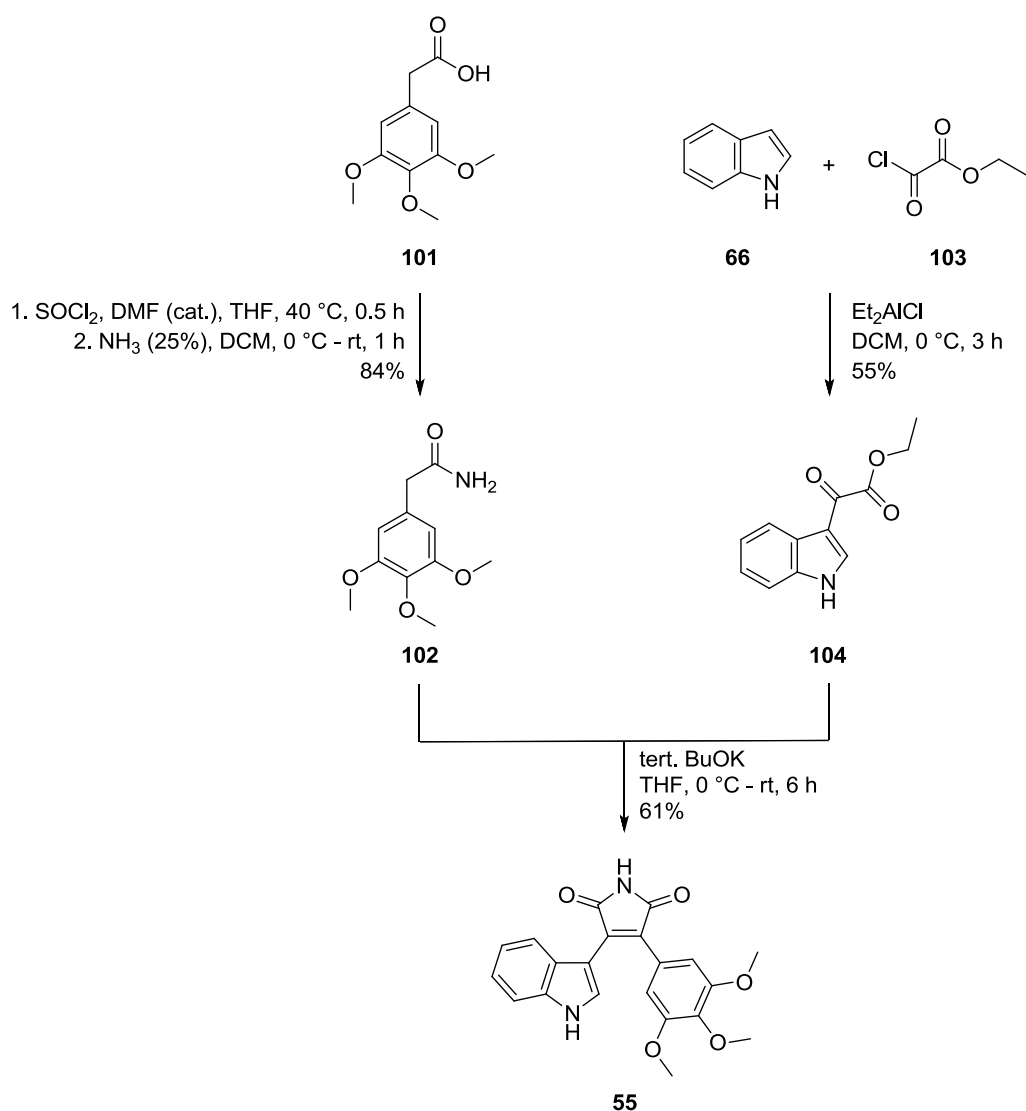


Figure 50. Synthesis of the diarylmaleimide **55**.

Due to light and atmospheric oxygen exposure during the synthesis of **55** its carbazole derivative **57** was formed by a 1,6- π -electrocyclization reaction and subsequent oxidation as illustrated in Figure 14 and discussed by Peifer *et al.*⁹⁸. Since **57** is a potent VEGFR inhibitor as well, this compound has also been incorporated in the caging project.

The *o*-nitrobenzyl (NB) PPG was introduced into **55** by a base catalyzed S_N reaction using 1-(bromomethyl)-2-nitrobenzene (NB-Br) as a reactant. Apart from the protected maleimide **98**, the doubly protected derivative **105** was obtained as a by-product (Figure 51).

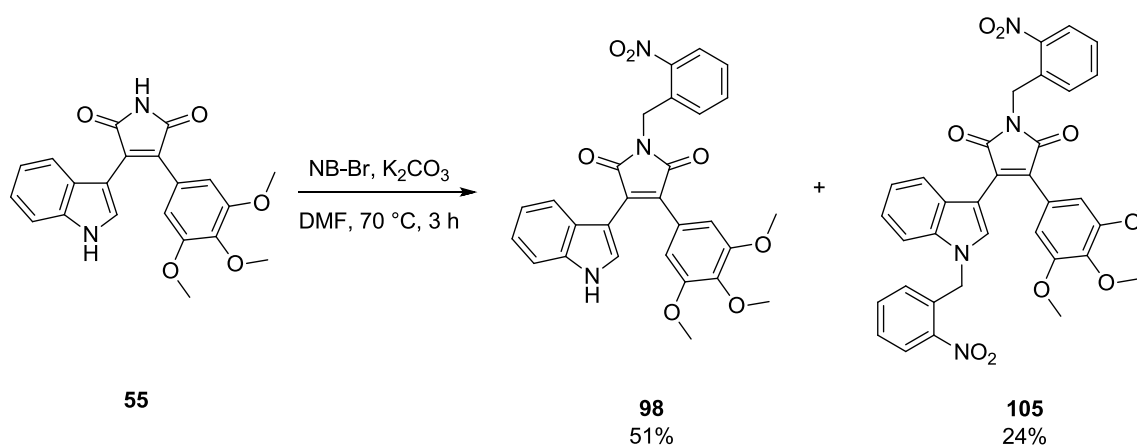


Figure 51. Synthesis of the NB protected diarylmaleimide (**98**) and formation of the doubly protected by-product (**105**).

The DMNB protected maleimide **99** was synthesized in an analog manner using DMNB-Br as PPG. The doubly protected derivative **106** was again formed as a by-product (Figure 52).

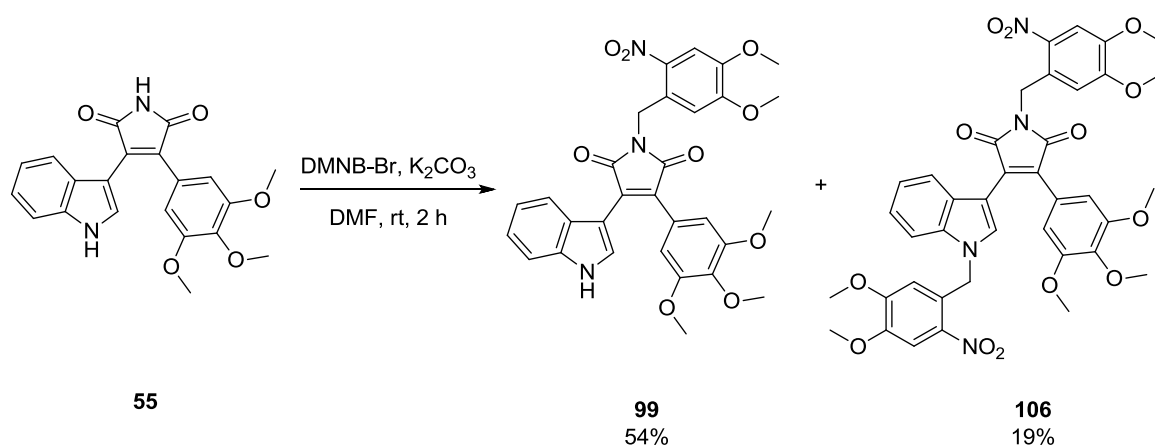


Figure 52. Synthesis of the DMNB protected diarylmaleimide (**99**) and formation of the doubly protected by-product (**106**).

The corresponding synthesis of the DMNB protected carbazole **100** is shown in Figure 53. Due to sterical hindrance of the carbazole nitrogen atom **100** was formed as the single product of this reaction.

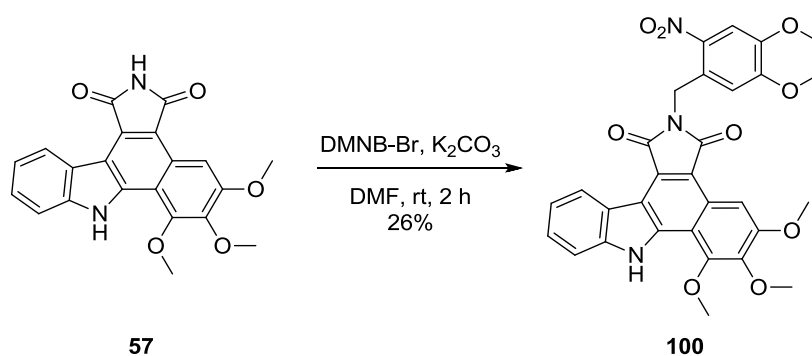


Figure 53. Synthesis of the DMNB protected carbazole (**100**).

3.2.3 Photochemical Characterization

UV/vis absorption spectra of the unprotected compounds were first recorded (chapter 5.2.1) and UV stability of compound solutions was examined (Figure 54, chapter 5.2.2). The diarylmaleimide **55** showed two absorption peaks around 350 and 440 nm. Irradiation at 365 nm presumably initiated the cyclization reaction presented in Figure 14. Based on LC-MS analysis, only the intermediate **56** was quantitatively formed after 10 min of irradiation (chapter 5.3.7). Under these experimental conditions the subsequent oxidative reaction step to the carbazole **57** apparently did not take place. The carbazole itself, on the other hand, showed only marginal light absorbance at 365 nm and was stable against irradiation at this wavelength over a period of 10 min.

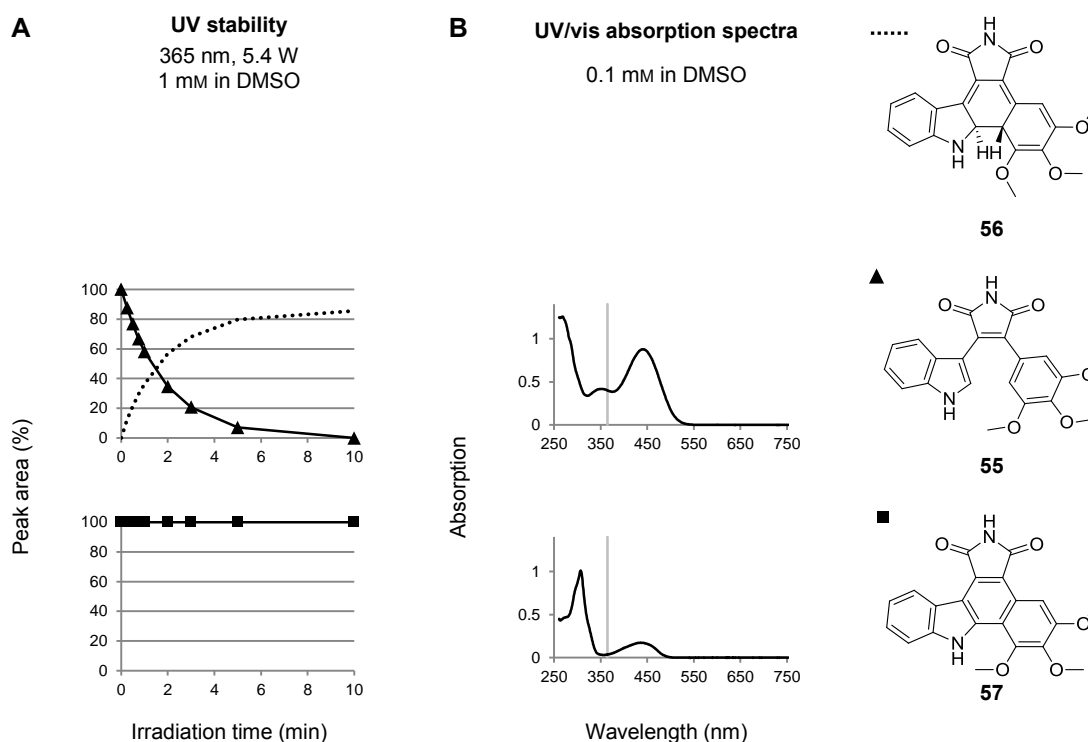


Figure 54. UV stability and UV/vis absorption spectra of the unprotected diarylmaleimide **55** and carbazole **57**. (A) 1 mM (DMSO) compound solutions of **55** (triangles) and **57** (squares) were irradiated at 365 nm (5.4 W) for up to 10 min and analyzed time dependently by HPLC. Based on LC-MS analysis, irradiation of **55** afforded the intermediate product **56** (dotted line) by an electrocyclization reaction (Figure 14). The carbazole **57** was stable at the described conditions. (B) UV/vis absorption spectra of 0.1 mM (DMSO) compound solutions of **55** and **57** are shown.

In the next step, the photocharacteristics of the caged compounds were investigated (Figure 55, chapters 5.2.1 and 5.2.3). In the area of interest the UV/vis absorption spectrum of the NB caged diarylmaleimide **98** was similar to that of its unprotected derivative. DMNB protected compounds **99** and **100**, on the other hand, showed an increased absorption around 350 nm in comparison to their unprotected derivatives.

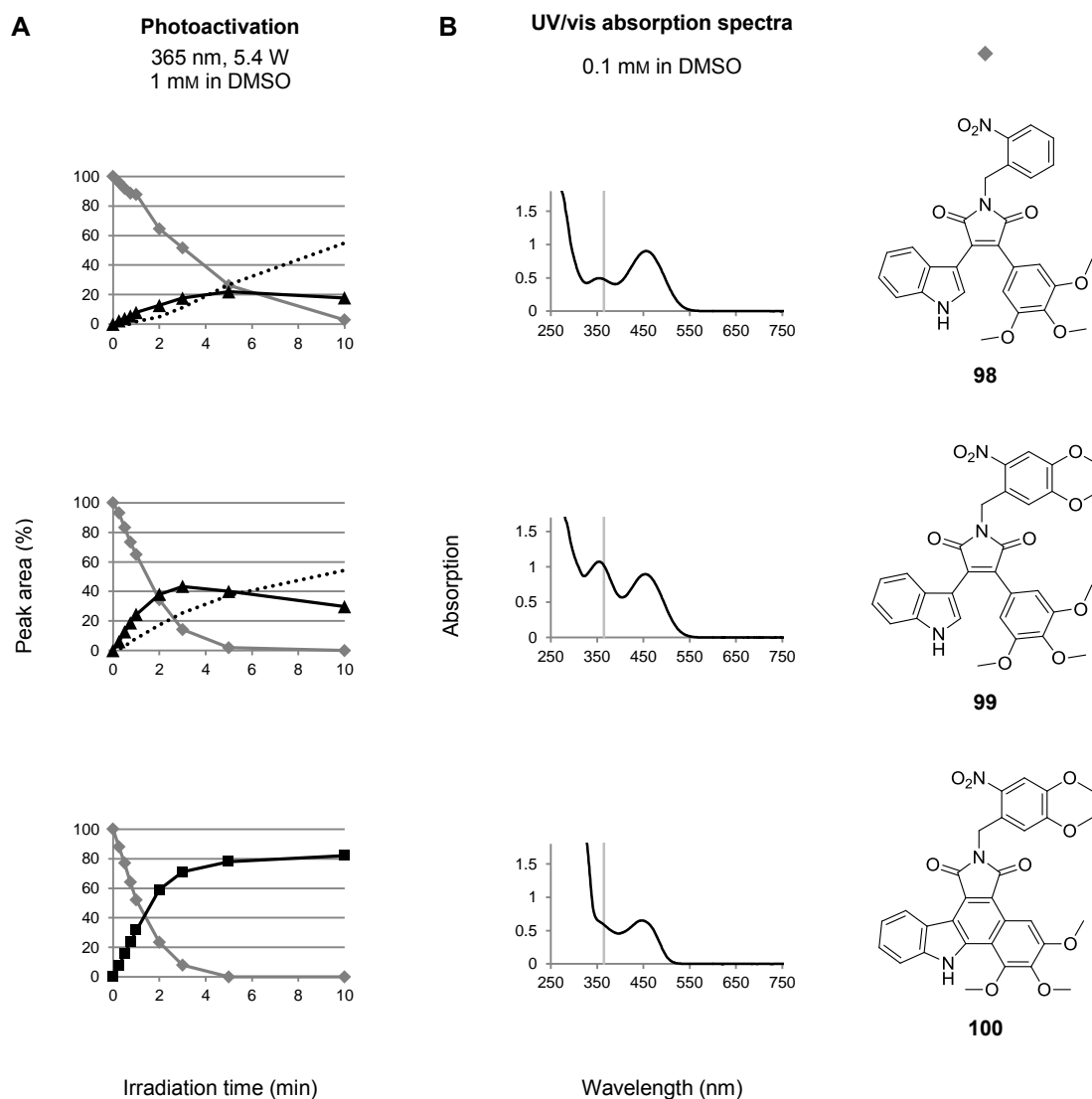


Figure 55. UV stability and UV/vis absorption spectra of caged **98**, **99**, and **100**. Photoactivation of NB/DMNB caged diarylmaleimide **98** resp. **99** and DMNB caged carbazole **100**. 1 mM (DMSO) compound solutions were irradiated at 365 nm (5.4 W) for up to 10 min and analyzed time dependently by HPLC. Symbols are used as follows: caged compounds (grey diamonds), released diarylmaleimide **55** (black triangles), electrocyclization intermediate **56** (dotted line), and released carbazole **57** (black squares). (B) UV/vis absorption spectra of 0.1 mM (DMSO) compound solutions are shown.

Although the NB protecting group itself shows very low quantum yields at the utilized wavelength of 365 nm¹⁰, irradiation of **98** led to the cleavage of this PPG and a comparably slow release of the parent compound **55**. The reason for this might be the extended mesomeric system of the leaving group. The maximum detected concentration of **55** was 27% after 5 min. The cyclization intermediate **56** was again formed to a large extent and increased with the duration of light exposure (more than 50% after 10 min). Irradiation of the related DMNB protected derivative **99** yielded comparable results. The cleavage proceeded more rapidly and a concentration of 43% of the parent compound could be achieved after 3 min of irradiation. Continuing light exposure led to a conversion from **55** to **56**. Irradiation of the DMNB protected **100** led to a tolerably clean cleavage reaction and a nearly quantitative release of **57** (more than 80%) within a few minutes. Small quantities of several not specified by-products were formed upon irradiation (not shown in the diagrams).

In conclusion, irradiation of the protected diarylmaleimide prodrugs **98** and **99** did not provide clean cleavage reactions. A mixture of the parent compound and the cyclized **56** was formed. The influence of medium and concentration should be further studied to enable a final assessment. An *in situ* formation of **56** could however have an additional effect in biological assays and was therefore evaluated in the following chapter 3.2.4. Uncaging of **100** proceeded straightforwardly within several minutes of irradiation and the carbazole **57** was released to a high extent.

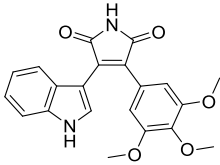
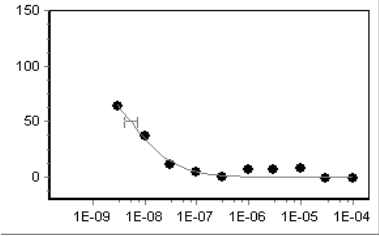
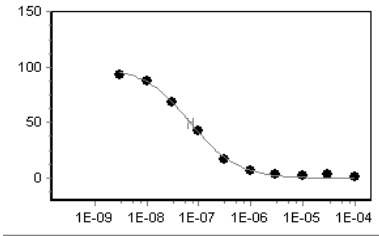
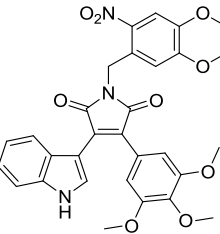
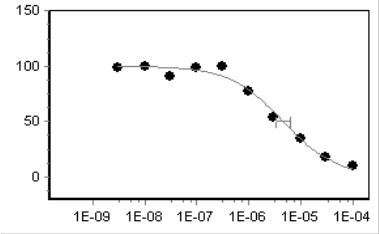
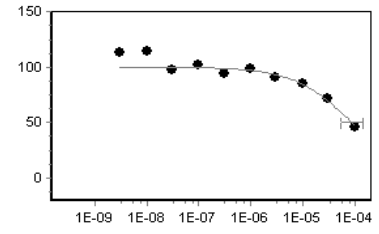
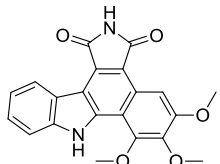
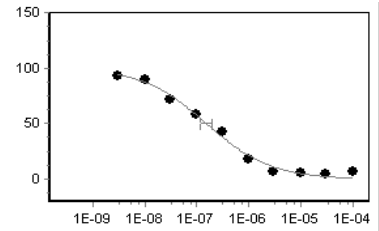
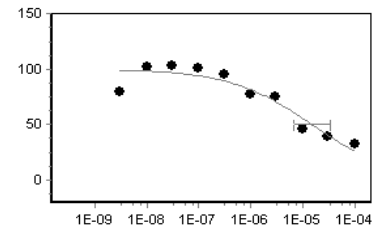
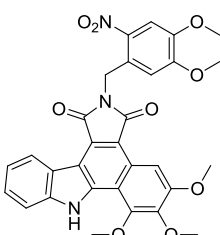
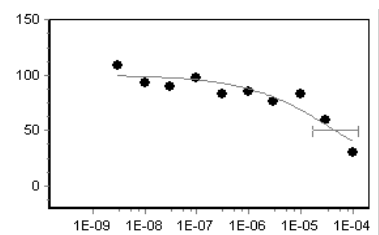
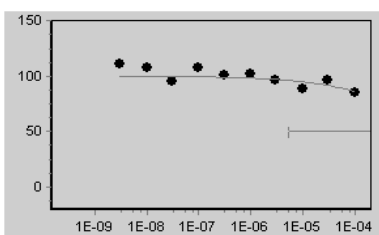
3.2.4 Biological Evaluation

The next question to be addressed was whether caging of the imide function in the DMNB protected diarylmaleimide **99** resp. carbazole **100** would actually diminish the effect on VEGFR2 as well as the antiproliferative effect in cells. **99** was chosen disfavoring its NB caged derivative **98** because of the faster cleaving kinetics and higher release of the parent compound. It had furthermore to be investigated if irradiation could restore the inhibitory activity of both prodrugs **99** and **100**, respectively. In kinase assays the inhibitory effect of the prodrugs were compared with their parent compounds on an enzymatic level. Cell proliferation assays were performed in order to assess the biological effects of the prodrugs **99** and **100** before and after irradiation.

Kinase assays

Inhibition curves and IC_{50} values were determined in a radiometric and a non-radiometric enzymatic VEGFR2 assay (see Table 6, chapter 5.4.2).¹²²

Table 6. Inhibitory effect of caged and uncaged inhibitors in VEGFR2 kinase assays.¹²² Inhibition curves and IC_{50} values of diarylmaleimide **55** resp. carbazole **57** and their DMNB caged prodrugs **99** resp. **100** in radiometric and non-radiometric enzymatic VEGFR2 assays are shown (ProQinase, Freiburg).

Compound	VEGFR2 IC_{50} radiometric	VEGFR2 IC_{50} non-radiometric
 55	 0.005 μM	 0.068 μM
 99	 4.6 μM	 87 μM
 57	 0.15 μM	 15 μM
 100	 45 μM	 > 100 μM

The diarylmaleimide **55** proved to be highly potent with an IC_{50} value of $0.005 \mu\text{M}$ in the radiometric and $0.068 \mu\text{M}$ in the non-radiometric VEGFR2 kinase assay. The less potent carbazole **57** showed IC_{50} values of $0.15 \mu\text{M}$ and $15 \mu\text{M}$, respectively. The variation of the results between the two test systems is probably due to the different experimental settings. Besides the differences in the detection method, the complete VEGFR enzyme is utilized in the radiometric assay. In the non-radiometric assay, on the other hand, only the purified kinase domain is used. The differences of the IC_{50} values between **55** and its prodrug **99** were particularly profound, both in the radiometric and in the non-radiometric assay. The DMNB protected **99** showed a by a factor of 1000 diminished potency compared to the unprotected diarylmaleimide **55**. The caged carbazole **100** was 300-fold less active than **57** in the radiometric assay and not active in the non-radiometric assay.

Moreover, a selectivity profile over 79 kinases was recorded (chapter 5.4.3). The results are presented as a heatmap in Figure 56. The graphic shows that the diarylmaleimide **55** is more selective than its carbazole derivative **57**. The most inhibited kinases of **55** were PIM3 (5% residual activity) resp. VEGFR (10%) and of **57** PIM3/1 (4% resp. 5%), GSK3b (5%), and HIPK2 (7%). VEGFR showed a residual activity of 37% when treated with **57**.

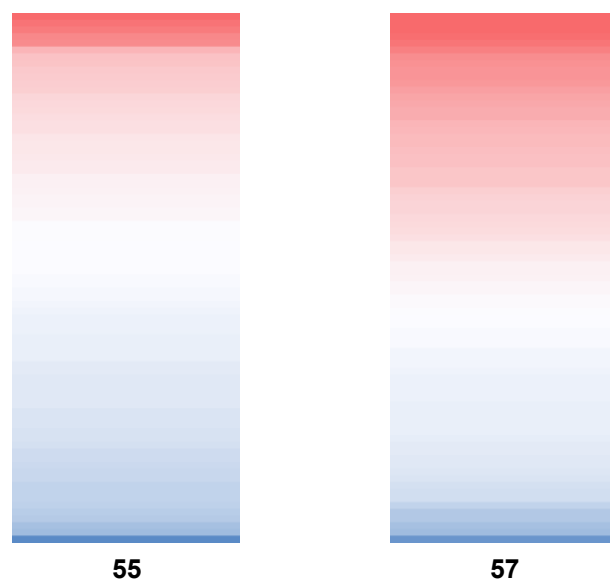


Figure 56. Selectivity profile of diarylmaleimide **55** and carbazole **57** in a panel over 79 kinases. The inhibitory effect was tested at a concentration of $0.1 \mu\text{M}$ by determination of the residual kinase activity. In the presented heatmap the columns have been individually ranked from low (red) to high (blue) residual activity values. Details are shown in Supplementary Table 2 (Appendix).

Cellular assays

The antiproliferative effects of the compounds were tested in cellular assays and it was explored if irradiation with UV light could restore the efficacy of the photo prodrugs (chapters 5.4.4 and 5.4.5).¹²³

Due to the results of the enzymatic data, it was supposed that the caged prodrugs would be considerably less active in cellular assays compared to their parent compounds. To prove this hypothesis, the antiproliferative activities in cellular growth assays were examined using the VEGFR dependent PC3 cell line.^{124,125} Dose-response curves for the non-irradiated compounds are presented in Figure 57 (A). The diarylmaleimide **55** showed potent cytotoxic activity with a GI₅₀ value of 6.4 μM. In contrast, its caged derivative **99** exhibited only low cell toxicity (GI₅₀ not reached). The antiproliferative activity of the carbazole **57** was measured with a GI₅₀ value of 0.24 μM, the considerably less active **100** with 35 μM. The marginal cytostatic effects of the caged probes at higher concentrations might again be caused by minor impurities of the unprotected derivatives in the samples or by off-target effects of the caged prodrugs.

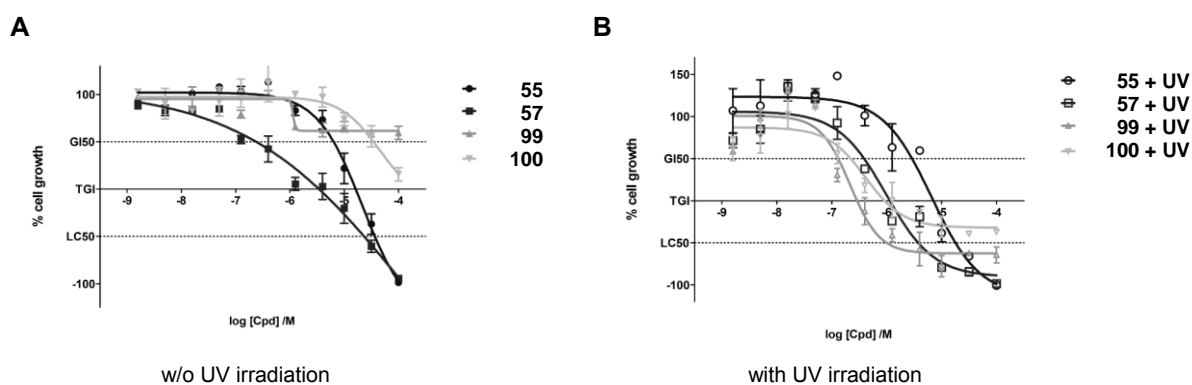


Figure 57. Activation of caged prodrugs in cell proliferation assays.¹²³ (A) Dose-response curves of diarylmaleimide **55** resp. carbazole **57** and their corresponding DMNB caged prodrugs **99** resp. **100** were determined without UV irradiation. (B) Cells with the compounds were irradiated at 365 nm (1.8 W) for 5 min. After irradiation the caged derivatives showed similar dose-response curves or even increased effects in comparison to the parent compounds. GI₅₀ = 50% growth inhibition; TGI = total growth inhibition; LC₅₀ = 50% lethal concentration. (±SD, *n*=3)

The next question addressed was whether the antiproliferative activity of the caged inhibitors could be recovered by UV irradiation. The cell growth assays were repeated with irradiation of the compound treated cells at 365 nm (1.8 W, 5 min). The dose-response curves are presented in Figure 57 (B). In control experiments was shown that the used dosage of UV irradiation was well-tolerated by the cells. After irradiation, the prodrugs showed comparable or even increased efficacy compared to that of the unprotected compounds. The GI₅₀ value of the diarylmaleimide **55** (2.9 μM) was very similar to that without irradiation (6.4 μM). A strongly increased antiproliferative effect could be recognized for its prodrug **99** (GI₅₀ value 0.39 μM). Surprisingly, the prodrug was even 10-fold more active after irradiation than its parent drug. Synergistic effects of the released inhibitor, the irradiation and the cleaved protecting group can be discussed. The carbazole **57** and its prodrug **100** showed similar results after irradiation (GI₅₀ values 0.13 μM resp. 0.22 μM). In conclusion, irradiation of the prodrugs **99** and **100** restored the activity of the corresponding diarylmaleimide (**55**) and carbazole (**57**), respectively.

3.3 PHOTOSWITCHABLE AXITINIB

3.3.1 Molecular Modeling

The impact of the *E-Z* isomerization of axitinib on its molecular binding mode was investigated by molecular modeling (chapter 5.1). In Figure 58 (left) the ligand-protein interactions of the crystallized complex of (*E*)-axitinib (**19**) in the ATP pocket of VEGFR2 (pdb 4AG8)⁶⁷ are presented. Figure 59 shows the corresponding 2D ligand-interaction diagram. Superposition of (*Z*)-axitinib (**19a**) on (*E*)-axitinib resulted in significant sterical clashes with the backbone of the protein (Figure 58, right). Similarly, when (*Z*)-axitinib was docked in the active site of VEGFR2 no plausible binding mode could be found (data not shown).⁸⁹

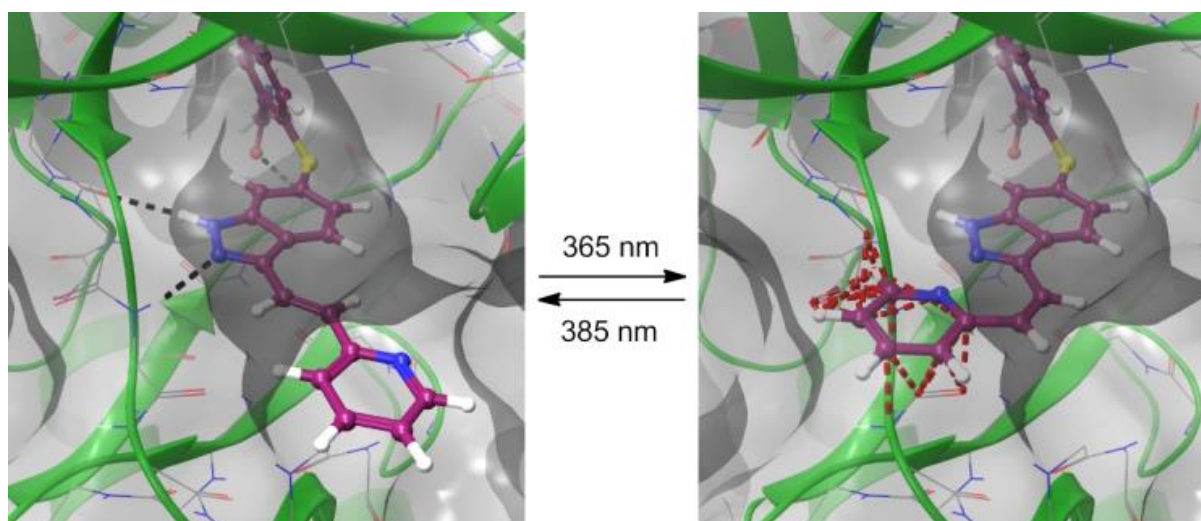


Figure 58. Molecular binding mode of (*E*)-axitinib (19**) in the active site of VEGFR2 and superposition of (*Z*)-axitinib (**19a**).** Left: Binding mode of (*E*)-axitinib in VEGFR2 determined by X-ray analysis (pdb 4AG8).⁶⁷ Black dotted lines represent H-bonds between the ligand and the backbone of the protein. Right: (*Z*)-Axitinib modeled in the binding pocket maintaining the core binding mode of (*E*)-axitinib. Red dotted lines indicate predicted sterical clashes between the pyridine moiety of the (*Z*)-isomer and the protein backbone of the hinge loop in the target kinase.

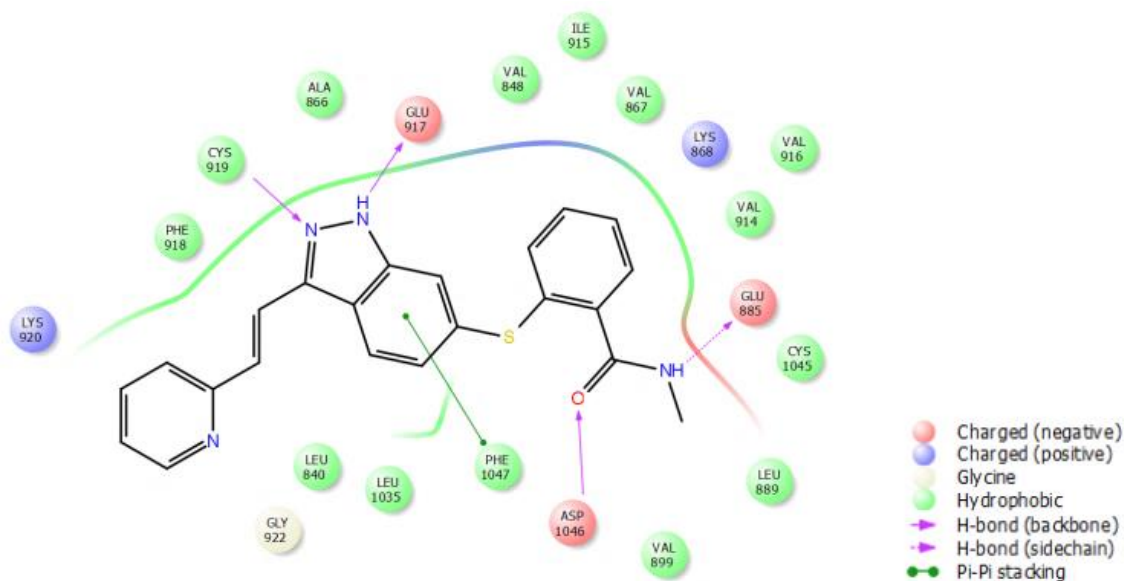


Figure 59. Ligand-interaction diagram of (*E*)-axitinib (19) in the active site of VEGFR2 (pdb 4AG8⁶⁷). Key ligand-protein interactions are shown.

The interactions were additionally modeled between both axitinib stereoisomers and VEGFR1 (pdb 3HNG)¹²⁶, PDGFR β (DFG in/out, homology model)¹²⁷ resp. cKIT (pdb 3G0E, 4HVS)^{128,129}. No plausible docking modes could again be found for the (*Z*)-isomer in contrast to the (*E*)-isomer.⁸⁹ It was thus postulated that (*Z*)-axitinib should not be able to inhibit these kinases.

3.3.2 Synthesis and Tautomerism

Encouraged by the molecular modeling data, a DMSO solution of commercially available (*E*)-axitinib was irradiated at 365 nm (10 min, 5.4 W) to produce the (*Z*)-isomer (chapter 5.3.10). The resulting mixture of both isomers could then be separated by flash chromatography (chapter 5.3.2). NMR analysis of the separated (*Z*)-isomer surprisingly revealed a mixed spectrum (see Figure 60 and 61, chapter 5.3.6), indicating the existence of two different (*Z*)-axitinib species (**19a** and **19b**) at a ratio of 7:3. Both spectra sets showed the characteristic smaller H-C=C-H coupling constant (12.8 Hz) of a (*Z*)-isomer compared to the (*E*)-isomer (16.4 Hz). Since indazoles are known to show annular NH-tautomerism^{130,131}, it was hypothesized that two (*Z*)-axitinib tautomers were formed, namely the indazole 1*H*- and the 2*H*-tautomer (Figure 62).⁸⁹

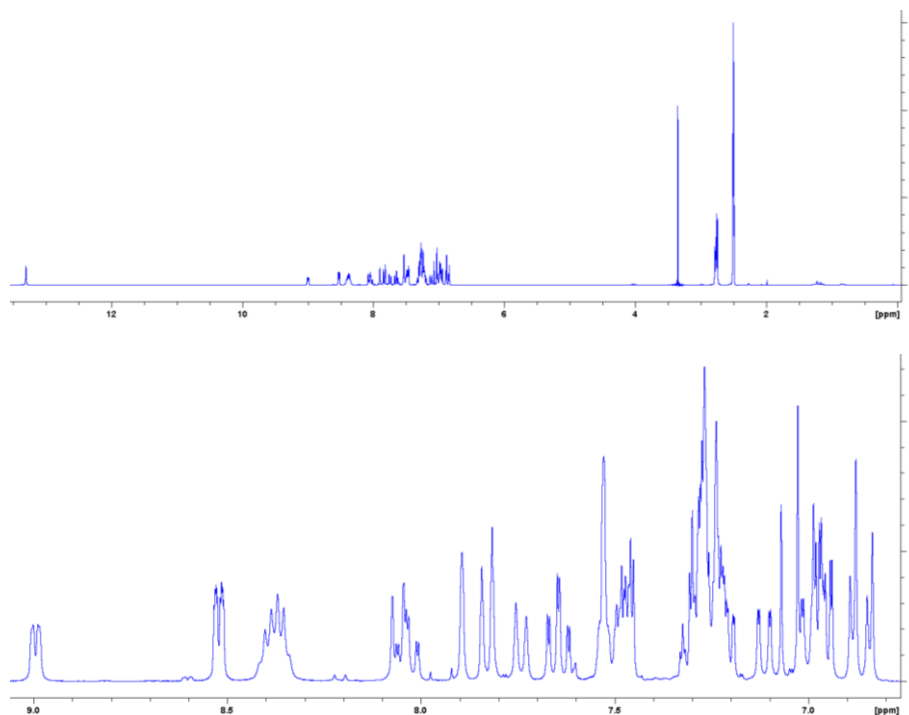


Figure 60. ^1H NMR spectrum (300 MHz, DMSO-d_6 , 294 K) and detailed view of the aromatic region of (*Z*)-axitinib (7:3 mixture of *1H*- and *2H*-tautomer).⁸⁹

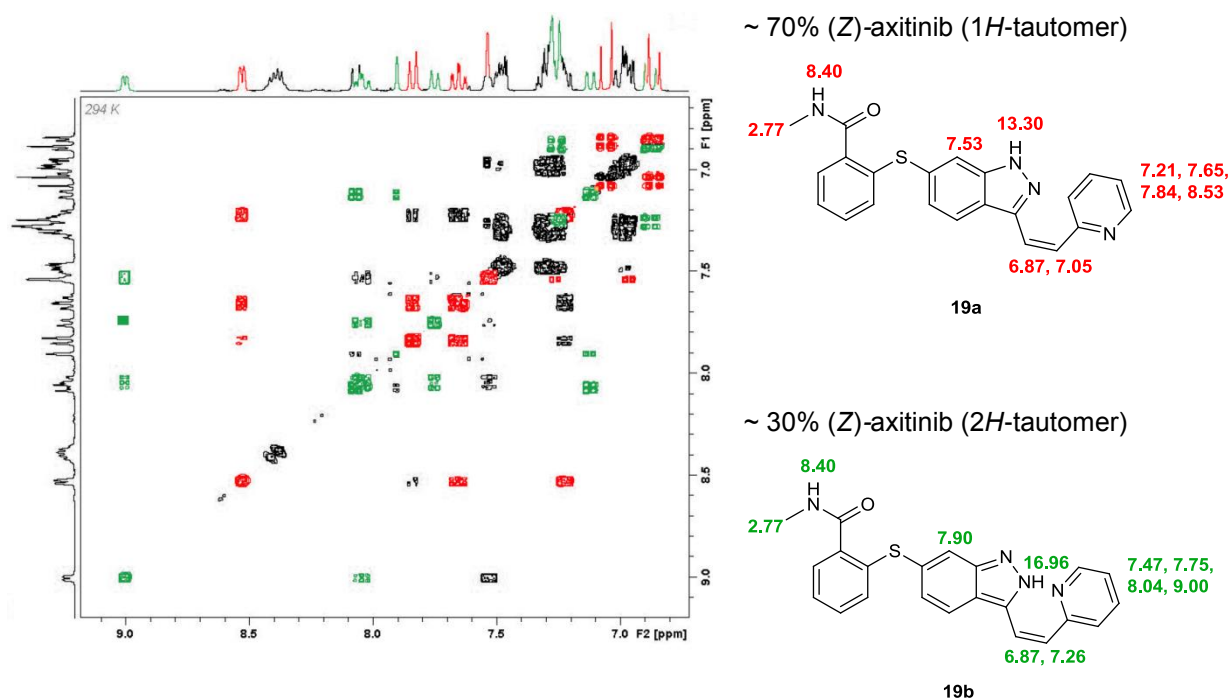


Figure 61. Signals of aromatic hydrocarbons in a ^1H - ^1H COSY spectrum and signal assignment to the *1H*- and *2H*-tautomer of (*Z*)-axitinib.⁸⁹

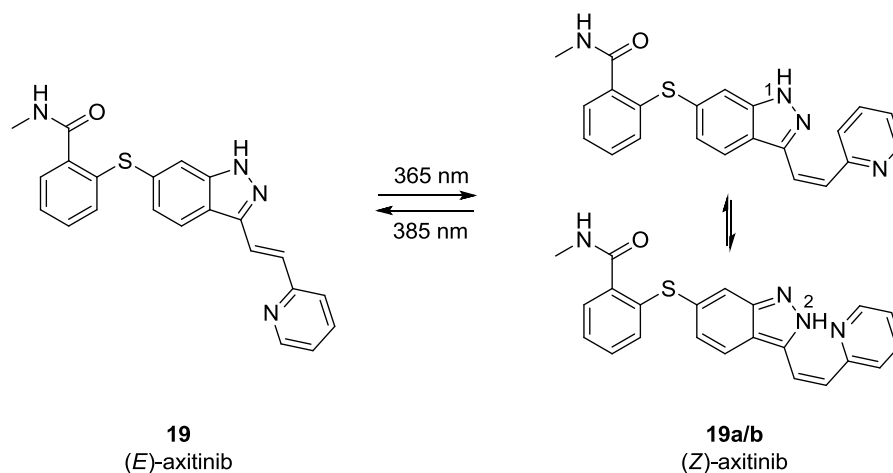


Figure 62. Photoinduced *E-Z* isomerization of axitinib and formation of *1H*- and *2H*-indazole annular tautomers.⁸⁹

X-ray crystallography (chapter 5.3.9) indeed proved the existence of the *2H*-tautomer (Figure 63) which is stabilized by an intramolecular hydrogen bond between the indazole 2N-H and the pyridine nitrogen.⁸⁹ In solution, however, two tautomers were existent. The term (*Z*)-axitinib describes in the following the mixture of both tautomers **19a** and **19b**.

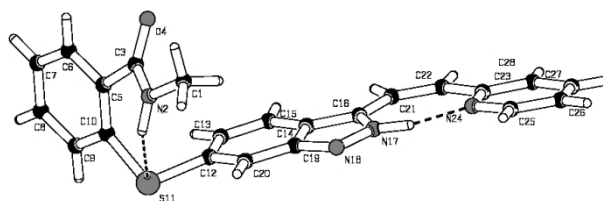


Figure 63. X-ray crystal structure of the *2H*-tautomer of (*Z*)-axitinib (**19b**, CCDC 1419085).⁸⁹ In the solid state only the *2H*-tautomer was detected by X-ray analysis, which is stabilized by an intramolecular H-bond between the indazole 2N-H and the pyridine nitrogen. In DMSO solution, a 7:3 ratio of the *1H*- to the *2H*-tautomer was contrarily observed (based on NMR analysis).

3.3.3 Photochemical Characterization

With both the separated (*E*)- and the (*Z*)-isomer in hand, the light induced *E-Z* isomerization was further examined depending on the irradiated wavelength. According to the respective UV/vis spectra (Figure 64, chapter 5.2.1), (*E*)-axitinib possessed an absorption maximum at 330 nm. In the range between 380 and 410 nm only (*Z*)-axitinib showed light absorbance.⁸⁹

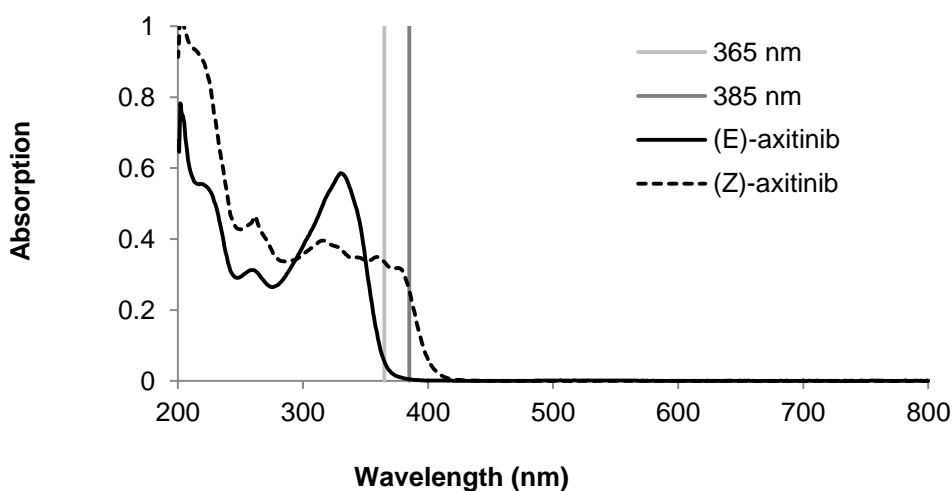


Figure 64. UV/vis absorption spectra of (*E*)-axitinib (solid line) and (*Z*)-axitinib (dashed line) solutions (0.02 mM in methanol).⁸⁹ Wavelengths of the used LED sources (365 resp. 385 nm) are illustrated as grey bars.

LEDs with emission wavelengths of 365 resp. 385 nm were chosen for the irradiation experiments because of their high intensity and commercial availability. Figure 65 shows the photoisomerization of (*E*)-axitinib resp. (*Z*)-axitinib solutions after irradiation with these two wavelengths (chapter 5.2.4). The conversion was monitored by HPLC analysis (chapter 5.3.4). LC-MS was used besides retention time for proof of identity (chapter 5.3.7). Within a few minutes, irradiation at 365 nm resulted in a photostationary state (PSS) of 35-45% (*E*)-axitinib and 55-65% (*Z*)-axitinib. On the other hand, irradiation at 385 nm afforded 85% (*E*)-axitinib and 15% (*Z*)-axitinib.⁸⁹

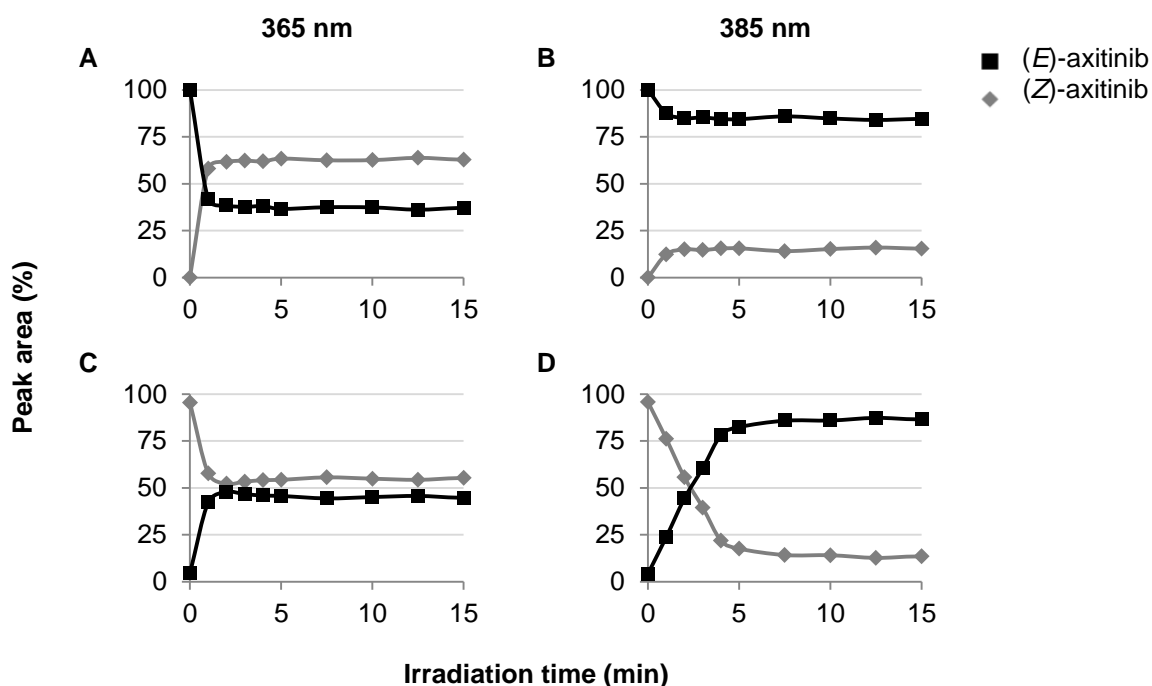


Figure 65. Photoisomerization of (*E*)-axitinib and (*Z*)-axitinib.⁸⁹ Irradiation of an (*E*)-axitinib solution (5 mM in DMSO) at (A) 365 nm resp. (B) 385 nm led to photoisomerization resulting in different photostationary states of (*E*)-axitinib (black squares) to its (*Z*)-isomer (grey diamonds) quantified time dependently by HPLC analysis. Irradiation of an equally concentrated (*Z*)-axitinib solution at (C) 365 nm resp. (D) 385 nm evolved similar ratios.

Summing up, the PSS of both isomers could be shifted to either side depending on the irradiated wavelength, but a total conversion could not be achieved. In biological settings, however, there are typically much lower compound concentration levels compared to the analytical situation described above. After UV triggered activation of the (*Z*)-isomer, (*E*)-axitinib might thus be tightly bound by the target and therefore withdrawn from the chemical balance, enabling a more quantitative shift to the bioactive (*E*)-configuration.

3.3.4 Biological Evaluation

To provide evidence for the hypothesis regarding different affinities of (*E*)-axitinib and (*Z*)-axitinib towards relevant kinases, the biological activities of both isomers were compared using *in vitro* assays. Inhibition curves were therefore determined in both a radiometric and a non-radiometric enzymatic VEGFR2 assay (Figure 66, chapter 5.4.2). The inhibitory effect of (*E*)-axitinib and (*Z*)-axitinib was additionally tested in a photometric PDGFR β assay (Figure 67).¹³² The IC₅₀ values of both stereoisomers toward these target kinases are shown in Table 7. In conclusion, (*E*)-axitinib was at least 30-fold more potent toward VEGFR2 than (*Z*)-axitinib in the radiometric ³³PanQinase[®] assay and 2 to 3-fold more active in the non-radiometric ADP-Glo[™] assay. Regarding PDGFR β , (*E*)-axitinib was about 20-fold more potent than its (*Z*)-isomer. In line with the modeling data it could hence be demonstrated by these enzymatic test systems that (*Z*)-axitinib is biologically less active than (*E*)-axitinib.

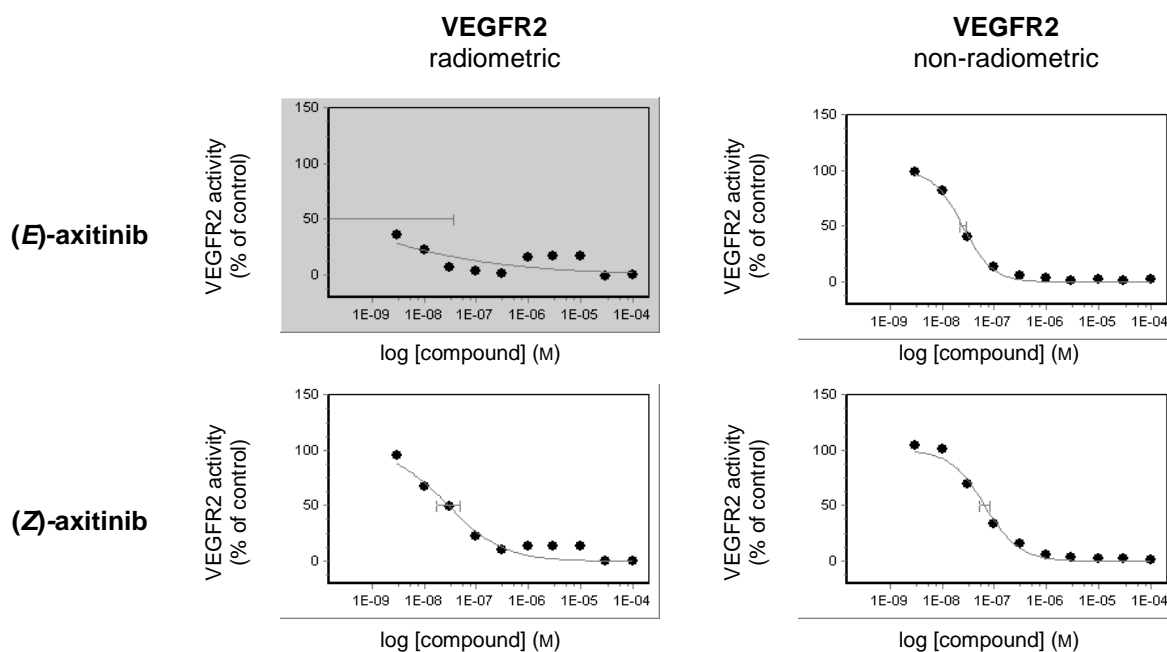


Figure 66. Inhibition curves of (*E*)-axitinib and (*Z*)-axitinib for VEGFR2 kinase.¹²² (*E*)-Axitinib was at least 30-fold more potent toward VEGFR2 than (*Z*)-axitinib in the radiometric ³³PanQinase[®] assay and 2 to 3-fold more active in the non-radiometric ADP-Glo[™] assay (ProQinase, Freiburg).

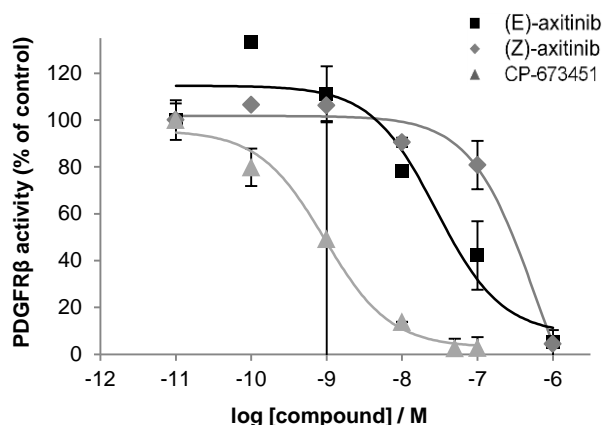


Figure 67. Inhibition curves of (*E*)-axitinib, (*Z*)-axitinib and the reference inhibitor CP-673451 for PDGFR β kinase.¹³² (*E*)-Axitinib was about 20-fold more potent (IC_{50} 30 nM) than (*Z*)-axitinib (IC_{50} 600 nM). The experimental compound CP-673451 was used as a control and showed an IC_{50} of 1 nM which is in good accordance with the literature.¹³³ (\pm SD, $n=3$)

Table 7. Inhibitory effect of (*E*)-axitinib and (*Z*)-axitinib in enzymatic assays.^{122,132}

Inhibitor	VEGFR2 IC_{50} (radiometric)	VEGFR2 IC_{50} (non-radiometric)	PDGFR β IC_{50}
(<i>E</i>)-axitinib	< 1 nM	25 nM	30 nM
(<i>Z</i>)-axitinib	29 nM	65 nM	600 nM

Since the biological activities were significantly different regarding PDGFR β the compounds were furthermore tested on PDGFR β dependent NIH/3T3 cells (chapters 5.4.4 and 5.4.5).^{124,125} In non-irradiated cells all three compounds herein showed cytotoxic effects above concentrations of 10 μ M. (*E*)-Axitinib appeared to be slightly more potent compared to (*Z*)-axitinib (Figure 68). The control data using only UV irradiation demonstrated, however, that the NIH/3T3 cells did not tolerate UV irradiation.¹²³ In order to examine if (*Z*)-axitinib was converted to (*E*)-axitinib in the aqueous environment of the cellular assays, the stability of the (*Z*)-stereoisomer was tested under similar conditions (chapter 5.4.6). Herein, no significant conversion could be detected (Figure 69).

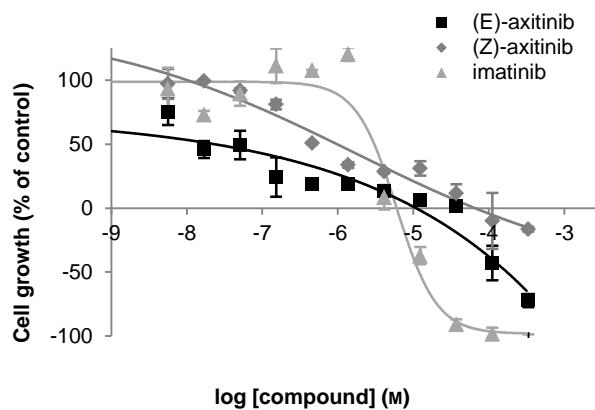


Figure 68. Anti-proliferative effect of (*E*)-axitinib, (*Z*)-axitinib and the reference inhibitor imatinib on PDGFR dependent NIH/3T3 cells.¹²³ Dose-response curves of (*E*)-axitinib, (*Z*)-axitinib and imatinib in NIH/3T3 cell proliferative assays (without irradiation) measured *via* the resazurin assay. Imatinib was used as a control. NIH/3T3 cells did not tolerate UV irradiation (data not shown). (\pm SD, $n=3$)

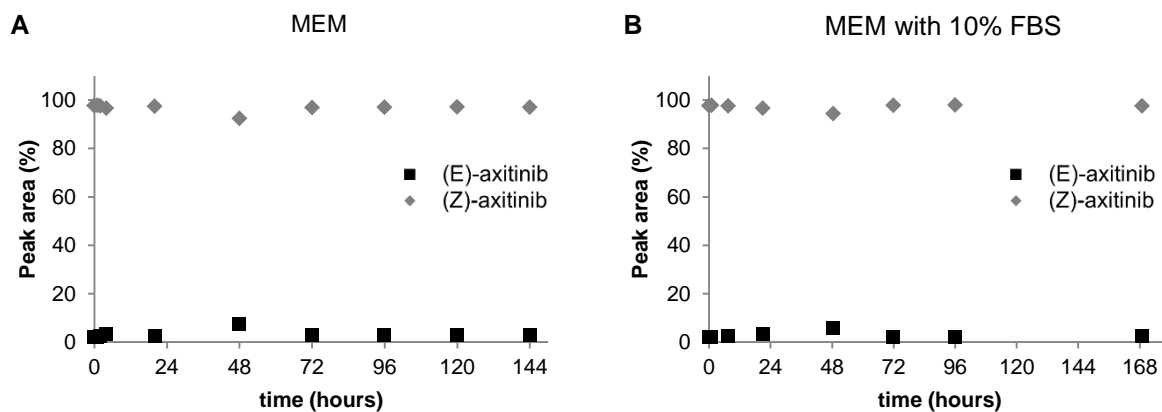


Figure 69. Stability of (*Z*)-axitinib under assay conditions.¹³² Stability of (*Z*)-axitinib in minimum essential medium (MEM) at 37 °C without (A) and with (B) fetal bovine serum (FBS). Concentrations were monitored time dependently by HPLC analysis.

The impact of both isomers on PDGFR β signaling *in vitro* was consequently studied in greater detail using NIH/3T3 cells without UV irradiation. Western blot analyses herein showed the inhibition of the phosphorylation of PDGFR β and its downstream kinases AKT and ERK, respectively (Figure 70, chapter 5.4.7). The comparison between the impact of both axitinib stereoisomers illustrates that the phosphorylation of PDGFR β was slightly less inhibited by (*Z*)-axitinib compared to (*E*)-axitinib at 0.01 μM . More clearly, AKT and ERK phosphorylation was effectively blocked by (*E*)-axitinib at 0.01 μM whereas these kinases were still phosphorylated at (*Z*)-axitinib concentrations of 0.01 μM (p-PDGFR β) and 0.1 μM (p-AKT, p-ERK).¹³² These results were thus in line with the enzymatic data.

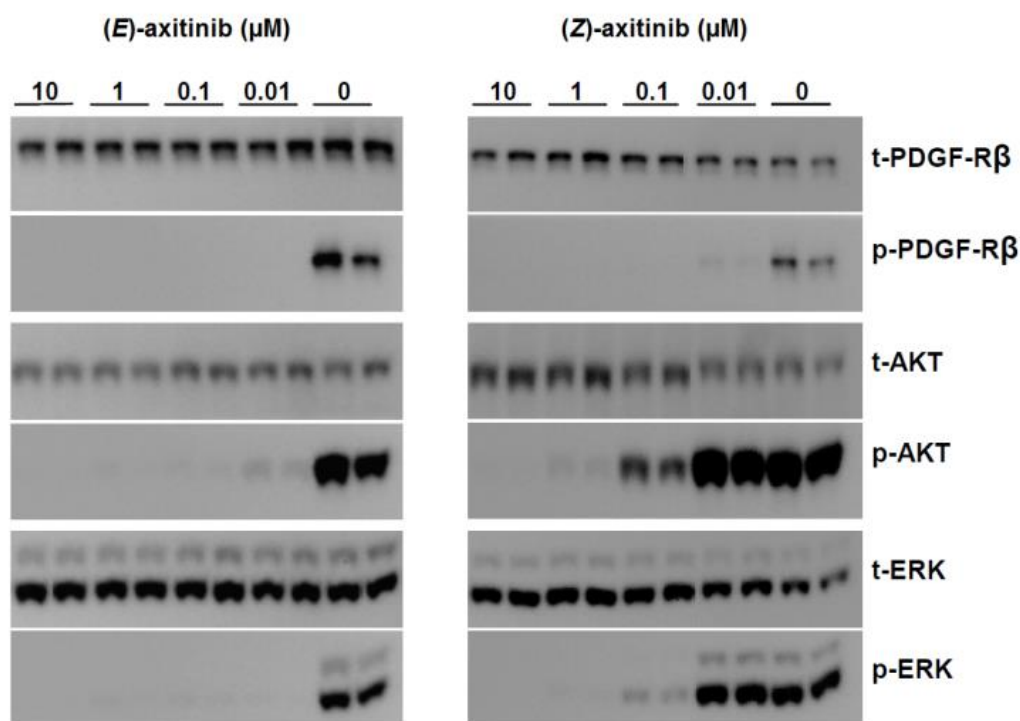


Figure 70. Inhibitory effect of (*E*)-axitinib and (*Z*)-axitinib on PDGFR β signaling in western blot analyses.¹³² Concentrations are indicated in μM . t = total; p = phosphorylated.

It was next investigated if these findings could be transferred to cellular settings using VEGFR dependent PC3 cells¹³⁴ (chapters 5.4.4 and 5.4.5). Dose-response curves were measured without and with UV irradiation (Figure 71). As expected, the reference inhibitor imatinib showed cytostatic effects above 10 μM and cytotoxic effects above 100 μM , respectively. At concentrations above 10 μM without irradiation, (*Z*)-axitinib appeared to be as cytostatic as (*E*)-axitinib. After irradiation of the cells at 365 nm (5 min, 1.8 W) both axitinib isomers appeared to have gained potency. Surprisingly, (*Z*)-axitinib was even more cytotoxic than its (*E*)-isomer. UV irradiation showed a smaller effect on the dose-response curve of imatinib.¹²³ Although the PC3 cells seemed to tolerate the irradiation well, cell stress based on the UV application might have had an effect on their viability resp. the permeability of membranes and therefore modulating the bioavailability of the tested compounds.

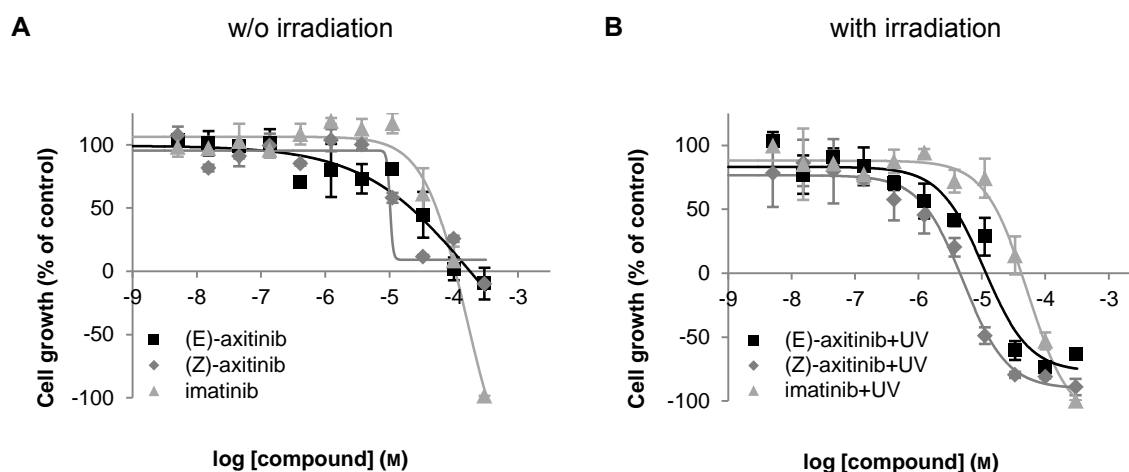


Figure 71. Anti-proliferative effect of (*E*)-axitinib, (*Z*)-axitinib and the reference inhibitor imatinib on VEGFR dependent PC3 cells.¹²³ The anti-proliferative effect of (*E*)-axitinib and (*Z*)-axitinib on VEGFR dependent PC3 cells was demonstrated *via* resazurin assay. Imatinib was used as a control. (A) Cells were not irradiated. (B) Cells were irradiated at 365 nm (1.8 W) for 5 min. (\pm SD, $n=3$)

It was thus hypothesized that, in these cells, (*Z*)-axitinib might hit a target different from the kinases that had been investigated so far. To address this question, a selectivity profile in a panel of 300 kinases was determined for both axitinib stereoisomers at a concentration of 1 μM (chapter 5.4.3). The results are presented as a heat map in Figure 72. Both (*E*)-axitinib and (*Z*)-axitinib showed a quite similar profile and no additional kinase target(s) could be identified for (*Z*)-axitinib.



Figure 72. Selectivity profiles of (*E*)- and (*Z*)-axitinib. The assay concentration was 1 μM in a panel of 300 kinases. The inhibitory effect of (*E*)-axitinib and (*Z*)-axitinib was tested by determination of the residual kinase activity. In the presented heatmap the color code is ranging from grey (low residual activity) to white (high residual activity). Details are shown in Supplementary Table 3 (Appendix).

Residual activity values of exemplary target receptor tyrosine kinases of (*E*)-axitinib are shown in Table 1. (*E*)-Axitinib seems again to block these kinases more effectively than (*Z*)-axitinib even though the differences are not significant.

Table 8. Inhibitory effect of (*E*)-axitinib and (*Z*)-axitinib toward selected receptor tyrosine kinases. The residual kinase activity was measured at a compound concentration of 1 μM .

Residual activity (%)	VEGFR1	VEGFR2	PDGFR α	PDGFR β	cKIT
(<i>E</i>)-axitinib	4	0	-4	1	6
(<i>Z</i>)-axitinib	8	1	2	4	9

Due to the high potency of axitinib, the lack of differentiation might be caused by a saturation of the system. With regard to the western blot analysis (Figure 70) a concentration of 0.01 μM might allow an enhanced distinction between the effects of both isomers and should therefore be considered for further testing.

4. CONCLUSION

4.1 CAGED VEMURAFENIB

This project included the successful design, synthesis, photochemical, and *in vitro* characterization of novel caged prodrugs of the kinase inhibitor vemurafenib (**44**). Molecular modeling studies predicted the loss of inhibitory potency by blocking a pharmacophore moiety with a PPG. UV stability of the kinase inhibitor was subsequently confirmed. The next goal of this study was to identify the minimal structural requirement for light-induced deprotection of vemurafenib's hinge binder. In conclusion, DMNB protected 7-azaindole (**69**) could not be cleaved and DMNB protected 3-acetyl-7azaindole (**70**) only at slow reaction rates. 3-Benzoyl-7-azaindole (**67**) was therefore considered to be the crucial fragment for deprotection of azaindole derivatives and was consequently used as a dummy compound for the following experiments.

The subsequent goal was to compare various classes of PPGs with regard to chemical accessibility and photochemical release rates. Among the tested classes only *o*-nitrobenzyl protection groups released the utilized *N*-heterocycle at applicable reaction rates and with few side products. The phenacyl, coumarin, and desyl group did in contrast not produce acceptable results. These groups were thus not further investigated. No significant differences regarding photocharacteristics could be detected between the different tested *o*-nitrobenzyl derivatives. DMNB and DMNPE were therefore chosen for photoprotection of vemurafenib and the corresponding prodrugs were synthesized.

After photoactivation of the caged inhibitors had been confirmed, the compounds were tested in different *in vitro* assays. It was demonstrated that caging significantly diminishes the inhibitory efficacy and promiscuity of vemurafenib. In particular, azaindole protected compound **58** revealed hardly measurable activity even at high concentrations, both in biochemical and cellular assays. The nonspecific interactions toward off-target kinases could be drastically reduced by protecting the hinge binder, the azaindole moiety. It was finally demonstrated that UV irradiation at 365 nm restored the inhibitory potency in proliferative and signal transduction assays. Cellular growth assays verified that the applied UV dosage was well-tolerated by the melanoma cells.

The herein presented caged compounds are the first photoactivatable derivatives of an approved small-molecule kinase inhibitor providing an exciting option for novel therapeutic applications. Targeted irradiation might allow a controlled, high-concentrated release of active compound selectively in disease-afflicted tissues. With this approach, systemic side effects might be prevented and acquired resistances reduced.

The implementation of light for the release of therapeutically active substances may be restricted due to low tissue penetration. Several solutions for this problem are conceivable: the required light could be transmitted *via* optical fibers or endoscopic probes. Tissues could moreover be irradiated during surgery. By variation of the PPG the required wavelength can be adjusted. The deepest permeation into biological tissue can be achieved by wavelengths around 800 nm (biological optical window). Hence, two-photon excitation might be an interesting approach.¹⁰

For future therapeutic applications, biological effects of the cleaved PPG and the cyclic benzisoxazolidine intermediate should be thoroughly explored. UV irradiation of the herein utilized *o*-nitrobenzylc PPGs generates potentially toxic nitroso compounds. In the presented cellular proliferation assays, the released 4,5-dimethoxy-2-nitroso-benzaldehyde (the cleaved DMNB) showed intrinsic toxicity only at concentrations above 10 μM . This might not be critical because the caged compounds could be applied at much lower concentrations. The caged vemurafenib derivatives exhibit antiproliferative effects already at concentrations around 0.1 μM . Therefore, there might still be a wide therapeutic window for possible applications. Due to its short half-life, the biological effect of the cyclic intermediate **93** could not be explored in the described assays. Further investigations in cellular assays and animal studies could reveal the effects of cleaved PPGs on biological tissue more thoroughly.

In conclusion, novel caged derivatives of the approved kinase inhibitor vemurafenib were created and it was demonstrated that these prodrugs can be photoactivated *in vitro*. The presented strategy involved (1) the determination of suitable pharmacophore moieties, (2) UV stability testing of the active inhibitor, (3) synthesis of caged prodrugs, (4) characterization of photoactivation, and (5) evaluation of the photoactivation *in vitro*.

This approach can also be transferred to other (kinase) inhibitors and PPGs. Caged kinase inhibitors represent a powerful biochemical tool for studying the kinetics and regulation of phosphorylation processes in signal transduction cascades. On the other hand, caged kinase inhibitors create new possibilities for therapeutic applications. Profound research regarding the stability, bioavailability, metabolism, and toxicity of the caged kinase inhibitors is required to promote their medical applicability.

4.2 CAGED DIARYLMALEIMIDES AND CARBAZOLE

In this study, the design, synthesis, photochemical, and biochemical evaluation of caged prodrugs of two potent, experimental VEGFR kinase inhibitors was demonstrated. Molecular modeling studies revealed that the imide function of the presented diarylmaleimide resp. carbazole acts as the hinge binding moiety. Protection with a PPG was therefore a promising caging approach in order to diminish the inhibitors' efficacies.

Examination of the UV stability indicated that irradiation of the diarylmaleimide **55** triggered the formation of a photocyclized product, namely the intermediate **56** of the reaction from the diarylmaleimide to the carbazole (**57**). Since this compound could not be isolated, an *in situ* formation was an interesting approach.

The compounds were tested in a VEGFR2 kinase assay. It could be demonstrated that DMNB caging significantly diminished the inhibitory efficacy of both inhibitors. In cell proliferation assays it was further proved that UV irradiation at 365 nm restored the inhibitory activity of both prodrugs **99** and **100**, respectively. In the case of the caged diarylmaleimide (**99**), the antiproliferative effect of the irradiated prodrug was interestingly even increased by a factor of 10 compared to the parent compound. A synergistic effect of the released inhibitor, the cleaved protecting group, formation of the intermediate, and influence of the irradiation on the cells can therefore be discussed.

Notably, irradiation of the unprotected diarylmaleimide did not have an impact on the dose-response curve. Thus, the anticipated formation of the intermediate did not lead to an increased biological effect.

In conclusion, the herein presented VEGFR inhibitor prodrugs can serve as novel pharmacological tools in a variety of experiments. It has to be mentioned though that irradiation of the diarylmaleimide prodrugs does not provide a clean photoreaction. The formation of the cyclized **56** has to be considered. Its biological effect should therefore be investigated in further detail.

4.3 PHOTOSWITCHABLE AXITINIB

The aim of this study was to examine axitinib's applicability as a photoswitchable kinase inhibitor.

According to the molecular modeling studies, the (*Z*)-stereoisomer should significantly less inhibit target kinases of (*E*)-axitinib because of sterical hindrance. The (*Z*)-isomer was then afforded by irradiation of a DMSO solution of the (*E*)-isomer and subsequent separation by flash chromatography. NMR studies and X-ray crystallography proved that due to annular NH-tautomerism of the indazole two tautomers were formed. Photochemical characterization revealed that both stereoisomers showed quite divergent UV/vis absorption spectra and that the PSS of both isomers could be shifted to either side depending on the irradiated wavelength. Photoswitching from one stereoisomer to the other by irradiation with UV light (365 and 385 nm) was thus possible in solution although no complete conversion could be achieved.

Enzymatic *in vitro* VEGFR2 and PDGFR β assays using the isolated stereoisomers actually proved that the potency of (*Z*)-axitinib could be diminished up to 30-fold compared to (*E*)-axitinib. These results also translated into cellular settings as demonstrated by western blot based signal transduction analysis using PDGFR β dependent NIH/3T3 cells. Herein, the respective inhibitory effects of both axitinib stereoisomers were in a similar range as compared to the enzymatic level.

Cell proliferation assays using VEGFR2 dependent PC3 cells, however, demonstrated similar inhibitory effects for both axitinib stereoisomers. Further investigations, therefore, have to be made to understand the biological activities of (*E*)- and (*Z*)-axitinib in more detail.

5. EXPERIMENTAL

5.1 MOLECULAR MODELING

Molecular modeling was performed on a DELL 8 core system. For visualization Maestro, version 9.7, Schrödinger, LLC, New York, NY, 2014 was used. Protein crystal structures were prepared prior to docking by the Protein Preparation Wizard¹³⁵ utilizing the following programs: Epik¹³⁶, version 2.7, 2013; Impact, version 6.2, 2014; Prime^{137,138}, version 3.4, 2014. Thus, the X-ray crystal structure refinement process included addition of hydrogen atoms, optimization of hydrogen bonds, and removal of atomic clashes. Default settings were used. Missing side chains and loops were filled in with Prime. Furthermore, selenomethionines were converted to methionines and water molecules were deleted.

Additionally, ligands were prepared in order to create energetically minimized 3D geometries and assign proper bond orders (MacroModel, version 10.3, 2014). Accessible tautomer and ionization states were calculated prior to screening (LigPrep, version 2.9, 2014). To generate bioactive conformers a conformational search method was used (ConfGen¹³⁹, version 2.7, 2014). Receptor grid generation was performed by Glide^{140,141}, version 6.2, 2014. For ligand docking and screening the Glide SP workflow was used. Energetically minimized ligand conformations were docked into the active site of the protein; possible binding poses were determined and subsequently ranked based on their calculated binding affinities.

Furthermore, caged ligands were investigated regarding their interactions within the ATP binding pocket. The structures were therefore superimposed with crystallized or modeled inhibitors by the flexible ligand alignment function. Afterwards, steric hindrance was determined by calculation of ligand-protein contacts. Ugly contacts with a contact cutoff ratio < 0.5 were indicated by red dashed lines. The cutoff ratio was calculated by Maestro based on the following formula: $C = D_{1,2} / (R_1 + R_2)$ where $D_{1,2}$ is the distance between the two atomic centers and where R_1 resp. R_2 are the radii of the atomic centers. C increases monotonically for each contact type, that is $C(\text{ugly}) < C(\text{bad}) < C(\text{good})$.

5.2 PHOTOEXPERIMENTS

5.2.1 UV/vis Absorption Spectra

Spectra were recorded on UV/vis spectrophotometer Varian Cary® 50 Scan, Agilent Technologies. UV/vis absorbance was measured in methanol, DMSO or PBS buffer with 10% DMSO. Concentration is either indicated or compounds were solved and diluted until peak absorbance was in a range of 0.6 to 0.8. Subsequently, graphs were normalized on basis of area under the curve between 260 and 320 nm.

5.2.2 UV Stability

Vemurafenib

Vemurafenib (**44**) was dissolved in DMSO (10 mM) resp. in PBS buffer with 10% DMSO at 0.01 mM and irradiated at 365 nm (LED source: 12 x Nichia NCSU033B, Sahlmann Photochemical Solutions, 100%, 5.4 W) up to 20 min. Aliquots were diluted 1:10 resp. 1:1 with methanol and analyzed by HPLC. Additional to HPLC analysis LC-MS was used to confirm compound identity.

Diarylmaleimide and carbazole

Compounds **55** and **57** were dissolved in DMSO (1 mM) and irradiated at 365 nm (LED source: 12 x Nichia NCSU033B, Sahlmann Photochemical Solutions, 100%, 5.4 W) up to 10 min. Aliquots were diluted 1:10 with methanol and analyzed by HPLC. Additional to HPLC analysis LC-MS was used to confirm compound identity.

5.2.3 Photoactivation

Caged vemurafenib

Compounds **58**, **59**, and **60** were dissolved in DMSO (1 mM) resp. in PBS buffer with 10% DMSO (0.01 mM). The solutions were irradiated at 365 nm (LED source: 12 x Nichia NCSU033B, Sahlmann Photochemical Solutions, 100%, 5.4 W) up to 10 min. After 0.25, 0.5, 0.75, 1, 2, 3, 5 and 10 min of irradiation samples were taken. Aliquots were diluted 1:5 resp. 1:1 with methanol and subsequently analyzed by HPLC. Additional to retention time LC-MS was used to proof identity.

Caged diarylmaleimides and carbazole

Compounds **98**, **99**, and **100** were dissolved in DMSO (1 mM) and the solutions were irradiated at 365 nm (LED source: 12 x Nichia NCSU033B, Sahlmann Photochemical Solutions, 100%, 5.4 W) up to 10 min. After 0.25, 0.5, 0.75, 1, 2, 3, 5 and 10 min of irradiation samples were taken. Aliquots were diluted 1:5 resp. 1:1 with methanol and subsequently analyzed by HPLC. Additional to retention time LC-MS was used to proof identity.

5.2.4 Photoswitching Experiments

Photoswitchable axitinib

Compounds **19** and **19a/b** were dissolved in DMSO (5 mM) and irradiated either at 365 nm (LED source: 12 x Nichia NCSU033B, Sahlmann Photochemical Solutions, 100%, 5.4 W) or at 385 nm (LED source: 3 x Nichia NCSU034A, Sahlmann Photochemical Solutions, 1.2 W) up to 15 min. After 0, 1, 2, 3, 4, 5, 7.5, 10, 12.5 and 15 min aliquots were 1:5 diluted with methanol and subsequently analyzed by HPLC. Additional to retention time LC-MS was used to proof identity.

Experiments have been carried out by Jantje Weber.⁸⁹

5.3 CHEMICAL SYNTHESIS AND CHARACTERIZATION

5.3.1 Reagents and Solvents

All reagents and solvents were obtained from the following commercial sources: abcr GmbH, Fisher Scientific GmbH/Acros, Sigma-Aldrich Chemie or VWR International GmbH.

5.3.2 Flash Chromatography

Column chromatography was performed on a LaFlash system (VWR) using silica gel columns (PF-30SIHP, 30 μm , 40 g, puriFlash) or RP18 columns (PF-15C18HP, 15 μm , 55 g, puriFlash). The crude product was loaded on Merck silica gel 60 (15-40 μm).

5.3.3 TLC

The progress of reactions was monitored by thin-layer chromatography (TLC) utilizing silica gel polyester sheets (SIL G/UV254, 0.2 mm, Polygram®, Macherey-Nagel).

5.3.4 HPLC

High-performance liquid chromatography (HPLC) analyses were performed on a Hewlett Packard 1050 Series. As column either a Phenomenex Kinetex™ C8, 5 μm (4.6 mm \times 150 mm) or an Agilent ZORBAX® Eclipse XDB-C8, 5 μm (4.6 mm \times 150 mm) was used. Injection volume of the compound solutions was 20 μL resp. 30 μL . As mobile phase (flow rate 1.5 mL/min) served a gradient of KH_2PO_4 buffer (10 mM, pH 2.3) and methanol over 14 min resp. 16 min. The detection wavelength was adapted to the according UV/vis absorption spectra. All key compounds submitted to biological assays were proven by this method to show $\geq 98\%$ purity.

5.3.5 Melting Point

Melting points were determined on a Stuart Scientific SMP3 apparatus and are uncorrected.

5.3.6 NMR

^1H , ^{13}C , ^{15}N , and ^{19}F NMR spectra were recorded on a Bruker Avance III 300 instrument at 294 K resp. 300 K with a multinuclear probe head using the manufacturer's pulse programs. Spectra were referenced to internal DMSO- d_5 /CHCl $_3$ (^1H NMR: δ 2.50/7.26 ppm), internal DMSO- d_6 /CDCl $_3$ (^{13}C NMR: δ 39.5/77.2 ppm), external CFCl $_3$ (^{19}F NMR: δ 0.0 ppm) resp. external nitromethane (^{15}N NMR: δ 0.0 ppm) which was corrected to ammonia scale by addition of 381.6 ppm. The following NMR abbreviations are used: b (broad), s (singlet), d (doublet), t (triplet), m (unresolved multiplet). NMR assignments were determined by analysis of multidimensional spectra (H,H COSY, HSQC, HMBC).

NMR spectroscopy was performed by Dr. Ulrich Girreser and his NMR team.

5.3.7 LC-MS

LC-MS samples were chromatographically separated utilizing an Agilent 1100 HPLC system consisting of a thermostated autosampler, diode array detection, and an Agilent ZORBAX® Eclipse XDB-C8, 5 μm (4.6 mm \times 150 mm). Elution was achieved with a solvent gradient system of water and acetonitrile, with 0.1% of acetic acid and a flow rate of 1 mL/min. The eluent flow was splitted to the mass spectrometer. Mass spectrometry was carried out using a Bruker Esquire ~LC instrument with electrospray ionization (ESI) operating in the positive ion mode. Following parameters were used: drying gas nitrogen 8 L/min, nebulizer 35 psi, dry gas heating 350 °C, HV capillary 4000 V, HV EndPlate offset -500 V.

LC-MS analyses were performed by Dr. Ulrich Girreser and Sven Wichmann.

5.3.8 HRMS

High resolution mass spectra (HRMS) were recorded on a Finnigan MAT 8200 mass spectrometer with electron ionization (EI).

HRMS analyses were performed at the Institute of Organic Chemistry, Christian Albrechts University (Kiel, Germany).

5.3.9 X-ray Crystallography

X-ray crystal structure analysis was performed on a Stoe IPDS 2T with Cu / Mo-X ray tubes and Oxford Cryostream.

X-ray analyses were performed by Dr. Dieter Schollmeyer at the Institute of Organic Chemistry, Johannes Gutenberg University (Mainz, Germany).

5.3.10 Chemical Synthesis

Caged vemurafenib

Chemical synthesis and characterization of the following compounds has also been described in ¹¹⁵.

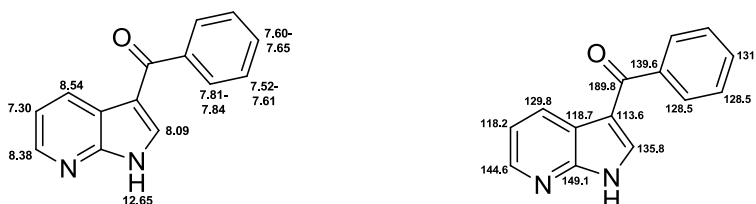
Phenyl-(1*H*-pyrrolo[2,3-*b*]pyridin-3-yl)methanone (67)

RH_038

C₁₄H₁₀N₂O (M_r 222.24)

Synthesis was performed by Martin Schütt.

AlCl₃ (42 mmol, 5.6 g) was suspended in DCM (150 mL) and 7-azaindole (8.4 mmol, 1.0 g) was added portionwise. Subsequently, the reaction mixture was stirred for 1 h at room temperature. Benzoyl chloride (42 mmol, 4.9 mL) was added dropwise and the solution was stirred for another 8 h at room temperature. Afterwards, methanol (20 mL) was used to quench the reaction. After evaporation of the solvent, the crude product was purified by flash silica gel chromatography with a gradient of petroleum ether and ethyl acetate to afford light pink crystals (6.7 mmol, 1.5 g, 80%). Purity (HPLC) 95%; m.p. 189 °C; ¹H NMR (300 MHz, CDCl₃): δ 7.30 (dd, ³J = 7.9 Hz, ³J = 4.7 Hz, 1H), 7.52-7.61 (m, 2H), 7.60-7.65 (m, 1H), 7.81-7.84 (m, 2H), 8.09 (s, 1H), 8.34 (dd, ³J = 4.7 Hz, ⁴J = 1.7 Hz, 1H), 8.54 (dd, ³J = 7.9 Hz, ⁴J = 1.7 Hz, 1H), 12.65 (bs, 1H); ¹³C NMR (75 MHz, CDCl₃): δ 113.6, 118.2, 118.7, 128.5, 129.8, 131.4, 135.8, 139.6, 144.6, 149.1, 189.8.



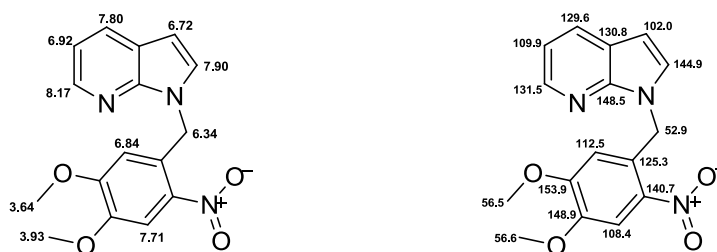
1-(4,5-Dimethoxy-2-nitrobenzyl)-1*H*-pyrrolo[2,3-*b*]pyridine (69)

RH_035

C₁₆H₁₅N₃O₄ (M_r 313.31)

Synthesis was performed by Martin Schütt.

7-Azaindole (0.5 mmol, 60 mg), 4,5-dimethoxy-2-nitrobenzyl bromide (0.75 mmol, 207 mg) and Li₂CO₃ (2.0 mmol, 150 mg) were dissolved in DMF (20 mL) and the reaction mixture stirred for 18 h at room temperature. After evaporation of the solvent, the syrup-like crude product was washed with ice water. This procedure was repeated twice. The residue was dissolved in ethyl acetate, dried over Na₂SO₄, filtered and concentrated to give a bright yellow solid (0.32 mmol, 100 mg, 64%). Purity (HPLC) > 98%; m.p. 121 °C; ¹H NMR (300 MHz, CDCl₃): δ 3.64 (s, 3H), 3.93 (s, 3H), 6.34 (s, 2H), 6.72 (d, ³J = 2.7 Hz, 1 H), 6.84 (bs, 1H), 6.92 (t, ³J = 6.8 Hz, 1H), 7.71 (s, 1H), 7.80 (d, ³J = 6.3 Hz, 1H), 7.90 (d, ³J = 2.7 Hz, 1H), 8.17 (d, ³J = 7.3 Hz, 1H); ¹³C NMR (75 MHz, CDCl₃): δ 52.9, 56.5, 56.6, 102.0, 108.4, 109.9, 112.5, 125.3, 129.6, 130.8, 131.5, 140.7, 144.9, 148.5, 148.9, 153.9; LC-MS (ESD): *m/z* 314 [MH]⁺.



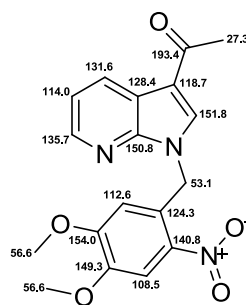
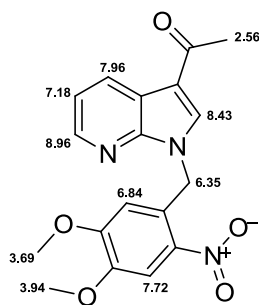
1-(1-(4,5-Dimethoxy-2-nitrobenzyl)-1*H*-pyrrolo[2,3-*b*]pyridin-3-yl)ethanone (70)

RH_036

C₁₈H₁₇N₃O₅ (M_r 355.34)

Synthesis was performed by Martin Schütt.

3-Acetyl-7-azaindole (1.0 mmol, 160 mg), 4,5-dimethoxy-2-nitrobenzyl bromide (1.5 mmol, 414 mg) and Li₂CO₃ (4.0 mmol, 300 mg) were dissolved in DMF (40 mL) and the reaction mixture was stirred for 18 h at room temperature. After evaporation of the solvent, the crude product was washed with ice water (20 mL). The residue was dissolved in DCM, dried over Na₂SO₄, filtered and concentrated to give a pale yellow solid (0.47 mmol, 167 mg, 47%). Purity (HPLC) > 98%; m.p. 202 °C; ¹H NMR (300 MHz, CDCl₃): δ 2.56 (s, 3H), 3.69 (s, 3H), 3.94 (s, 3H), 6.35 (s, 2H), 6.84 (s, 1H), 7.18 (dd, ³J = 7.5 Hz, ³J = 6.3 Hz, 1H), 7.72 (s, 1H), 7.96 (dd, ³J = 6.3 Hz, ⁴J = 1.1 Hz, 1H), 8.43 (s, 1H), 8.96 (dd, ³J = 7.5 Hz, ⁴J = 1.1 Hz, 1H); ¹³C NMR (75 MHz, CDCl₃): δ 27.3, 53.1, 56.6, 56.6, 108.5, 112.6, 114.0, 118.7, 124.3, 128.4, 131.5, 135.7, 140.8, 149.3, 150.8, 151.8, 153.9, 193.4; LC-MS (ESI): *m/z* 356 [MH]⁺.



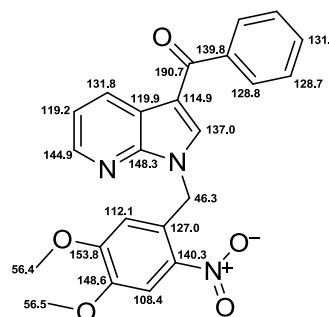
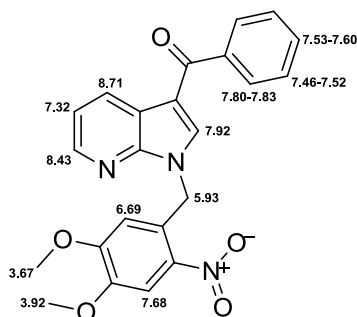
(1-(4,5-Dimethoxy-2-nitrobenzyl)-1*H*-pyrrolo[2,3-*b*]pyridin-3-yl)(phenyl)methanone
(71)

RH_037

C₂₃H₁₉N₃O₅ (M_r 417.41)

Synthesis was performed by Martin Schütt.

3-Benzoyl-7-azaindole (0.5 mmol, 111 mg), 4,5-dimethoxy-2-nitrobenzyl bromide (0.75 mmol, 207 mg) and Li₂CO₃ (2.0 mmol, 150 mg) were dissolved in DMF (15 mL) and stirred for 72 h at room temperature. After evaporation of the solvent, the crude product was washed with ice water (20 mL). The residue was dissolved in DCM, dried over Na₂SO₄, filtered and concentrated to give a pale yellow solid (0.21 mmol, 171 mg, 41%). Purity (HPLC) > 98%; m.p. 162 °C; ¹H NMR (300 MHz, CDCl₃): δ 3.67 (s, 3H), 3.92 (s, 3H), 5.93 (s, 2H), 6.69 (s, 1H), 7.32 (dd, ³J = 7.9 Hz, ³J = 4.8 Hz, 1H), 7.46-7.52 (m, 2H), 7.53-7.60 (m, 1H), 7.68 (s, 1H), 7.80-7.83 (m, 2H), 7.92 (s, 1H), 8.43 (dd, ³J = 4.7 Hz, ⁴J = 1.6 Hz, 1H), 8.71 (dd, ³J = 7.9 Hz, ⁴J = 1.6 Hz, 1H); ¹³C NMR (75 MHz, CDCl₃): δ 46.3, 56.4, 56.5, 108.4, 112.1, 114.9, 119.2, 119.9, 127.0, 128.7, 128.8, 131.8, 131.9, 137.0, 139.8, 140.3, 144.9, 148.3, 148.6, 153.8, 190.7; LC-MS (ESI): *m/z* 418 [MH]⁺.

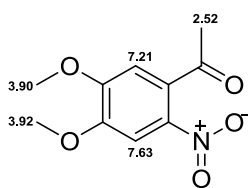


1-(4,5-Dimethoxy-2-nitrophenyl)ethanone (73)

RH_021

 $C_{10}H_{11}NO_5$ (M_r 225.20)

1-(3,4-Dimethoxyphenyl)ethanone (28 mmol, 5.0 g) was added portionwise to a cooled mixture of 65% nitric acid (230 mmol, 15.6 mL) and concentrated sulfuric acid (140 mmol, 7.5 mL) at $-5\text{ }^\circ\text{C}$. Afterwards, the reaction mixture was stirred for further 30 min at $-5\text{ }^\circ\text{C}$. Next, the solution was poured onto ice, the precipitate was filtered off and washed with water. Recrystallization from methanol yielded yellow crystals (13 mmol, 3.0 g, 48%). Purity (HPLC) 86%; m.p. $137\text{ }^\circ\text{C}$; $^1\text{H NMR}$ (300 MHz, DMSO- d_6): δ 2.52 (s, 3H), 3.90 (s, 3H), 3.92 (s, 3H), 7.21 (s, 1H), 7.63 (s, 1H); LC-MS (ESI): m/z 226 $[\text{MH}]^+$.

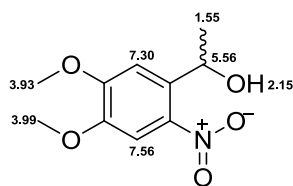


1-(4,5-Dimethoxy-2-nitrophenyl)ethanol (74)

RH_022

 $C_{10}H_{13}NO_5$ (M_r 227.21)

1-(4,5-Dimethoxy-2-nitrophenyl)ethanone (5.0 mmol, 1.13 g) was dissolved in boiling ethanol (15 mL) and $NaBH_4$ (2.4 mmol, 0.09 g) was then added portionwise. After stirring under reflux for 1 h the reaction mixture was poured into ice water (50 mL) and acidified with hydrochloric acid (20%) to pH 6. The product was filtered off and dried *in vacuo*. Recrystallization from a mixture of cyclohexane and ethanol afforded red crystals (2.8 mmol, 636 mg, 56%). Purity (HPLC) 94%; m.p. 124 °C; 1H NMR (300 MHz, $CDCl_3$): δ 1.55 (d, $^3J = 6.3$ Hz, 3H), 2.15 (bs, 1H), 3.93 (s, 3H), 3.99 (s, 3H), 5.56 (q, $^3J = 6.3$ Hz, 1H), 7.30 (s, 1H), 7.56 (s, 1H); LC-MS (ESI): m/z 210 $[M-OH]^+$.

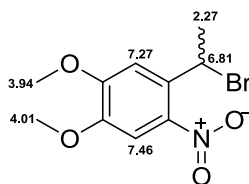


1-(1-Bromoethyl)-4,5-dimethoxy-2-nitrobenzene (75)

RH_029

 $C_{10}H_{12}BrNO_4$ (M_r 290.11)

1-(4,5-Dimethoxy-2-nitrophenyl)ethanol (0.5 mmol, 114 mg) was dissolved in DCM (3 mL). Subsequently, PBr_3 (1.5 mmol, 0.14 mL) was diluted with DCM (1 mL) and added dropwise under stirring at room temperature. The organic phase was washed with brine, dried over Na_2SO_4 and concentrated. Flash silica gel chromatography with a gradient of petroleum ether and ethyl acetate quantitatively afforded a brown-yellowish oil which was directly used for further synthesis. Purity (HPLC) > 98%; 1H NMR (300 MHz, $CDCl_3$): δ 2.27 (d, $^3J = 6.8$ Hz, 3H), 3.94 (s, 3H), 4.01 (s, 3H), 6.81 (q, $^3J = 6.8$ Hz, 1H), 7.27 (s, 1H), 7.46 (s, 1H).

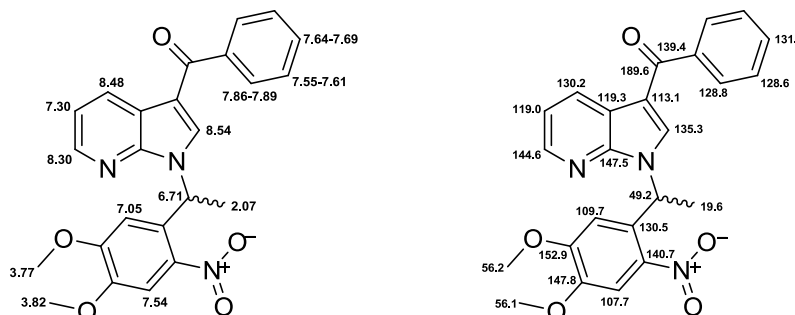


(1-(1-(4,5-Dimethoxy-2-nitrophenyl)ethyl)-1*H*-pyrrolo[2,3-*b*]pyridin-3-yl)(phenyl)methanone (76)

RH_044

C₂₄H₂₁N₃O₅ (M_r, 431.44)

1-(4,5-Dimethoxy-2-nitrophenyl)ethanol (0.45 mmol, 102 mg) was dissolved in DCM (5 mL) and PBr₃ (1.35 mmol, 0.13 mL), diluted with DCM (1 mL), was added dropwise at 0 °C. After stirring 15 min at room temperature the reaction mixture was washed with brine, dried over Na₂SO₄, filtered and used after evaporation of the solvent without further purification. The residue was dissolved in DMF (5 mL). 3-Benzoyl-7-azaindole (0.40 mmol, 89 mg) as well as K₂CO₃ (1.2 mmol, 166 mg) were added. The reaction mixture was stirred for 18 h at room temperature. After evaporation of the solvent, the yellowish oil was redissolved in ethyl acetate, washed with brine and dried over Na₂SO₄. The crude product was purified by flash silica gel chromatography with a gradient of petroleum ether and ethyl acetate to give a yellowish solid (0.07 mmol, 32 mg, 19%). Purity (HPLC) > 98%; m.p. 157 °C; ¹H NMR (300 MHz, DMSO-*d*₆): δ 2.07 (d, ³*J* = 7.1 Hz, 3H), 3.77 (s, 3H), 3.82 (s, 3H), 6.71 (q, ³*J* = 7.1 Hz, 1H), 7.05 (s, 1H), 7.30 (dd, ³*J* = 7.9 Hz, ³*J* = 4.7 Hz, 1H), 7.54 (s, 1H), 7.55-7.61 (m, 2H), 7.64-7.69 (m, 1H), 7.86-7.89 (m, 2H), 8.30 (dd, ³*J* = 4.7 Hz, ⁴*J* = 1.6 Hz, 1H), 8.48 (dd, ³*J* = 7.9 Hz, ⁴*J* = 1.6 Hz, 1H), 8.54 (s, 1H); ¹³C NMR (75 MHz, DMSO-*d*₆): δ 19.6, 49.2, 56.1, 56.2, 107.7, 109.7, 113.1, 119.0, 119.3, 128.6, 128.8, 130.2, 130.5, 131.8, 135.3, 139.4, 140.7, 144.6, 147.5, 147.8, 152.9, 189.6; LC-MS (ESI): *m/z* 432 [MH]⁺.

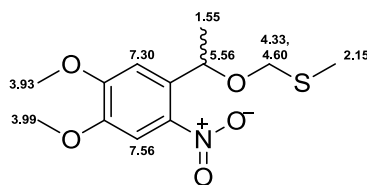


(1-(4,5-Dimethoxy-2-nitrophenyl)ethoxy)methyl(methyl)sulfane (77)

RH_023

C₁₂H₁₇NO₅S (M_r 287.33)

1-(4,5-Dimethoxy-2-nitrophenyl)ethanol (2.2 mmol, 0.5 g) was dissolved in acetonitrile (15 mL). Dimethyl sulfide (19.3 mmol, 1.2 g) was added at 0 °C. Over a period of 20 min benzoyl peroxide (12.4 mmol, 6.0 g, stabilized with dicyclohexyl phthalate at a ratio of 1:1) was slowly added. Subsequently, the reaction mixture was stirred for 2 h. Purification by flash silica gel chromatography with a gradient of petroleum ether and ethyl acetate afforded a yellow solid (1.1 mmol, 330 mg, 52%). Purity (HPLC) 94%; m.p. 70 °C; ¹H NMR (300 MHz, CDCl₃): δ 1.55 (d, ³J = 6.3 Hz, 3H), 2.15 (s, 3H), 3.93 (s, 3H), 3.99 (s, 3H), 4.33 (d, ²J = 11.3 Hz, 1H), 4.60 (d, ²J = 11.3 Hz, 1H), 5.56 (q, ³J = 6.3 Hz, 1H), 7.30 (s, 1H), 7.56 (s, 1H); ¹³C NMR (75 MHz, CDCl₃): δ 14.36, 23.50, 56.49, 56.59, 70.48, 73.40, 107.76, 108.74, 134.84, 140.67, 148.01, 153.98; LC-MS (ESI): *m/z* 210 [M-OCH₂SCH₃]⁺.

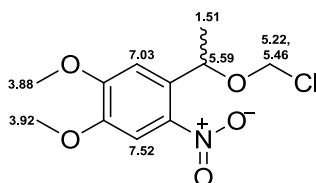


1-(1-(Chloromethoxy)ethyl)-4,5-dimethoxy-2-nitrobenzene (78)

RH_024

 $C_{11}H_{14}ClNO_5$ (M_r 275.69)

(1-(4,5-Dimethoxy-2-nitrophenyl)ethoxy)methyl(methyl)sulfane (0.3 mmol, 100 mg) was dissolved in DCM (5 mL). Subsequently, sulfuryl chloride (1.2 mmol, 0.1 mL) was diluted with DCM (1 mL) and added dropwise at 0 °C to the reaction mixture. After stirring for 4 h at room temperature the reaction was completed. The solvent was removed under reduced pressure to give a yellow oil. The product was used without further purification. 1H NMR (300 MHz, $CDCl_3$): δ 1.51 (d, $^3J = 6.3$ Hz, 3H), 3.88 (s, 3H), 3.92 (s, 3H), 5.22 (d, $^2J = 5.9$ Hz, 1H), 5.46 (d, $^2J = 5.9$ Hz, 1H), 5.59 (q, $^3J = 6.3$ Hz, 1H), 7.03 (s, 1H), 7.52 (s, 1H); ^{13}C NMR (75 MHz, $CDCl_3$): δ 23.17, 56.50, 56.60, 73.46, 80.59, 107.77, 108.80, 133.44, 140.31, 148.26, 153.91.

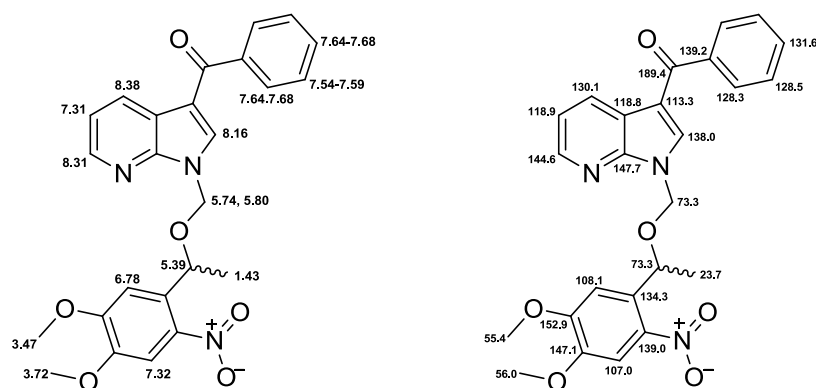


(1-((1-(4,5-Dimethoxy-2-nitrophenyl)ethoxy)methyl)-1*H*-pyrrolo[2,3-*b*]pyridin-3-yl)(phenyl)methanone (79)

RH_043

C₂₅H₂₃N₃O₆ (M_r, 461.47)

(1-(4,5-Dimethoxy-2-nitrophenyl)ethoxy)methyl(methyl)sulfane (0.44 mmol, 127 mg) was dissolved in DCM (5 mL). Subsequently, sulfonyl chloride (1.2 mmol, 0.1 mL) was diluted with DCM (1 mL) and added dropwise at 0 °C. After stirring at room temperature for 4 h, the reaction mixture was evacuated by using a water suction pump. The residue was redissolved in DMF (5 mL) and K₂CO₃ (1.23 mmol, 170 mg) was added. 3-Benzoyl-7-azaindole (0.41 mmol, 91 mg) was dissolved in DMF (5 mL), added dropwise and the solution was stirred for 1 h at room temperature. After evaporation of the solvent, the crude product was redissolved in ethyl acetate and washed with hydrochloric acid (0.1M) and brine. The organic layer was dried over Na₂SO₄, filtered and evacuated. Purification by flash silica gel chromatography with a gradient of petroleum ether and ethyl acetate afforded an orange solid (0.16 mmol, 73 mg, 39%). Purity (HPLC) 97%; m.p. 70 °C; ¹H NMR (300 MHz, DMSO-*d*₆): δ 1.43 (d, ³*J* = 6.1 Hz, 3H), 3.47 (s, 3H), 3.72 (s, 3H), 5.39 (q, ³*J* = 6.1 Hz, 1H), 5.74 (d, ²*J* = 11.1 Hz, 1H), 5.80 (d, ²*J* = 11.1 Hz, 1H), 6.78 (s, 1H), 7.31 (dd, ³*J* = 7.9 Hz, ³*J* = 4.7 Hz, 1H), 7.32 (s, 1H), 7.54-7.59 (m, 2H), 7.64-7.68 (m, 1H), 8.16 (s, 1H), 8.31 (dd, ³*J* = 4.7 Hz, ⁴*J* = 1.4 Hz, 1H), 8.38 (dd, ³*J* = 7.9 Hz, ⁴*J* = 1.4 Hz, 1H); ¹³C NMR (75 MHz, DMSO-*d*₆): δ 23.7, 55.4, 56.0, 73.3, 107.0, 108.1, 113.3, 118.8, 118.9, 128.3, 128.5, 130.1, 131.6, 134.3, 138.0, 139.0, 139.2, 144.6, 147.1, 147.7, 152.9, 189.42; LC-MS (ESI): *m/z* 462 [MH]⁺.

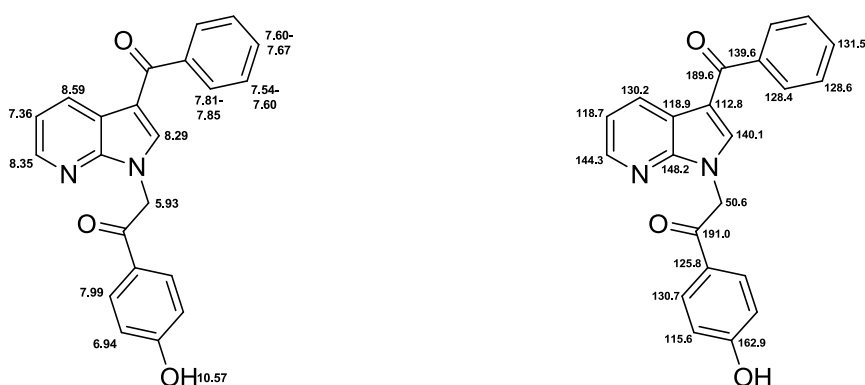


2-(3-Benzoyl-1*H*-pyrrolo[2,3-*b*]pyridin-1-yl)-1-(4-hydroxyphenyl)ethanone (82)

RH_039

C₂₂H₁₆N₂O₃ (M_r 356.37)

3-Benzoyl-7-azaindole (0.45 mmol, 100 mg) and K₂CO₃ (1.35 mmol, 187 mg) were dissolved in DMF (10 mL) and stirred for 15 min at room temperature. 4-Hydroxyphenacylbromide (0.4 mmol, 97 mg) was dissolved in DMF (10 mL) and added dropwise at 0 °C. Afterwards, the reaction mixture was stirred for another 30 min at room temperature. After evaporation of the solvent, the remainder was redissolved in ethyl acetate, washed with hydrochloric acid (1M) and brine and subsequently dried over Na₂SO₄. The crude product was purified by flash silica gel chromatography with a gradient of petroleum ether and ethyl acetate to give grey needles (0.16 mmol, 58 mg, 36%). Purity (HPLC) 96%; m.p. 215 °C; ¹H NMR (300 MHz, CDCl₃): δ 5.93 (s, 2H), 6.94 (d, ³J = 8.8 Hz, 2H), 7.36 (dd, ³J = 7.9 Hz, ³J = 4.7 Hz, 1H), 7.54-7.60 (m, 2H), 7.60-7.67 (m, 1H), 7.81-7.85 (m, 2H), 7.99 (d, ³J = 8.8 Hz, 2H), 8.29 (s, 1H), 8.35 (dd, ³J = 4.7 Hz, ⁴J = 1.6 Hz, 1H), 8.59 (dd, ³J = 7.9 Hz, ⁴J = 1.6 Hz, 1H), 10.57 (bs, 1H); ¹³C NMR (75 MHz, CDCl₃): δ 50.6, 112.8, 115.6, 118.7, 118.9, 125.8, 128.4, 128.6, 130.2, 130.7, 131.5, 139.6, 140.1, 144.3, 148.2, 162.9, 189.6, 191.0; LC-MS (ESD): *m/z* 357 [MH]⁺.

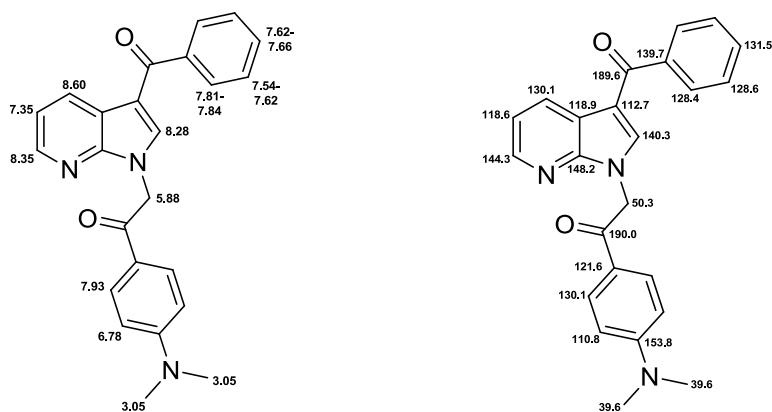


2-(3-Benzoyl-1*H*-pyrrolo[2,3-*b*]pyridin-1-yl)-1-(4-(dimethylamino)phenyl)ethanone (83)

RH_040

C₂₄H₂₁N₃O₂ (M_r 383.44)

3-Benzoyl-7-azaindole (0.45 mmol, 100 mg) and K₂CO₃ (1.35 mmol, 187 mg) were dissolved in DMF (10 mL) and stirred for 15 min at room temperature. 4-(Dimethylamino)phenacyl bromide (0.4 mmol, 109 mg) was dissolved in DMF (10 mL) and was added dropwise at 0 °C. Afterwards, the reaction mixture was stirred for 1 h at room temperature. After evaporation of the solvent, the crude product was redissolved in ethyl acetate, washed with hydrochloric acid (1M) and brine and dried over Na₂SO₄. Subsequently, the solvent was removed under reduced pressure and the residue washed with diethyl ether to afford a white powder (0.26 mmol, 101 mg, 59%). Purity (HPLC) > 98%; m.p. 147 °C; ¹H NMR (300 MHz, DMSO-*d*₆): δ 3.05 (s, 6H), 5.88 (s, 2H), 6.78 (d, ³*J* = 9.1 Hz, 2H), 7.35 (dd, ³*J* = 7.8 Hz, ³*J* = 4.7 Hz, 1H), 7.54-7.62 (m, 2H), 7.62-7.66 (m, 1H), 7.81-7.84 (m, 2H), 7.93 (d, ³*J* = 9.1 Hz, 2H), 8.28 (s, 1H), 8.35 (dd, ³*J* = 4.7 Hz, ⁴*J* = 1.6 Hz, 1H), 8.60 (dd, ³*J* = 7.8 Hz, ⁴*J* = 1.6 Hz, 1H); ¹³C NMR (75 MHz, DMSO-*d*₆): δ 39.6, 50.3, 110.8, 112.7, 118.6, 118.9, 121.6, 128.4, 128.6, 130.1, 130.1, 131.5, 139.7, 140.3, 144.3, 148.2, 153.8, 189.6, 189.97; LC-MS (ESI): *m/z* 384 [MH]⁺.

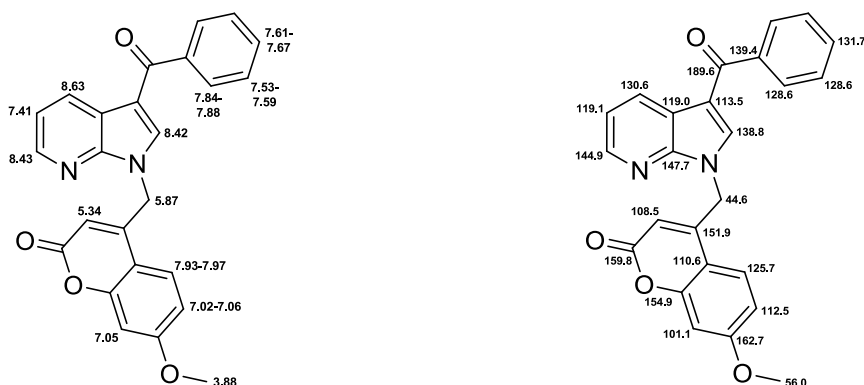


4-((3-Benzoyl-1*H*-pyrrolo[2,3-*b*]pyridin-1-yl)methyl)-7-methoxy-2*H*-chromen-2-one (84)

RH_042

C₂₅H₁₈N₂O₄ (M_r, 410.42)Synthesis was performed by Dr. Melanie Zindler.¹⁴²

3-Benzoyl-7-azaindole (0.5 mmol, 111 mg) and Li₂CO₃ (2.0 mmol, 148 mg) were dissolved in DMF (5 mL) and stirred for 15 min at room temperature. 4-Bromomethyl-7-methoxycoumarin (0.5 mmol, 134 mg) was dissolved in DMF (5 mL) and added dropwise. Afterwards, the reaction mixture was stirred for 18 h at room temperature. After evaporation of the solvent, the remainder was redissolved in ethyl acetate, washed with hydrochloric acid (1M) and brine and dried over Na₂SO₄. The crude product was purified by flash silica gel chromatography with a gradient of petroleum ether and ethyl acetate to afford a white powder (0.23 mmol, 94 mg, 46%). Purity (HPLC) 96%; m.p. 214 °C; ¹H NMR (300 MHz, DMSO-*d*₆): δ 3.88 (s, 3H), 5.34 (s, 1H), 5.87 (s, 2H), 7.05 (s, 1H), 7.02-7.06 (m, 1H), 7.41 (dd, ³*J* = 7.9 Hz, ³*J* = 4.7 Hz, 1H), 7.53-7.59 (m, 2H), 7.61-7.67 (m, 1H), 7.84-7.88 (m, 2H), 7.93-7.97 (m, 1H), 8.42 (s, 1H), 8.43 (dd, ³*J* = 4.7 Hz, ⁴*J* = 1.6 Hz, 1H), 8.63 (dd, ³*J* = 7.9 Hz, ⁴*J* = 1.6 Hz, 1H); ¹³C NMR (75 MHz, DMSO-*d*₆): δ 44.6, 56.1, 101.2, 108.5, 110.6, 112.5, 113.5, 119.0, 119.1, 125.7, 128.6, 130.6, 131.7, 138.8, 139.4, 144.9, 147.7, 151.9, 154.9, 159.8, 162.7, 189.6; LC-MS (ESI): *m/z* 411 [MH]⁺.

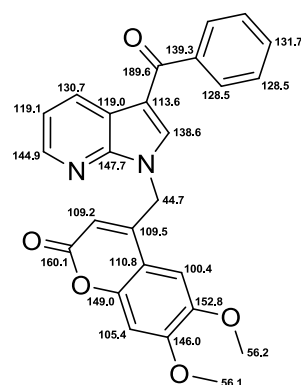
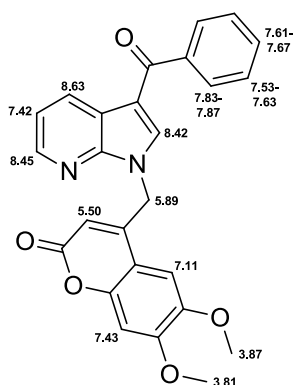


4-((3-Benzoyl-1*H*-pyrrolo[2,3-*b*]pyridin-1-yl)methyl)-6,7-dimethoxy-2*H*-chromen-2-one (85)

RH_041

C₂₆H₂₀N₂O₅ (M_r 440.45)

3-Benzoyl-7-azaindole (0.45 mmol, 100 mg) and K₂CO₃ (1.35 mmol, 187 mg) were dissolved in DMF (10 mL) and stirred for 15 min at room temperature. 4-Bromomethyl-6,7-dimethoxycoumarin (0.4 mmol, 135 mg) was dissolved in DMF (10 mL) and added dropwise. Afterwards, the reaction mixture was stirred for 1 h at room temperature. After evaporation of the solvent, the remainder was redissolved in ethyl acetate, washed with hydrochloric acid (1M) and brine and dried over Na₂SO₄. Purification of the crude product by flash silica gel chromatography with a gradient of petroleum ether and ethyl acetate gave a white powder (0.31 mmol, 135 mg, 68%). Purity (HPLC) > 98%; m.p. 226 °C; ¹H NMR (300 MHz, DMSO-*d*₆): δ 3.81 (s, 3H), 3.87 (s, 3H), 5.50 (s, 1H), 5.89 (s, 2H), 7.11 (s, 1H), 7.42 (dd, ³*J* = 7.9 Hz, ³*J* = 4.7 Hz, 1H), 7.43 (s, 1H), 7.53-7.63 (m, 2H), 7.61-7.67 (m, 1H), 7.83-7.87 (m, 2H), 8.42 (s, 1H), 8.45 (dd, ³*J* = 4.7 Hz, ⁴*J* = 1.6 Hz, 1H), 8.63 (dd, ³*J* = 7.9 Hz, ⁴*J* = 1.6 Hz, 1H); ¹³C NMR (75 MHz, DMSO-*d*₆): δ 44.7, 56.1, 56.2, 100.4, 105.4, 109.2, 109.5, 113.6, 119.0, 119.1, 128.5, 130.7, 131.7, 138.6, 139.3, 144.9, 146.0, 147.7, 149.0, 151.7, 152.8, 160.1, 189.6; LC-MS (ESI): *m/z* 441 [MH]⁺.

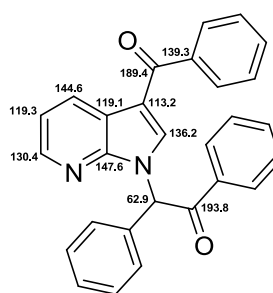
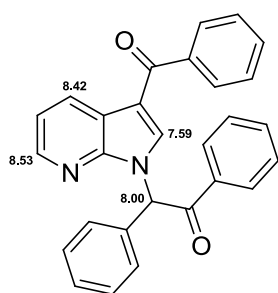


2-(3-Benzoyl-1*H*-pyrrolo[2,3-*b*]pyridin-1-yl)-1,2-diphenylethanone (86)

RH_046

C₂₈H₂₀N₂O₂ (M_r 416.47)

3-Benzoyl-7-azaindole (0.45 mmol, 100 mg) and K₂CO₃ (1.35 mmol, 187 mg) were dissolved in DMF (10 mL) and stirred for 15 min at room temperature. Subsequently, desyl bromide (0.4 mmol, 124 mg) was dissolved in DMF (10 mL) and added dropwise at room temperature, where upon the color changed to orange. After stirring for 1 h at room temperature, the solvent was removed *in vacuo*. In the next step, the remainder was redissolved in ethyl acetate and washed with hydrochloric acid (0.1M) and brine. Afterwards, the organic layer was dried over Na₂SO₄, filtered and concentrated to afford a brown oil. The crude product was purified by flash silica gel chromatography with a gradient of petroleum ether and ethyl acetate to give an orange solid (0.22 mmol, 90 mg, 48%). Purity (HPLC) 97%; m.p. 152 °C; ¹H NMR (300 MHz, DMSO-*d*₆): δ 7.37-7.69 (m, 14H), 7.59 (s, 1H), 8.00 (s, 1H), 8.09-8.12 (m, 2H), 8.42 (dd, ³*J* = 4.7 Hz, ⁴*J* = 1.6 Hz, 1H), 8.53 (dd, ³*J* = 7.9 Hz, ⁴*J* = 1.6 Hz, 1H); ¹³C NMR (75 MHz, DMSO-*d*₆): δ 62.9, 113.2, 119.1, 119.3, 128.2, 128.6, 128.9, 129.1, 129.6, 129.6, 129.7, 130.4, 131.7, 133.1, 134.2, 134.2, 136.2, 139.3, 144.6, 147.6, 189.4, 193.8; LC-MS (ESI): *m/z* 417 [MH]⁺.

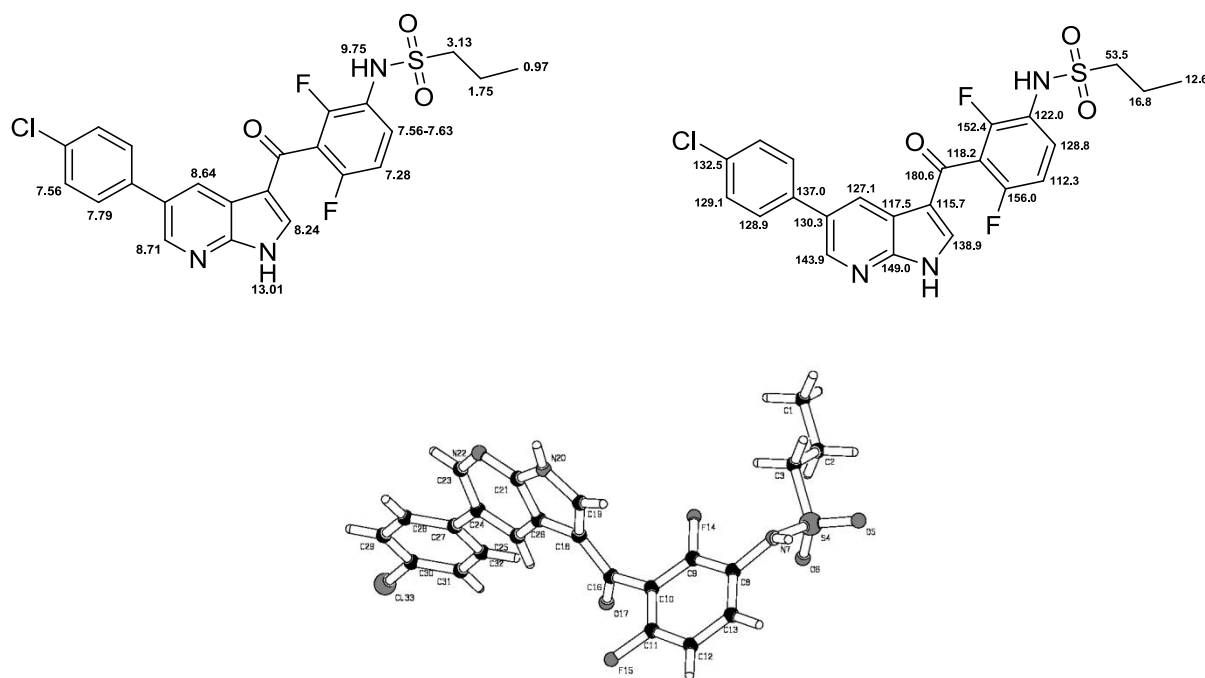


***N*-(3-(5-(4-Chlorophenyl)-1*H*-pyrrolo[2,3-*b*]pyridine-3-carbonyl)-2,4-difluorophenyl)propane-1-sulfonamide (44), INN: vemurafenib**

RH_007

C₂₃H₁₈ClF₂N₃O₃S (M_r 489.92)

One tablet of Zelboraf (vemurafenib content 0.49 mmol, 240 mg) was pestle, absorbed onto silica gel and eluted with DCM and ethyl acetate to afford white needles (0.46 mmol, 228 mg, 95%). Purity (HPLC) > 98%; m.p. 271 °C; ¹H NMR (300 MHz, DMSO-d₆): δ 0.97 (t, ³J = 7.4 Hz, 3H), 1.75 (tq, ³J = 7.7 Hz, ³J = 7.4 Hz, 2H), 3.13 (t, ³J = 7.7 Hz, 2H), 7.28 (ddd, ³J = 8.8 Hz, ³J_{HF} = 8.8 Hz, ⁵J_{HF} = 1.4 Hz, 1H), 7.56 (d, ³J = 8.6 Hz, 2H), 7.56-7.63 (m, 1H), 7.79 (d, ³J = 8.6 Hz, 2H), 8.24 (s, 1H), 8.64 (d, ⁴J = 1.7 Hz, 1H), 8.71 (d, ⁴J = 2.3 Hz, 1H), 9.75 (bs, 1H); ¹³C NMR (75 MHz, DMSO-d₆): δ 12.6, 16.8, 53.5, 112.3 (dd, ²J_{CF} = 22.5 Hz, ⁴J_{CF} = 3.7 Hz), 115.7, 117.5, 118.2 (dd, ²J_{CF} = 24.6 Hz, ²J_{CF} = 22.4 Hz), 122.0 (dd, ²J_{CF} = 13.6 Hz, ⁴J_{CF} = 3.7 Hz), 127.1, 128.8 (dd, ³J_{CF} = 10.0 Hz, ³J_{CF} = 1.6 Hz), 128.9, 129.1, 130.3, 132.5, 137.0, 138.9, 143.9, 149.0, 152.4 (dd, ¹J_{CF} = 249.5 Hz, ³J_{CF} = 8.5 Hz), 156.0 (dd, ¹J_{CF} = 246.5 Hz, ³J_{CF} = 7.0 Hz), 180.6; ¹⁹F NMR (282 MHz, DMSO-d₆): δ -122.0, -116.7; LC-MS (ESI): *m/z* 490, 492 [MH]⁺.



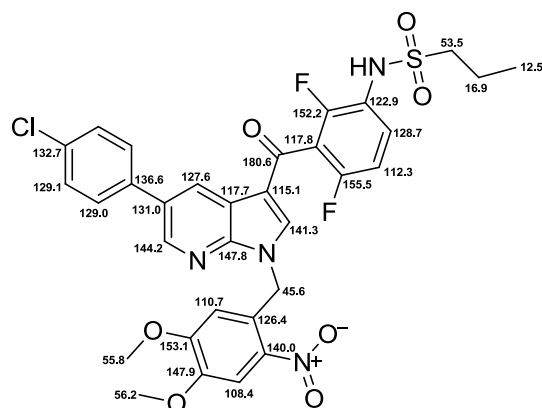
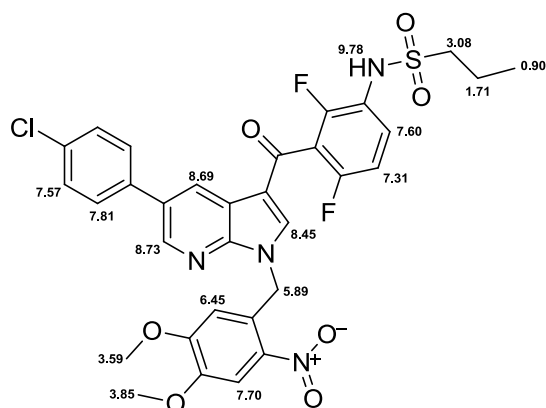
Molecular structure determined by X-ray crystallography: CCDC 1044606

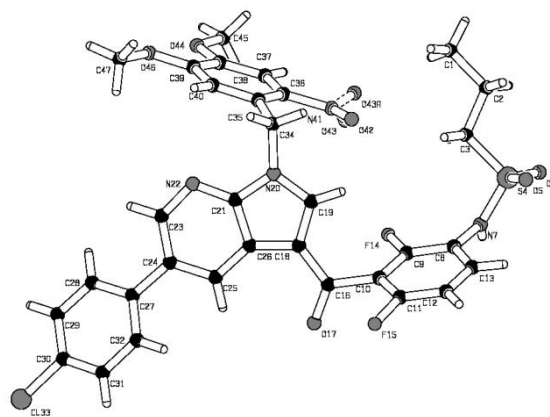
***N*-(3-(5-(4-Chlorophenyl)-1-(4,5-dimethoxy-2-nitrobenzyl)-1*H*-pyrrolo[2,3-*b*]pyridine-3-carbonyl)-2,4-difluorophenyl)propane-1-sulfonamide (58)**

RH_015

C₃₂H₂₇ClF₂N₄O₇S (M_r 685.09)

Vemurafenib (0.25 mmol, 122 mg), 4,5-dimethoxy-2-nitrobenzyl bromide (0.25 mmol, 69 mg) and K₂CO₃ (1.25 mmol, 173 mg) were dissolved in DMF (10 mL). The reaction mixture was stirred for 1 h at room temperature. After evaporation of the solvent, the yellowish oil was redissolved in ethyl acetate, washed with brine and dried over Na₂SO₄. The crude product was purified by flash silica gel chromatography with a gradient of petroleum ether and ethyl acetate to give a yellowish solid (0.026 mmol, 18 mg, 11%). Purity (HPLC) > 98%; m.p. 200 °C; ¹H NMR (300 MHz, DMSO-d₆): δ 0.90 (t, ³J = 7.4 Hz, 3H), 1.71 (tq, ³J = 7.5 Hz, ³J = 7.4 Hz, 2H), 3.08 (t, ³J = 7.5 Hz, 2H), 3.59 (s, 3H), 3.85 (s, 3H), 5.89 (s, 2H), 6.45 (s, 1H), 7.31 (ddd, ³J_{HF} = 9.0 Hz, ³J = 8.7 Hz, ⁵J_{HF} = 1.6 Hz, 1H), 7.57 (d, ³J = 8.5 Hz, 2H), 7.60 (dd, ³J = 8.7 Hz, ⁴J_{HF} = 6.1 Hz, 1H), 7.70 (s, 1H), 7.81 (d, ³J = 8.5 Hz, 2H), 8.45 (s, 1H), 8.69 (bs, 1H), 8.73 (d, ⁴J = 2.0 Hz, 1H), 9.78 (bs, 1H); ¹³C NMR (75 MHz, DMSO-d₆): δ 12.5, 16.9, 45.6, 53.5, 55.8, 56.2, 108.4, 110.7, 112.3 (d, ²J_{CF} = 22.7 Hz), 115.1, 117.7, 117.8 (t, ²J_{CF} = 23.5 Hz), 122.9 (d, ²J_{CF} = 15.5 Hz), 126.4, 127.6, 128.7 (d, ³J_{CF} = 8.1 Hz), 129.0, 129.1, 131.0, 132.7, 136.6, 140.0, 141.3, 144.2, 147.8, 147.9, 152.2 (dd, ¹J_{CF} = 252.6 Hz, ³J_{CF} = 8.4 Hz), 153.1, 155.5 (dd, ¹J_{CF} = 251.1 Hz, ³J_{CF} = 6.8 Hz), 180.6; ¹⁹F NMR (282 MHz, DMSO-d₆): δ -122.2, -116.7; LC-MS (ESI): *m/z* 685, 687 [MH]⁺.





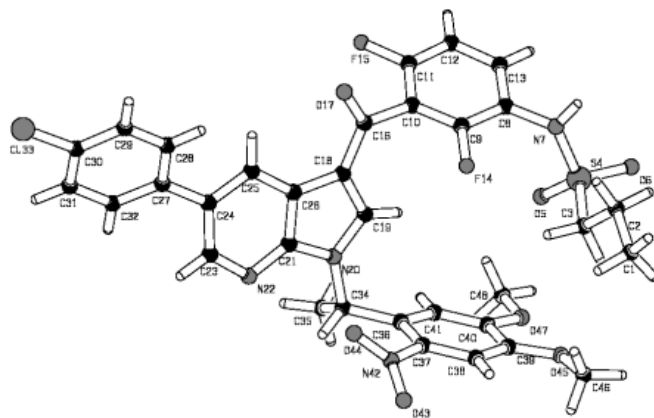
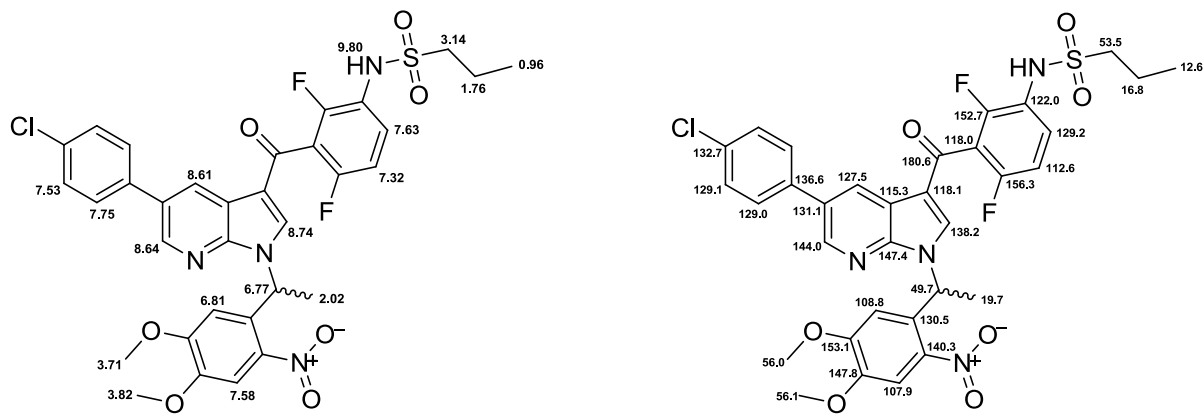
Molecular structure determined by X-ray crystallography: CCDC 1044607

***N*-(3-(5-(4-Chlorophenyl)-1-(1-(4,5-dimethoxy-2-nitrophenyl)ethyl)-1*H*-pyrrolo[2,3-*b*]pyridine-3-carbonyl)-2,4-difluorophenyl)propane-1-sulfonamide (59)**

RH_032

C₃₃H₂₉ClF₂N₄O₇S (M_r, 699.12)

1-(4,5-Dimethoxy-2-nitrophenyl)ethanol (1.0 mmol, 230 mg) was dissolved in DCM (8 mL) and PBr₃ (3.0 mmol, 0.28 mL), diluted with DCM (1 mL), was added dropwise at 0 °C. After stirring of the reaction mixture for 30 min at 0 °C and another 15 min at room temperature, the reaction mixture was washed with brine, dried over Na₂SO₄, filtered and concentrated. The residue was used in the next step without further purification. The formed 1-(1-bromoethyl)-4,5-dimethoxy-2-nitrobenzene was dissolved in DMF (15 mL). Vemurafenib (0.6 mmol, 295 mg) and K₂CO₃ (2.4 mmol, 330 mg) were added and stirred for 18 h at room temperature. After evaporation of the solvent, the yellowish oil was redissolved in ethyl acetate, washed with brine and dried over Na₂SO₄. Purification by flash silica gel chromatography with a gradient of petroleum ether and ethyl acetate afforded a yellowish solid (0.14 mmol, 98 mg, 23%). Purity (HPLC) > 98%; m.p. 218 °C; ¹H NMR (300 MHz, DMSO-d₆): δ 0.96 (t, ³J = 7.5 Hz, 3H), 1.71 (tq, ³J = 7.6 Hz, ³J = 7.5 Hz, 2H), 2.02 (d, ³J = 7.1 Hz, 3H), 3.14 (t, ³J = 7.6 Hz, 2H), 3.71 (s, 3H), 3.82 (s, 3H), 6.77 (q, ³J = 7.1 Hz, 1H), 6.81 (s, 1H), 7.32 (ddd, ³J = 8.9 Hz, ³J_{HF} = 8.8 Hz, ⁵J_{HF} = 1.5 Hz, 1H), 7.53 (d, ³J = 8.8 Hz, 2H), 7.58 (s, 1H), 7.63 (ddd, ³J = 8.9 Hz, ⁴J_{HF} = 5.9 Hz, ⁴J_{HF} = 5.9 Hz, 1H), 7.75 (d, ³J = 8.8 Hz, 2H), 8.61 (bs, 1H), 8.64 (d, ⁶J = 2.2 Hz, 1H), 8.74 (s, 1H), 9.80 (bs, 1H); ¹³C NMR (75 MHz, DMSO-d₆): δ 12.6, 16.8, 19.7, 49.7, 53.5, 55.6, 56.1, 107.9, 108.8, 112.6 (dd, ³J_{CF} = 22.8 Hz, ⁵J_{CF} = 2.8 Hz), 115.3, 118.0 (dd, ²J_{CF} = 24.2 Hz, ²J_{CF} = 21.9 Hz), 118.1, 122.0 (dd, ²J_{CF} = 13.5 Hz, ⁴J_{CF} = 3.4 Hz), 127.5, 129.0, 129.1, 129.2 (d, ⁴J_{CF} = 0.2 Hz), 130.5, 131.1, 132.7, 136.6, 138.2, 140.3, 144.0, 147.4, 147.8, 152.7 (dd, ¹J_{CF} = 250.2 Hz, ³J_{CF} = 8.4 Hz), 153.1, 156.3 (dd, ¹J_{CF} = 247.2 Hz, ³J_{CF} = 6.6 Hz), 180.6; ¹⁹F NMR (282 MHz, DMSO-d₆): δ -121.5, -116.5; LC-MS (ESI): *m/z* 699, 701 [MH]⁺.



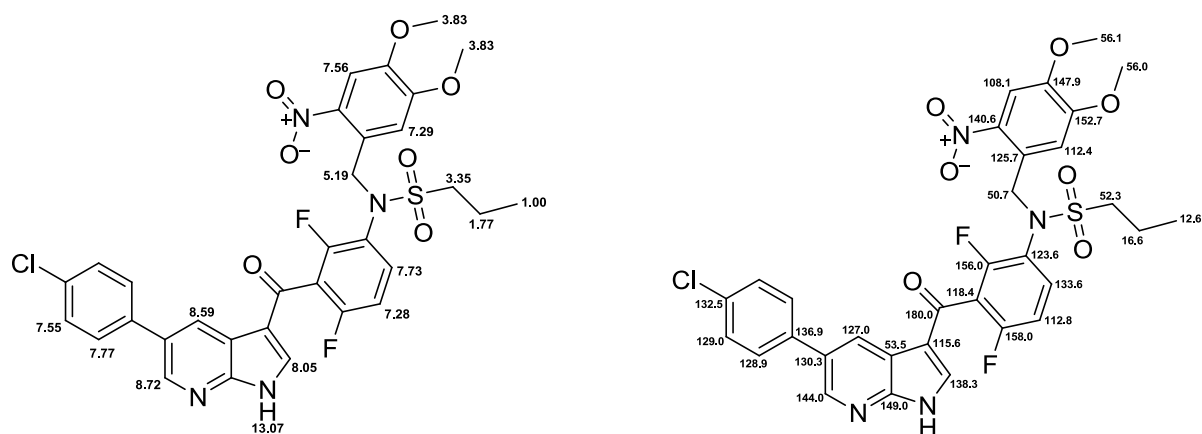
Molecular structure determined by X-ray crystallography: CCDC 1044608

***N*-(3-(5-(4-Chlorophenyl)-1*H*-pyrrolo[2,3-*b*]pyridine-3-carbonyl)-2,4-difluorophenyl)-*N*-(4,5-dimethoxy-2-nitrobenzyl)propane-1-sulfonamide (60)**

RH_015*

C₃₂H₂₇ClF₂N₄O₇S (M_r 685.09)

Vemurafenib (0.5 mmol, 245 mg) and 4,5-dimethoxy-2-nitrobenzyl bromide (0.7 mmol, 179 mg) were dissolved in DMF (15 mL). *N,N*-Diisopropylethylamine (2.0 mmol, 0.34 mL, Hunig's base) was diluted with DMF (5 mL) and added dropwise over 30 min. The mixture was stirred for 18 h at room temperature. After evaporation of the solvent, the yellowish oil was redissolved in ethyl acetate, washed with brine and dried over Na₂SO₄. Purification by flash silica gel chromatography with a gradient of petroleum ether and ethyl acetate afforded a pale yellow solid (0.1 mmol, 67 mg, 20%). Purity (HPLC) > 98%; m.p. 237 °C; ¹H NMR (300 MHz, DMSO-*d*₆): δ 1.00 (t, ³*J* = 7.4 Hz, 3H), 1.77 (tq, ³*J* = 7.5 Hz, ³*J* = 7.4 Hz, 2H), 3.35 (t, ³*J* = 7.5 Hz, 2H), 3.83 (s, 6H), 5.19 (s, 2H), 7.28 (dd, ³*J* = 8.4 Hz, ³*J*_{HF} = 8.1 Hz, 1H), 7.29 (s, 1H), 7.55 (d, ³*J* = 8.5 Hz, 2H), 7.56 (s, 1H), 7.73 (ddd, ³*J* = 8.4 Hz, ⁴*J*_{HF} = 6.0 Hz, ⁴*J*_{HF} = 6.0 Hz, 1H), 7.77 (d, ³*J* = 8.5 Hz, 2H), 8.05 (d, ³*J* = 2.7, 1H), 8.59 (bs, 1H), 8.72 (d, ⁴*J* = 2.3 Hz, 1H), 13.07 (d, ³*J* = 2.7, 1H); ¹³C NMR (75 MHz, DMSO-*d*₆): δ 12.6, 16.6, 50.7, 52.3, 56.0, 56.1, 108.1, 112.4, 112.8 (dd, ²*J*_{CF} = 22.9 Hz, ⁴*J*_{CF} = 2.6 Hz), 115.6, 117.4, 118.4 (dd, ²*J*_{CF} = 23.6 Hz, ²*J*_{CF} = 22.8 Hz), 123.6 (dd, ²*J*_{CF} = 12.9 Hz, ⁴*J*_{CF} = 3.5 Hz), 125.7, 127.0, 128.9, 129.0, 130.3, 132.5, 133.6 (d, ³*J*_{CF} = 10.1 Hz), 136.9, 138.3, 140.6, 144.0, 147.9, 149.0, 152.7, 156.0 (dd, ¹*J*_{CF} = 252.4 Hz, ³*J*_{CF} = 8.8 Hz), 158.0 (dd, ¹*J*_{CF} = 250.3 Hz, ³*J*_{CF} = 7.7 Hz), 180.0; ¹⁹F NMR (282 MHz, DMSO-*d*₆): δ -116.3, -112.2; LC-MS (ESI): *m/z* 685, 687 [MH]⁺; HRMS (EI): *m/z* calculated 684.1257, found 684.1264.

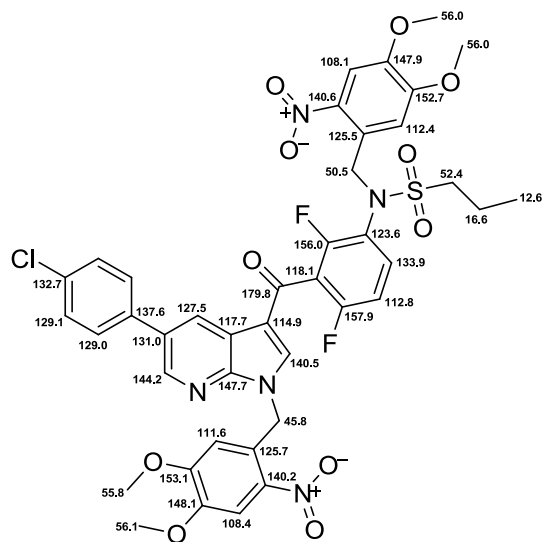
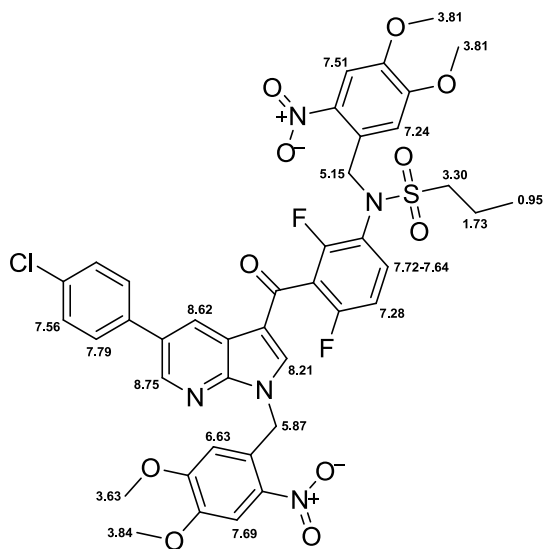


***N*-(3-(5-(4-Chlorophenyl)-1-(4,5-dimethoxy-2-nitrobenzyl)-1*H*-pyrrolo[2,3-*b*]pyridine-3-carbonyl)-2,4-difluorophenyl)-*N*-(4,5-dimethoxy-2-nitrobenzyl)propane-1-sulfonamide (87)**

RH_016

C₄₁H₃₆ClF₂N₅O₁₁S (M_r 880.27)

Vemurafenib (0.5 mmol, 245 mg) and 4,5-dimethoxy-2-nitrobenzyl bromide (0.7 mmol, 179 mg) were dissolved in DMF (15 mL). *N,N*-Diisopropylethylamine (2.0 mmol, 0.34 mL, Hunig's base) was diluted with DMF (5 mL) and added dropwise over 30 min. The mixture was stirred for 18 h at room temperature. After evaporation of the solvent, the yellow oil was redissolved in ethyl acetate, washed with brine and dried over Na₂SO₄. The crude product was purified by flash silica gel chromatography with a gradient of petroleum ether and ethyl acetate to give a yellow solid (0.1 mmol, 100 mg, 23%). Purity (HPLC) > 98%; m.p. 254 °C; ¹H NMR (300 MHz, DMSO-*d*₆): δ 0.95 (t, ³*J* = 7.4 Hz, 3H), 1.73 (tq, ³*J* = 7.5 Hz, ³*J* = 7.4 Hz, 2H), 3.30 (t, ³*J* = 7.5 Hz, 2H), 3.63 (s, 3H), 3.81 (s, 6H), 3.84 (s, 3H), 5.15 (s, 2H), 5.87 (s, 2H), 6.63 (s, 1H), 7.24 (s, 1H), 7.28 (dd, ³*J* = 8.4 Hz, ³*J*_{HF} = 8.4 Hz, 1H), 7.51 (s, 1H), 7.56 (d, ³*J* = 8.5 Hz, 2H), 7.72-7.64 (m, 1H), 7.69 (s, 1H), 7.79 (d, ³*J* = 8.5 Hz, 2H), 8.21 (s, 1H), 8.62 (bs, 1H), 8.75 (d, ⁴*J* = 2.2 Hz, 1H); ¹³C NMR (75 MHz, DMSO-*d*₆): δ 12.6, 16.6, 45.8, 50.5, 52.4, 55.8, 56.0, 56.0, 56.1, 108.1, 108.4, 111.6, 112.4, 112.8 (dd, ²*J*_{CF} = 22.1 Hz, ⁴*J*_{CF} = 3.3 Hz), 114.9, 117.7, 118.1 (dd, ²*J*_{CF} = 26.1 Hz, ²*J*_{CF} = 23.2 Hz), 123.6 (dd, ²*J*_{CF} = 11.9 Hz, ⁴*J*_{CF} = 3.0 Hz), 125.5, 125.7, 127.5, 129.0, 129.1, 131.0, 132.7, 133.9 (d, ³*J*_{CF} = 10.2 Hz), 136.6, 140.2, 140.5, 140.6, 144.2, 147.7, 147.9, 148.1, 152.7, 153.1, 156.0 (dd, ¹*J*_{CF} = 251.7 Hz, ³*J*_{CF} = 7.3 Hz), 157.9 (dd, ¹*J*_{CF} = 250.7 Hz, ³*J*_{CF} = 7.0 Hz), 179.8; ¹⁹F NMR (282 MHz, DMSO-*d*₆): δ -112.0, -112.2; LC-MS (ESI): *m/z* 880, 882 [MH]⁺.



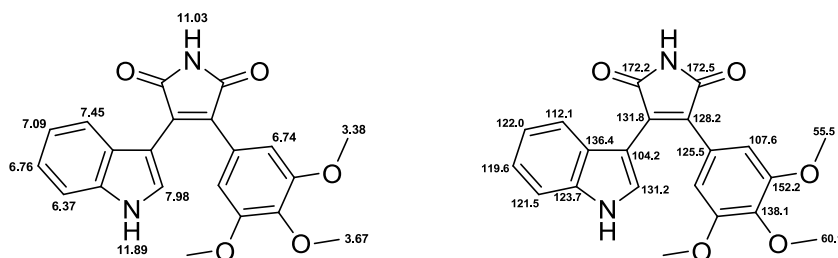
Caged diarylmaleimides and carbazole

3-(1*H*-Indol-3-yl)-4-(3,4,5-trimethoxyphenyl)-1*H*-pyrrole-2,5-dione (55)

RH_003

C₂₁H₁₈N₂O₂ (M_r 378.38)

2-(3,4,5-Trimethoxyphenyl)acetamide (10 mmol, 2.25 g) was dissolved in dry THF (30 mL) under nitrogen atmosphere and the reaction mixture was cooled to 0 °C. Ethyl 2-(1*H*-indol-3-yl)-2-oxoacetate (13 mmol, 2.82 g) dissolved in dry THF (40 mL) was added dropwise. Afterwards, potassium tert-butoxide solution (1M in THF, 40 mmol, 40 mL) was added. Subsequently, the deep purple reaction mixture was stirred for 6 h at room temperature. Quenching of the reaction with saturated ammonium chloride solution (40 mL) changed the color to orange. After addition of ethyl acetate (50 mL), the solution was stirred for another 15 min. After filtration, the organic layer was washed with brine, dried over Na₂SO₄ and evacuated. The crude product was purified by flash silica gel chromatography with a gradient of petroleum ether and ethyl acetate to give an orange solid (5.9 mmol, 2.25 g, 59%). Purity (HPLC) > 98%; m.p. 243 °C; ¹H NMR (300 MHz, DMSO-d₆): δ 3.38 (s, 6H), 3.67 (s, 3H), 6.37 (d, ³J = 8.0 Hz, 1H), 6.74 (s, 2H), 6.76 (t, ³J = 7.9 Hz, 1H), 7.09 (t, ³J = 7.6 Hz, 1H), 7.45 (d, ³J = 8.0 Hz, 1H), 7.98 (d, ³J = 1.7 Hz, 1H), 11.03 (s, 1H), 11.89 (bs, 1H); ¹³C NMR (75 MHz, DMSO-d₆): δ 55.5, 60.1, 104.2, 107.6, 112.1, 119.6, 121.5, 122.0, 123.7, 125.5, 128.2, 131.2, 131.8, 136.4, 138.1, 152.2, 172.2, 172.5; LC-MS (ESI): *m/z* 379 [MH]⁺.

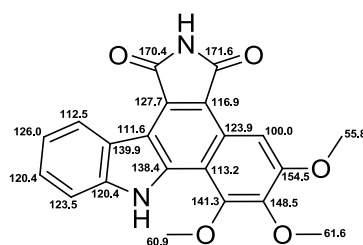
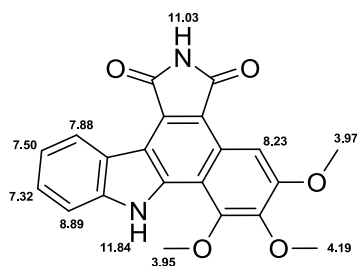


5,6,7-Trimethoxybenzo[*a*]pyrrolo[3,4-*c*]carbazole-1,3(2*H*,8*H*)-dione (57)

RH_004

C₂₁H₁₆N₂O₅ (M_r 376.36)

3-(1*H*-Indol-3-yl)-4-(3,4,5-trimethoxyphenyl)-1*H*-pyrrole-2,5-dione (0.3 mmol, 114 mg) was dissolved in DMSO (20 mL) and irradiated with an LED reactor at 365 nm (5.4 W) for 30 min. Ethyl acetate (100 mL) was added and washed thoroughly with water, dried over Na₂SO₄ and concentrated. Purification by flash silica gel chromatography with a gradient of petroleum ether and ethyl acetate afforded an orange solid (0.03 mmol, 12 mg, 11%). Purity (HPLC) > 98%; m.p. 275 °C; ¹H NMR (300 MHz, DMSO-*d*₆): δ 3.95 (s, 3H), 3.97 (s, 3H), 4.19 (s, 3H), 7.32 (t, ³*J* = 7.6, 1H), 7.50 (t, ³*J* = 7.6, 1H), 7.88 (d, ³*J* = 8.1, 1H), 8.23 (s, 1H), 8.89 (d, ³*J* = 7.8, 1H), 11.03 (s, 1H), 11.84 (s, 1H); ¹³C NMR (75 MHz, DMSO-*d*₆): δ 55.8, 60.9, 61.6, 100.0, 111.6, 112.5, 113.2, 116.9, 120.4, 120.4, 123.5, 123.9, 126.0, 127.7, 138.4, 139.9, 141.3, 148.5, 154.5, 170.4, 171.6; LC-MS (ESI): *m/z* 377 [MH]⁺.

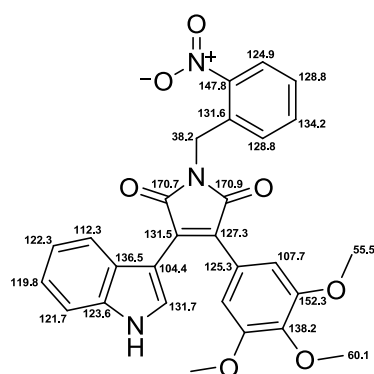
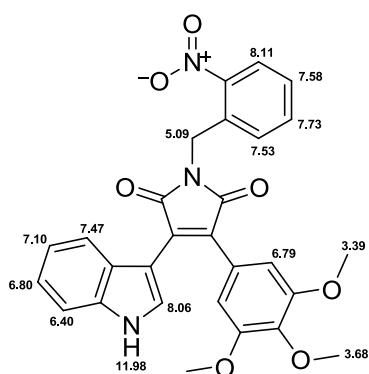


3-(1*H*-Indol-3-yl)-1-(2-nitrobenzyl)-4-(3,4,5-trimethoxyphenyl)-1*H*-pyrrole-2,5-dione (98)

RH_005

C₂₈H₂₃N₃O₇ (M_r 513.15)

3-(1*H*-Indol-3-yl)-4-(3,4,5-trimethoxyphenyl)-1*H*-pyrrole-2,5-dione (0.5 mmol, 189 mg), K₂CO₃ (1 mmol, 138 mg) and 2-nitrobenzyl bromide (0.6 mmol, 130 mg) were dissolved in dry DMF (8 mL). The reaction mixture was stirred at 70 °C for 3 h. After evaporation of the solvent, the crude product was redissolved in ethyl acetate (10 mL), washed with brine, dried over Na₂SO₄ and concentrated. Purification by flash silica gel chromatography with a gradient of petroleum ether and ethyl acetate afforded an orange solid (0.26 mmol, 132 mg, 51%). Purity (HPLC) > 98%; m.p. 209 °C; ¹H NMR (300 MHz, DMSO-d₆): δ 3.39 (s, 6H), 3.68 (s, 3H), 5.09 (s, 2H), 6.40 (d, ³J = 8.1 Hz, 1H), 6.79 (s, 2H), 6.80 (dd, ³J = 7.5 Hz, ⁴J = 0.8 Hz, 1H), 7.10 (dd, ³J = 7.6 Hz, ⁴J = 0.9 Hz, 1H), 7.47 (d, ³J = 8.1 Hz, 1H), 7.53 (dd, ³J = 7.8 Hz, ⁴J = 0.9 Hz, 1H), 7.58 (dd, ³J = 7.8 Hz, ⁴J = 1.3 Hz, 1H), 7.73 (dd, ³J = 7.6 Hz, ⁴J = 1.3 Hz, 1H), 8.06 (d, ³J = 2.9 Hz, 1H), 8.11 (dd, ³J = 8.2 Hz, ⁴J = 1.2 Hz, 1H), 11.98 (d, ³J = 2.1 Hz, 1H); ¹³C NMR (75 MHz, DMSO-d₆): δ 38.2, 55.5, 60.1, 104.4, 107.7, 112.3, 119.8, 121.7, 122.3, 123.6, 124.9, 125.3, 127.3, 128.8, 131.5, 131.6, 131.7, 134.2, 136.5, 138.2, 147.8, 152.3, 170.7, 170.9; LC-MS (ESI): *m/z* 514 [MH]⁺.

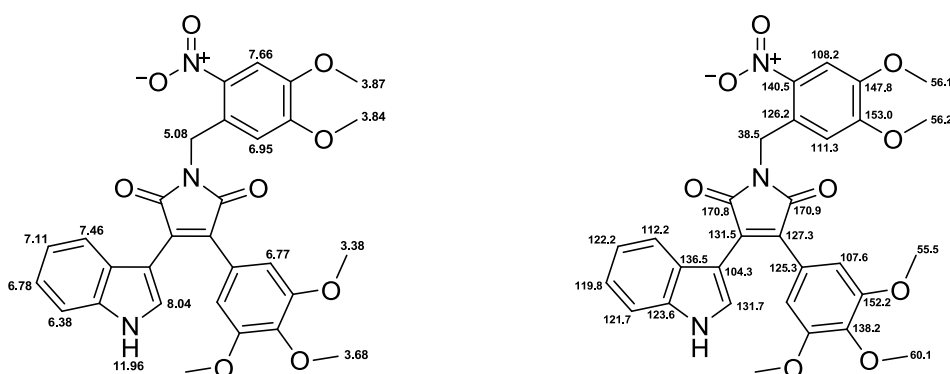


1-(4,5-Dimethoxy-2-nitrobenzyl)-3-(1*H*-indol-3-yl)-4-(3,4,5-trimethoxyphenyl)-1*H*-pyrrole-2,5-dione (99)

RH_013

C₃₀H₂₇N₃O₉ (M_r 573.55)

3-(1*H*-Indol-3-yl)-4-(3,4,5-trimethoxyphenyl)-1*H*-pyrrole-2,5-dione (0.5 mmol, 189 mg) and K₂CO₃ (1 mmol, 138 mg) were dissolved in dry DMF (15 mL). 4,5-dimethoxy-2-nitrobenzyl bromide (0.5 mmol, 138 mg) was dissolved in dry DMF (2 mL) and added dropwise to the reaction mixture. After stirring at room temperature for 2 h, the solvent was evaporated and the crude product was redissolved in ethyl acetate, washed with brine, dried over Na₂SO₄ and concentrated. Purification by flash silica gel chromatography with a gradient of petroleum ether and ethyl acetate afforded an orange solid (0.27 mmol, 155 mg, 54%). Purity (HPLC) > 98%; m.p. 205 °C; ¹H NMR (300 MHz, DMSO-d₆): δ 3.38 (s, 6H), 3.68 (s, 3H), 3.84 (s, 3H), 3.87 (s, 3H), 5.08 (s, 2H), 6.38 (d, ³J = 8.1 Hz, 1H), 6.77 (s, 2H), 6.78 (t, ³J = 7.3 Hz, 1H), 6.95 (s, 1H), 7.11 (t, ³J = 7.5 Hz, 1H), 7.46 (d, ³J = 8.0 Hz, 1H), 7.66 (s, 1H), 8.04 (d, ³J = 2.6 Hz, 1H), 11.96 (s, 1H); ¹³C NMR (75 MHz, DMSO-d₆): δ 38.5, 55.5, 56.1, 56.2, 60.1, 104.3, 107.6, 108.2, 111.3, 112.2, 119.8, 121.7, 122.2, 123.6, 125.3, 126.2, 127.3, 131.5, 131.7, 136.5, 138.2, 140.5, 147.8, 152.2, 153.0, 170.8, 170.9; LC-MS (ESI): *m/z* 574 [MH]⁺.

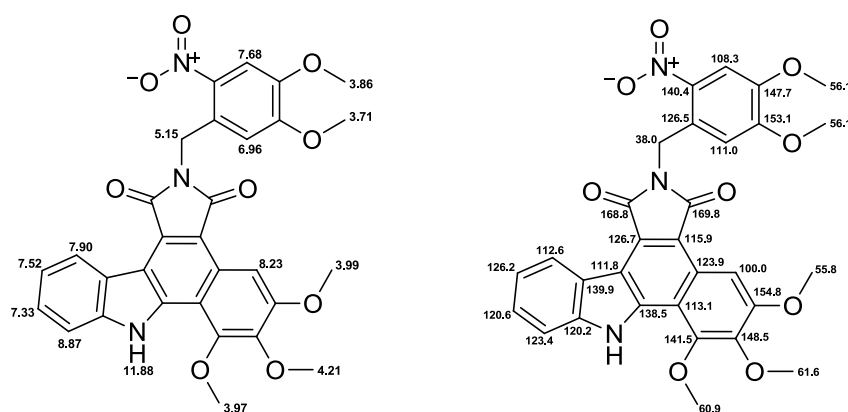


2-(4,5-Dimethoxy-2-nitrobenzyl)-5,6,7-trimethoxybenzo[*a*]pyrrolo[3,4-*c*]carbazole-1,3(2*H*,8*H*)-dione (100)

RH_049

C₃₀H₂₅N₃O₉ (M_r 571.53)

5,6,7-Trimethoxybenzo[*a*]pyrrolo[3,4-*c*]carbazole-1,3(2*H*,8*H*)-dione (0.13 mmol, 28 mg) and K₂CO₃ (0.38 mmol, 52 mg) were dissolved in dry DMF (5 mL). 4,5-Dimethoxy-2-nitrobenzyl bromide (0.13 mmol, 33 mg) was dissolved in dry DMF (2 mL) and added dropwise to the reaction mixture. After stirring at room temperature for 2 h, the solvent was evaporated and the crude product redissolved in ethyl acetate, washed with brine, dried over Na₂SO₄ and concentrated. Recrystallization from ethyl acetate gave an orange solid (0.03 mmol, 19 mg, 26%). Purity (HPLC) > 98%; m.p. 283 °C; ¹H NMR (300 MHz, DMSO-*d*₆): δ 3.71 (s, 3H), 3.86 (s, 3H), 3.97 (s, 3H), 3.99 (s, 3H), 4.21 (s, 3H), 5.15 (s, 2H), 6.96 (s, 1H), 7.33 (t, ³*J* = 7.4 Hz, 1H), 7.52 (t, ³*J* = 7.4 Hz, 1H), 7.68 (s, 1H), 7.90 (d, ³*J* = 7.6 Hz, 1H), 8.23 (s, 1H), 8.87 (d, ³*J* = 7.6 Hz, 1H), 11.88 (s, 1H); ¹³C NMR (75 MHz, DMSO-*d*₆): δ 38.0, 55.8, 56.1, 60.9, 61.6, 100.0, 108.3, 111.0, 111.8, 112.6, 113.1, 115.9, 120.2, 120.6, 123.4, 123.9, 126.2, 126.5, 126.7, 138.5, 139.9, 140.4, 141.5, 147.7, 148.5, 153.1, 154.8, 168.8, 169.8; LC-MS (ESI): *m/z* 571 [MH]⁺.

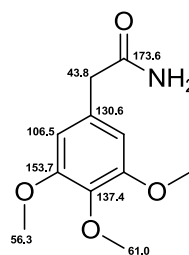
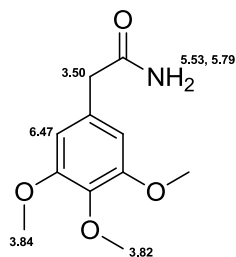


2-(3,4,5-Trimethoxyphenyl)acetamide (102)

RH_001

 $C_{11}H_{15}NO_4$ (M_r 225.24)

2-(3,4,5-Trimethoxyphenyl)acetic acid (20 mmol, 4.6 g) was dissolved in anhydrous THF (30 mL). After addition of thionyl chloride (40 mmol, 3 mL) and a catalytic amount of DMF, the reaction mixture was heated to 40 °C until gas formation was completed (30 min). Subsequently, the solvent and excessive thionyl chloride were removed under reduced pressure. This step was repeated after addition of THF (10 mL). The remaining brown oil was dissolved in DCM (50 mL) and cooled to 0 °C. Next, ammonia solution (25%, 10 mL) was added to the mixture and stirred for 1 h at room temperature. After addition of hydrochloric acid (1M, 20 mL), the organic layer was washed with brine and dried over Na_2SO_4 . Evacuation and recrystallization from ethanol afforded grey needles (16.8 mmol, 3.86 g, 84%). Purity (HPLC) > 98%; m.p. 124 °C; 1H NMR (300 MHz, $CDCl_3$): δ 3.50 (s, 2H), 3.82 (s, 3H), 3.84 (s, 6H), 5.53 (bs, 1H), 5.79 (bs, 1H), 6.47 (s, 2H); ^{13}C NMR (75 MHz, $CDCl_3$): δ 43.8, 56.3, 61.0, 106.5, 130.6, 137.4, 153.7, 173.6; LC-MS (ESI): m/z 226 $[MH]^+$.



Ethyl 2-(1*H*-indol-3-yl)-2-oxoacetate (104)

RH_002

C₁₂H₁₁NO₃ (M_r 217.22)

Indole (40 mmol, 4.8 g) was dissolved in dry DCM (70 mL) under nitrogen atmosphere and stirred at 0 °C. After dropwise addition of diethylaluminium chloride solution (1M in hexane, 60 mmol, 60 mL), the reaction mixture was stirred for 30 min at 0 °C. Subsequently, ethyl oxalyl chloride (60 mmol, 6.8 mL) was added dropwise followed by stirring for further 3 h. In the next step, ice was carefully added to the reaction mixture for hydrolysis. The organic layer was washed with saturated ammonium chloride solution and brine, dried over Na₂SO₄ and concentrated. Purification by flash silica gel chromatography with a gradient of petroleum ether and ethyl acetate afforded light-pink needles (21.9 mmol, 4.75 g, 55%). Purity (HPLC) > 98%; m.p. 186 °C; ¹H NMR (300 MHz, CDCl₃): δ 1.34 (t, ³J = 7.1 Hz, 3H), 4.36 (q, ³J = 7.1, 2H), 7.24-7.33 (m, 2H), 7.53-7.58 (m, 1H), 8.14-8.19 (m, 1H), 8.42 (d, ³J = 3.3, 1H), 12.38 (bs, 1H); ¹³C NMR (75 MHz, CDCl₃): δ 13.9, 61.6, 112.4, 112.7, 121.1, 122.8, 123.8, 125.5, 136.7, 138.2, 163.6, 179.1; LC-MS (ESI): *m/z* 218 [MH]⁺.

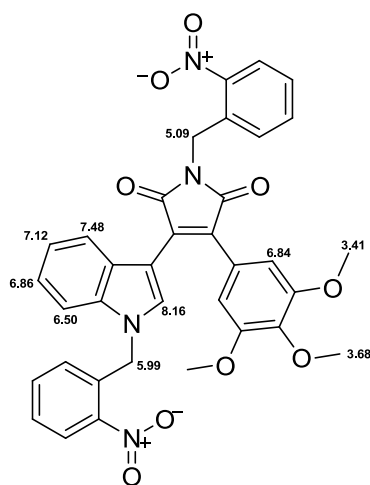


1-(2-Nitrobenzyl)-3-(1-(2-nitrobenzyl)-1*H*-indol-3-yl)-4-(3,4,5-trimethoxyphenyl)-1*H*-pyrrole-2,5-dione (105)

RH_006

C₃₅H₂₈N₄O₉ (M_r 648.62)

3-(1*H*-Indol-3-yl)-4-(3,4,5-trimethoxyphenyl)-1*H*-pyrrole-2,5-dione (0.5 mmol, 189 mg), K₂CO₃ (1 mmol, 138 mg) and 2-nitrobenzyl bromide (0.6 mmol, 130 mg) were dissolved in dry DMF (8 mL). The reaction mixture was stirred at 70 °C for 3 h. After evaporation of the solvent, the crude product was redissolved in ethyl acetate (10 mL), washed with brine, dried over Na₂SO₄ and concentrated. Purification by flash silica gel chromatography with a gradient of petroleum ether and ethyl acetate afforded an orange solid (0.12 mmol, 94 mg, 24%). Purity (HPLC) > 98%; m.p. 127 °C; ¹H NMR (300 MHz, DMSO-d₆): δ 3.41 (s, 6H), 3.68 (s, 3H), 5.09 (s, 2H), 5.99 (s, 2H), 6.50 (d, ³J = 8.0 Hz, 1H), 6.53-6.56 (m, 1H), 6.84 (s, 2H), 6.86 (ddd, ³J = 7.9 Hz, ³J = 7.1 Hz, ⁴J = 0.8 Hz, 1H), 7.12 (ddd, ³J = 8.2 Hz, ³J = 7.2 Hz, ⁴J = 1.0 Hz, 1H), 7.48 (d, ³J = 8.3 Hz, 1H), 7.52-7.61 (m, 4H), 7.73 (td, ³J = 7.6 Hz, ⁴J = 1.3 Hz, 1H), 8.10 (dd, ³J = 8.1 Hz, ⁴J = 1.2 Hz, 1H), 8.16 (s, 1H), 8.15-8.19 (m, 1H); ¹³C NMR (75 MHz, DMSO-d₆): δ 38.3, 47.1, 55.4, 60.1, 104.5, 107.5, 111.1, 120.4, 122.0, 122.7, 124.2, 124.9, 125.0, 125.1, 127.5, 128.5, 128.8, 128.8, 128.9, 130.8, 131.5, 133.3, 134.1, 134.1, 134.7, 136.6, 138.3, 147.3, 147.8, 152.3, 170.4, 170.7; LC-MS (ESI): *m/z* 649 [MH]⁺.

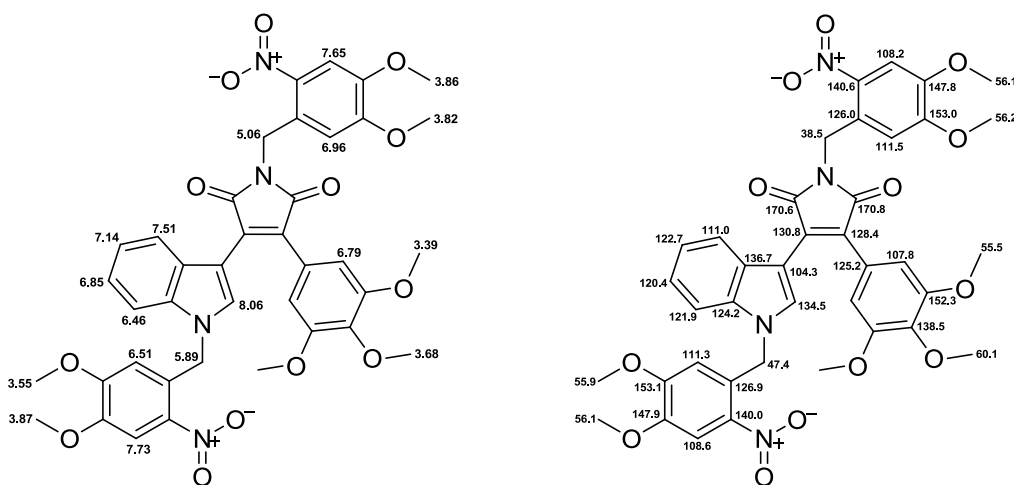


1-(4,5-Dimethoxy-2-nitrobenzyl)-3-(1-(4,5-dimethoxy-2-nitrobenzyl)-1*H*-indol-3-yl)-4-(3,4,5-trimethoxyphenyl)-1*H*-pyrrole-2,5-dione (106)

RH_014

C₃₉H₃₆N₄O₁₃ (M_r 768.72)

3-(1*H*-Indol-3-yl)-4-(3,4,5-trimethoxyphenyl)-1*H*-pyrrole-2,5-dione (0.5 mmol, 189 mg) and K₂CO₃ (1 mmol, 138 mg) were dissolved in dry DMF (15 mL). 4,5-Dimethoxy-2-nitrobenzyl bromide (0.5 mmol, 138 mg) was dissolved in dry DMF (2 mL) and added dropwise to the reaction mixture. After stirring at room temperature for 2 h, the solvent was evaporated and the crude product redissolved in ethyl acetate, washed with brine, dried over Na₂SO₄ and evacuated. Purification by flash silica gel chromatography with a gradient of petroleum ether and ethyl acetate afforded an orange solid (0.10 mmol, 73 mg, 19%). Purity (HPLC) > 98%; m.p. 228 °C; ¹H NMR (300 MHz, DMSO-*d*₆): δ 3.39 (s, 6H), 3.55 (s, 3H), 3.68 (s, 3H), 3.82 (s, 3H), 3.86 (s, 3H), 3.87 (s, 3H), 5.06 (s, 2H), 5.89 (s, 2H), 6.46 (d, ³*J* = 8.0 Hz, 1H), 6.51 (s, 1H), 6.79 (s, 2H), 6.85 (t, ³*J* = 7.4 Hz, 1H), 6.96 (s, 1H), 7.14 (t, ³*J* = 7.7 Hz, 1H), 7.51 (d, ³*J* = 8.3 Hz, 1 H), 7.65 (s, 1H), 7.73 (s, 1H), 8.06 (s, 1H); ¹³C NMR (75 MHz, DMSO-*d*₆): δ 38.5, 47.4, 55.5, 55.9, 56.1, 56.2, 60.1, 104.3, 107.8, 108.2, 108.6, 111.0, 111.3, 111.5, 120.4, 121.9, 122.7, 124.2, 125.2, 126.0, 126.9, 128.4, 130.8, 134.5, 136.7, 138.5, 140.0, 140.6, 147.8, 147.9, 152.3, 153.0, 153.1, 170.6, 170.8; LC-MS (ESI): *m/z* 769 [MH]⁺.



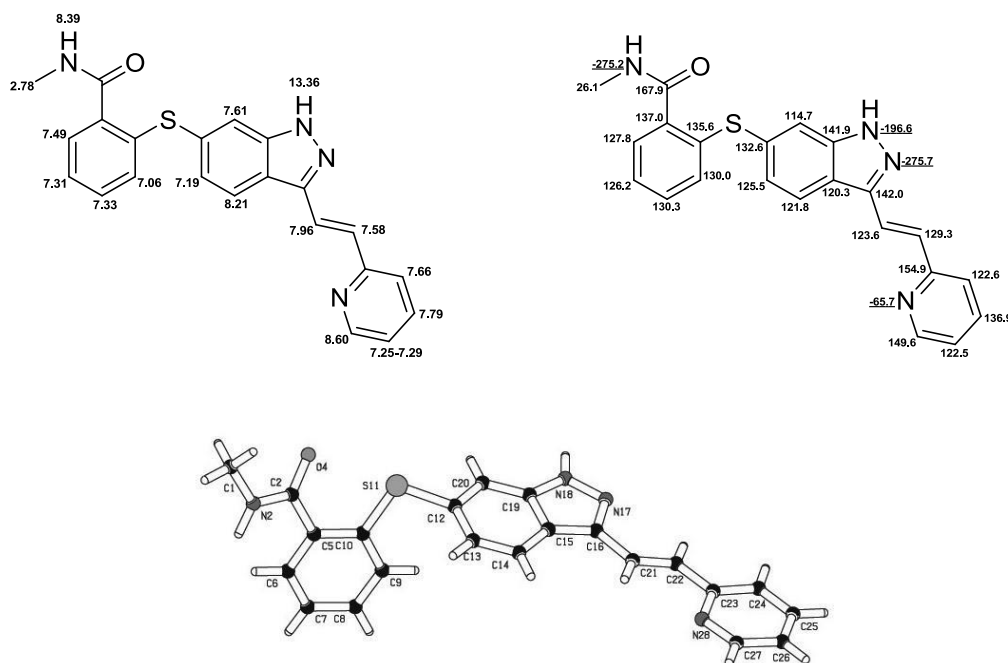
Photoswitchable axitinib

(E)-axitinib, (E)-N-methyl-2-((3-(2-(pyridin-2-yl)vinyl)-1H-indazol-6-yl)thio)benzamide (19), INN: axitinib

JW_01

C₂₂H₁₈N₄OS (M_r 386.47)Analytical characterization was partially performed by Jantje Weber.⁸⁹

The pale yellow compound was purchased from LC Laboratories, Woburn, MA, USA. Purity (HPLC) > 98%; m.p. 219 °C; ¹H NMR (300 MHz, DMSO-d₆): δ 2.78 (d, ³J = 4.5 Hz, 3H), 7.06 (dd, ³J = 7.3 Hz, ⁴J = 1.7 Hz, 1H), 7.19 (dd, ³J = 8.5 Hz, ⁴J = 1.4 Hz, 1H), 7.25-7.29 (m, 1H), 7.31 (dd, ³J = 7.3 Hz, ⁴J = 1.7 Hz, 1H), 7.33 (dd, ³J = 7.3 Hz, ⁴J = 1.9 Hz, 1H), 7.49 (dd, ³J = 7.3 Hz, ⁴J = 1.9 Hz, 1H), 7.58 (d, ³J = 16.4 Hz, 1H), 7.61 (s, 1H), 7.66 (d, ³J = 7.8 Hz, 1H), 7.79 (ddd, ³J = 7.8 Hz, ³J = 7.6 Hz, ⁴J = 1.8 Hz, 1H), 7.96 (d, ³J = 16.4 Hz, 1H), 8.21 (d, ³J = 8.5 Hz, 1H), 8.39 (q, ³J = 4.5 Hz, 1H), 8.60 (ddd, ³J = 4.7 Hz, ⁴J = 1.8 Hz, ⁵J = 0.9 Hz, 1H), 13.36 (s, 1H); ¹³C NMR (75 MHz, DMSO-d₆): δ 26.1, 114.7, 120.3, 121.8, 122.5, 122.6, 123.6, 125.5, 126.2, 127.8, 129.3, 130.0, 130.3, 132.6, 135.6, 136.9, 137.0, 141.9, 142.0, 149.6, 154.9, 167.9; ¹⁵N NMR (30 MHz, DMSO-d₆): δ -275.7, -275.2, -196.6, -65.7; LC-MS (ESI): m/z 387 [MH]⁺.



Molecular structure determined by X-ray crystallography: CCDC 1419084

(Z)-axitinib (19a/b), (Z)-N-methyl-2-((3-(2-(pyridin-2-yl)vinyl)-1H-indazol-6-yl)thio)benzamide (19a) and (Z)-N-methyl-2-((3-(2-(pyridin-2-yl)vinyl)-2H-indazol-6-yl)thio)benzamide

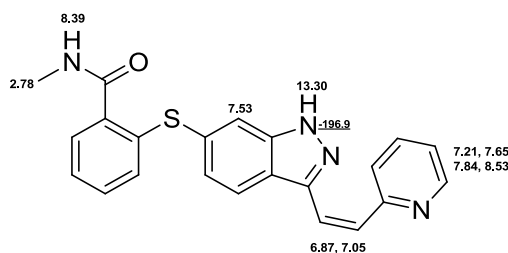
JW_02

C₂₂H₁₈N₄OS (M_r 386.47)

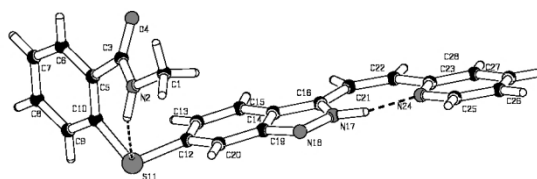
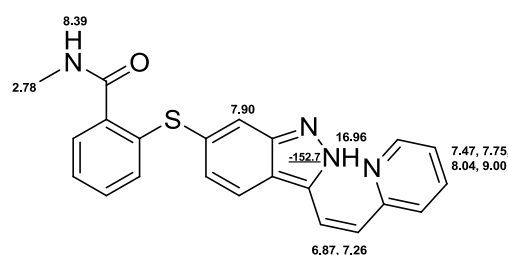
Synthesis and analytical characterization was partially performed by Jantje Weber.⁸⁹

(E)-Axitinib (100 mg, 0.26 mmol) was dissolved in DMSO (10 mL) and the solution was stirred and irradiated (365 nm, 5.4 W) for 15 min. Subsequently, ethyl acetate (100 mL) was added. DMSO was removed by washing the organic phase thoroughly with water. Next, the organic layer was dried over Na₂SO₄, filtered and concentrated. Flash silica gel chromatography with a gradient of petroleum ether and ethyl acetate afforded a yellow solid (21 mg, 0.05 mmol, 21%). Purity (HPLC) 97%; m.p. 174 °C; LC-MS (ESI): *m/z* 387 [MH]⁺.

1H-tautomer



2H-tautomer



Molecular structure determined by X-ray crystallography: CCDC 1419085

5.4 BIOLOGICAL EVALUATION

5.4.1 Kinase Assays (Kd values)

Caged vemurafenib: BRAF^{V600E}

Binding affinities of **44**, **58**, **59**, and **60** toward BRAF^{V600E} were measured in the *Kd*ELECTSM assay.¹⁴³ KINOMEscanTM is a competition binding assay that quantitatively measures the ability of a compound to compete with an immobilized active-site directed ligand. Binding constants (Kd values) were calculated from duplicate 11-point dose-response curves. The highest tested compound concentration was 30 μ M. The 3-fold serial dilution of each tested inhibitor was prepared in 100% DMSO. The final DMSO concentration in the assay was 1%.

Analyses were performed by DiscoverRx (San Diego, CA, USA).

5.4.2 Kinase Assays (IC₅₀ values)

Caged diarylmaleimides resp. carbazole and photoswitchable axitinib: VEGFR2

The VEGFR2 IC₅₀ profile for **55**, **57**, **99**, **100**, **19**, and **19a/b** was determined using VEGFR2 protein kinase by a radiometric ³³PanQinase[®] assay¹²² and a luminescent ADP-GloTM assay (Promega)¹⁴⁴. IC₅₀ values were measured by testing 10 semi-log concentrations of each compound in the range from 1 x 10⁻⁰⁴ M to 3 x 10⁻⁰⁹ M, in singlicate. Prior to testing, the compounds were dissolved to 1 x 10⁻⁰² M stock solutions in 100% DMSO. The final DMSO concentration in the reaction cocktails was 1% in all cases.

Analyses were performed by ProQinase (Freiburg, Germany).

Photoswitchable axitinib: PDGFR β

PDGFR β inhibition curves of **19** and **19a/b** were determined by a luminescent PDGFR β kinase assay using an ADP-Glo™ assay kit (Promega).¹⁴⁴ The compounds were dissolved in 100% DMSO and tested in a range of 1×10^{-11} M to 1×10^{-6} M, in duplicate. The reaction cocktails were incubated at 20 °C for 60 min. ATP concentration was 10 μ M and the final DMSO concentration was 1%.

Analyses were performed by Boris Pinchuk¹²³ and Christian Renn¹³².

5.4.3 Kinase Profiling

Caged vemurafenib

Compounds **44**, **58**, and **60** were screened against 140 kinases in the Premier Screen.¹⁴⁵ The used method was a radioactive filter binding assay using ³³P ATP, for details see references ^{146,147}. The substances were dissolved in DMSO at a tested concentration of 10 μ M. The mean percentage residual kinase activity and standard deviations of assay duplicates were determined.

Analyses were performed by the International Center for Kinase Profiling at the University of Dundee, UK.

Caged diarylmaleimides resp. carbazole

Compounds **55** and **57** were screened against 79 kinases. The used method was a radioactive filter binding assay using ³³P ATP, for details see references ^{146,147}. The substances were dissolved in DMSO at tested concentrations of 0.1 μ M and 1 μ M. The mean percentage residual kinase activity and standard deviations of assay duplicates were determined.

Analyses were performed by the International Center for Kinase Profiling at the University of Dundee, UK.

Photoswitchable axitinib

Kinase inhibition profiles of **19** and **19a/b** were determined by measuring residual activity values in duplicate in 300 wild-type protein kinase assays. A radiometric ³³PanQinase[®] assay was used for measuring the kinase activity.¹²² The substances were dissolved in 100% DMSO. The reaction cocktails were incubated at 30 °C for 60 min at a concentration of 1 μM. The final DMSO concentration was 1%.

Analyses were performed by ProQinase (Freiburg, Germany).

5.4.4 Cell Culture

Caged vemurafenib: SKMel13 cells

SKMel13 cells were kindly provided by Dr. Kumara Dissanayake from the MRC Protein Phosphorylation Unit, College of Life Sciences, Dundee, UK. Cells were grown in RPMI 1640 Glutamax with 10% FCS. All cells were incubated in a 5% CO₂ humidified atmosphere at 37 °C.

Cell culture was performed by Boris Pinchuk.¹¹⁵

Caged diarylmaleimides resp. carbazole and photoswitchable axitinib: NIH/3T3 and PC-3 cells

NIH/3T3 cells were kindly provided by Dr. Athena Chalaris-Rissmann from the Biochemistry Institute, University of Kiel, Germany. PC-3 cells were purchased from CLS Cell Lines Service GmbH, Germany. NIH/3T3 cells were grown in DMEM medium with 2 mM *L*-Glutamine, 1 mM Sodium Pyruvate and 10% FCS. PC-3 cells were grown in DMEM:Hams F12 (1:1) medium with 5% FCS. Both cell lines were incubated in a 5% CO₂ humidified atmosphere at 37 °C.

Cell culture was performed by Boris Pinchuk¹²³ and Christian Renn¹³².

5.4.5 Proliferative Assays

Caged vemurafenib, caged diarylmaleimides and carbazole resp. photoswitchable axitinib

The cells were grown in cell flasks until approximately 90% confluence and then seeded to give 7000 resp. 15000 cells in 100 μ L per well into 96-well CulturePlatesTM (PerkinElmer, US). In addition to the test plates, one plate was prepared for reference measurement at day zero. All plates were incubated for 24 h at 37 °C in a humidified atmosphere with 5% CO₂. Compounds **44**, **58**, **59**, **60**, **55**, **57**, **99**, **100**, **19**, and **19a/b** were dissolved in 100% DMSO (v/v) and added to the test plates. The final DMSO concentration in the assay was 0.5% (v/v). Viability of the cells in the day zero control plates were determined on the same day without adding any compounds. For viability measurement the resazurin assay was used. The shift in the fluorescence signal was measured at the LS55 Fluorescence spectrometer (PerkinElmer, Waltham, US). For the photoactivation experiments the test plates were irradiated at 365 nm for 5 min (LED source: 8x Nichia NCSU033B, Sahlmann Photochemical Solutions, 50%, 1.8 W). Test plates were incubated for further 48 h and cell viability was defined as described above. Measured raw data was converted into percent of cell growth by using the high control (0.5% DMSO (v/v) without compound) and the day zero control. For dose-response studies, 11 different concentrations of compounds were tested in duplicates. IC₅₀ values were calculated using the 4-parameter logistic fit option of GraphPad Prism 5.

Proliferation assays were performed by Boris Pinchuk^{115,123} and Christian Renn¹³².

5.4.6 Stability in Cellular Medium

Caged vemurafenib

A vemurafenib (**44**) solution (0.01 mM) was prepared in Dulbecco's Modified Eagle Medium (DMEM) with 2 mM *L*-glutamine, 1 mM sodium pyruvate and 10% DMSO. The probe was incubated in a 5% CO₂ humidified atmosphere at 37 °C for 48 h. At different time points aliquots were taken, diluted with methanol (1:2), and analyzed by HPLC. Proteins were removed prior to HPLC analysis by centrifugation at 9500g for 5 min (Mikro 200, Hettich).

Analyses were performed by Boris Pinchuk.¹¹⁵

Photoswitchable axitinib

A (*Z*)-axitinib solution (**19**, 1 mM) was prepared in minimum essential medium (MEM) with and without fetal bovine serum (FBS). For that purpose (*Z*)-axitinib was dissolved in DMSO and diluted with MEM. The final DMSO concentration was 0.5%. The solutions were incubated at 37 °C for up to 180 h. At different time points aliquots were taken, diluted with methanol (1:2) and analyzed by HPLC. In the FBS samples, proteins were removed prior to HPLC analysis by centrifugation at 9500g for 5 min (Mikro 200, Hettich).

Analyses were performed by Christian Renn.¹³²

5.4.7 Western Blot Analyses

Caged vemurafenib

Cells were treated with the indicated concentrations for 1 h at 37 °C. The same experiments were repeated with irradiation. 30 min after addition to the cells, the compound solutions of **44**, **58**, and **60** were irradiated at 365 nm (1.8 W) for 5 min. Cells were lysed and lysates immunoblotted with the indicated antibodies. The lysis buffer contained both phosphatase and protease inhibitors. Similar results were obtained in duplicate experiments.

Primary antibodies

- p44/42 MAPK (Erk1/2) (137F5) rabbit m-ab (t-Erk) Ref: #4695S Cell signaling technology (CST)
- P-p44/42 MAPK (T202/Y204) (197G2) rabbit m-ab (p-Erk) Ref: #4377S CST
- P-Akt (T308) (244F9) rabbit mAb Ref: #4056S CST
- Anti-PKB alpha S742B 1st Bleed (t-Akt), 1 x 0,05 mg; 0,28 mg/mL (courtesy by the lab of Prof. Dario Alessi, MRC, Dundee, Scotland)

Secondary antibodies

- Anti-rabbit IgG, HRP-linked Antibody Ref: #7074P2 CST
- Rabbit anti-sheep, HRP-linked Antibody (courtesy by the lab of Prof. Dario Alessi, MRC, Dundee, Scotland)

Western blot analyses were performed by Boris Pinchuk.¹¹⁵

Photoswitchable axitinib

Cells were treated with the indicated concentrations of test compounds **19** and **19a/b** for 1 h at 37 °C. Cells were lysed and lysates immunoblotted with the indicated antibodies. The lysis buffer contained both phosphatase and protease inhibitors. Similar results were obtained in duplicate experiments.

Primary antibodies

- p44/42 MAPK (Erk1/2) (137F5) rabbit mAb (t-Erk), Ref: #4695S, CST
- P-p44/42 MAPK (T202/Y204) (197G2) rabbit mAb (p-Erk), Ref: #4370P, CST
- P-Akt (Thr308) (D25E6) XP[®] Rabbit mAb (p-Akt), Ref: #13038S, CST
- Anti-PKB alpha S742B 1st Bleed (t-Akt), 1 x 0,05 mg; 0,28 mg/mL (courtesy by the lab of Prof. Dario Alessi, MRC, Dundee, Scotland)
- PDGF Receptor β (28E1) Rabbit mAb (t-PDGFR), Ref #3169P, CST
- Phospho-PDGF Receptor β (Tyr751) (C63G6) Rabbit mAb (p-PDGFR), Ref #4549P, CST

Secondary antibodies

- Anti-rabbit IgG, HRP-linked Antibody, Ref: #7074P2, CST
- Rabbit anti-sheep, HRP-linked Antibody, (courtesy by the lab of Prof. Dario Alessi, MRC, Dundee, Scotland)

Western blot analyses were performed by Christian Renn.¹³²

6. REFERENCES

1. Klán, P. & Wirz, J. *Photochemistry of organic compounds. From concepts to practice* (Wiley, Chichester, U.K. 2009).
2. Ellis-Davies, Graham C R. Caged compounds: photorelease technology for control of cellular chemistry and physiology. *Nat. Methods* **4**, 619–628 (2007).
3. Szymański, W. Beierle, J. M. Kistemaker, Hans A V, Velema, W. A. & Feringa, B. L. Reversible photocontrol of biological systems by the incorporation of molecular photoswitches. *Chem. Rev.* **113**, 6114–6178 (2013).
4. Mayer, G. & Heckel, A. Biologically active molecules with a "light switch". *Angew. Chem. Int. Ed. Engl.* **45**, 4900–4921 (2006).
5. Velema, W. A. Szymanski, W. & Feringa, B. L. Photopharmacology: beyond proof of principle. *J. Am. Chem. Soc.* **136**, 2178–2191 (2014).
6. Levitzki, A. Tyrosine Kinase Inhibitors: Views of Selectivity, Sensitivity, and Clinical Performance. *Annu. Rev. Pharmacol. Toxicol.* **53**, 161–185 (2013).
7. Dar, A. C. & Shokat, K. M. The Evolution of Protein Kinase Inhibitors from Antagonists to Agonists of Cellular Signaling. *Annu. Rev. Biochem.* **80**, 769–795 (2011).
8. Fang, Z. Grütter, C. & Rauh, D. Strategies for the Selective Regulation of Kinases with Allosteric Modulators: Exploiting Exclusive Structural Features. *ACS Chem. Biol.* **8**, 58–70 (2013).
9. Dormán, G. & Prestwich, G. D. Using photolabile ligands in drug discovery and development. *Trends Biotechnol.* **18**, 64–77 (2000).
10. Klán, P. *et al.* Photoremovable Protecting Groups in Chemistry and Biology: Reaction Mechanisms and Efficacy. *Chem. Rev.* **113**, 119–191 (2013).
11. Deiters, A. Principles and Applications of the Photochemical Control of Cellular Processes. *ChemBioChem* **11**, 47–53 (2010).

12. Kaplan, J. H. Forbush, B. & Hoffman, J. F. Rapid photolytic release of adenosine 5'-triphosphate from a protected analog: utilization by the sodium:potassium pump of human red blood cell ghosts. *Biochemistry* **17**, 1929–1935 (1978).
13. Pelliccioli, A. P. & Wirz, J. Photoremovable protecting groups: reaction mechanisms and applications. *Photochem. Photobiol. Sci.* **1**, 441–458 (2002).
14. Goeldner, M. & Givens, R. *Dynamic studies in biology. Phototriggers, photoswitches and caged biomolecules* (Wiley-VCH, Weinheim, 2005).
15. Falvey, D. E. & Sundararajan, C. Photoremovable protecting groups based on electron transfer chemistry. *Photochem. Photobiol. Sci.* **3**, 831 (2004).
16. Gaplovsky, M. *et al.* Photochemical reaction mechanisms of 2-nitrobenzyl compounds: 2-Nitrobenzyl alcohols form 2-nitroso hydrates by dual proton transfer. *Photochem. Photobiol. Sci.* **4**, 33 (2005).
17. Il'ichev, Y. V. Schwörer, M. A. & Wirz, J. Photochemical Reaction Mechanisms of 2-Nitrobenzyl Compounds: Methyl Ethers and Caged ATP. *J. Am. Chem. Soc.* **126**, 4581–4595 (2004).
18. Lusic, H. & Deiters, A. A New Photocaging Group for Aromatic N -Heterocycles. *Synthesis* **2006**, 2147–2150 (2006).
19. Šolomek, T. Mercier, S. Bally, T. & Bochet, C. G. Photolysis of ortho-nitrobenzyl derivatives: the importance of the leaving group. *Photochem. Photobiol. Sci.* **11**, 548 (2012).
20. Morckel, A. R. *et al.* A photoactivatable small-molecule inhibitor for light-controlled spatiotemporal regulation of Rho kinase in live embryos. *J. Cell Sci.* **125**, e1 (2012).
21. Li, H. Hah, J.-M. & Lawrence, D. S. Light-mediated liberation of enzymatic activity: "small molecule" caged protein equivalents. *J. Am. Chem. Soc.* **130**, 10474–10475 (2008).
22. Curley, K. & Lawrence, D. S. Caged Regulators of Signaling Pathways. *Pharmacol. Ther.* **82**, 347–354 (1999).

23. Veldhuyzen, W. F. Nguyen, Q. McMaster, G. & Lawrence, D. S. A light-activated probe of intracellular protein kinase activity. *J. Am. Chem. Soc.* **125**, 13358–13359 (2003).
24. Wang, Q. Dai, Z. Cahill, S. M. Blumenstein, M. & Lawrence, D. S. Light-regulated sampling of protein tyrosine kinase activity. *J. Am. Chem. Soc.* **128**, 14016–14017 (2006).
25. Zindler, M. *et al.* Design, Synthesis, and Characterization of a Photoactivatable Caged Prodrug of Imatinib. *ChemMedChem* (2015).
26. Liu, R. S. H. & Asato, A. E. The primary process of vision and the structure of bathorhodopsin: A mechanism for photoisomerization of polyenes. *Proc. Natl. Acad. Sci. U.S.A.* 259–263 (1985).
27. Berg, J. M. Tymoczko, J. L. & Stryer, L. *Biochemistry. 5th edition. Chapter 19, The Light Reactions of Photosynthesis.* (W. H. Freeman, New York, 2002).
28. M. Nič, J. Jiráč, B. Košata, A. Jenkins & A. McNaught (eds.). *IUPAC Compendium of Chemical Terminology* (IUPAC, Research Triangle Park, NC, 2009).
29. Hamon, F. Djedaini-Pilard, F. Barbot, F. & Len, C. Azobenzenes—synthesis and carbohydrate applications. *Tetrahedron* **65**, 10105–10123 (2009).
30. Ferreira, R. Nilsson, J. R. Solano, C. Andréasson, J. & Grøtli, M. Design, Synthesis and Inhibitory Activity of Photoswitchable RET Kinase Inhibitors. *Sci. Rep.* **5**, 9769 (2015).
31. Bruijn, P. de *et al.* Bioanalytical method for the quantification of sunitinib and its n-desethyl metabolite SU12662 in human plasma by ultra performance liquid chromatography/tandem triple-quadrupole mass spectrometry. *J. Pharm. Biomed. Anal.* **51**, 934–941 (2010).
32. Sparidans, R. W. Iusuf, D. Schinkel, A. H. Schellens, J. H. & Beijnen, J. H. Liquid chromatography-tandem mass spectrometric assay for the light sensitive tyrosine kinase inhibitor axitinib in human plasma. *J. Chromatogr. B* **877**, 4090–4096 (2009).
33. Matsumura, Y. & Ananthaswamy, H. N. Toxic effects of ultraviolet radiation on the skin. *Toxicol. Appl. Pharmacol.* **195**, 298–308 (2004).

34. Hunnius, C. & Ammon, H. P. T. *Hunnius Pharmazeutisches Wörterbuch*. 9th ed. (de Gruyter, Berlin [u.a.], 2004).
35. Albini, A. & Fagnoni, M. *Handbook of synthetic photochemistry* (Wiley-VCH, Weinheim, 2010).
36. El-Mofty, A.-M. A preliminary clinical report on the treatment of leucodermia with *Ammi majus* Linn. *J. Egypt. Med. Assoc.* **31**, 651–665 (1948).
37. El-Mofty, A.-M. Observations on the use of *Ammi Majus* Linn. in Vitiligo. *Br. J. Dermatol.* **64**, 431–441 (1952).
38. Parrish, J. A. Fitzpatrick, T. B. Tanenbaum, L. & Pathak, M. A. Photochemotherapy of psoriasis with oral methoxsalen and longwave ultraviolet light. *N. Engl. J. Med.* **291**, 1207–1211 (1974).
39. Straub, K. Kanne, D. Hearst, J. E. & Rapoport, H. Isolation and characterization of pyrimidine-psoralen photoadducts from DNA. *J. Am. Chem. Soc.* **103**, 2347–2355 (1981).
40. Weelden, H. Baart de la Faille, H. Young, E. & Leun J. C. A new development in UVB phototherapy of psoriasis. *Br. J. Dermatol.* **119**, 11–19 (1988).
41. Studniberg, H. M. & Weller, P. PUVA, UVB, psoriasis, and nonmelanoma skin cancer. *J. Am. Acad. Dermatol.* **29**, 1013–1022 (1993).
42. Wu, P. Nielsen, T. E. & Clausen, M. H. FDA-approved small-molecule kinase inhibitors. *Trends Pharmacol. Sci.* **36**, 422–439 (2015).
43. Johnson, G. L. Dohlman, H. G. & Graves, L. M. MAPK kinase kinases (MKKKs) as a target class for small-molecule inhibition to modulate signaling networks and gene expression. *Curr. Opin. Chem. Biol.* **9**, 325–331 (2005).
44. Ishii, H. Koya, D. & King, G. L. Protein kinase C activation and its role in the development of vascular complications in diabetes mellitus. *J. Mol. Med.* **76**, 21–31 (1997).
45. Zhang, J. Yang, P. L. & Gray, N. S. Targeting cancer with small molecule kinase inhibitors. *Nat. Rev. Cancer* **9**, 28–39 (2009).

46. Fabbro, D. 25 years of small molecular weight kinase inhibitors: potentials and limitations. *Mol. Pharmacol.* **87**, 766–775 (2015).
47. Savage, D. G. & Antman, K. H. Imatinib mesylate--a new oral targeted therapy. *N. Engl. J. Med.* **346**, 683–693 (2002).
48. Furman, R. R. *et al.* Idelalisib and rituximab in relapsed chronic lymphocytic leukemia. *N. Engl. J. Med.* **370**, 997–1007 (2014).
49. Miller, B. W. *et al.* FDA approval: idelalisib monotherapy for the treatment of patients with follicular lymphoma and small lymphocytic lymphoma. *Clin. Cancer Res.* **21**, 1525–1529 (2015).
50. Sequist, L. V. *et al.* Phase III study of afatinib or cisplatin plus pemetrexed in patients with metastatic lung adenocarcinoma with EGFR mutations. *J. Clin. Oncol.* **31**, 3327–3334 (2013).
51. Byrd, J. C. *et al.* Ibrutinib versus ofatumumab in previously treated chronic lymphoid leukemia. *N. Engl. J. Med.* **371**, 213–223 (2014).
52. Carmi, C. Mor, M. Petronini, P. G. & Alfieri, R. R. Clinical perspectives for irreversible tyrosine kinase inhibitors in cancer. *Biochem. Pharmacol.* **84**, 1388–1399 (2012).
53. Robert, C. *et al.* Improved overall survival in melanoma with combined dabrafenib and trametinib. *N. Engl. J. Med.* **372**, 30–39 (2015).
54. Wu, P. Nielsen, T. E. & Clausen, M. H. Small-molecule kinase inhibitors: an analysis of FDA-approved drugs. *Drug Discov. Today* (2015).
55. Okamoto, K. *et al.* Distinct binding mode of multikinase inhibitor lenvatinib revealed by biochemical characterization. *ACS Med. Chem. Lett.* **6**, 89–94 (2015).
56. Zhao, Z. *et al.* Exploration of type II binding mode: A privileged approach for kinase inhibitor focused drug discovery? *ACS Chem. Biol.* **9**, 1230–1241 (2014).
57. Wilson, J. N. Liu, W. Brown, A. S. & Landgraf, R. Binding-induced, turn-on fluorescence of the EGFR/ERBB kinase inhibitor, lapatinib. *Org. Biomol. Chem.* **13**, 5006–5011 (2015).

58. Schwartz, P. A. & Murray, B. W. Protein kinase biochemistry and drug discovery. *Bioorg. Chem.* **39**, 192–210 (2011).
59. Adams, J. A. Kinetic and Catalytic Mechanisms of Protein Kinases. *Chem. Rev.* **101**, 2271–2290 (2001).
60. Philip Cohen. Protein kinases — the major drug targets of the twenty-first century? *Nat. Rev. Drug Discov.* **1**, 309–315 (2002).
61. Vulpetti, A. & Bosotti, R. Sequence and structural analysis of kinase ATP pocket residues. *Farmaco (Società chimica italiana : 1989)* **59**, 759–765 (2004).
62. Bollag, G. *et al.* Clinical efficacy of a RAF inhibitor needs broad target blockade in BRAF-mutant melanoma. *Nature* **467**, 596–599 (2010).
63. Rabiller, M. *et al.* Proteus in the world of proteins: conformational changes in protein kinases. *Arch. Pharm.* **343**, 193–206 (2010).
64. Traxler, P. & Furet, P. Strategies toward the Design of Novel and Selective Protein Tyrosine Kinase Inhibitors. *Pharmacol. Ther.* **82**, 195–206 (1999).
65. Liao, J. J.-L. Molecular recognition of protein kinase binding pockets for design of potent and selective kinase inhibitors. *J. Med. Chem.* **50**, 409–424 (2007).
66. Gibbons, D. L. Priel, S. Kantarjian, H. Cortes, J. & Quintás-Cardama, A. The rise and fall of gatekeeper mutations? The BCR-ABL1 T315I paradigm. *Cancer* **118**, 293–299 (2012).
67. McTigue, M. *et al.* Molecular conformations, interactions, and properties associated with drug efficiency and clinical performance among VEGFR TK inhibitors. *Proc. Natl. Acad. Sci. U.S.A.* **109**, 18281–18289 (2012).
68. Müller, G. & Klebl, B. *Protein kinases as drug targets* (Wiley-VCH; John Wiley [distributor], Weinheim, Chichester, 2011).
69. Iwata, H. *et al.* Biochemical characterization of TAK-593, a novel VEGFR/PDGFR inhibitor with a two-step slow binding mechanism. *Biochemistry* **50**, 738–751 (2011).

70. Gaumann, A. K. A. *et al.* Receptor tyrosine kinase inhibitors: Are they real tumor killers? *Int. J. Cancer* (2015).
71. Hoi, P. M. *et al.* Recent advances in structure-based drug design and virtual screening of VEGFR tyrosine kinase inhibitors. *Methods* **71**, 85–91 (2015).
72. Cox, K. J. Shomin, C. D. & Ghosh, I. Tinkering outside the kinase ATP box: allosteric (type IV) and bivalent (type V) inhibitors of protein kinases. *Future Med. Chem.* **3**, 29–43 (2011).
73. Hill, Z. B. Perera, B. G. K. Andrews, S. S. & Maly, D. J. Targeting diverse signaling interaction sites allows the rapid generation of bivalent kinase inhibitors. *ACS Chem. Biol.* **7**, 487–495 (2012).
74. Kornev, A. P. Haste, N. M. Taylor, S. S. & Eyck, L. F. T. Surface comparison of active and inactive protein kinases identifies a conserved activation mechanism. *Proc. Natl. Acad. Sci. U.S.A.* **103**, 17783–17788 (2006).
75. Wong, K.-K. Recent Developments in Anti-Cancer Agents Targeting the Ras/Raf/MEK/ERK Pathway. *Recent Pat. Anti-Canc. Drug Discov.* **4**, 28–35 (2009).
76. Kolch, W. Meaningful relationships: the regulation of the Ras/Raf/MEK/ERK pathway by protein interactions. *Biochem. J.* **351**, 289–305 (2000).
77. Kumar, R. *et al.* BRAF Mutations in Metastatic Melanoma: A Possible Association with Clinical Outcome. *Clin. Cancer Res.* **9**, 3362–3368 (2003).
78. Bollag, G. *et al.* Vemurafenib: the first drug approved for BRAF-mutant cancer. *Nat. Rev. Drug Discov.* **11**, 873–886 (2012).
79. Davies, H. *et al.* Mutations of the BRAF gene in human cancer. *Nature* **417**, 949–954 (2002).
80. Flaherty, K. T. Yasothan, U. & Kirkpatrick, P. Vemurafenib. *Nat. Rev. Drug Discov.* **10**, 811–812 (2011).
81. Eisen, T. *et al.* Sorafenib in advanced melanoma: a Phase II randomised discontinuation trial analysis. *Br. J. Cancer* **95**, 581–586 (2006).

82. Llovet, J. M. *et al.* Sorafenib in advanced hepatocellular carcinoma. *N. Engl. J. Med.* **359**, 378–390 (2008).
83. Escudier, B. *et al.* Sorafenib in advanced clear-cell renal-cell carcinoma. *N. Engl. J. Med.* **356**, 125–134 (2007).
84. Chapman, P. B. *et al.* Improved survival with vemurafenib in melanoma with BRAF V600E mutation. *N. Engl. J. Med.* **364**, 2507–2516 (2011).
85. Sosman, J. A. *et al.* Survival in BRAF V600-mutant advanced melanoma treated with vemurafenib. *N. Engl. J. Med.* **366**, 707–714 (2012).
86. Flaherty, K. T. *et al.* Inhibition of mutated, activated BRAF in metastatic melanoma. *N. Engl. J. Med.* **363**, 809–819 (2010).
87. Das Thakur, M. *et al.* Modelling vemurafenib resistance in melanoma reveals a strategy to forestall drug resistance. *Nature* **494**, 251–255 (2013).
88. clinicaltrials.gov. Available at <https://clinicaltrials.gov/>.
89. Weber, J. *Design, Synthese und Charakterisierung von photoschaltbaren Axitinib-Derivaten. Bachelor Thesis* (2014).
90. Leung, D. Cachianes, G. Kuang, W. Goeddel, D. & Ferrara, N. Vascular endothelial growth factor is a secreted angiogenic mitogen. *Science* **246**, 1306–1309 (1989).
91. Ferrara, N. Gerber, H.-P. & LeCouter, J. The biology of VEGF and its receptors. *Nat. Med.* **9**, 669–676 (2003).
92. Li, R. & Stafford, J. A. *Kinase inhibitor drugs* (J. Wiley, Hoboken, N.J. 2009).
93. Shojaei, F. Anti-angiogenesis therapy in cancer: current challenges and future perspectives. *Cancer Lett.* **320**, 130–137 (2012).
94. Ferrara, N. Hillan, K. J. & Novotny, W. Bevacizumab (Avastin), a humanized anti-VEGF monoclonal antibody for cancer therapy. *Biochem. Biophys. Res. Commun.* **333**, 328–335 (2005).

95. Holmes, K. Roberts, O. L. Thomas, A. M. & Cross, M. J. Vascular endothelial growth factor receptor-2: structure, function, intracellular signalling and therapeutic inhibition. *Cell. Signal.* **19**, 2003–2012 (2007).
96. Aaronson, S. Growth factors and cancer. *Science* **254**, 1146–1153 (1991).
97. Rini, B. I. & Small, E. J. Biology and clinical development of vascular endothelial growth factor-targeted therapy in renal cell carcinoma. *J. Clin. Oncol.* **23**, 1028–1043 (2005).
98. Peifer, C. *et al.* Design, Synthesis, and Biological Evaluation of 3,4-Diarylmaleimides as Angiogenesis Inhibitors. *J. Med. Chem.* **49**, 1271–1281 (2006).
99. Peifer, C. *et al.* Profile and Molecular Modeling of 3-(Indole-3-yl)-4-(3,4,5-trimethoxyphenyl)-1H-pyrrole-2,5dione as a Highly Selective VEGF-R2/3 Inhibitor. *J. Med. Chem.* **49**, 7549–7553 (2006).
100. Escudier, B. & Gore, M. Axitinib for the management of metastatic renal cell carcinoma. *Drugs R. D.* **11**, 113–126 (2011).
101. Mittal, K. Wood, L. S. & Rini, B. I. Axitinib in Metastatic Renal Cell Carcinoma. *Biol. Ther.* **2**, 5 (2012).
102. Pemovska, T. *et al.* Axitinib effectively inhibits BCR-ABL1(T315I) with a distinct binding conformation. *Nature* **519**, 102–105 (2015).
103. Kelly, R. J. & Rixe, O. Axitinib—a selective inhibitor of the vascular endothelial growth factor (VEGF) receptor. *Target Oncol.* **4**, 297–305 (2009).
104. Hu-Lowe, D. D. *et al.* Nonclinical antiangiogenesis and antitumor activities of axitinib (AG-013736), an oral, potent, and selective inhibitor of vascular endothelial growth factor receptor tyrosine kinases 1, 2, 3. *Clin. Cancer Res.* **14**, 7272–7283 (2008).
105. Specht, A. Bolze, F. Omran, Z. Nicoud, J.-F. & Goeldner, M. Photochemical tools to study dynamic biological processes. *HFSP journal* **3**, 255–264 (2009).
106. Rabiller, M. *et al.* Proteus in the world of proteins: conformational changes in protein kinases. *Archiv der Pharmazie* **343**, 193–206 (2010).

107. Collins, I. & Workman, P. Design and Development of Signal Transduction Inhibitors for Cancer Treatment: Experience and Challenges with Kinase Targets. *Curr. Signal Transduct. Ther.* **1**, 13–23 (2006).
108. Yip, R. W. Sharma, D. K. Giasson, R. & Gravel, D. Photochemistry of the o-nitrobenzyl system in solution. Evidence for singlet-state intramolecular hydrogen abstraction. *J. Phys. Chem.* **89**, 5328–5330 (1985).
109. Zhang, Z. *et al.* An Effective Procedure for the Acylation of Azaindoles at C-3. *J. Org. Chem.* **67**, 6226–6227 (2002).
110. Lin, W. *et al.* A Model for Light-Triggered Porphyrin Anticancer Prodrugs Based on ano-Nitrobenzyl Photolabile Group. *Eur. J. Org. Chem.* **2008**, 793–796 (2008).
111. Simpson, J. C. E. 26. 6-Aminoacetoveratrone and 5. 6-dimethoxy-3-methylantranil. *J. Chem. Soc.* 94 (1946).
112. Smirnov, S. Stroganova, T. & Butin, A. 4,5-Dimethoxy-2-nitrobenzhydrol. *Molecules* **4**, M113 (1999).
113. Griffin, D. R. *et al.* Synthesis of Photodegradable Macromers for Conjugation and Release of Bioactive Molecules. *Biomacromolecules* **14**, 1199–1207 (2013).
114. Il'ichev, Y. V. & Wirz, J. Rearrangements of 2-Nitrobenzyl Compounds. 1. Potential Energy Surface of 2-Nitrotoluene and Its Isomers Explored with ab Initio and Density Functional Theory Methods. *J. Phys. Chem. A* **104**, 7856–7870 (2000).
115. Horbert, R. Pinchuk, B. Davies, P. Alessi, D. & Peifer, C. Photoactivatable prodrugs of anti-melanoma agent vemurafenib. *ACS Chem. Biol.* **10**, 2099–2107 (2015).
116. Dissanayake, K. *et al.* ERK/p90(RSK)/14-3-3 signalling has an impact on expression of PEA3 Ets transcription factors via the transcriptional repressor capicúa. *Biochem. J.* **433**, 515–525 (2011).
117. Søndergaard, J. N. *et al.* Differential sensitivity of melanoma cell lines with BRAFV600E mutation to the specific Raf inhibitor PLX4032. *J. Transl. Med.* **8**, 39 (2010).

118. Lee, J. T. *et al.* PLX4032, a potent inhibitor of the B-Raf V600E oncogene, selectively inhibits V600E-positive melanomas. *Pigment Cell Melanoma Res.* **23**, 820–827 (2010).
119. Yang, H. *et al.* RG7204 (PLX4032), a selective BRAFV600E inhibitor, displays potent antitumor activity in preclinical melanoma models. *Cancer Res.* **70**, 5518–5527 (2010).
120. Harris, P. A. *et al.* Discovery of 5-[[4-[(2,3-Dimethyl-2 H -indazol-6-yl)methylamino]-2-pyrimidinyl]amino]-2-methyl-benzenesulfonamide (Pazopanib), a Novel and Potent Vascular Endothelial Growth Factor Receptor Inhibitor. *J. Med. Chem.* **51**, 4632–4640 (2008).
121. Faul, M. M. Winneroski, L. L. & Krumrich, C. A. A New, Efficient Method for the Synthesis of Bisindolylmaleimides. *J. Org. Chem.* **63**, 6053–6058 (1998).
122. ProQinase GmbH: Radiometric 33PanQinase® assay. Available at <http://www.proqinase.com/content/view/27>.
123. Pinchuk, B. *Current Work* (2015).
124. Dev, I. K. *et al.* Antitumour efficacy of VEGFR2 tyrosine kinase inhibitor correlates with expression of VEGF and its receptor VEGFR2 in tumour models. *Br. J. Cancer* **91**, 1391–1398 (2004).
125. Yi, T. *et al.* Gambogic acid inhibits angiogenesis and prostate tumor growth by suppressing vascular endothelial growth factor receptor 2 signaling. *Cancer Res.* **68**, 1843–1850 (2008).
126. Tresaugues, L. *et al.* Crystal structure of VEGFR1 in complex with N-(4-Chlorophenyl)-2-((pyridin-4-ylmethyl)amino)benzamide (2009).
127. Pinchuk, B. *et al.* Marine derived hamacanthins as lead for the development of novel PDGFR β protein kinase inhibitors. *Mar. Drugs* **11**, 3209–3223 (2013).
128. Zhang, C. *et al.* Design and pharmacology of a highly specific dual FMS and KIT kinase inhibitor. *Proc. Natl. Acad. Sci. U.S.A.* **110**, 5689–5694 (2013).

129. Gajiwala, K. S. *et al.* KIT kinase mutants show unique mechanisms of drug resistance to imatinib and sunitinib in gastrointestinal stromal tumor patients. *Proc. Natl. Acad. Sci. U.S.A.* **106**, 1542–1547 (2009).
130. Catalán, J. de Paz, José Luis G. & Elguero, J. Importance of aromaticity on the relative stabilities of indazole annular tautomers. An ab initio study. *J. Chem. Soc.* 57 (1996).
131. Alkorta, I. & Elguero, J. Theoretical estimation of the annular tautomerism of indazoles. *J. Phys. Org. Chem.* **18**, 719–724 (2005).
132. Renn, C. *Biochemische Charakterisierung von DFGin/out Kinaseinhibitoren. Master Thesis* (2015).
133. Roberts, W. G. *et al.* Antiangiogenic and antitumor activity of a selective PDGFR tyrosine kinase inhibitor, CP-673,451. *Cancer Res.* **65**, 957–966 (2005).
134. Donatis, A. de *et al.* Proliferation versus migration in platelet-derived growth factor signaling: the key role of endocytosis. *J. Biol. Chem.* **283**, 19948–19956 (2008).
135. Sastry, G. M. Adzhigirey, M. Day, T. Annabhimoju, R. & Sherman, W. Protein and ligand preparation: parameters, protocols, and influence on virtual screening enrichments. *J. Comput. Aided Mol. Des.* **27**, 221–234 (2013).
136. Greenwood, J. R. Calkins, D. Sullivan, A. P. & Shelley, J. C. Towards the comprehensive, rapid, and accurate prediction of the favorable tautomeric states of drug-like molecules in aqueous solution. *J. Comput. Aided Mol. Des.* **24**, 591–604 (2010).
137. Jacobson, M. P. Friesner, R. A. Xiang, Z. & Honig, B. On the Role of the Crystal Environment in Determining Protein Side-chain Conformations. *J. Mol. Biol.* **320**, 597–608 (2002).
138. Jacobson, M. P. *et al.* A hierarchical approach to all-atom protein loop prediction. *Proteins* **55**, 351–367 (2004).
139. Watts, K. S. *et al.* ConfGen: a conformational search method for efficient generation of bioactive conformers. *J. Chem. Inf. Model.* **50**, 534–546 (2010).

140. Halgren, T. A. *et al.* Glide: a new approach for rapid, accurate docking and scoring. 2. Enrichment factors in database screening. *J. Med. Chem.* **47**, 1750–1759 (2004).
141. Friesner, R. A. *et al.* Glide: a new approach for rapid, accurate docking and scoring. 1. Method and assessment of docking accuracy. *J. Med. Chem.* **47**, 1739–1749 (2004).
142. Zindler, M. *Current Work* (2015).
143. DiscoverX: KdELECTSM Kinase Assay Panel. Available at <http://www.discoverx.com/services/drug-discovery-development-services/kinase-profiling/kinomescan/kdelect>.
144. ADP-GloTM Kinase Assay Technical Manual. Available at <https://www.promega.de/resources/protocols/technical-manuals/0/adp-glo-kinase-assay-protocol/>.
145. International Center for Kinase Profiling. Available at <http://www.kinase-screen.mrc.ac.uk/premier-screen>.
146. Bain, J. *et al.* The selectivity of protein kinase inhibitors: a further update. *Biochem. J.* **408**, 297–315 (2007).
147. Hastie, C. J. McLauchlan, H. J. & Cohen, P. Assay of protein kinases using radiolabeled ATP: a protocol. *Nat. Protoc.* **1**, 968–971 (2006).
148. Manning, G. Whyte, D. B. Martinez, R. Hunter, T. & Sudarsanam, S. The protein kinase complement of the human genome. *Science* **298**, 1912–1934 (2002).

7. APPENDIX

Supplementary Table 1. Kinase profiling of vemurafenib and caged prodrugs 58 and 60. The inhibitory effect was tested on a panel of 140 kinases. The residual activity (RA) of kinases was measured after incubation with 10 μ M of each compound. The data is portrayed as mean percentage activity and standard deviation (SD) of assay duplicates.

#	Kinase Name	vemurafenib		DMNB-vemurafenib (sulfonamide)		DMNB-vemurafenib (azaindole)	
		44		60		58	
		RA (%)	SD	RA (%)	SD	RA (%)	SD
1	MAP4K5	1	0	2	1	7	1
2	RIPK2	11	9	9	1	26	13
3	GCK	7	3	6	3	36	21
4	DDR2	1	0	6	1	45	2
5	BRK	1	0	2	1	46	4
6	TrkA	21	7	7	3	51	8
7	MST2	15	12	16	0	54	14
8	MLK1	8	8	10	0	68	2
9	MAP4K3	3	0	20	0	79	4
10	BRSK2	67	17	73	2	79	5
11	BTk	14	1	50	1	79	6
12	DYRK2	57	8	58	12	80	4
13	Aurora B	5	1	36	8	82	10
14	CSK	20	15	22	1	82	1
15	PLK1	74	6	77	10	85	0
16	MKK2	26	8	67	2	86	5
17	TTK	57	6	60	5	86	1
18	MKK1	49	7	71	5	86	8
19	EIF2AK3	9	1	48	0	87	4
20	MKK6	74	5	98	16	88	17
21	CAMK1	20	0	15	2	88	6
22	MINK1	27	7	61	21	89	1
23	TSSK1	63	14	53	4	89	4
24	p38a MAPK	70	27	85	13	90	0
25	PDGFRA	7	2	34	1	90	3
26	ROCK 2	49	3	72	6	90	10
27	AMPK (hum)	77	5	54	9	90	10
28	DYRK3	53	1	77	2	91	5
29	JNK3	68	7	83	13	91	1
30	TESK1	8	1	51	2	91	17
31	ERK5	70	2	81	16	92	5
32	MST4	43	4	90	13	92	5
33	PINK	80	10	96	6	92	3
34	MARK4	74	10	66	10	93	1
35	LKB1	82	1	88	17	93	7
36	IKKe	32	1	57	2	93	3
37	OSR1	50	0	90	4	94	2
38	MAPKAP-K3	70	14	73	3	94	2
39	PKD1	83	14	98	30	94	6
40	SGK1	73	4	83	0	94	11
41	JNK2	61	24	85	1	94	15
42	MARK2	80	1	93	17	95	0

43	MAPKAP-K2	86	7	86	6	95	3
44	PRK2	73	11	75	3	96	2
45	VEG-FR	7	3	19	5	96	6
46	HER4	25	2	78	3	96	2
47	STK33	83	5	93	6	96	7
48	BRSK1	84	0	78	12	97	8
49	CK2	104	1	104	7	97	1
50	MEKK1	73	11	84	1	97	2
51	SmMLCK	69	15	70	1	97	4
52	PKBa	96	7	84	5	97	9
53	WNK1	78	13	85	8	98	7
54	RSK1	88	0	70	5	98	6
55	Aurora A	46	9	68	12	98	14
56	MNK2	39	3	67	7	98	4
57	PKA	102	1	106	9	98	12
58	SIK3	30	1	90	8	98	22
59	PIM3	75	2	55	4	99	4
60	MARK1	74	5	84	5	99	20
61	ERK8	15	1	53	4	99	2
62	MNK1	48	7	50	11	99	7
63	EPH-B4	72	5	115	18	99	6
64	YES1	3	0	18	6	99	14
65	PIM1	65	4	89	1	100	15
66	PIM2	87	3	89	6	100	11
67	ASK1	89	17	88	5	100	24
68	MSK1	61	3	61	0	100	0
69	IKKb	88	1	83	4	100	13
70	ERK2	84	8	95	19	101	9
71	DYRK1A	61	7	84	6	101	4
72	HIPK3	95	9	100	1	101	1
73	SIK2	20	2	66	15	101	21
74	TTBK1	89	6	92	9	101	0
75	ERK1	103	13	102	19	102	5
76	NEK2a	22	5	67	2	102	2
77	ULK2	56	3	87	6	102	15
78	EPH-A4	93	19	98	13	102	1
79	PRAK	90	14	80	7	102	10
80	PAK4	53	16	97	7	103	5
81	IGF-1R	16	1	68	5	103	6
82	HIPK1	95	13	101	0	103	13
83	TLK1	81	0	89	9	103	4
84	DAPK1	95	11	95	11	104	6
85	IR	22	5	36	2	104	4
86	IRR	36	7	60	8	104	12
87	MLK3	6	1	60	16	104	2
88	CAMKKb	93	2	101	3	105	2
89	SRPK1	81	3	91	0	105	5
90	CK1δ	100	7	95	7	106	13
91	Src	3	1	45	9	106	8
92	CHK2	87	6	66	11	106	8
93	IRAK1	63	2	90	7	107	2
94	MST3	62	1	87	2	107	2
95	TBK1	96	3	90	5	107	3
96	MPSK1	48	9	76	8	107	5
97	TAK1	25	0	74	4	107	1
98	TGFBR1	45	2	96	28	107	8
99	HIPK2	66	4	71	4	107	2
100	TAO1	45	7	92	10	107	7
101	ULK1	69	5	98	10	108	5
102	GSK3b	32	4	41	8	108	3

103	p38g MAPK	121	3	104	12	108	6
104	EF2K	90	10	108	14	108	1
105	FGF-R1	29	5	72	9	108	4
106	SYK	43	4	93	0	108	23
107	MELK	103	1	80	28	108	11
108	p38d MAPK	99	13	120	36	109	4
109	PKCa	101	2	98	5	109	12
110	PHK	90	7	101	3	110	5
111	NUAK1	30	5	89	5	111	6
112	CDK9-Cyclin T1	80	8	96	8	111	1
113	PKBb	99	12	102	6	111	3
114	S6K1	80	13	83	2	111	13
115	CK1γ2	109	10	107	14	111	20
116	JNK1	62	43	77	3	111	8
117	RSK2	79	3	82	20	111	1
118	EPH-A2	91	3	101	9	112	10
119	MARK3	86	7	98	3	112	5
120	TIE2	77	2	95	11	112	6
121	EPH-B3	96	8	73	5	112	0
122	CDK2-Cyclin A	63	3	57	4	113	6
123	JAK2	32	11	36	2	113	2
124	PAK2	32	6	101	15	114	11
125	ABL	35	9	70	5	114	15
126	NEK6	117	7	97	2	115	11
127	PKCγ	104	15	94	16	115	6
128	p38b MAPK	32	1	86	7	117	6
129	ZAP70	84	6	98	0	118	5
130	CLK2	22	1	65	13	118	7
131	TTBK2	108	13	136	30	121	4
132	Lck	6	0	41	4	123	1
133	PKD1	70	8	84	5	124	8
134	PAK6	87	2	117	21	124	5
135	IRAK4	88	2	125	11	125	3
136	PAK5	78	3	137	2	130	14
137	EPH-B2	57	2	102	6	134	2
138	PKCz	101	1	128	27	139	6
139	CHK1	123	3	160	18	139	1
140	EPH-B1	133	9	170	18	177	32

Supplementary Table 2. Kinase profiling of diarylmaleimide 55 and carbazole 57. The inhibitory effect of the compounds was tested on the panel of 79 kinases in duplicates. The residual activity (RA) of kinases was measured after incubation with 0.1 μM resp. 1 μM of each compound. The data is portrayed as mean percentage activity and standard deviation (SD) of assay duplicates.

#	Kinase Name	diarylmaleimide 55				carbazole 57			
		0.1 μM		1 μM		0.1 μM		1 μM	
		RA (%)	SD	RA (%)	SD	RA (%)	SD	RA (%)	SD
1	MKK1	54	27	44	5	67	5	9	0
2	ERK1	100	5	88	8	91	25	40	12
3	ERK2	94	5	86	10	93	0	81	4
4	JNK1	96	13	92	3	96	5	69	0
5	JNK2	78	14	46	2	93	16	62	3
6	p38a MAPK	89	0	87	19	78	12	79	4
7	P38b MAPK	86	8	85	4	89	17	79	5
8	p38g MAPK	91	2	81	8	86	7	53	7
9	p38s MAPK	108	0	103	6	90	17	88	3
10	ERK8	46	5	10	2	11	1	4	0
11	RSK1	96	7	50	3	51	6	20	0
12	RSK2	91	1	54	5	62	6	20	3
13	PDK1	68	4	38	3	39	1	18	1
14	PKBa	66	4	81	12	81	16	83	2
15	PKBb	98	2	91	8	91	9	86	6
16	SGK1	75	5	51	13	52	15	36	3
17	S6K1	65	4	22	0	28	1	6	2
18	PKA	93	13	88	6	90	5	72	4
19	ROCK 2	97	2	88	3	88	6	55	3
20	PRK2	84	4	51	3	52	2	22	3
21	PKCa	113	5	95	3	90	14	90	2
22	PKC zeta	102	6	97	6	98	2	97	5
23	PKD1	100	12	64	22	60	9	35	4
24	MSK1	69	1	44	4	55	10	21	0
25	MNK1	80	0	72	3	79	4	67	18
26	MNK2	90	15	78	3	81	1	46	3
27	MAPKAP-K2	94	2	90	3	95	4	83	0
28	PRAK	91	7	90	2	85	2	71	1
29	CAMKKb	81	3	44	5	49	3	15	0
30	CAMK1	107	1	74	12	94	18	58	3
31	SmMLCK	60	17	28	2	30	5	10	0
32	PHK	73	8	41	3	41	6	7	0
33	CHK1	72	0	36	2	34	3	10	2
34	CHK2	64	9	54	5	63	2	20	1
35	GSK3b	21	2	4	1	5	1	2	1
36	CDK2-Cyclin A	59	5	28	8	28	4	6	1
37	PLK1	79	9	58	2	49	5	31	4
38	PLK1 (Okadaic Acid)	85	2	72	2	83	0	47	12
39	Aurora B	84	12	40	3	47	14	26	6
40	AMPK	78	8	69	13	75	13	38	4
41	MARK3	90	5	71	19	73	3	33	6
42	BRSK2	94	8	61	2	66	2	44	6
43	MELK	74	13	45	3	55	7	15	0
44	CK1	86	5	76	4	78	2	59	12
45	CK2	94	9	101	2	91	10	73	15
46	DYRK1A	73	2	29	2	26	0	13	3
47	DYRK2	57	15	18	4	17	0	5	1

48	DYRK3	85	6	53	5	46	5	16	3
49	NEK2a	87	1	97	4	91	6	67	4
50	NEK6	96	2	97	20	104	9	92	2
51	IKKb	102	7	104	2	113	25	94	2
52	PIM1	14	1	3	0	5	1	1	0
53	PIM2	115	5	102	1	115	12	100	7
54	PIM3	5	1	2	1	4	2	2	1
55	SRPK1	85	1	85	16	83	5	67	5
56	MST2	53	0	19	4	24	2	10	4
57	EFK2	104	3	102	10	109	15	91	5
58	HIPK2	23	2	4	1	7	1	3	1
59	PAK4	75	3	48	3	55	6	29	3
60	PAK5	105	1	79	3	84	4	49	2
61	PAK6	97	5	91	7	99	2	70	2
62	Src	81	0	78	12	86	1	88	5
63	Lck	91	2	67	16	91	4	60	13
64	CSK	138	8	102	9	99	1	97	8
65	FGF-R1	69	9	15	4	92	1	44	1
66	IRR	58	1	35	2	41	0	19	3
67	EPH A2	104	6	89	1	109	4	110	26
68	MST4	94	7	59	1	69	3	42	6
69	SYK	85	5	87	7	86	16	61	6
70	YES1	84	14	68	10	88	5	43	9
71	IKKe	80	3	58	5	63	8	31	1
72	TBK1	87	1	72	4	85	7	79	3
73	IGF1-R	90	24	54	1	65	4	23	9
74	VEG-FR	10	0	3	0	37	2	10	1
75	BTK	93	14	79	19	90	1	68	4
76	IR-HIS	101	11	73	3	88	15	30	2
77	EPH-B3	104	14	131	26	133	4	115	28
78	TBK1 (DU12569)	88	5	69	1	73	2	39	3
79	IKK epsilon (14231)	85	7	83	2	94	5	58	8

Supplementary Table 3. Kinase profiling of (E)- and (Z)-axitinib. The inhibitory effect of both axitinib isomers was tested on the panel of 300 kinases in duplicates. The residual activity of kinases was measured after incubation with 1 μ M of each compound.

#	Kinase Name	Kinase Family*	(E)-axitinib 19		Mean	(Z)-axitinib 19a/b		Mean
1	ABL1	TK	5	5	5	20	19	20
2	ABL2	TK	6	7	6	12	16	14
3	ACK1	TK	63	62	63	89	77	83
4	ACV-R1	TKL	90	94	92	98	90	94
5	ACV-R1B	TKL	71	63	67	73	69	71
6	ACV-R2A	TKL	86	100	93	95	99	97
7	ACV-R2B	TKL	75	76	76	83	72	78
8	ACV-RL1	TKL	84	77	80	85	91	88
9	AKT1	AGC	106	102	104	103	104	104
10	AKT2	AGC	102	89	96	113	106	109
11	AKT3	AGC	99	97	98	103	94	99
12	ALK (GST-HIS-tag)	TK	84	80	82	95	94	94
13	AMPK-alpha1 aa1-550	CAMK	71	68	70	83	86	85
14	ARK5	CAMK	52	48	50	72	65	69
15	ASK1	STE	81	88	84	98	97	98
16	Aurora-A	OTHER	8	11	10	24	22	23
17	Aurora-B	OTHER	7	8	8	13	11	12
18	Aurora-C	OTHER	7	6	6	9	12	11
19	AXL	TK	54	58	56	63	59	61
20	BLK	TK	65	71	68	90	81	86
21	BMPR1A	TKL	91	81	86	104	89	97
22	BMX	TK	97	100	99	100	101	100
23	B-RAF	TKL	95	101	98	94	108	101
24	BRK	TK	93	97	95	110	116	113
25	BRSK1	CAMK	87	84	85	95	100	98
26	BTK	TK	89	95	92	103	104	104
27	CAMK1D	CAMK	97	99	98	96	91	93
28	CAMK2A	CAMK	89	86	87	88	81	85
29	CAMK2B	CAMK	91	90	90	79	88	83
30	CAMK2D	CAMK	94	94	94	99	97	98
31	CAMK4	CAMK	99	126	112	120	106	113
32	CAMKK1	OTHER	95	93	94	101	102	101
33	CAMKK2	OTHER	68	73	70	91	89	90
34	CDC42BPA	AGC	90	86	88	92	95	94
35	CDC42BPB	AGC	97	108	102	112	106	109
36	CDK1/CycA2	CMGC	99	95	97	98	100	99
37	CDK1/CycB1	CMGC	94	89	91	102	102	102
38	CDK1/CycE1	CMGC	73	82	78	86	87	87
39	CDK2/CycA2	CMGC	97	101	99	107	105	106
40	CDK2/CycE1	CMGC	95	94	95	107	105	106
41	CDK3/CycE1	CMGC	96	99	98	99	106	103
42	CDK4/CycD1	CMGC	99	91	95	95	93	94
43	CDK4/CycD3	CMGC	102	103	103	116	115	116
44	CDK5/p25NCK	CMGC	100	99	99	102	101	102
45	CDK5/p35NCK	CMGC	93	94	94	99	99	99
46	CDK6/CycD1	CMGC	87	91	89	99	95	97
47	CDK7/CycH/MAT1	CMGC	107	106	107	104	97	100
48	CDK8/CycC	CMGC	98	101	100	113	107	110
49	CDK9/CycK	CMGC	106	96	101	117	97	107
50	CDK9/CycT1	CMGC	100	96	98	105	112	109
51	CHK1	CAMK	94	94	94	110	108	109

52	CHK2	CAMK	92	96	94	99	93	96
53	CK1-alpha1	CK1	99	99	99	104	97	100
54	CK1-delta	CK1	98	95	97	108	104	106
55	CK1-epsilon	CK1	83	85	84	86	80	83
56	CK1-gamma1	CK1	91	97	94	87	93	90
57	CK1-gamma2	CK1	92	89	91	98	96	97
58	CK1-gamma3	CK1	93	91	92	99	93	96
59	CK2-alpha1	OTHER	99	103	101	102	100	101
60	CK2-alpha2	OTHER	102	114	108	96	103	100
61	CLK1	CMGC	91	84	88	100	94	97
62	CLK2	CMGC	104	92	98	102	100	101
63	CLK3	CMGC	87	97	92	93	93	93
64	CLK4	CMGC	96	81	88	96	86	91
65	COT	STE	104	102	103	101	133	117
66	CSF1-R	TK	51	46	49	60	59	60
67	CSK	TK	92	88	90	104	101	103
68	DAPK1	CAMK	90	85	87	85	81	83
69	DAPK2	CAMK	94	92	93	103	87	95
70	DAPK3	CAMK	96	91	94	94	95	94
71	DCAMKL2	CAMK	90	90	90	91	93	92
72	DDR2	TK	67	64	66	85	79	82
73	DMPK	AGC	88	94	91	103	97	100
74	DANN-PK	ATYP	99	97	98	99	95	97
75	DYRK1A	CMGC	105	96	101	100	97	98
76	DYRK1B	CMGC	100	112	106	103	113	108
77	DYRK2	CMGC	90	93	91	98	95	97
78	DYRK3	CMGC	82	81	81	86	80	83
79	DYRK4	CMGC	102	101	102	98	100	99
80	EEF2K	ATYPICAL	104	104	104	111	111	111
81	EGF-R	TK	101	96	98	109	99	104
82	EIF2AK2	OTHER	113	106	110	109	107	108
83	EIF2AK3	OTHER	87	99	93	99	98	99
84	EPHA1	TK	88	103	95	104	110	107
85	EPHA2	TK	103	104	104	107	107	107
86	EPHA3	TK	96	93	95	92	100	96
87	EPHA4	TK	93	91	92	101	104	102
88	EPHA5	TK	87	91	89	116	94	105
89	EPHA7	TK	101	86	94	105	106	105
90	EPHA8	TK	94	100	97	111	104	107
91	EPHB1	TK	94	93	94	107	103	105
92	EPHB2	TK	50	48	49	70	67	69
93	EPHB3	TK	100	95	98	107	105	106
94	EPHB4	TK	104	111	108	113	112	112
95	ERBB2	TK	93	95	94	116	112	114
96	ERBB4	TK	109	103	106	104	98	101
97	ERK1	CMGC	103	103	103	105	97	101
98	ERK2	CMGC	102	97	99	103	94	98
99	ERK7	CMGC	90	84	87	87	81	84
100	FAK aa2-1052	TK	111	97	104	111	97	104
101	FER	TK	93	88	90	104	100	102
102	FES	TK	84	88	86	98	95	97
103	FGF-R1	TK	3	3	3	6	4	5
104	FGF-R2	TK	6	5	6	9	10	9
105	FGF-R3	TK	45	34	39	65	49	57
106	FGF-R4	TK	85	89	87	96	96	96
107	FGR	TK	16	17	16	25	27	26
108	FLT3	TK	93	96	94	93	98	95
109	FRK	TK	95	91	93	106	91	99
110	FYN	TK	58	55	56	102	85	94
111	GRK2	AGC	95	88	92	92	91	91

112	GRK3	AGC	90	86	88	89	77	83
113	GRK4	AGC	84	76	80	83	74	78
114	GRK5	AGC	91	87	89	85	92	88
115	GRK6	AGC	80	80	80	83	87	85
116	GRK7	AGC	89	91	90	95	93	94
117	GSG2	OTHER	95	95	95	106	102	104
118	GSK3-alpha	CMGC	96	89	92	92	89	90
119	GSK3-beta	CMGC	93	94	93	101	107	104
120	HCK	TK	91	94	92	98	107	103
121	HIPK1	CMGC	103	105	104	101	103	102
122	HIPK2	CMGC	102	98	100	111	102	106
123	HIPK3	CMGC	109	97	103	103	105	104
124	HIPK4	CMGC	90	91	90	90	90	90
125	HRI	OTHER	93	104	98	86	104	95
126	IGF1-R	TK	113	101	107	109	97	103
127	IKK-alpha	OTHER	84	93	88	92	93	93
128	IKK-beta	OTHER	101	106	104	110	105	107
129	IKK-epsilon	OTHER	87	85	86	100	95	97
130	INS-R	TK	100	89	94	96	109	102
131	INSR-R	TK	98	98	98	100	105	103
132	IRAK1	TKL	77	77	77	86	83	84
133	IRAK4 (untagged)	TKL	86	95	91	89	102	95
134	ITK	TK	85	79	82	93	97	95
135	JAK1	TK	96	92	94	89	96	93
136	JAK2	TK	70	73	71	90	92	91
137	JAK3	TK	79	81	80	85	97	91
138	JNK1	CMGC	91	84	88	84	95	89
139	JNK2	CMGC	90	97	94	102	105	104
140	JNK3	CMGC	85	91	88	105	112	108
141	KIT	TK	6	6	6	9	8	9
142	LCK	TK	68	67	67	70	69	70
143	LIMK1	TKL	95	92	94	104	104	104
144	LIMK2	TKL	114	87	100	101	90	96
145	LRRK2	TKL	26	28	27	32	34	33
146	LTK	TK	97	96	97	99	101	100
147	LYN	TK	62	54	58	80	78	79
148	MAP3K1	STE	106	106	106	110	109	109
149	MAP3K10	STE	80	82	81	92	92	92
150	MAP3K11	STE	33	35	34	53	59	56
151	MAP3K7/MAP3K7IP1	STE	81	84	82	94	87	90
152	MAP3K9	STE	69	62	65	85	77	81
153	MAP4K2	STE	21	21	21	62	57	59
154	MAP4K4	STE	7	6	6	9	12	10
155	MAP4K5	STE	18	18	18	35	32	34
156	MAPKAPK2	CAMK	79	72	76	69	74	71
157	MAPKAPK3	CAMK	98	101	100	101	100	100
158	MAPKAPK5	CAMK	89	82	85	83	81	82
159	MARK1	CAMK	87	95	91	98	91	94
160	MARK2	CAMK	94	76	85	94	90	92
161	MARK3	CAMK	90	88	89	96	89	93
162	MARK4	CAMK	103	99	101	108	106	107
163	MATK	TK	107	118	113	116	122	119
164	MEK1	STE	66	65	66	77	74	76
165	MEK2	STE	104	94	99	98	98	98
166	MEKK2	STE	85	82	83	86	89	87
167	MEKK3	STE	87	77	82	89	81	85
168	MELK	CAMK	91	89	90	94	102	98
169	MERTK	TK	48	48	48	78	66	72
170	MET	TK	77	76	76	85	90	87
171	MINK1	STE	7	7	7	13	13	13

172	MKK6 S207D/T211D**	STE	97	106	102	99	115	107
173	MKNK1	CAMK	98	90	94	100	107	103
174	MKNK2	CAMK	91	90	90	93	90	91
175	MST1	STE	61	59	60	68	73	71
176	MST2	STE	53	57	55	93	73	83
177	MST3	STE	100	102	101	102	101	102
178	MST4	STE	89	92	91	90	103	96
179	mTOR	ATYPICAL	92	92	92	97	103	100
180	MUSK	TK	24	13	18	60	49	55
181	MYLK	CAMK	93	86	89	92	88	90
182	MYLK2	CAMK	92	102	97	105	103	104
183	MYLK3	CAMK	87	85	86	90	102	96
184	NEK1	OTHER	100	103	101	105	107	106
185	NEK11	OTHER	89	90	89	101	98	100
186	NEK2	OTHER	100	90	95	98	110	104
187	NEK3	OTHER	99	95	97	87	96	92
188	NEK4	OTHER	100	93	96	103	100	102
189	NEK6	OTHER	107	97	102	111	111	111
190	NEK7	OTHER	90	83	86	88	85	86
191	NEK9	OTHER	89	94	91	97	95	96
192	NIK	STE	112	90	101	110	103	106
193	NLK	CMGC	95	109	102	102	118	110
194	p38-alpha	CMGC	98	92	95	99	100	99
195	p38-beta	CMGC	98	97	98	95	106	100
196	p38-delta	CMGC	91	99	95	84	86	85
197	p38-gamma	CMGC	99	94	97	96	97	96
198	PAK1	STE	92	92	92	90	90	90
199	PAK2	STE	93	87	90	94	88	91
200	PAK3	STE	95	100	97	100	95	98
201	PAK4	STE	73	82	77	85	84	84
202	PAK6	STE	74	70	72	88	88	88
203	PAK7	STE	81	76	78	82	83	82
204	PASK	CAMK	101	101	101	106	99	102
205	PBK	OTHER	115	110	112	126	103	115
206	PCTAIRE1/CycY	CMGC	94	98	96	101	102	101
207	PDGFR-alpha	TK	-5	-3	-4	3	0	2
208	PDGFR-beta	TK	1	1	1	4	5	4
209	PDK1	AGC	75	74	74	83	74	79
210	PHKG1	CAMK	113	104	109	113	118	116
211	PHKG2	CAMK	95	100	97	102	103	102
212	PIM1	CAMK	101	93	97	99	104	101
213	PIM2	CAMK	91	90	90	77	75	76
214	PIM3	CAMK	98	93	95	101	103	102
215	PKA	AGC	89	103	96	105	103	104
216	PKC-alpha	AGC	102	101	101	96	90	93
217	PKC-beta1	AGC	94	88	91	100	95	98
218	PKC-beta2	AGC	99	98	99	102	97	100
219	PKC-delta	AGC	104	113	109	108	109	108
220	PKC-epsilon	AGC	96	94	95	105	107	106
221	PKC-eta	AGC	95	94	95	95	106	101
222	PKC-gamma	AGC	102	105	103	105	93	99
223	PKC-iota	AGC	87	98	93	101	101	101
224	PKC-mu	AGC	92	95	93	95	96	96
225	PKC-nu	AGC	94	93	93	91	92	91
226	PKC-theta	AGC	99	94	97	86	92	89
227	PKC-zeta	AGC	100	104	102	105	99	102
228	PLK1	OTHER	94	95	94	92	88	90
229	PLK3	OTHER	115	113	114	114	110	112
230	PRK1	AGC	99	92	96	103	105	104
231	PRK2	AGC	77	78	77	86	86	86

232	PRKD2	CAMK	94	96	95	89	104	97
233	PRKG1	AGC	101	107	104	104	105	105
234	PRKG2	AGC	99	85	92	95	85	90
235	PRKX	AGC	77	74	75	68	71	69
236	PYK2	TK	82	83	83	91	98	94
237	RAF1 Y340D/Y341D (untagged)**	TKL	103	104	104	105	109	107
238	RET	TK	16	17	17	49	44	47
239	RIPK2	TKL	75	68	71	76	79	78
240	RIPK5	TKL	102	102	102	108	110	109
241	ROCK1	AGC	83	93	88	88	91	89
242	ROCK2	AGC	83	80	82	92	90	91
243	RON	TK	89	94	91	95	97	96
244	ROS	TK	32	32	32	45	45	45
245	RPS6KA1	AGC	94	84	89	104	82	93
246	RPS6KA2	AGC	80	79	79	84	90	87
247	RPS6KA3	AGC	68	70	69	90	87	88
248	RPS6KA4	AGC	98	94	96	103	109	106
249	RPS6KA5	AGC	91	101	96	97	104	100
250	RPS6KA6	AGC	74	68	71	85	89	87
251	S6K	AGC	87	108	97	99	91	95
252	S6K-beta	AGC	95	100	98	99	106	103
253	SAK	OTHER	3	6	4	7	4	5
254	SGK1	AGC	83	79	81	93	85	89
255	SGK2	AGC	96	93	95	99	103	101
256	SGK3	AGC	96	99	98	100	97	99
257	SLK	STE	36	32	34	65	61	63
258	SNARK	CAMK	23	23	23	36	33	35
259	SNF1LK2	CAMK	98	93	96	107	102	105
260	SNK	OTHER	98	93	96	99	100	99
261	SRC (GST-HIS-tag)	TK	90	91	91	94	94	94
262	SRMS	TK	99	89	94	97	99	98
263	SRPK1	CMGC	103	94	98	100	107	103
264	SRPK2	CMGC	109	94	102	107	102	104
265	STK17A	CAMK	22	26	24	36	35	35
266	STK23	CAMK	90	82	86	91	88	89
267	STK25	STE	99	94	97	91	92	91
268	STK33	CAMK	91	86	89	93	94	93
269	STK39	STE	90	93	91	88	99	93
270	SYK aa1-635	TK	98	91	95	104	96	100
271	TAOK2	STE	77	72	74	86	84	85
272	TAOK3	STE	91	92	92	106	98	102
273	TBK1	OTHER	74	77	75	82	71	76
274	TEC	TK	109	106	108	109	104	106
275	TGFB-R1	TKL	93	100	96	110	101	105
276	TGFB-R2	TKL	78	80	79	87	83	85
277	TIE2	TK	39	38	39	60	55	57
278	TLK1	AGC	93	99	96	90	87	89
279	TLK2	AGC	98	92	95	99	99	99
280	TRK-A	TK	22	20	21	34	32	33
281	TRK-B	TK	49	45	47	51	51	51
282	TRK-C	TK	32	30	31	44	42	43
283	TSF1	OTHER	50	50	50	63	65	64
284	TSK2	CAMK	95	99	97	108	100	104
285	TSSK1	CAMK	81	74	78	86	93	90
286	TTK	OTHER	98	100	99	101	98	100
287	TXK	TK	94	87	90	93	101	97
288	TYK2	TK	64	69	66	76	91	84
289	TYRO3	TK	96	93	95	88	107	97
290	VEGF-R1	TK	3	4	4	8	7	8

291	VEGF-R2	TK	0	1	0	1	1	1
292	VEGF-R3	TK	13	16	14	19	17	18
293	VRK1	CK1	103	103	103	114	105	110
294	WEE1	OTHER	88	97	93	102	106	104
295	WNK1	OTHER	94	102	98	91	98	94
296	WNK2	OTHER	95	93	94	95	91	93
297	WNK3	OTHER	96	109	102	105	96	100
298	YES	TK	59	61	60	78	72	75
299	ZAK	TKL	61	56	58	69	72	71
300	ZAP70	TK	104	101	102	109	104	106
Selectivity Score (< 50 % residual activity):					0.117			0.083

***Classification of protein kinase families¹⁴⁸:**

AGC: containing PKA, PKG and PKC families

CAMK: Calcium/Calmoduline-dependent protein kinases

CK1: Casein kinase 1 –like

CMGC: containing CDK, MAPK ,GSK3 and CLK families

TK: Tyrosine Kinase

TKL: Tyrosine Kinase-like

STE: Homologs of Yeast Sterile 7, Sterile 11, Sterile 20 Kinases

**** Constitutively active kinase**

TABLE OF ABBREVIATIONS

°C	degrees Celsius
μ	micro
2D / 3D	two-dimensional / three-dimensional
8-MOP	8-methoxypsoralen
ALL	acute lymphoblastic leukemia
A-loop	activation loop
ATP	adenosine triphosphate
b (NMR)	broad
BOC	<i>tert</i> -butyloxycarbonyl
Bu	butyl
C, Cys	cysteine (amino acid one-letter code)
cat.	catalytic
CCDC	Cambridge Crystallographic Data Centre
CLL	chronic lymphocytic leukemia
C-lobe	C-terminal lobe
CML	chronic myeloid leukemia
CO ₂	carbon dioxide
COSY (NMR)	correlation spectroscopy
CRC	colorectal cancer
CST	Cell signaling technology
d (NMR)	doublet
DCM	dichloromethane
DDR2	discoidin domain-containing receptor 2
DFG, Asp-Phe-Gly	aspartic acid, phenylalanine, glycine (amino acid one-letter code)
DMEM	Dulbecco's modified Eagle's medium
DMF	dimethylformamide
DMNB	4,5-dimethoxy-2-nitrobenzyl
DMNPE	1-(4,5-dimethoxy-2-nitrophenyl)ethyl
DMSO	dimethyl sulfoxide
E, Glu	glutamic acid (amino acid one-letter code)
<i>e.g.</i>	<i>exempli gratiā</i> (lat. for example)
EMA	European Medicine Agency
Erk	extracellular signal-regulated kinase
ESI	electrospray ionization
Et	ethyl
FBS	fetal bovine serum
FDA	Food and Drug Administration
FL	follicular lymphoma
g	gram

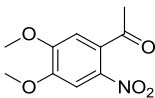
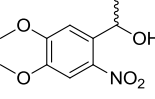
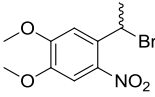
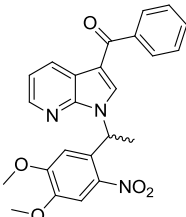
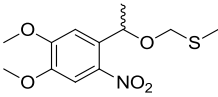
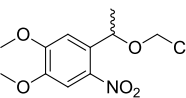
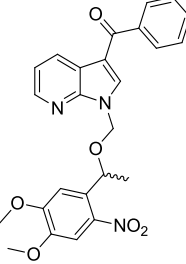
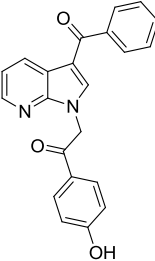
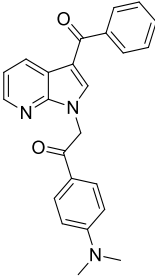
<i>g</i>	gravitational force
GF	growth factor
GI ₅₀	50% growth inhibition
GIST	gastrointestinal stromal tumor
h	hour(s)
HCC	hepatocellular cancer
HMBC (NMR)	heteronuclear multiple-bond correlation spectroscopy
HP I/II	hydrophobic pocket I/II
HPLC	high-performance liquid chromatography
HRMS	high-resolution mass spectrometry
HSQC (NMR)	heteronuclear single-quantum correlation spectroscopy
Hz	hertz
IC ₅₀	half maximal inhibitory concentration
INN	international nonproprietary name
<i>J</i> (NMR)	coupling constant
K	Kelvin
L	liter
LC ₅₀	50% lethal concentration
LC-MS	liquid chromatography–mass spectrometry
LED	light-emitting diode
LG	leaving group
m	meter
m	milli
M	molar
m (NMR)	unresolved multiplet
m.p.	melting point
<i>m/z</i>	mass-to-charge ratio
MAP4K5	mitogen-activated protein kinase kinase kinase kinase 5
MAPK	mitogen-activated protein kinase
MCL	mantle cell lymphoma
MEK	mitogen-activated protein kinase kinase
MEM	minimum essential medium
MeOH	methanol
MHz	megahertz
min	minute(s)
mol	mole
<i>M_r</i>	relative molecular mass
MS	mass spectrometry
n	nano
n/a	not applicable
NB	<i>o</i> -nitrobenzyl
N-lobe	N-terminal lobe

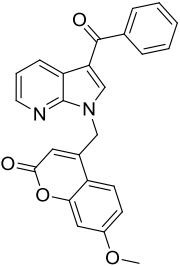
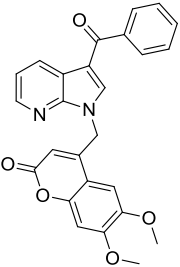
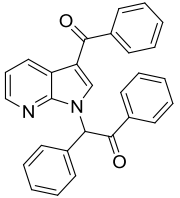
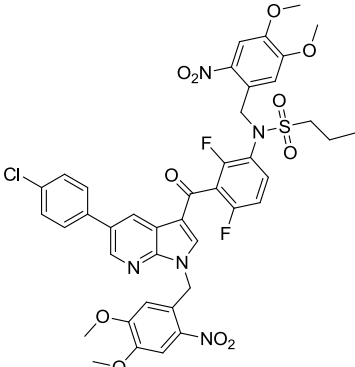
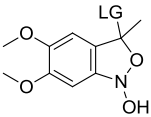
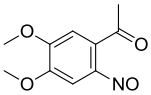
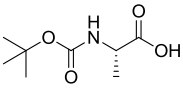
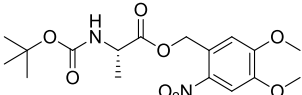
nm	nanometer
NMR	nuclear magnetic resonance spectroscopy
NSCLC	non-small cell lung cancer
NVOC	6-nitroveratryloxycarbonyl
NVOM	6-nitroveratryloxymethyl
PBS	phosphate-buffered saline
pdb	protein data bank (RCSB)
PDGFR	platelet-derived growth factor receptor
p-Erk	phosphorylated Erk
pHP	4-hydroxy-phenacyl
PPG	photoremovable protection group
ppm	parts per million
prep.	preparation
psi	pounds per square inch
PUVA	psoralen plus UV-A
RA	residual activity
RCC	renal cell carcinoma
RCT	receptor tyrosine kinase
resp.	respectively
RIPK2	receptor-interacting serine/threonine-protein kinase 2
RP	reversed phase
rt	room temperature
s	second(s)
s (NMR)	singlet
SD	standard deviation
SLL	small lymphocytic leukemia
smKI	small-molecule kinase inhibitor
S _N	nucleophilic substitution
t (NMR)	triplet
t-Erk	total Erk
TGI	total growth inhibition
THF	tetrahydrofuran
TKI	tyrosine kinase inhibitor
TLC	thin-layer chromatography
UV	ultraviolet
V	volt
v/v	volume fraction
VEGFR	vascular endothelial growth factor receptor
VHL	Von Hippel-Lindau
vis	visible
vs.	<i>versus</i>
W	watt

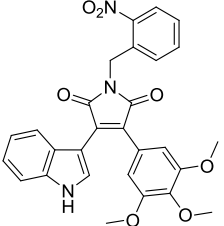
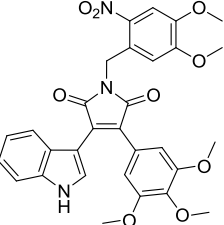
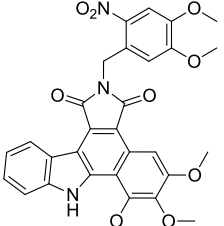
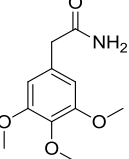
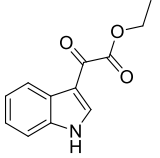
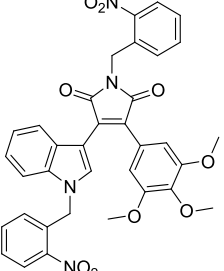
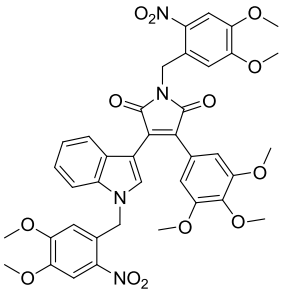
TABLE OF COMPOUNDS

#	Code	Formula	Nomenclature	Pages	Prep.
19	JW_01		(E)-axitinib, (E)-N-methyl-2-((3-(2-(pyridin-2-yl)vinyl)-1H-indazol-6-yl)thio)benzamide, INN: axitinib	6, 13, 28, 82	138
19a/b	JW_02		(Z)-axitinib, mixture of 1H-tautomer (a), (Z)-N-methyl-2-((3-(2-(pyridin-2-yl)vinyl)-1H-indazol-6-yl)thio)benzamide and 2H-tautomer (b), (Z)-N-Methyl-2-((3-(2-(pyridin-2-yl)vinyl)-2H-indazol-6-yl)thio)benzamide	82	139
44	RH_007		N-(3-(5-(4-chlorophenyl)-1H-pyrrolo[2,3-b]pyridine-3-carbonyl)-2,4-difluorophenyl)propane-1-sulfonamide, INN: vemurafenib	13, 31, 46	119
55	RH_003		3-(1H-indol-3-yl)-4-(3,4,5-trimethoxyphenyl)-1H-pyrrole-2,5-dione	27, 67, 68, 69, 74	128
56	n/a		(7aR,7bR)-5,6,7-trimethoxy-7b,8-dihydrobenzo[a]pyrrolo[3,4-c]carbazole-1,3(2H,7aH)-dione	27, 69	n/a
57	RH_004		5,6,7-trimethoxybenzo[a]pyrrolo[3,4-c]carbazole-1,3(2H,8H)-dione	27, 74	129

58	RH_015		<i>N</i> -(3-(5-(4-chlorophenyl)-1-(4,5-dimethoxy-2-nitrobenzyl)-1 <i>H</i> -pyrrolo[2,3- <i>b</i>]pyridine-3-carbonyl)-2,4-difluorophenyl)propane-1-sulfonamide	37, 46, 55	120
59	RH_032		<i>N</i> -(3-(5-(4-chlorophenyl)-1-(1-(4,5-dimethoxy-2-nitrophenyl)ethyl)-1 <i>H</i> -pyrrolo[2,3- <i>b</i>]pyridine-3-carbonyl)-2,4-difluorophenyl)propane-1-sulfonamide	37, 46, 55	122
60	RH_015*		<i>N</i> -(3-(5-(4-chlorophenyl)-1 <i>H</i> -pyrrolo[2,3- <i>b</i>]pyridine-3-carbonyl)-2,4-difluorophenyl)- <i>N</i> -(4,5-dimethoxy-2-nitrobenzyl)propane-1-sulfonamide	37, 46, 55	124
67	RH_038		phenyl-(1 <i>H</i> -pyrrolo[2,3- <i>b</i>]pyridin-3-yl)-methanone	40, 48, 49	103
69	RH_035		1-(4,5-dimethoxy-2-nitrobenzyl)-1 <i>H</i> -pyrrolo[2,3- <i>b</i>]pyridine	40, 48, 49	104
70	RH_036		1-(1-(4,5-dimethoxy-2-nitrobenzyl)-1 <i>H</i> -pyrrolo[2,3- <i>b</i>]pyridin-3-yl)-ethanone	40, 48, 49	105
71	RH_037		(1-(4,5-dimethoxy-2-nitrobenzyl)-1 <i>H</i> -pyrrolo[2,3- <i>b</i>]pyridin-3-yl)(phenyl)-methanone	40, 48, 49	106

73	RH_021		1-(4,5-dimethoxy-2-nitrophenyl)-ethanone	42	107
74	RH_022		1-(4,5-dimethoxy-2-nitrophenyl)-ethanol	42	108
75	RH_029		1-(1-bromoethyl)-4,5-dimethoxy-2-nitrobenzene	42	109
76	RH_044		(1-(1-(4,5-dimethoxy-2-nitrophenyl)-ethyl)-1 <i>H</i> -pyrrolo[2,3- <i>b</i>]pyridin-3-yl)-(phenyl)methanone	42, 51	110
77	RH_023		(1-(4,5-dimethoxy-2-nitrophenyl)-ethoxy)methyl(methyl)-sulfane	42	111
78	RH_024		1-(1-(chloromethoxy)ethyl)-4,5-dimethoxy-2-nitrobenzene	42	112
79	RH_043		(1-((1-(4,5-dimethoxy-2-nitrophenyl)-ethoxy)methyl)-1 <i>H</i> -pyrrolo[2,3- <i>b</i>]pyridin-3-yl)(phenyl)methanone	42, 51	113
82	RH_039		2-(3-benzoyl-1 <i>H</i> -pyrrolo[2,3- <i>b</i>]pyridin-1-yl)-1-(4-hydroxyphenyl)ethanone	44, 52	114
83	RH_040		2-(3-benzoyl-1 <i>H</i> -pyrrolo[2,3- <i>b</i>]pyridin-1-yl)-1-(4-(dimethylamino)phenyl)-ethanone	44, 51	115

84	RH_042		4-((3-benzoyl-1H-pyrrolo[2,3-b]pyridin-1-yl)methyl)-7-methoxy-2H-chromen-2-one	44, 51	116
85	RH_041		4-((3-benzoyl-1H-pyrrolo[2,3-b]pyridin-1-yl)methyl)-6,7-dimethoxy-2H-chromen-2-one	44, 51	117
86	RH_046		2-(3-benzoyl-1H-pyrrolo[2,3-b]pyridin-1-yl)-1,2-diphenylethanone	44, 51	118
87	RH_016		<i>N</i> -(3-(5-(4-chlorophenyl)-1-(4,5-dimethoxy-2-nitrobenzyl)-1H-pyrrolo[2,3-b]pyridine-3-carbonyl)-2,4-difluorophenyl)- <i>N</i> -(4,5-dimethoxy-2-nitrobenzyl)propane-1-sulfonamide	46	125
93	n/a		n/a LG = leaving group	56	n/a
95	n/a		1-(4,5-dimethoxy-2-nitrosophenyl)ethanone	56	n/a
96	n/a		(<i>S</i>)-2-((<i>tert</i> -butoxycarbonyl)amino)propanoic acid	61	n/a
97	n/a		(<i>S</i>)-4,5-dimethoxy-2-nitrobenzyl 2-((<i>tert</i> -butoxycarbonyl)amino)propanoate	61	n/a

98	RH_005		3-(1 <i>H</i> -indol-3-yl)-1-(2-nitrobenzyl)-4-(3,4,5-trimethoxyphenyl)-1 <i>H</i> -pyrrole-2,5-dione	65, 68, 71	130
99	RH_013		1-(4,5-dimethoxy-2-nitrobenzyl)-3-(1 <i>H</i> -indol-3-yl)-4-(3,4,5-trimethoxyphenyl)-1 <i>H</i> -pyrrole-2,5-dione	65, 69, 71, 74	131
100	RH_049		2-(4,5-dimethoxy-2-nitrobenzyl)-5,6,7-trimethoxybenzo[<i>a</i>]pyrrolo[3,4- <i>c</i>]carbazole-1,3(2 <i>H</i> ,8 <i>H</i>)-dione	65, 69, 71, 74	132
102	RH_001		2-(3,4,5-trimethoxyphenyl)acetamide	67	133
104	RH_002		ethyl 2-(1 <i>H</i> -indol-3-yl)-2-oxoacetate	67	134
105	RH_006		1-(2-nitrobenzyl)-3-(1-(2-nitrobenzyl)-1 <i>H</i> -indol-3-yl)-4-(3,4,5-trimethoxyphenyl)-1 <i>H</i> -pyrrole-2,5-dione	68	135
106	RH_014		1-(4,5-dimethoxy-2-nitrobenzyl)-3-(1-(4,5-dimethoxy-2-nitrobenzyl)-1 <i>H</i> -indol-3-yl)-4-(3,4,5-trimethoxyphenyl)-1 <i>H</i> -pyrrole-2,5-dione	69	136

LEBENS LAUF

Persönliche Daten

Name	Rebecca Marisa Horbert
Geburtsdatum	18. August 1986
Geburtsort	Simmern/Hunsrück
Staatsangehörigkeit	deutsch

Schul Ausbildung und Studium

1993 - 1997	Grundschule Kirchberg/Hunsrück
1997 - 2005	Herzog-Johann-Gymnasium Simmern/Hunsrück
03/2005	Abitur
10/2006 - 09/2010	Studium der Pharmazie an der MLU Halle-Wittenberg

Weitere Ausbildung und beruflicher Werdegang

11/2010 - 04/2011	Pharmaziepraktikantin bei Beiersdorf in Hamburg
05/2011 - 10/2011	Pharmaziepraktikantin in der Hirsch-Apotheke in Kiel
11/2011	Approbation als Apothekerin
Seit 01/2012	Wissenschaftliche Mitarbeiterin und Doktorandin am Pharmazeutischen Institut der Universität zu Kiel
Seit 02/2012	Weiterbildung zur Fachapothekerin für pharmazeutische Analytik

ERKLÄRUNG

Die vorliegende Arbeit wurde unter Anleitung von Herrn Prof. Dr. Christian Peifer an der Christian-Albrechts-Universität zu Kiel, Pharmazeutisches Institut, Abteilung Pharmazeutische Chemie, im Zeitraum von Januar 2012 bis Oktober 2015 angefertigt.

Der Inhalt wurde, abgesehen von der Beratung durch meinen Betreuer, selbstständig von mir erarbeitet und in dieser Form zusammengestellt. Die Arbeit hat an keiner Stelle im Rahmen eines anderen Prüfungsverfahrens vorgelegen und ist unter Einhaltung der Regeln guter wissenschaftlicher Praxis entstanden.

Kiel, Oktober 2015

Rebecca Horbert

Teile dieser Arbeit wurden bereits an folgenden Stellen veröffentlicht:

Fachzeitschriften

1. R. Horbert, B. Pinchuk, P. Davies, D. Alessi, C. Peifer:
Photoactivatable Prodrugs of Antimelanoma Agent Vemurafenib,
ACS Chemical Biology, **2015**, 10 (9), pp 2099–2107.

Posterbeiträge

1. J. Weber, R. Horbert, C. Peifer:
Photoschaltbare Kinaseinhibitoren,
Life Science Studierendentagung, **2014**, Kiel, Deutschland.
2. R. Horbert, B. Pinchuk, P. Davies, D. Alessi, C. Peifer:
Photoactivatable Prodrugs of Antimelanoma Agent Vemurafenib,
Drug Discovery Chemistry, **2015**, San Diego (CA), USA.
2. B. Pinchuk, R. Horbert, P. Davies, D. Alessi, C. Peifer:
Photoactivatable Prodrugs of Approved Kinase Inhibitor Vemurafenib,
250th ACS National Meeting, **2015**, Boston (MA), USA.

DANKSAGUNG

An erster Stelle möchte ich meinem Doktorvater, Herrn Prof. Dr. Christian Peifer, für seine engagierte und motivierende Unterstützung sowie fortwährende Förderung besonders herzlich danken. Die Aufnahme in seinen sich über die Zeit stets wandelnden und weiter entwickelnden Arbeitskreis ermöglichte mir die Mitwirkung an vielseitigen und spannenden Projekten und Fragestellungen. Ich danke ihm für das entgegengebrachte Vertrauen und seine stete Bereitschaft zur wissenschaftlichen Diskussion.

Ein besonderer Dank gilt Boris Pinchuk für die fruchtbare Zusammenarbeit in diversen Projekten und das reibungslose Abstimmen von Arbeitsabläufen. Herzlich danke ich Jantje Weber, die mit ihrer Bachelorarbeit einen wesentlichen Beitrag im Axitinib-Projekt geleistet hat. Ein großes Dankeschön geht an Dr. Melanie Zindler und Alexander Döbber, mit denen sich weitere Schnittpunkte in den Photoprojekten ergeben haben.

Herzlicher Dank geht an Eugen Johannes, der meine Zeit am Institut von Anfang an begleitet hat und mir mit zahlreichen Hilfestellungen und Ratschlägen zur Seite stand. Ich danke Jakob Halekotte für seinen unerschütterlichen Humor und seine wunderbare Art. Eine fabelhaftere Bürogemeinschaft als mit euch beiden hätte ich mir nicht vorstellen können.

Miriam Schehr danke ich für die eine oder andere auswärtige Messung. Bei Lydia Kuhl und Dorian Schmidt möchte ich mich für den chemischen Input bedanken. Ich danke meinem ganzen Arbeitskreis für die angenehme und produktive Zusammenarbeit, das fröhliche Miteinander und den humorvollen Umgangston. Danke, dass durch euch Kaffee und Kuchen solch eine Bedeutung erzielen konnten. Vielen Dank an alle für das gründliche Korrekturlesen.

Martin Schütt danke ich für seine stete und kompetente Hilfsbereitschaft. Bei Dr. Ulrich Girreser möchte ich mich für die Beratung in zahlreichen analytischen Fragestellungen bedanken. Sven Wichmann gilt besonderer Dank für die zahlreichen und schnellen Rettungsaktionen bei HPLC-Problemen. Karl Willi Bock war unverzichtbar für den reibungslosen Betrieb diverser Geräte, ob im Praktikum oder Forschungslabor - ein großes Dankeschön für all die unverzüglichen Reparaturen. Dr. Dieter Schollmeyer danke ich für die Kristallstrukturanalysen.

Für die stets unkomplizierte und heitere Atmosphäre bei der Betreuung des 2. Semesters danke ich André Golldack, Eugen Johannes, Christopher Meier, Janis Rambow und Tamara Steinhauer. Ohne euch wäre die Zeit im Praktikum, bei der Aufsicht und beim Korrigieren nur halb so lustig gewesen.

Großer Dank gilt Carmen Krischkowski, die mir eine gute Freundin ist und mit der ich tolle Erinnerungen verbinde. Danke Birte Plitzko, für deine direkte Art und die Einführung in den Klettersport. Ich danke Julia Gudd, auf die man jederzeit zählen kann, für ihr tolles Engagement in jeder Hinsicht. Für die großartige Atmosphäre am Institut, sowie zahlreiche Ausflüge zum Strand, sonnige Stunden auf dem Mensarasen, gemeinsame Urlaube und so manche Feierlichkeit danke ich darüber hinaus: Björn Cohrs, Swetlana Gabel, Franziska Gersonde, Lena Knudsen, Jennifer Schneider, Laura Schwarz sowie zahlreichen bereits genannten Personen. Danke euch allen von ganzem Herzen für die unvergessliche Zeit.

Mein allergrößter Dank gilt meinen tollen Eltern und meiner unersetzlichen Schwester, die in jeder Lebenslage für mich da sind und auf die immer Verlass ist. Danke für eure uneingeschränkte Liebe und Unterstützung, ohne die ich nie so weit gekommen wäre.